

From the
Walter-Brendel-Zentrum für Experimentelle Medizin
At the Biomedical Center of the Ludwig-Maximilians-Universität München
Interim Director: Prof. Dr. med. Markus Sperandio

Time-of-Day Dependent Trafficking of Leukocytes Across
Lymphatics

Dissertation zum Erwerb des
Doctor of Philosophy (PhD) in Medical Research
an der Medizinischen Fakultät der Ludwig-Maximilians-Universität

submitted by
Stephan Jonas Holtkamp

from
Warburg, Germany

On
08.10.2020



Supervisor: Prof. Dr. Christoph Scheiermann

Second evaluator: Prof. Dr. Eloi Montañez Miralles

Dean: Prof. Dr. Reinhard HICKEL

Date of oral defense: 13.01.2021

Acknowledgements

I would like to express my gratitude towards my supervisor Christoph Scheiermann for giving me the opportunity to conduct fundamental research in his laboratory. Not only did he help designing this project, he was also constantly available for feedback, advice and ideas. I am thankful for his patience, providing me a lot of freedom in performing experiments and his trust. Without his exceptional guidance and contribution, this project would not have been realized.

I am grateful for having Jasmin Weber on my side in the laboratory. We basically started our PhDs together and I could not think of a more professional, organized and charming lab mate. Together we organized and ran the laboratory in Munich in Christoph's absence and without her this would not have been possible. We helped each other a lot in numerous experiments, thoroughly enjoyed working together and together organized a conference for IMPRS-LS.

Of course, I am very happy to be part of a lab that has various inspiring, friendly and welcoming current and past members including Louise Ince (she provided me with many skills to work on this project and initiated the project), Robert Pick (he helped lot for the analysis of migration data), Chien-Sin Chen (his experimental expertise was very helpful for this project), Coline Barnoud (she conducted experiments for this project in Geneva), Sophia Hergenhan (she helped during experiments). Likewise I would like to acknowledge Alba de Juan, Wenyan He, Chen Wang, Burak Kizil and Stéphane Jemelin for being a help throughout my time in the lab.

Furthermore, I appreciate the help of Markus Sperandio through which we could stay in Munich and the open environment of the whole second floor of the BMC for always having time for my questions.

Additionally, I would like to give credit to Lisa Richter and Pardis Khosravami from the BMC Flow Cytometry Core Facility, Nadine Ntaraklitsas from the Core Facility Animal Models, Julia Philippou-Massier from the LMU gene center, Cornelia Halin and George Aparisi from the ETH Zurich, Dietmar Vestweber and Leonie Holtermann from the MPI Münster and David Laubender (my flat mate from the beginning to the end) for their provided help and expertise.

I am proud to be a member of the IRTG914 and IMPRS-LS graduate schools, as I enjoyed the lectures, seminars, activities and courses. A special thank you goes to Verena Kochan, Hans-

Jörg Schaeffer, Ingrid Wolf and Marta Cipinska who supported me during my time being a student representative and helped a lot surviving as a PhD student. Last but not least I am very happy for every friend I made in each graduate school, such as Sergi Masgerau, Laura Perez, and many others.

I would also like to thank my friends and family, more specifically my...

... friends in Munich who helped relaxing after over-night experiments.

... brothers, Patrick and Christoph Holtkamp, for providing a helping hand and teaching me how to manage sarcasm and humor on a professional level.

...dad from which I got my drive to ambitiously work on projects (who funnily is a clock repairer by training)

... my best friend Lara Meier, which never failed cheering me up when experiments did not work.

... and my partner in crime, Viktor de la Motte, without him I would not be writing this thesis and would have not finished the PhD

Finally I cannot find words to express the full extent of gratitude towards my mom, who sadly cannot see me finishing, as she passed away half-way through the PhD. However I do know that she gave me the best skills I could think off that helped me to become a researcher and not lose the focus in life.

Abstract

232 words

The skin harbors numerous immune cells and a lymphatic vessel network coordinating initial steps of any immune response. Although the circadian clock has been identified as a key regulator of the immune system, influence of this clock on dermal lymphatic networks remains elusive. Here, I examined dermal dendritic cell (DC) trafficking using *ex-vivo* ear explant crawl-in assays allowing for the analysis of their migratory behavior. Assessment of cellular trafficking unveiled a time-of-day dependent migration of tissue-specific DCs towards and across lymphatic vessels, with the most prominent migration observed during the behavioral rest phase of mice. This circadian migration behavior was concerted by temporal up-regulation of trafficking molecules and enhanced chemokine micro patterning in lymphatic endothelial cells (LECs) as shown by quantitative immuno-fluorescence profiling. Moreover RNA sequencing of sorted dermal LECs uncovered an elevated adhesion gene expression during the rest phase. Chrono-pharmacological blockade and disturbance of chemotaxis, adhesion and transmigration of DCs within the lymphatic network abrogated circadian migration exclusively during the rest phase. Molecular oscillators of lymphatic vessels and DCs were then identified as key players since the genetic ablation of the core clock component *Bmal1* in either cell type diminished the circadian phenotype in cell migration. Together, this study establishes a novel link between the circadian clock and lymphatic leukocyte trafficking in the skin and provides potential targets for the optimization of both timed treatment of immune-dermatological diseases and vaccination strategies.

Table of Contents

Acknowledgements.....	V
Abstract	VII
List of figures.....	XI
List of tables.....	XIII
List of abbreviations.....	XIV
1 Rationale	1
2 Introduction.....	2
2.1 Basic concepts of immunity.....	2
2.1.1 Early steps of an immune response	3
2.2 Lymphatic vasculature	4
2.2.1 Anatomy and organization of the lymphatic system	5
2.2.1.1 Lymphatic biomarkers	7
2.2.2 Lymphatic heterogeneity	8
2.2.2.1 The lung lymphatic system.....	8
2.2.2.2 The small intestinal lymphatic system.....	8
2.2.2.3 The lymph node lymphatic system	11
2.3 The immune system of the skin.....	12
2.3.1 The functional anatomy of the skin	12
2.3.2 The immunological landscape of the skin	13
2.3.2.1 Dendritic cells.....	13
2.3.2.1.1 Langerhans cells	14
2.3.2.1.2 Skin conventional dendritic cell 1 and 2	14
2.3.2.2 T cells.....	17
2.3.2.3 Keratinocytes and innate lymphoid cells.....	18
2.3.2.4 Other immune cells	19
2.4 Dermal lymphatic leukocyte trafficking.....	19
2.4.1 The skin lymphatic system	19
2.4.2 Dendritic cell migration through skin lymphatic vessels	21
2.4.2.1 Interstitial migration.....	21
2.4.2.2 Adhesion and transmigration.....	24
2.4.2.3 Intraluminal crawling.....	26
2.5 Circadian rhythms.....	27
2.5.1 The clock machinery	27
2.5.2 Synergy of clocks and entrainment.....	30
2.5.2.1 Circadian terminologies.....	31
2.5.3 Circadian rhythms in immunity	31
2.5.3.1 Circadian leukocyte trafficking.....	32
2.5.3.2 Circadian rhythms in skin	35
2.5.4 Chronotherapy and the benefit of rhythms in immunity	36
2.6 Objective & aims.....	37
3 Materials and Methods.....	38
3.1 Materials.....	38

3.1.1	Buffers and media.....	38
3.1.2	Kits	38
3.1.3	Primers	39
3.1.4	Antibodies and staining reagents.....	39
3.1.4.1	Primary antibodies.....	39
3.1.4.2	Secondary antibodies and streptavidin	42
3.1.4.3	Isotype antibodies	43
3.1.4.4	Neutralization antibodies	44
3.1.5	Chemicals and reagents.....	45
3.1.6	Utilities.....	46
3.1.7	Machines	46
3.1.7.1	Microscope & flow-cytometer configurations	47
3.1.8	Softwares.....	48
3.2	Methods	49
3.2.1	Animals	49
3.2.1.1	Housing & animal law regulations	49
3.2.1.2	Light / darkness (LD) experiments	50
3.2.1.3	Tamoxifen treatment.....	50
3.2.1.4	DNA isolation	51
3.2.1.5	Genotyping PCR	51
3.2.1.6	Genotyping gel electrophoresis	53
3.2.2	Organ harvest & surgeries.....	54
3.2.2.1	Ear harvest	54
3.2.2.2	Bone harvest for bone marrow-derived dendritic cell isolation	55
3.2.2.3	Superior cervical ganglionectomy.....	55
3.2.3	Cell culture	56
3.2.3.1	Bone marrow-derived dendritic cell culture	56
3.2.3.2	CellTrace Violet bone marrow-derived dendritic cell stain	57
3.2.3.3	Granulocyte-macrophage colony-stimulating factor producing hybridoma cell culture.....	57
3.2.4	Crawl-in assays (cell trafficking assays)	58
3.2.4.1	Exogenous crawl-in assay (end-point)	58
3.2.4.2	Endogenous crawl-in assay	60
3.2.4.3	Live imaging of exogenous crawl-in assays	61
3.2.4.4	Short crawl-in assays with zone segmentation	61
3.2.5	Flow cytometry	62
3.2.5.1	Crawl-out assay and ear cellularity quantification.....	62
3.2.5.2	Sorting of skin LECs	65
3.2.6	Functional neutralization of proteins and chemokine gradient disturbance	66
3.2.7	Immunofluorescence staining.....	66
3.2.7.1	Quantitative immunofluorescence staining	66
3.2.7.2	Whole mount immuno-fluorescence staining	68
3.2.7.3	Intracellular whole mount staining of CCL21, GOLPH4, PROX-1 and KI67	68
3.2.7.4	CCL21 whole mount staining and gradient analysis	69
3.2.8	RNA sequencing of lymphatic endothelial cells	70
3.2.9	Statistical analysis	71
4	Results.....	72
4.1	Visualization of lymphatic vessels.....	72
4.2	Demonstration of rhythmic dendritic cell migration into dermal lymphatic capillaries..	75
4.3	Rhythmic protein and RNA levels in lymphatic endothelial cells.....	78
4.4	Evaluation of migratory behavior and chemotaxis ability amongst dendritic cell subtypes	87
4.5	Assessment of diurnal CCL21 gradient micro-patterning, adhesion and transmigration	93

4.6	Effects of lineage-specific clock deficiency on lymphatic dendritic cell migration.....	99
5	Discussion and future perspectives.....	106
5.1	Circadian rhythms in lymphatic dendritic cell migration.....	106
5.2	The role of oscillations in lymphatic protein and RNA expression.....	108
5.3	Temporal chemokine patterning during steady state – pointing towards rhythmic tolerance induction?	112
5.4	Chrono-pharmacological targeting of lymphatic leukocyte trafficking.....	114
5.5	Do cell type-specific intrinsic clocks govern rhythmic dermal leukocyte trafficking? ...	118
5.6	Outlook.....	119
5.7	Conclusion	122
6	Bibliography.....	i
7	Appendices	xix
7.1	Additional data.....	xix
7.2	Codes and algorithms.....	xx
7.3	Promoter binding sites of clock genes.....	xxxii
7.5	List of publications	xxxviii
7.6	Affidavit	xxxix
7.7	Confirmation of congruency between printed and electronic version of the doctoral thesis	xl

List of figures

Figure 2-1: Anatomy of lymphatic vessels	6
Figure 2-2: Lymphatic heterogeneity	10
Figure 2-3: The lymphatic leukocyte trafficking cascade	23
Figure 2-4: Components and interactions of the molecular clock.....	29
Figure 3-1: Genotyping gel electrophoresis.....	54
Figure 3-2: Bone marrow-derived dendritic cell culture viability and purity	57
Figure 3-3: Imaging chamber for ear whole mounts.....	58
Figure 3-4: Exogenous bone marrow-derived dendritic cell crawl-in assay.....	59
Figure 3-5: Endogenous crawl-in assay.....	60
Figure 3-6: Zone segmentation of the lymphatic interstitium.....	62
Figure 3-7: Skin dendritic cell & crawl-out assay gating strategy	64
Figure 3-8: Gating strategy of sorted lymphatic endothelial cells	65
Figure 3-9: Quantitative immunofluorescence analysis.....	67
Figure 3-10: Extracellular CCL21 gradient analysis	69
Figure 4-1: 2D Fluorescence microscopy of lymphatic biomarkers.....	73
Figure 4-2: 3D Lymphatic whole mounts of biomarkers in skin and small intestine.....	74
Figure 4-3: Higher trafficking capacity during the day in dermal lymphatic vessels	76
Figure 4-4: Circadian rhythm in dermal dendritic cell migration into lymphatic vessels	78
Figure 4-5: Tissue-specific oscillations in lymphatic adhesion and transmigration molecules....	80
Figure 4-6: Elevated expression, storage and traffic of intracellular CCL21 in dermal lymphatic endothelial cells	82
Figure 4-7: Lymphatic endothelial cells express a molecular clock and are transcriptionally most distinct between ZT1 and ZT19	85
Figure 4-8: Rhythmic adhesion gene signature in lymphatic endothelial cells	87
Figure 4-9: Diurnal rhythmicity in skin cellularity.....	88
Figure 4-10: Dermal dendritic cell subtype-specific rhythms in migration	90
Figure 4-11: Elevated activation and chemotaxis of dendritic cells during the day.....	92
Figure 4-12: Rhythmic CCL21 micro-patterning influences dermal dendritic cell distribution....	94
Figure 4-13: Manipulation of the CCL21 gradient leads to dysfunctional dendritic cell migration during the day.....	96
Figure 4-14: Chrono-pharmacological block of adhesion and transmigration reduces dendritic cell migration during the day	98

Figure 4-15: Lineage-specific clock deficiency leads to dysfunctional dermal dendritic cell trafficking.....	101
Figure 4-16: Loss of Bmal1 in lymphatic endothelial cells leads to downregulation of trafficking factors and chemokine micro-patterning	103
Figure 4-17: Genetic ablation of Bmal1 leads to alteration in ear cellularity and increased dendritic cell emigration	105
Figure 5-1: Future directions and arising projects	121
Figure 5-2: Time-of-day dependent trafficking of leukocytes across lymphatics.....	123
Figure 7-1: Live imaging of exogenous crawl-in assays	xix
Figure 7-2: Expression of genes associated with tolerance induction	xix
Figure 7-3: Ear cellularity and crawl-out assay using SCGx and <i>Myd88</i> ^{-/-} mice	xx

List of tables

Table 2-1: Activation and migration markers of dermal dendritic cells.....	17
Table 2-2: Molecules involved in dermal lymphatic dendritic cell trafficking.....	25
Table 2-3: Rhythms in murine trafficking molecules & chemokines	35
Table 3-1: Buffers and media	38
Table 3-2: Kits	38
Table 3-3: Genotyping primers.....	39
Table 3-4: Primary antibodies	42
Table 3-5: Secondary antibodies and streptavidin.....	42
Table 3-6: Isotype control antibodies.....	43
Table 3-7: Neutralization antibodies	44
Table 3-8: Chemicals and reagents.....	46
Table 3-9: Utilities and materials.....	46
Table 3-10: Machines.....	47
Table 3-11: Flow-cytometer configurations.....	48
Table 3-12: Microscope configurations	48
Table 3-13: Softwares	48
Table 3-14: Genotyping PCR master mix	52
Table 3-15: Genotyping PCR reactions	52
Table 3-16: Genotyping PCR product sizes	53
Table 3-17: Viability and purity check of bone marrow-derived dendritic cells.....	56
Table 3-18: Staining panels for crawl-outs, ear cellularity and phenotyping.....	63
Table 3-19: Staining panel for lymphatic endothelial cell sort	65
Table 3-20: Cell counts of sorted lymphatic endothelial cells.....	70
Table 5-1: Number of promoter binding sites for clock genes <i>Bmal1</i> , <i>Dbp</i> , <i>Nfil</i> and <i>Rora</i>	111

List of abbreviations

ACKR4	Atypical chemokine receptor 4
ALCAM	Activated leukocyte cell adhesion molecule
APC	Antigen presenting cell
<i>Arntl</i>	Aryl hydrocarbon receptor nuclear translocator-like protein 1
BEC	Blood endothelial cell
BM	Bone marrow
BMAL1	Brain and muscle ARNT-like 1
BrdU	Bromodeoxyuridine
BV	Blood vessel
CADM1	Cell adhesion molecule 1
CCG	Clock-controlled gene
CCL21	C-C motif ligand 21
CCR7	C-C chemokine receptor type 7
cDC	Conventional dendritic cell
ChIP	Chromatin immunoprecipitation
CLEC9a	C-type lectin domain family 9
CLOCK	Circadian locomotor output cycles kaput
Cry	Cryptochrome
CS	Cortical sinus
CSF1	Colony-stimulating factor 1
CT	Circadian time
CXCL1	CXC-chemokine ligand 1
DBP	D-box binding protein
DC	Dendritic cell
<i>Deaf1</i>	Deformed epidermal auto-regulatory factor 1
DETC	Dendritic epidermal T cells
dLN	Draining lymph node
DNGR-1	Dendritic cell natural killer cell lectin group receptor-1
EC	Endothelial cell
ECM	Extracellular matrix
EdU	5-ethynyl-2'-desoxyuridine
EPCAM	Epithelial cell adhesion molecule
ESAM	Endothelial selective adhesion molecule
FLT3	Fms-like tyrosine kinase 3
FTT3L	Fms-like tyrosine kinase 3 ligand
HA	Hyaluronan
HAT	Histone acetyl transferase
HSC	Hematopoietic stem cell
ICAM1	Intercellular adhesion molecule 1
iLN	Inguinal Lymph node
IRF8	Interferon regulating factor 8
JAM-A	Junctional adhesion molecule
L1CAM	L1 cell adhesion molecule
LC	Langerhans cell
LEC	Lymphatic endothelial cell
LFA-1	Lymphocyte function-associated antigen-1
LN	Lymph node
LTR	Leukotrienes
LV	Lymphatic vessel
LYVE-1	Lymphatic vessel endothelial hyaluronan receptor

MADCAM-1	Mucosal vascular addressin cell adhesion molecule 1
MALT	Mucosal-associated lymphoid tissue
MERTK	Proto-oncogene tyrosine-protein kinase MER
MHC	Major histocompatibility complex
MIP1	Macrophage inflammatory protein 1
MMP	Matrix-metalloproteinase
MMR1	Macrophage mannose receptor 1
MS	Medullary sinus
NFIL3	Nuclear factor interleukin 3
NK	Natural killer cell
PAMP	Pathogen-associated molecular pattern
PD-L1	Programmed death ligand 1
PDPLN	PODOPLANIN
PECAM-1	Platelet and endothelial cell adhesion molecule 1
Per	Period
PGE2	Prostaglandin E2
Plt	Paucity of lymph node T cell
PPAR	Peroxisome proliferator-activated receptor
PRC	Polycomb repressive complexes
<i>Prox-1</i>	Prospero homeobox protein 1
PTA	Peripheral tissue antigen
RAC1	Ras-related C3 botulinum toxin substrate 1
ROCK	RHO associated kinase
ROR	Retinoid-related orphan receptor
SCN	Suprachiasmatic nucleus
SCS	Sub-capsular sinus
SI	Small intestine
SIRP- α	Signal regulatory protein α
SMC	Smooth muscle cells
SMLV	Sub-mucosal lymphatic vessel
STR	Stromal cell
T _{CM}	Circulating T
TEM	Effector/memory T
TGF- β	Transforming growth factor β
T _H 17	T helper 17
TLR	Toll-like receptor
TNF	Tumor necrosis factor
TNFR	Tumor necrosis factor receptor
T _{reg}	Regulatory T
T _{RM}	Resident memory T
US-FDA	United States food and drug administration
VCAM1	Vascular cell adhesion molecule 1
VE-Cadherin	Vascular-endothelial-cadherin
VEGFR3	Vascular endothelial growth factor receptor 3
XCR1	X-c motif chemokine receptor 1
ZT	Zeitgeber time

1 Rationale

Our immune system is in daily contact with the environment. Every contact shapes and develops the immune system. As a result of this, microbes are continuously adapting as well, leading to new inflammatory challenges. Despite success and advances in modern research and therapies, it becomes more and more challenging to quickly tackle new diseases and develop therapeutic agents and strategies. One recent example to be mentioned here is the outbreak of the severe acute respiratory syndrome coronavirus 2 (SARS-CoV-2), highlighting how difficult and time consuming discovery of new therapies and treatment is. Thus, innovative strategies and improvements in therapy are required to successfully face currently existing and future diseases.

One way to more efficiently respond to potential threats is to partition immune responses to specific time windows during the day when they are most likely to occur. Daily, recurring rhythms in the environment greatly affect rhythms in intrinsic biological processes. Intrinsic rhythms are found in every aspect of physiology and allow for the adaptation and evolution of biological processes. In the last decades, researchers have identified biological rhythms to also occur in the immune system. Although research has uncovered circadian clocks in virtually every mature immune cell type, our understanding of how clocks influence the cell and overall immunity still remains relatively obscure. Thus, a better understanding of the rhythmic immune system is essential for the time-tailored application of immunotherapies.

The skin is the largest organ of the body and harbors a great diversity of immune cells as it presents one of the predominant entry points for pathogens. Thus, it is not surprising that the skin is a major site of infection and disease. The lymphatic system is crucial for fluid control, nutrient uptake, can be a site of bacterial dissemination and is exploited by cancer. For immune cells to initiate an immune response, the skin lymphatic vessel network is of high importance as it facilitates the correct and fast transport of antigens to the lymph node. Although basic concepts of the skin lymphatic biology are understood, it is not known how biological rhythms influence the skin lymphatic system. Thus, uncovering circadian mechanisms in the biology of skin lymphatics might be beneficial for basic immunology research and therapeutic strategies in vaccination, inflammation and diseases.

2 Introduction

2.1 Basic concepts of immunity

Although the immune system functions as one entity, it consists of various distinct cell types, each having unique and important roles. In general, it can be divided into the innate and adaptive immune system. The term 'innate' implies that receptors and mediators involved in an innate immune response are genetically encoded and do not undergo rearrangements or genetic variations. On the other hand, 'adaptive' immunity describes the genetic rearrangement of proteins involved in the adaptive response to ensure greater immune diversity. Together, the major roles of both are the adequate and correct elimination of microbial agents via the innate immune system, activation of the adaptive immune system via innate immune cells if it is appropriate to initiate an adaptive response, creating memory of adaptive responses and tolerance of self-antigens (sources used for chapters 2.1 and 2.1.1 include [1-3]).

The adaptive immune system consists of lymphocytes, which are together made up by B and T cells. Although they occupy a central stage in an immune response by determining the specificity of immunity, they rely on the innate immune system. The innate immune system presents antigens to the adaptive immune system and mediates immunologic functions. It entails dendritic cells (DCs), Langerhans cells (LCs), monocytes/macrophages, natural killer (NK) cells, neutrophils, mast cells, basophils and eosinophils. Together with the lymphocytes, they are grouped as leukocytes. Importantly, every leukocyte is presented with a great heterogeneity between organs and is highly specialized according to the organ it is residing in or migrating to.

The primary lymphoid organs, including thymus and bone marrow (BM), are the site of maturation of naïve leukocytes. Mature leukocytes then migrate to secondary lymphoid organs, consisting of lymph nodes (LNs), spleen, Peyer's patches and mucosal-associated lymphoid tissues (MALTs), and in the case of lymphocytes are scanning tissues for the presence of antigens to commence adaptive immune responses.

2.1.1 Early steps of an immune response

Early steps of an immune response include the capture of pathogens by antigen presenting cells (APCs) such as DCs, the processing of native antigens into peptides and their presentation by major histocompatibility complex (MHC) molecules, the migration of APCs through the extracellular matrix (ECM) and transmigration through blood and lymphatic vessels as well as the APC entry into LNs to activate and initiate the adaptive immune response. In this thesis the focus is on peripheral tissues and DCs. Therefore, the full adaptive immune response will not be discussed here.

Before DCs encounter any pathogen, they are resting in a steady-state homeostasis. During this mode, they are capable of capturing and presenting antigens to T cells with an outcome of tolerance but not an immune response. The encounter with potentially harmful agents, however, allows the DC to become fully activated and initiate an immune response. This diverse response is possible due to the DC's ability to sense changes in the environment by expression of different pattern recognition and activation receptors. These receptors, e.g. toll-like receptors (TLRs), engage with viruses and microbes (pathogen-associated molecular patterns (PAMPs) or danger-associated molecular patterns (DAMPs)) as well as inflammatory cytokines and help internalizing the native antigen.

Upon contact, DCs take up antigens by endocytosis, specifically macropinocytosis or receptor-mediated phagocytosis. After internalization, antigens are processed into peptides, targeted to MHCII-positive endosomes, sequestered, and bound to MHCII dimers within the endosome. MHCII dimers carry the processed peptides and present them to by-passing cells on their cell surface. In the absence of harmful antigens or danger signals, however, the MHCII complex is loaded with self-peptides to limit the auto-immune reactivity and promote self-tolerance. MHCI is expressed on every nucleated cell, while MHCII is restricted to APCs and specific cells like epithelial cells, important for tolerance. MHCI on DCs initiates elimination of infected and malignant cells by CD8⁺ T cells, whereas MHCII initiate the CD4⁺ T cell immune response. Different DCs are better in sensing specific types of antigens (bacterial membrane proteins, nucleic acids, etc.) and are adapted to the microenvironment they reside in.

To reach the LN and initiate an immune response or establish peripheral tolerance, the DC migrates through the ECM with the help of chemotactic gradients like chemokine C-C motif ligand 21 (CCL21). Due to receptors expressed on their surface, such as C-C chemokine receptor type 7 (CCR7), they are capable of following chemotactic gradients. DCs then utilize

lymphatic vessels (LV) as a route to reach the LN. The orchestrated mechanism of leukocyte trafficking into and through vessels depends on the type of vessel, but in general requires adhesion of the leukocyte to endothelial cells (ECs) lining the vessel wall and their subsequent transmigration through the endothelial layer.

If DCs arrive at the LN via the lymphatic route, they enter the stromal layer through a sinus of lymphatic endothelial cells (LECs), from which they migrate into the T cell zone and initiate the immune response. After activation of T cells, DCs undergo apoptosis, as their presence is no longer required.

2.2 Lymphatic vasculature

Mice and humans harbor two distinct types of vessel systems. The closed blood circulatory system is the mediator of continuous movement of body fluids, transporting oxygen and nutrients to the tissues. Moreover, it regulates the migration of molecules and immune cells to and from tissues with the help of a muscular pump, the heart.

On the other hand, the lymphatic system is a uni-directional and blind-ended system required for the high-pressure blood circulation. Small lymphatic capillaries line almost every major tissue, transport tissue draining fluid through larger collecting vessels into LN, from which it flows back to the blood stream. Movement of lymph through larger LVs is mediated by three major components: physical forces driving the initial formation of lymph in tissues, an intrinsic pump mechanism that pushes lymph forward, and extrinsic tissue pressures. Generally, LVs maintain fluid balances in every tissue by draining the blood capillary ultrafiltrate and extravasated plasma proteins back to the blood circulation. Furthermore, they are key players in transport of lipids and nutrients absorbed in the microvilli of the small intestine and are crucial for the transport of antigens and immune cells in case of an immune response and establishment of tolerance. Recently, it was also demonstrated that LVs play important roles in T cell development, are providing space for immune cell interactions and are targets of bacterial dissemination [4, 5].

The lymphatic system was first described by Hippocrates and Aristotle around 400 BC and, later, the Greek physician Claudius Galen described the mesenteric lymph nodes to be filled with a milky lymph or chyle, consisting of fats originating from the small intestine [6]. From 1622 onwards, first the small intestine villus LV (also called 'lacteal') was described [7], the back-flow of lymph from lacteals through larger LVs into the subclavian vein was found [8] and

the term *vasae lymphaticae* leading to the current term 'lymphatic vessel' was coined [6, 7]. With the help of electron microscopy [9], intra-vital microscopy [10], the development of LEC isolation techniques [11] and the generation of genetic reporter mice expressing fluorescent proteins under the promoters of biomarkers such as *prospero homeobox protein 1(Prox-1)-GFP* [12], many aspects of the lymphatic role in the immune system have been revealed in modern research.

2.2.1 Anatomy and organization of the lymphatic system

LVs are described in almost every type of tissue. Although lymphatics in cartilage, cornea, or the central nervous system are yet to be fully understood, there are hints that also these organs harbor LVs either under steady-state or inflammatory conditions [13-16].

The lymphatic system has a fractal and tree-like geometric organization, allowing for large surface area coverage with small initial lymphatics or capillaries. Lymphatic capillaries are located in close proximity to the microcirculation and – depending on the organ – form either a network/plexus or are completely blind-ended. They consist of a single layer of LECs and a discontinuous/porous basal membrane [17]. Capillary LECs have a distinct oak leaf shape allowing them to interdigitate and form loose discontinuous junctions and flaps (**Figure 2-1**). The formation of these 'primary lymphatic valves' is hypothesized to create a balance between high permeability for lymph uptake and adequate amounts of cellular trafficking [18-20]. Necessary for functional valves are aggregates of junctional proteins forming tight junctions, which are anatomically and functionally different to blood EC (BEC) tight junctions, and called 'buttons'. These contain junctional proteins like vascular endothelial (VE)-CADHERIN, OCCLUDIN, CLAUDIN-5, endothelial selective adhesion molecule (ESAM) and junctional adhesion molecule A and C (JAM-A/C) holding LECs together [21]. The space between the buttons, also described as 'flaps', showcase another set of proteins like lymphatic vessel endothelial hyaluronan receptor 1 (LYVE-1) and platelet and endothelial cell adhesion molecule 1 (PECAM-1/CD31; absent in buttons), and is the major site of leukocyte entry providing the lowest resistance [21, 22]. However, the exact shape of lymphatic capillaries depends largely on the tissue location (**Figure 2-1** and **Figure 2-2**).

Lymphatic capillaries drain into collecting lymphatics which are morphologically and functionally dissimilar. Collecting vessels have a single layer of LECs surrounded by a medial layer of circular smooth muscle cells (SMC), which can either be continuous or discontinuous

[23]. The larger the collecting vessels, the more layers of SMCs can be found. In contrast to capillary button structures, collecting vessel LECs form ‘zipper-like’ tight junctions, allowing for a more sealed vasculature prohibiting any fluid uptake or transmigration of cells under steady-state conditions [21, 24]. In addition to this, they embody periodic ‘secondary lymphatic valves’. These bicuspid valves prevent the backflow of lymph [25, 26] (**Figure 2-1**). Each space between two consecutive valves form a functional contractile unit or *lymphangion*, translated as ‘lymph heart’ [27]. The coordinated contraction of lymphangions together with functional secondary valves grants effective intrinsic pumping of the lymph and its content. Some tissues like the skin also have pre-collecting vessels that do not have SMCs but secondary valves, a mix of oak leaf- and rhombic-shaped LECs, together acting as conduits [21, 28] (**Figure 2-2**).

Collecting vessels merge into large LVs (*afferent lymphatics*) that transport the lymph to the draining LN (dLN), from which the lymph is transported back to the blood circulation via *efferent lymphatics* (notably, in some parts of the system the lymph passes multiple LNs before coalescing into the blood circulation) [29]. Usually, 1 – 2 efferent lymphatics leave the LN and drain into the cisterna chyli, which leads into the left lymphatic duct, also known as the thoracic duct, depending on the site of origin [30, 31]. These large LVs flow back into the blood stream via the left and right subclavian vein [30]. In summary, most of the transported lymph reenters the blood circulation via the thoracic duct, the rest via the right lymphatic duct [32, 33].

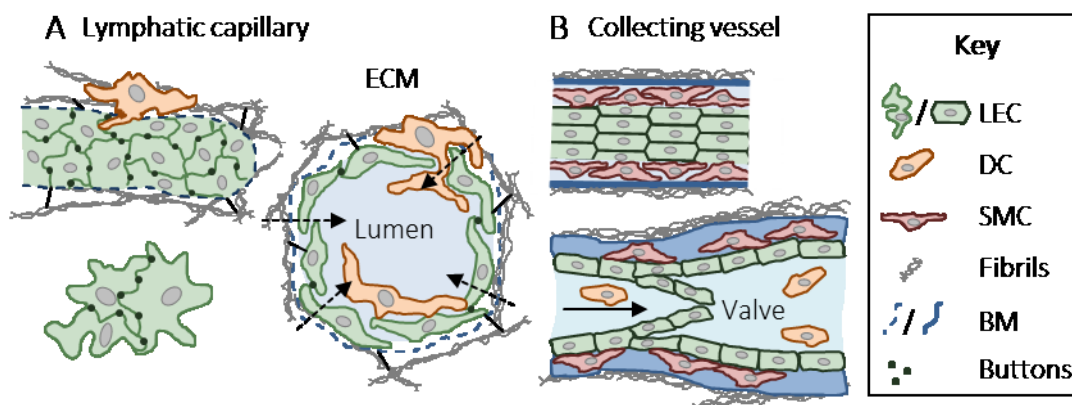


Figure 2-1: Anatomy of lymphatic vessels

(A) Lymphatic capillaries are blind-ended vessels surrounded by a discontinuous basal membrane (BM), embedded into an extracellular matrix (ECM) using anchoring filaments and fibrils. The oak leaf-shaped lymphatic endothelial cells (LECs) line the capillary and partly overlap each other at the junctions. LECs are connected via buttons, small aggregates of junctional proteins. Between buttons, flaps are formed helping cells such as dendritic cells (DCs) transmigrate.

(B) Collecting vessels consist of rhombic-shaped LECs, covered with layers of smooth muscle cells (SMCs), inserted in a wide and continuous BM. They promote passive flow by generating pressure gradients. Valves made up by LECs prevent backflow and thus ensure uni-directional flow.

2.2.1.1 Lymphatic biomarkers

In order to identify LECs and distinguish them from other types of ECs or stromal cells, research has uncovered several proteins currently used as common lymphatic biomarkers. Importantly, all these markers are expressed on other cells as well, but the combination of different markers allow for LEC discrimination.

Probably the most important protein in lymphatic biology is PROX-1. Already at day 9.5 to 14.5 of the embryological state the entire skin of the murine embryo is covered by lymphatic vasculature [34]. It is not surprising, that these initial LEC precursors are PROX-1⁺, as *Prox1* encodes a transcription factor directing lymphangiogenesis, LEC development and LEC movement during sprouting [35]. It is often described as the lymphatic master control gene, as it regulates the expression of other lymphatic markers such as the vascular endothelial growth factor receptor 3 (VEGFR3) and LYVE-1 [36].

VEGFR3 (also known as fms-related tyrosine kinase 4 (FLT4)) is a receptor tyrosine kinase binding VEGF-C and VEGF-D and mediating lymphangiogenesis [37-40]. Besides its expression on BECs during development, it is strongly expressed on LECs, with a high expression on lymphatic capillaries and lower expression on lymphatic collecting vessels [40].

The integral membrane glycoprotein LYVE-1 is a homologue of CD44, involved in leukocyte migration [41] and, because of this, highly expressed in lymphatic capillaries (depending on the organ of interest) [42, 43]. Although LYVE-1 expression is also found on macrophages, liver and spleen sinusoidal endothelium, it is a commonly used marker for immunofluorescence staining of LECs in tissues [44]. Its specific role in lymphatic leukocyte trafficking is thoroughly discussed in **2.4.2.2**.

PODOPLANIN (PDPLN), initially described on rat kidney podocytes, is a mucin-type transmembrane glycoprotein suggested to be involved in intraluminal crawling of leukocytes within LVs [45, 46]. PDPLN together with CD31, a pan-endothelial marker, are widely used in fluorescence-activated cell sorting (FACS) of LECs as they are expressed in capillary and collecting LVs albeit differences in their degree of expression [20, 43]. PDPLN is also expressed on stromal cells, like fibroblastic reticular cells, in the LN [47]. The proposed role in lymphatic leukocyte trafficking is further discussed in **2.4.2.3**.

These proteins, together with Forkhead box protein C2 (FOXC2), important for lymphatic secondary valve maturation [48], REELIN, expressed especially in collecting LVs and important in T cell trafficking and leukocyte trafficking in the CNS [42, 49], and VE-CADHERIN have been extensively used as reporters for deletion, mutation or addition of genes in LECs [12, 50-53].

2.2.2 Lymphatic heterogeneity

In the past years, researchers recognized the influence of the microenvironment of different organs in shaping their vessels, whether it is blood vessels or LVs, and creating a tissue-specific entity and molecular heterogeneity [54-58]. The great majority of experiments performed in this thesis are focusing on the skin lymphatic system (*see 2.4*). However, some experiments also focus on the lymphatic system of the lung, small intestine and LN. Consequently, these lymphatic systems will be briefly introduced and their importance in the immune system highlighted.

2.2.2.1 The lung lymphatic system

The lymphatic system of the lung is heavily involved in fluid balance of alveoli, allowing for optimal gas exchange. In mice, LYVE-1⁺ lung capillary LECs are observed in lung lymphatic networks in juxta-alveolar connective tissue lining with airway or blood vessels but not within thinner alveolar walls. They further converge into larger collecting vessels having valves and SMCs [59-62] (**Figure 2-2**).

Apart from clearing excess fluids, the lung lymphatic system is involved in trafficking of immune cells. Lung lymphatics express chemokines like CCL21 and facilitate the transport of antigen loaded APCs to dLNs [63]. Lung lymphatics show strong chemokine immunoreactivity and increase expression after infection with *Mycoplasma pulmonis* [59]. Furthermore, lung LECs have unique expression patterns of surface molecules supporting the trafficking of immune cells like the activated leukocyte cell adhesion molecule (ALCAM) [64]. However, extensive research is required to further understand how immune cells use the lymphatic route in the lung to migrate to dLNs and initiate immune responses or tolerance.

2.2.2.2 The small intestinal lymphatic system

In comparison to the lung lymphatic system, the small intestinal lymphatic system is understood in more detail. Roles of LECs in the small intestine are very diverse, as they range between dietary absorption, tolerance of symbiotic microflora and food antigens to protection against infections [62].

The small intestine contains millions of micro-villi, each comprising a central lacteal that is surrounded by a dense network of villus blood capillaries [65]. Lacteals branch into a submucosal network of lymphatics [66]. Additionally, the small intestine harbors another lymphatic network, located in parallel with circular or longitudinal muscle fibers in the *muscularis mucosae* [66]. These two networks then merge near the mesenteric border and flow into mesenteric dLNs via mesenteric LVs [66]. Notably, the small intestinal lymphatic system by definition does not have collecting vessels [67] (**Figure 2-2**).

For its role in fat metabolism, lacteal LECs can take up chylomicrons containing fatty acids and nutrients released from enterocytes by transcellular crossing [68, 69]. Lacteals then transport the chylomicrons with the help of SMCs into the submucosal lymphatics [70, 71].

Small intestinal LECs support tolerance induction and aid in immunity against pathogens from the lumen of the small intestine. It has been shown that lymphatics are established in close relation to parafollicular regions in the small intestine [62]. Loss of intestinal and mesenteric dLN LECs in mice expressing diphtheria toxin under the promoter of *Lyve1* resulted in severe gut inflammation, sepsis and lethality [52].

Generally, small intestinal lymphatics express common markers such as LYVE-1, PROX-1, NEUROFILIN-2 and VEGFR3 [72]. Nevertheless, global transcriptomic analyses of intestinal LECs have proven their uniqueness in comparison to for example skin LECs [73].

In the small intestine, DCs are one of the major cell types migrating through lymphatics to mesenteric dLNs. Vital for migration is a CCL21 gradient as *CCR7^{-/-}* mice have reduced numbers of mesenteric dLN DCs [74, 75]. Likewise, innate lymphoid cells (ILCs) use the CCL21 gradient and lymphatic route for trafficking to mesenteric dLNs [76]. Currently, it is not known, how neutrophils and T cells migrate through intestinal lymphatics and more research is required to fully understand the immune function of the lymphatic system in the small intestine.

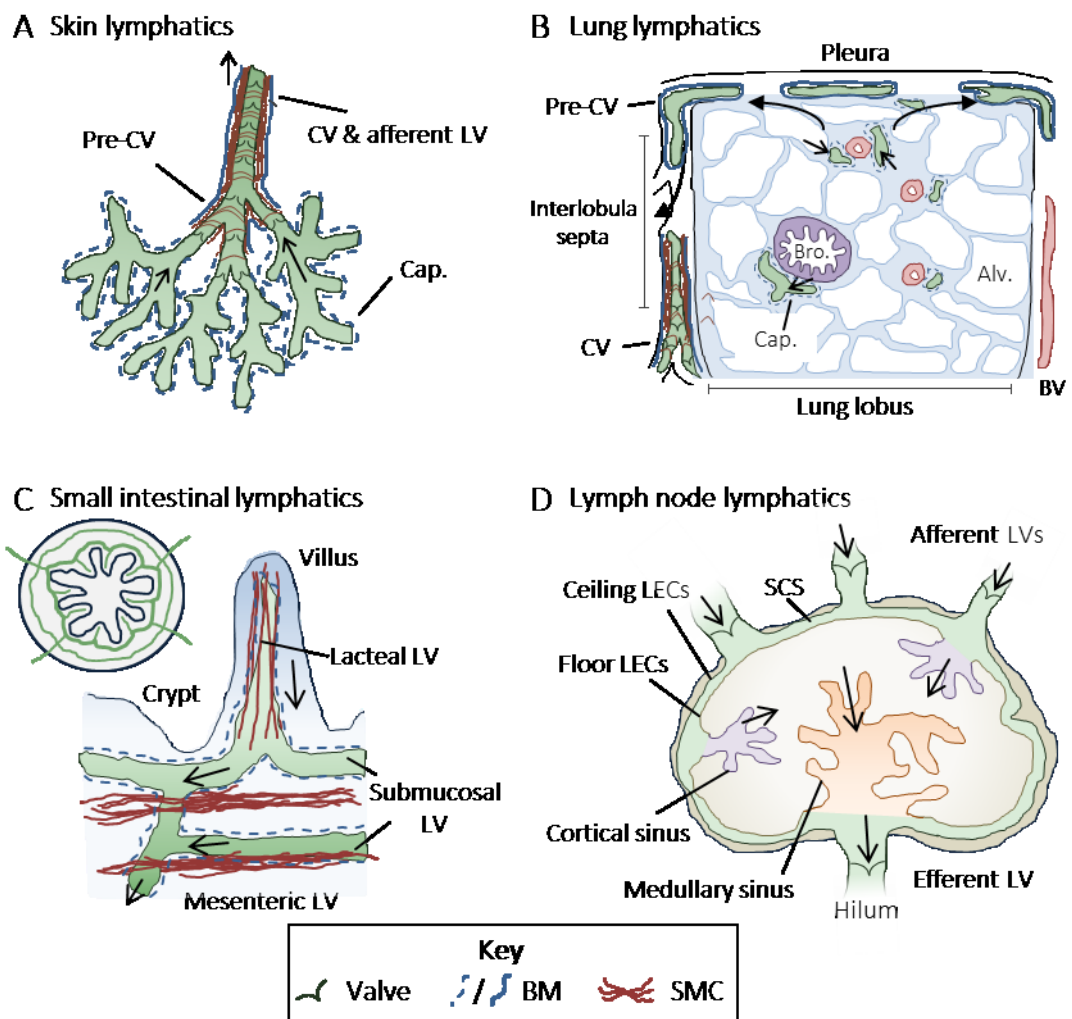


Figure 2-2: Lymphatic heterogeneity

(A) Skin lymphatics comprise blind-ended capillaries (Cap.) flowing into pre-collecting vessels (Pre-CV) and drain into collecting vessels (CV) resembling the afferent lymphatic vessels (LV). While capillaries have a discontinuous basal membrane (BM), Pre-CVs and CVs are mounted with smooth muscle cells (SMCs) and a sealing BM. Afferent LVs transport lymph to draining lymph nodes (dLN).

(B) Within the lung lobe, small lymphatic capillaries reside in the juxta-alveolar space and neighbor blood vessels (BVs) and bronchioles (Bro.). Capillaries then drain into CVs via pre-CVs in the interlobular septa, shown as a cross-section. Alv. = alveolus.

(C) Small intestinal lymphatics start with singular capillaries / lacteal LVs in the villus, embedded in SMCs. They flow into submucosal LVs, which converge and form mesenteric LVs, flowing to mesenteric LNs. The submucosal LVs can be divided into two networks. All lymphatics in the small intestine are capillaries as they have a discontinuous BM, only mesenteric LVs outside the small intestine resemble a CV shape.

(D) Afferent lymphatics feed into the LN and merge into a subcapsular sinus (SCS), that consist of two layers, ceiling and floor LECs. The floor LECs form cortical sinusoids, which coalesce into the interstitial space, from which the medullary sinus drains towards the hilum. Efferent LVs then leave the LN via the hilum containing the drained lymph from the medullary sinus.

2.2.2.3 The lymph node lymphatic system

The lymphatic system of the LN is one of the best studied lymphatic systems. The LN creates a special environment for LEC and BEC interaction and is the major site for the initiation of an immune response.

Modern approaches using single-cell RNA sequencing and immunofluorescence microscopy have shown molecularly and geographically distinct lymphatic beds within the LN [58]. Afferent lymphatics feed into a subcapsular sinus (SCS) that is lined by two different layers of LECs, ceiling and floor LECs. Ceiling LECs are adhering to the collagenous matrix of the capsule and floor LECs rest on a meshwork of stromal cells and conduit bundles [77]. The SCS contains migrating leukocytes from the afferent lymph, as well as resident SCS macrophages, that constantly survey the lumen and bypassing DCs [78] (**Figure 2-2**).

Further downstream are several LEC sinusoids. Due to high complexity, exact lining and morphology of medullary and cortical sinusoids are not completely understood. However, recent advances in optical tissue clearing of LNs have opened new possibilities in the analysis of sinus architectures [79, 80]. In mice, at the hilum of the LN, LECs form a medullary sinus (MS) that traverses through the medulla into the cortical area of the LN and thus becomes a cortical sinus (CS). At the hilum, this medullary sinus converges into an efferent lymphatic vessel, leaving the LN. These sinusoids are filled with egressing lymphocytes and resident medullary sinus macrophages [81] (**Figure 2-2**).

Every type of LEC in the LN expresses numerous biomarkers (PROX-1, LYVE-1, mucosal vascular addressin cell adhesion molecule 1 (MADCAM1), CCL20, programmed death-ligand 1 (PD-L1), macrophage receptor MARCO and PENTRAXIN3) enabling molecular differentiation. Additionally, they express cytokines (IL-7, macrophage colony-stimulating factor 1 (CSF1) or VEGF), chemokines (CCL21, CCL20, CXC-chemokine ligand 1 (CXCL1), CCL5, CXCL19 and atypical chemokine receptor 4 (ACKR4)), trafficking molecules (intercellular adhesion molecule 1 (ICAM1) and vascular cell adhesion molecule 1 (VCAM1)), C-type lectins, scavenging receptors, Fc receptors as well as TLRs [82, 83]. A strong geographical and molecular heterogeneity promotes diverse immunological roles for LN LECs, including the adequate transport of leukocytes, antigen binding and uptake, interaction with resident macrophages, shaping of stromal cells and BECs as well as the immune response.

2.3 The immune system of the skin

The skin is the major focus point of this thesis. In the following parts, the functional anatomy, and immune cell landscape of the skin will be introduced in detail.

2.3.1 The functional anatomy of the skin

Histologically, murine skin does not differ much from that of other mammals. From outside to inside, the outer epithelial *epidermis* covers the connective tissue of the *dermis*, separated by a basement membrane, which in turn covers an underlying *hypodermis* composed of mostly fatty tissue. Between the hypodermis and a layer of loose connective tissue called *adventitia* are fine layers of skeletal muscle (*panniculus carnosus*) [84].

Although the epidermis is rather thin, it consists of four distinct layers (top to bottom), the keratinized *stratum corneum*, *stratum granulosum* (containing granules feeding the chemical barrier of the skin), *stratum spinosum* (supporting the integrity of the epidermal layer) and *stratum basale* (accommodating stem cells as well as melanin pigment). The dermis contains connective tissue together with blood and lymphatic vessels, hair follicles, associated adnexal glands and a strong innervation. The mouse ear skin specifically contains a thick layer of cartilage at the hypodermal / adventitial layer [84].

Physiologically, the skin can be divided into four distinct layers or barriers (outside to inside): The microbiome barrier, chemical barrier, physical barrier, and immune barrier. Although their functions are distinct, they partly overlap.

The outermost microbiome barrier hosts commensal bacteria, fungi, and viruses, covering all surface areas of the skin. The microbiome of the skin in mice and humans is unique and differs from the microbiome of the large intestine [85, 86]. The skin microbiome serves as a barrier as it actively stimulates immune cells to produce antimicrobial peptides and proteins, increases innate immune alertness and produces antibiotics to prevent survival of harmful, non-symbiotic bacteria, as shown in human studies [87-89].

Although the second barrier, called the chemical barrier, is less defined, it is pivotal for the third, the physical barrier. The chemical barrier contains factors that create an acidic milieu and together with amino acids and their derivatives, electrolytes, urea, and lactates form the natural moisturizing factor of the skin [90, 91].

The physical barrier is built up by the *stratum corneum* and incorporates a vast system of tight junctions. Corneocytes (cells making up the *stratum corneum*) are continuously built up by terminal differentiation of maturing and moving keratinocytes [92, 93]. Additionally, the granulocytes of the *stratum granulosum* secrete granules containing keratin filaments and lipids [92].

Lastly, the immune barrier contains an armada of resident and migratory immune cells. Together, they maintain barrier integrity, sense PAMPs and DAMPs, initiate adequate immune responses and local dermal inflammations, recruit cells from the circulation and further contribute to barrier repair and homeostasis [94].

2.3.2 The immunological landscape of the skin

Under steady-state conditions, the cellular composition of epidermis and dermis spans a variety of resident immune sentinels like DCs (and other APCs), T cells, keratinocytes, innate-like cells, as well as adaptive tissue-resident memory cells. Together they form one unit to build up a functional immune system. During an inflammation or pathological conditions, macrophages, monocytes, mast cells, B cells, neutrophils and eosinophils become key players as well.

2.3.2.1 Dendritic cells

DCs are the major APC type in the immune system and observed in every tissue. Since DCs are mainly responsible for the generation of the adaptive immune response, they are vital for the establishment of long-term and protective immunity. DCs make up a major leukocyte population in the skin and are highly motile considering they can enter the skin from the circulation, migrate and patrol through the ECM, and traffic into dLN via lymphatics.

Skin DCs are a highly heterogeneous population with functionally specialized subsets. Ontogenetically, LCs do not belong to DCs but arise from yolk-sac derived macrophages while dermal DCs are closely related to conventional DCs (cDCs, henceforth named as dermal cDCs), and derive from hematopoietic stem cells (HSC) and thus the BM. During steady-state conditions, LCs reside in the epidermis, whereas dermal cDCs localize in the dermis. Generally, DCs are phenotypically described as CD3⁻, CD66b⁻, CD19⁻, CD20⁻ but MHCII⁺ cells, separating them from T cells, B cells and neutrophils. All DC subsets interact with skin-resident and –

infiltrating immune cells during steady state and inflammation and transport cutaneous antigens to dLNs to initiate T cell responses. In order to fulfill their immune functions, DCs utilize and up-regulate a great variety of activation markers. An overview can be seen in **Table 2-1**.

2.3.2.1.1 Langerhans cells

During skin homeostasis, LCs are the only resident APCs in the epidermis, making up for 3-5% of epidermal cells, and protrude their dendrites into the interstitial space of the epidermis to acquire antigens [95]. Murine LCs are CD11c⁺, LANGERIN/CD207⁺, epithelial cell adhesion molecule positive (EPCAM⁺), as well as CD11b⁺, CX3CR1⁺ and signal regulatory protein α (SIRP α)/CD172 α ⁺ [96, 97] (**Table 2-1**). EPCAM is commonly used for FACS- and LANGERIN for immunofluorescence microscopy-based identification of LCs. LCs have a unique ontology as they do not need fms like tyrosine kinase 3 (FLT3) and its ligand FLT3L to develop (in contrast to cDCs). Instead, they require interactions with keratinocytes (see **2.3.2.3**) and derive from macrophage progenitors via IL-34, CSF1 signaling and transforming growth factor β (TGF- β) [98, 99].

Once LCs are activated by external stimuli, e.g. UV light exposure or haptens, they reduce their adhesion to epithelial cells by down-regulating E-CADHERIN and start migrating towards LVs in the dermis [100]. Emigration from the epidermis is particularly facilitated by EPCAM (reduction of adhesion to keratinocytes) and CXCR4/CXCL12 interaction [96, 101]. Additionally, IL-1 β , IL18 and tumor necrosis factor (TNF) secreted from keratinocytes are described to be important as *Il1b*^{-/-} and *Tnfr2*^{-/-} mice show decreased hapten-induced migration [102-105]. Within the dLN, LCs primarily initiate tolerogenic immune responses and promote the activation of T helper 17 (T_H17) cells. The migration of LCs through the ECM and into LVs is explained in more detail in 2.4.2. In this thesis, LCs are defined as MHCII^{high}, CD11c^{high}, EPCAM/LANGERIN⁺ and CD103⁻.

2.3.2.1.2 Skin conventional dendritic cell 1 and 2

Skin cDCs can be divided into cDC1s, cDC2s and double-negative (DN) cDCs, exclusively found in the skin, whereas cDC1s and cDC2s are found across all lymphoid tissues. In skin, cDCs are restricted to the dermis. The major focus of this thesis lies on cDC1 and cDC2.

In contrast to LCs, skin cDC1s, cDC2s and DN cDCs are derivatives of BM HSCs and make up the majority of DCs. In general, the development and differentiation of cDC1 and cDC2 is rather complex. Throughout development, cDCs share the same progenitors until they diverge into cDC1 and cDC2. Two of the major growth factors involved in their development are FLT3L and CSF2 [97]. One important protein to be mentioned here is C-type lectin domain family 9 member a (CLEC9a) also known as *dendritic cell natural killer lectin group receptor-1 (Dngr-1)*, which is a phenotypic marker of common cDC progenitor cells [106]. CLEC9a expression is preserved in cDC1s, whereas cDC2s lose CLEC9a expression during development [107]. This is particularly important for the mouse model of *EYFP;Clec9acre-Bmal1^{flox/flox}* used here. Due to the nature of cDC development, it is possible to only target cDCs and not LCs or macrophages by using the promoter of *Clec9a* [107].

cDC1s are characterized as X-C motif chemokine receptor 1 (XCR1)⁺, CLEC9a⁺, cell adhesion molecule 1 (CADM1)⁺, TLR3⁺, CD141⁺, CD11c⁺ and interferon regulatory factor 8 (IRF8)⁺ [108] (**Table 2-1**). Moreover, they are positive for CD103, which is a marker frequently used for identification in flow-cytometric analyses. One of the major differences between dermal cDC1s and lymphoid tissue cDC1s is the expression of CD103 instead of CD8 α [109]. cDC1s are highly mobile and have a high turnover rate, rapidly migrating into the T cell zone of the LN [110]. Although cDC1s are not as efficient as cDC2s in activating CD4⁺ T cells in the LN [111], they are adroit in the presentation of soluble exogenous and cell-associated antigens on MHC1 proteins, a process called cross-presentation or cross priming [112]. This is particularly important in herpes simplex virus-1, influenza virus or vaccinia virus infections [113-116]. It has also been shown that cDC1s are more efficient in priming CD8⁺ T cells due to their expression of XCR1, the receptor of XCL-1 expressed by memory CD8⁺ T cells, and initiating T_H1 immune responses [117]. Notably, a lot of knowledge is missing on dermal cDC1s, as the majority of knowledge derives from CD8 α ⁺ cDC1s.

cDC2s are the most common population of dermal DCs. cDC2s are described as IRF⁺, CD11b⁺, CX3CR1⁺, SIRP α ⁺, CCR2⁺ and CD11c⁺ [97] as well as negative for CD64, proto-oncogene tyrosine-protein kinase MER (MERTK) and Ly6C to allow absolute discrimination from macrophages and monocytes [118] (**Table 2-1**). In contrast to cDC1s, cDC2s co-express many genes associated with monocyte-derived DCs and their transcriptome is less unique [119]. However, this might be due to unresolved heterogeneity within cDC2s. Whereas cDC1s specifically migrate into the T cell zone, cDC2s are particularly described in the lymphatic sinusoids within the LN [120]. Functionally, cDC2s are specialized for detection of pathogens

within the cytoplasm, express a broad range of TLRs (except for TLR3 and TLR12) and are the only murine cDC subset expressing TLR7 [121, 122]. Furthermore, they seem to be involved in chemo-attraction, as they continuously express macrophage inflammatory protein 1 α/β (MIP1 α/β) and CCL5, especially after exposure to TLR7 and TLR9 agonists [123]. In addition, cDC2s are better in CD4⁺ T cell priming due to more efficient MHCII presentation and promote T_H2 immune responses [124, 125]. Given these data, more knowledge is required on dermal cDC2s, as most of the studies have focused on non-dermal cDC2s.

Finally, the mouse dermis contains a very minor population of DCs, which has been phenotyped as XCR1⁻, CD11b^{low} (coining the name 'double-negative') LANGERIN⁻, CD11c^{low-int}, CD103^{low}, CD301b⁻, EPCAM^{low}, CD64⁻, SIRP α ⁺, and CX3CR1⁺ [97]. This population is not described in any other mouse tissue than the skin and does not have a human homolog. Studies have shown that they are critical in a contact hypersensitivity response after administration of the agent dibutyl phthalate on the skin [110].

In this thesis, skin cDC1s and cDC2s are defined as MHCII^{high}, CD11c^{high}, EPCAM⁻/LANGERIN⁻ and CD103^{+/-} (respectively). DN DCs are not investigated in this study.

Protein	Function	LC	cDC1	cDC2	Ref
CD103	$\alpha_E\beta_7$ integrin, binding E-CADHERIN, adhesion	-	+	-	[108, 126]
XCR1	Chemokine receptor, CD8 ⁺ T cell activation	-	+	-	[108, 117]
CLEC9a	Antigen cross-presentation, dead cell receptor, binds F-ACTIN	-	+	-	[108, 127]
CD11b	CD18 binding integrin, adhesion, migration	+	-	+	[108, 128]
LANGERIN	Anti-viral immunity, pathogen binding	+	-	-	[108, 129]
CD301b	Antigen presentation, CD4 ⁺ T cell activation	-/+	-	+	[124, 125]
SIRP α	Docking SHP-1 & SHP-2, migration	+	-	+	[97, 130]
CCR2	Chemotaxis to inflammatory sites	-	-	+	[97]
F4/80	T cell activation and peripheral tolerance	+	-	+	[97, 131]
EPCAM	CLAUDIN, CADHERIN and general junctional interaction	+	-	-	[96, 100]
CX3CR1	CX3CL1 receptor, inflammation, chemotaxis	+	-	+	[97, 132]
CCR7	CCL21/19 receptor, chemotaxis	+	+	+	See 2.4.2.1
CD24	CD4 ⁺ T cell activation	+	+	-	[133, 134]
CD205	Cross-presentation, dead cell receptor antigen uptake	+	+	+	[133, 135]
CD80	Costimulatory molecule T cell activation	+	+	+	[136]
CD86	Costimulatory molecule T cell activation	+	+	+	[136]

Table 2-1: Activation and migration markers of dermal dendritic cells

Role and function of molecules in dendritic cell migration through skin lymphatics. LC= Langerhans cell, cDC1/2= conventional dendritic cell 1/2. All other abbreviations are explained in text.

2.3.2.2 T cells

The majority of T cells found in the skin are resident (epidermis and dermis), but to a lesser extend recirculating and adaptive T cells can also be found in the dermis: resident $\gamma\delta$ T cells and CD8⁺ resident memory T (T_{RM}) cells line the stratum spinosum of the epidermis (only in mice) and upper layers of the dermis. Less CD4⁺ T_{RM} are found in the dermis together with circulating CD4⁺ and CD8⁺ T cells (T_{CM}). In general, T cells are defined as CD3⁺ cells. $\gamma\delta$ T cells, also known as dendritic epidermal T cells (DETCs; only in mice) have a T cell receptor (TCR) with a single antigenic specificity [137]. It is believed that $\gamma\delta$ T cells in the epidermis are

representing a primitive and limited adaptive immune system that is replaced by T_{RM} over time after accumulating antigenic pathogen contacts. Albeit their inability to recognize peptides bound to MHC molecules [138], they are activated by stress proteins and can secrete IL-17 to activate other immune cells further downstream [139, 140].

In comparison to $\gamma\delta$ T cells, $CD8^+ T_{RM}$ are better understood. One unique feature of $CD8^+ T_{RM}$ throughout the body is that the core gene expression signature is conserved between organs [141]. $CD8^+ T_{RM}$ can directly kill virally infected cells [142] and promote an antiviral state in the skin by releasing type I interferons (IFNs) and thus activating keratinocytes and other skin cells [143]. $CD4^+ T_{RM}$ are rapidly activated by pathogen re-challenge and promote pathogen clearance from the skin [144].

In case of an inflammation, the skin is also accommodating regulatory T cells (T_{reg}) aiding in the local immune response [5].

2.3.2.3 Keratinocytes and innate lymphoid cells

Keratinocytes constitute a major element in the immune system of the epidermis. They are acting as a first line of defense against potentially harmful microbes [145] and release cytokines like IL-1 β , IL-18, IL-6, IL-10, TNFs and under specific circumstances chemokines like CXCL9, CXCL10, CXCL11, and CCL20 for immune cell activation and guidance [146]. Furthermore, keratinocytes express TLRs, thus contributing to their role in the forefront of an immune response [146]. An immune response is often induced by keratinocytes as the initial contact with PAMPs leads to a release of cytokines activating APCs, in turn upregulating MHCII molecules [146]. Keratinocytes are necessary for self-renewal and existence of LCs as they release IL-34 and express the keratinocyte-derived integrins $\alpha_v\beta_6$ and $\alpha_v\beta_8$ compulsory for LC residency [147].

Accumulating evidence has shown that also ILCs (ILC1-3) are found in skin [148]. Skin ILC subsets comprise migratory ILC1-3s. ILC1s are constantly trafficking between the circulation and LNs promoting T_H1 cell generation via IFN- γ production after immunization in a $CD62L^-$ and $CCR7^-$ -dependent manner. In contrast to this, ILC2s are resident in hypodermal areas whereas ILC3s are most likely residing in the epidermis [149].

2.3.2.4 Other immune cells

The dermal layer of the skin comprises various other immune cells, such as monocytes and macrophages, mast cells, neutrophils, eosinophils, and B cells.

Skin macrophages are MHCII^{int}, CD115⁺, F4/80⁺, CD11b⁺, CSF1R⁺, Ly6C[±] (monocytes are Ly6C⁺, macrophages Ly6C⁻), CCR2⁻, CD64⁺, and MERTK⁺ and thus just by the phenotype are similar to cDCs [133]. However, tracing of genetic lineage and for example specific expression levels of CD64 and MHCII allow for a differentiation between DCs and macrophages. Monocytes and macrophages closely associate with hair follicles and are pivotal to local immunity [150]. Monocyte derived macrophages and DCs are especially important in local inflammations (e.g. after hapten painting) and activation of T cells [151]. More importantly, macrophages actively contribute to a healthy skin homeostasis by being a positive regulator in hair regeneration, wound repair, cancer defense, and nutritional salt balance [152].

Mast cells play a crucial role in allergic responses and the recruitment of immune cells. Further they are involved in wound healing by interaction with fibroblasts [153]. Skin neutrophils (CD66b⁺) come into play during inflammatory events by phagocytosing invading pathogens in case of a skin barrier malfunction, releasing of neutrophil extracellular traps (NETs) to immobilize pathogens and releasing chemokines to recruit more neutrophils to inflamed sites [153]. Neutrophils also secrete LAMININ 5β-3 to induce adhesion of keratinocytes and are involved in angiogenesis to help out in wound repair [154, 155].

Likewise, B cells (CD19⁺/B220⁺) are involved in delayed-type hypersensitivity reactions and involved in cutaneous autoimmune diseases by producing skin specific autoantibodies [153].

2.4 Dermal lymphatic leukocyte trafficking

The major focus point in this thesis is the migration of skin DCs through LVs, as introduced in the following.

2.4.1 The skin lymphatic system

The skin lymphatic system is substantial for fluid homeostasis, transport of lymph containing various immune cells and antigens to the dLN as well as adequate immune responses, vaccinations and tolerance establishment [72, 156-158]. The structure of the network is

dependent on the thickness of the skin [159], but in general, capillaries and collecting vessels are lined in the upper and lower dermis and resemble a typical shape already described (see 2.2.1 and **Figure 2-1**). Just below the epidermis, lymphatic capillaries form a network of draining vessels with 10-30 μ m in diameter (but can reach up to 70 μ m depending on the type of skin and inflammatory state) [159, 160]. These capillaries then drain deeper into the lower cutaneous layer, forming a plexus of collecting vessels (via pre-collecting vessels) including intraluminal valves, a thick basement membrane and coverage of SMCs (see 2.2.1) [161]. These collecting LVs then merge and form large afferent LVs by decreasing their density but increasing their diameter in hypodermis and subcutaneous layers [159]. Finally, large collecting afferent LVs follow alongside arteries and eventually merge into the SCS of the dLN [162] (**Figure 2-2**).

Dermal LECs from the lymphatic capillaries are defined as CD31⁺, LYVE-1⁺, PDPLN^{int}, VEGFR3⁺, CCL21^{high}, VE-CADHERIN⁺ and PROX-1⁺; LECs from pre-collecting vessels are CD31⁺, LYVE-1^{low}, PDPLN⁺, VEGFR3^{intermediate}, CCL21^{high}, VE-CADHERIN⁺ and PROX-1⁺; collecting vessel LECs are CD31⁺, LYVE-1⁻, PDPLN⁺, VEGFR3^{low}, CCL21^{intermediate}, VE-CADHERIN⁺ and PROX-1⁺ [35, 40, 41, 45]. Another marker to identify the LVs of the skin is LAMININ, a structural protein in the basement membrane of vessels [163].

Under homeostatic, non-inflammatory conditions and based on early cannulation studies conducted in sheep and healthy humans, the lymph of the skin contains numerous leukocytes, such as T cells (80-90%), DCs (5-15%) and in lower numbers neutrophils, eosinophils, basophils, monocytes, and B cells [164-166]. The T cell fraction can be divided into effector/memory CD4⁺ T_{EMs} (majority), CD4⁺ T_{regs} (approximately 20%, numbers increased during inflammation) and CD8⁺ T cells (minority), as demonstrated using adoptive transfers of naïve lymphocytes and transgenic mice expressing photo-convertible proteins like *Kaede* or *Kikume* [167-173]. Interestingly, and in contrast to the studies presented above, in laboratory mice equal percentages of DCs and T cells migrate to the dLN [167]. This is likely due to housing within an almost-pathogen free and sterile environment, leading to general antigen-inexperience and thus, lower numbers of CD4⁺ T_{EMs} [174].

Herein, the focus of lymphatic trafficking is set onto DCs only. In general, trafficking of T cells and neutrophils through lymphatics is less well described, but has been concisely reviewed by Schineis and colleagues [175].

2.4.2 Dendritic cell migration through skin lymphatic vessels

In the past 20 years, the majority of the current understanding of DC trafficking has been established. Despite major efforts and great studies, the migration cascade is only now starting to be understood.

In summary, the DC trafficking cascade can be divided into interstitial migration, LV entry via adhesion and transmigration, intralymphatic crawling, and the passive transport for entering the dLN.

Except for passive transport in large collecting vessels, DCs rely on specific molecules involved in chemotactic guidance, and cell to cell contact. The current knowledge is largely based on either (time-lapse) imaging and flow-cytometric analyses of ear explants (crawl-in assay or crawl-out assay, see 3.2.4 or 3.2.5.1) or adoptive transfers of DCs into the skin and dLN [22, 176]. Together they could show, that DCs first actively migrate through small pores within the ECM of the skin [177]. They are guided by chemotactic cues to be able to reach capillaries [178]. Surpassing the flap valves of LECs, they first adhere to LECs and then transmigrate into the lumen of the vessel. Once intraluminal, DCs crawl back and forth on the inner wall of LECs, until they eventually enter the collecting vessels [179]. With the help of pressure gradients, the secondary valves and contractions, the DCs are then passively transported to the dLN [180, 181] (**Figure 2-3**). The current *state-of-the-art* research investigating proteins involved in DC migration to dLN via LVs is summarized in **Table 2-2**.

2.4.2.1 Interstitial migration

In order to migrate through LVs, DCs first need to arrive at the lymphatic capillary and become activated. To overcome a dense environment of heparin sulfate proteoglycans, hyaluronan (HA), fibronectin and type I collagen fibrils, DCs perform an amoeboid migration pattern [182-184]. Under steady-state conditions, DCs migrate through the ECM with a speed of approximately 4µm/min [185] and require about 1h for up to 100µm to navigate to a lymphatic capillary from the point of initial mobilization [186]. The number of DCs migrating towards lymphatics is considerably low at steady-state. However, under inflammatory conditions such as contact hypersensitivity the amount and speed of trafficking DCs is increased. This is due to keratinocyte-mediated activation of resident DCs via released prostaglandins, cytokines and leukotrienes [186, 187]. Additionally, inflammation also causes

increased interstitial fluid flow, accelerating the DC movement. Nevertheless, the interstitial migration appears to be random, unless a chemokine gradient has been reached [178].

Once the DC is activated, it relies on chemotactic guidance to reach the lymphatic capillary. To date, only a few chemokines and respective receptors have been functionally described to be involved in the DC guidance and migration within the skin: CCR7/CCL21/CCL19, ACKR4, CXCL12/CXCR4 as well as CX₃CL1/CX₃CL1R (**Table 2-2**).

The chemokine CCL21 (and its receptor CCR7) is by far the best-studied molecule in skin lymphatic trafficking. CCR7 is upregulated on maturing DCs [188], whereas CCL21 is continuously expressed and released from LECs [189, 190], with higher expression in capillaries than in collecting vessels [179]. Genetic ablation of CCR7 and antibody-mediated blockade of CCL21 led to a stark reduction of lymphatic DC migration, proving its importance [191-193]. The positively charged C-terminus of CCL21 is bound to heparan sulfate-containing glycosaminoglycans present in the ECM and on the surface of LECs [194, 195]. Due to this and to continuous release, CCL21 forms a haptotactic, interstitial gradient, radiating around LVs with a maximum length of 80µm [178]. In contrast to other chemotactic gradients, CCL21 is built up exponentially, which is uniquely sensed by DCs [178]. Upon binding to CCR7, CCL21 increases the activation state of DCs directing the amoeboid movement through a complex environment and intensifies both the actin polymerization through small GTPases Ras-related C3 botulinum toxin substrate 1 and 2 (RAC1/2) and the nuclear contraction via the RHO associated kinase ROCK [177, 185, 196].

In mice, CCL21 exists in two forms, CCL21-Leucine and CCL21-Serine (due to its two genes *Ccl21a* and *Ccl21b/c*). Experiments with paucity of LN T cells (*Plt^{-/-}*) KO mice could show, that CCL21-Leucine is mainly expressed by peripheral LVs, whereas CCL21-Serine by e.g. LN LECs [197, 198]. CCL21 is stored in the Golgi network of the LEC before release [199]. Besides its continuous release, CCL21 is immediately secreted upon docking of DCs onto LECs due to enhanced Ca²⁺ signaling and in turn boosts the activation of transmigrating DCs [199]. DCs can proteolytically cleave off the positively charged C-terminal of CCL21, which increases the solubility of CCL21 and leads to a stronger recruitment of DCs, but this has only been shown *in-vitro* [200] (**Figure 2-3**).

In contrast to CCL21, CCL19 is not expressed by LECs but by DCs playing only a minor role in trafficking as for example FITC-painting on CCL19^{-/-} ears did not reveal any DC migration defects through dermal LVs [201]. Other chemotactic pathways like ACKR4, CX3CL1 or CXCL12 are either involved in sequestering CCL19 to inhibit sensitization of CCR7 receptors or upregulated during inflammation to increase DC chemotaxis [202-206]. Dermal LECs also produce other chemokines and receptors, such as CCL26, CXCL1 or CXCR1, but these are

either utilized by other immune cells or functional studies about their impact on DC trafficking in the skin are lacking, which is why they are not further described here [206].

Before DCs can adhere to LECs, they need to migrate through a porous basement membrane. 1µm pores within the basement membrane can be extended to 2µm making enough room for transmigrating DCs. Additionally, small deposits of CCL21 within these pores aid DCs to ascertain correct migration via haptotaxis [22, 187] (**Figure 2-3**). Once the DCs have successfully crossed the basement membrane, they are ready to adhere to LECs and transmigrate into the lumen.

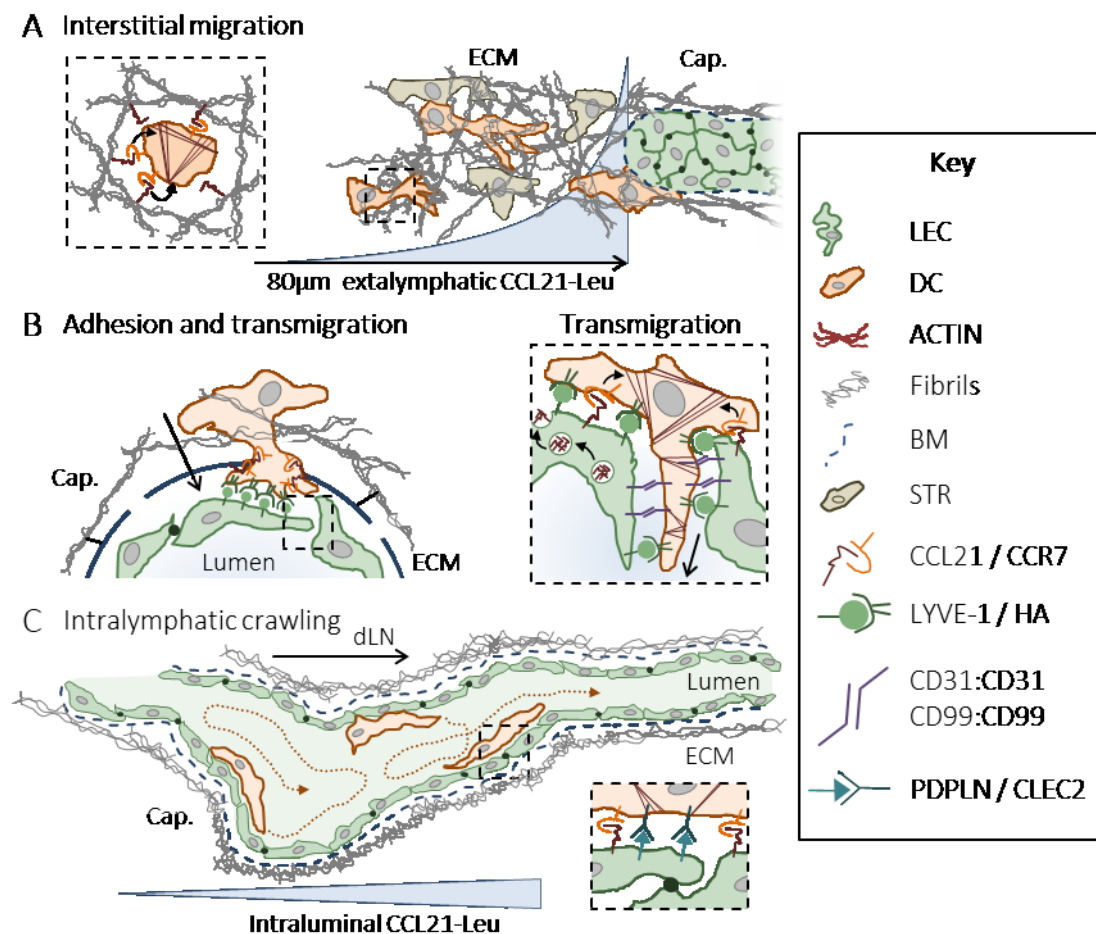


Figure 2-3: The lymphatic leukocyte trafficking cascade

(A) During interstitial migration, dendritic cells (DCs) perform an amoeboid movement towards a chemotactic CCL21-Leucine (Leu) gradient built-up by lymphatic endothelial cells (LECs) lining lymphatic capillaries (Cap.). The exponential, extralymphatic gradient has a length of approx. 80µm, is attached to extracellular matrix (ECM) fibrils and interacts with CCR7 on the surface of DCs. Upon binding of DCs, actin starts polymerizing and contractions occur, creating propulsions.

(B) Adhesion of DCs onto LECs is initiated by interactions of CCL21, residing in the pores of the basal membrane (BM). Upon contact, hyaluronan (HA) on the DC surface binds to LYVE-1 on the LEC surface. DCs dock onto LECs, which in turn release further CCL21 aiding in DC activation. Transmigration is facilitated by homophilic interactions between CD31 and CD99.

(C) Within the lumen of capillaries, DCs follow an intraluminal gradient of CCL21-Leu and bind molecules like PODOPLANIN (PDPLN) on the surface of LECs with CLEC2. Crawling of DCs on the luminal surface occurs bi-directionally. STR= stromal cell.

2.4.2.2 Adhesion and transmigration

In contrast to leukocyte transmigration through the blood vessel (BV) endothelium, for which interactions between $\beta 2$ integrins and their Ig superfamily counter receptors are crucial [207], the crossing of the lymphatic endothelium relies on a bipartite system. Early studies investigating the function of ICAM1 revealed a role in cDC and LC trafficking from skin to dLN – but only under inflammatory conditions [208]. Moreover, antibody-based blockade of ICAM1, VCAM1 or lymphocyte function-associated antigen 1 (LFA-1) markedly reduced inflammation-induced DC trafficking from the skin to the dLN [205]. On the contrary, a study using adoptively transferred pan-integrin^{-/-} DCs showed no defects in steady-state migration into lymphatic capillaries and dLNs, which was confirmed using CD11c YFP⁺/VE-CADHERIN *Cre/Rosa26* Fl RFP⁺ chimeric mice [177, 187]. Thus, under steady-state conditions, dermal DCs traffic in an integrin-independent manner, whereas during inflammation, integrins are important and upregulated to maximize DC recruitment [206].

As a consequence, recent studies started out identifying trafficking markers important under steady-state conditions. One marker strongly expressed by capillaries is LYVE-1. LYVE-1 and its interaction with HA on the DC surface is vital for skin DC transmigration as pharmacological blockage or genetic ablation of LYVE-1 reduced transmigration of dermal DCs [41]. Employing superselectivity, LYVE-1 is able to only interact with HA on the DC surface but not on the ECM [209]. This is possible due to a high density of HA on the DC surface glycocalyx, selectively required for homo-dimerization and finally binding to LYVE-1 [210-212]. Further LYVE-1 is involved in lymphatic endothelial junctional relaxation, promoting the diapedesis of DCs [213] (**Figure 2-3**). A full list of other proteins involved in transmigration or chemotaxis is summarized in **Table 2-2**.

Molecules	State of knowledge	ST?	Ref
ACKR2	On LECs, regulating discrimination between mature and immature DCs.	+	[214]
ACKR4	On keratinocytes, scavenges CCL19 in epidermis.	+	[202]
ALCAM	On hLECs, block reduces DC emigration from LVs.	-	[215]
CCR7/CCL21	DC chemotaxis by extra- and intravascular gradients, CCR7 ^{-/-} & CCL21 blockade reduce DC migration to dLNs, <i>plt</i> ^{-/-} mice do not reduce dermal DC trafficking.	+	[178, 179, 188, 190-193, 197, 198]
CCR8/CCL1	Regulation of monocyte-derived DC migration to dLN.	+	[216]
CD137	On LECs, potentiates DC transmigration by upregulating ICAM1, VCAM1 and CCL21, shown <i>in-vitro</i> .	-	[217]
CD31 & CD99	Support DC adhesion and transmigration by homophilic interaction, shown <i>in-vitro</i> .	+	[218]
CX ₃ CL1/CX ₃ CL1R	CX ₃ CL1 block and deletion reduces DC traffic to dLNs.	-	[204]
CXCL12/CXCR4	DC chemotaxis by extravascular gradient, CXCR4 block reduces DC traffic to dLNs.	+	[205]
ICAM1/VCAM1	On LECs, upregulated during inflammation & regulating DC migration.	-	[206, 208, 219]
JAM-A/C	JAM-A ^{-/-} mice & JAM-C block enhance DC migration to dLNs.	+	[220, 221]
L1CAM	On LCs and LECs during inflammation, <i>Tie2-Cre;L1cam</i> ^{fl/fl} mice reduce DC migration to dLNs.	+/-	[222]
LTR-B4 & LTR C4	Binding to DCs, upregulate CCR7 & CCL19, enhance migration to dLNs.	+	[223, 224]
LYVE-1	On LECs, mediates DC adhesion to LECs, <i>Lyve1</i> ^{-/-} & blockade reduces DC migration to dLNs	+	[209]
MMP-2 & MMP-9	In cDCs & LCs, block reduces LV emigration of DCs.	+/-	[225, 226]
MMR-1	On LECs, influencing migration of LCs to dLNs (not significant).	+	[227, 228]
PDPLN/CLEC2	Less intraluminal CLEC2 ^{-/-} DC crawling, reduced traffic to dLNs, CLEC2 initiates actin polymerization.	+	[229]
PGE2	Binds to DCs, enhances migration to dLN modulating CCR7 signaling and MMP-9 expression.	+	[226]
ROCK	In DCs, induces integrin de-adhesion, block reduces DC migration to dLNs	+	[185]
S1P ₁	Regulation of DC migration to dLNs.	+/-	[230]
SEMA3A	In LECs, activates nuclear contraction in DCs, DCs in <i>Sema3a</i> ^{-/-} mice reduce migration to dLNs & LV entry.	+/-	[231]

Table 2-2: Molecules involved in dermal lymphatic dendritic cell trafficking

ACKR= atypical chemokine receptor, ALCAM= activated leukocyte cell adhesion molecule, ICAM1= intercellular adhesion molecule 1, VCAM1= vascular cell adhesion molecule 1, JAM-A/C= junctional adhesion molecule A/C, L1CAM= L1 cell adhesion molecule, LTR= LEUKOTRIENE, LYVE-1= lymphatic vessel endothelial receptor 1, MMP-2 = matrix metalloproteinase-2, MMR-1= macrophage mannose receptor 1, PGE2= prostaglandin E2, ROCK= rho-associated protein kinase, Sema3A= SEMAPHORIN 3A, ST= steady state, Tie2= ANGIOPOIETIN-1 receptor tyrosine kinase. Other abbreviations are found in text.

2.4.2.3 Intraluminal crawling

After successful transmigration into the lumen of LVs, DCs start relocating to the dLN. In contrast to blood vessels, in LVs DCs crawl bi-directionally until they eventually enter collecting vessels, as shown by time-lapse imaging of YFP⁺ tagged DCs [179]. Recent studies have proposed, that the intra-capillary space is more than a highway to the dLN since DCs have been observed interacting with T cells within the space [179] (**Figure 2-3**).

The term 'intraluminal crawling' is based on the fact, that the movement of DCs is not or only partly based on passive flow and pressure gradients, but rather on protein interactions and chemotactic gradients, that stimulate physical propulsion of DCs. Initial capillaries are not contractile due to missing SMCs, have an estimated lymph flow rate of only 200-300 μ m/min (2-3 orders of magnitude slower than blood capillaries and only a bit faster than the interstitial flow rate) and do not provide secondary valves [185, 232, 233]. Together, these features do not favor passive flow. Instead, DCs follow an intraluminal CCL21 gradient together with interactions of proteins like PDPLN or ICAM1 on the intraluminal LEC surface with a speed of around 5.7 μ m/min [185] (**Figure 2-3**).

The intraluminal CCL21 gradient is sequestered on the surface of LECs and could be rebuilt *in-vitro*. During *in-vitro* shear stress of 0.015dynes/cm², close to physical lymph flow rates within the capillary, LECs secrete CCL21 from the luminal surface, which is rebound downstream to form a directionally oriented gradient [179]. The functionality of this gradient was further evidenced by employing CCL21 blocking antibodies or CCR7^{-/-} DCs ablating DC emigration from lymphatic capillaries [179] (**Figure 2-3**).

Despite required flow rates, CCL21 is likely sequestered with the help of other proteins like PDPLN. PDPLN is expressed on the intra- and extra luminal side of skin LECs, binds CCL21 with a high affinity and is involved in DC trafficking, as it binds CLEC2 on the surface of DCs [45, 229, 234]. Furthermore, *Clec2*-deficient DCs display decreased crawling on PDPLN⁺ vessels and reduced overall migration to dLN [229] (**Figure 2-3** and **Table 2-2**).

Under inflammatory conditions, proteins like ICAM1 are upregulated on the intra-luminal surface, promoting an accelerated DC movement, which could be pharmacologically reduced in an *in-vitro* environment [206]. As with adhesion to the outer LEC surface, the adhesion and retraction at the inner surface also requires ROCK [185]. Nevertheless, the intraluminal crawling is by far the least investigated part of lymphatic migration.

Once the DCs have reached the collecting vessels, passive transport takes over: internal (contractions through SMCs) and external pressure gradients together with controlled back-flow via secondary valves establish a passive flow of lymph. Recent observations reported by

Cornelia Halin (ETH Zurich, Switzerland) displayed direct trafficking of DCs into collecting vessels with the help of upregulated VCAM1 during inflammation (3rd Swiss vascular research symposium, Lucerne, November 14, 2019). This evokes the hypothesis that LVs under inflammation undergo a remodeling towards a venular phenotype, allowing for maximal and fast paced trafficking of DCs. This, however, remains to be elucidated.

The entry of DCs into the dLN is gated by numerous proteins, chemotactic gradients and interactions with other immune cells but will not be discussed here.

2.5 Circadian rhythms

Not only are many proteins on immune cells under the control of a circadian clock, but also factors in different vasculatures show rhythmicity in expression. In this part, the molecular clock and entrainment of peripheral clocks and their influence on rhythmic leukocyte trafficking are discussed.

2.5.1 The clock machinery

The majority of organisms on this planet coordinates its behavior to daily environmental changes generated by the earth's rotation. These changes include temperature, light/darkness and seasonal cycles. Additionally, behavior is adapted according to food uptake and availability. The continuous exposure to environmental cycles acts as a driving force for evolution and development of organisms. As a response organisms tune their metabolism and the immune system accordingly by establishing 24h rhythms in physiological processes [235]. These daily, circadian rhythms (*circa diem*, 'for about a day') impose oscillations in cells across many species, including fungi, cyanobacteria, plants, flies, birds and humans. Approximately 10-20% of the mammalian genome is under direct, more than 20% under indirect, circadian control [236, 237]. This means, that at least 20% of genes experience a peak in expression once every 24h.

This temporal programming is concerted by an intrinsic biological clock, preserved across different species [235]. In mice, virtually every cell contains the components of the clock machinery in its nucleus, including all leukocyte subsets [238]. Cells devoid of a nucleus, like erythrocytes, also possess a time-keeping mechanism, which, however, is driven by a

rhythmic redox sensing system [239, 240]. The most obvious output of this clock machinery is the sleep-wake cycle, but also many other aspects of the mouse are influenced, such as locomotor activity, body temperature, cardiovascular and digestive system as well as endocrine and immune system [241-243]. It is possible that these biological clocks evolved a billion years ago as a response to potential damage through ionizing radiation and oxidative stress during exposition of single-stranded nucleic acids, e.g. during cell division [244]. This might be supported by the fact that DNA excision repair is tightly controlled by the molecular clock as well [245].

The central circadian pacemaker, or central clock, is located in the suprachiasmatic nucleus (SCN) in the hypothalamus, consists of around 20,000 nerves [246] and entrains the peripheral clocks via endocrine and systemic cues [238, 247]. The SCN receives direct light input from the retina and resides above the optic chiasm, allowing it to translate the light information from the solar cycle into biological rhythms; it is furthermore resistant to phase perturbations from internal cues [238, 247]. Both the peripheral and central clocks work cell-autonomously. Yet, the interaction between both is required for synchrony. This synchrony is vital as otherwise oscillations in peripheral clocks of multicellular organisms become desynchronized and flatten out over time [238].

Essentially, both the master and peripheral clock share the same molecular architecture [248, 249] as demonstrated in serum shock experiments on fibroblasts in an *in-vitro* culture setting [250]. The core clock components consist of intertwined oscillatory transcription-translation feedback loops concentrating around the transcription factor aryl hydrocarbon receptor nuclear translocator-like protein 1 (ARNTL) or brain and muscle ARNT-Like 1 (BMAL1, encoded by *Arntl*) and its heterodimerization partner circadian locomotor output cycles kaput (CLOCK) [251]. Molecularly, the clock machinery consists of at least three interlocking feedback loops (Figure 2-4).

The BMAL1:CLOCK feedback loop.

Within the nucleus, BMAL1 and CLOCK form the heterodimeric basic helix-loop-helix-PAS (PER-ARNT-SIM) transcription factor complex BMAL1:CLOCK, which activates the transcription of clock controlled genes (CCGs) by binding to respective E-boxes [251]. Two of these genes are the repressor genes *Period 1/2/3* (*Per*) and *Cryptochrome 1/2* (*Cry*). PER and CRY heterodimerize in the cytoplasm, form the repressor complex PER:CRY and relocate into the nucleus to inhibit BMAL1:CLOCK, reducing further transcription of CCGs. PER:CRY are degraded via ubiquitin-dependent pathways and a 24h cycle starts anew with fresh

BMAL1:CLOCK dimers being formed [252-254] (**Figure 2-4**). In addition to this, kinases (CKI α , CKI δ , and CKI ϵ) and phosphatases (PP1, PP5) play an important role in PER:CRY degradation, nuclear movement as well as regulation of its activity, respectively [255, 256].

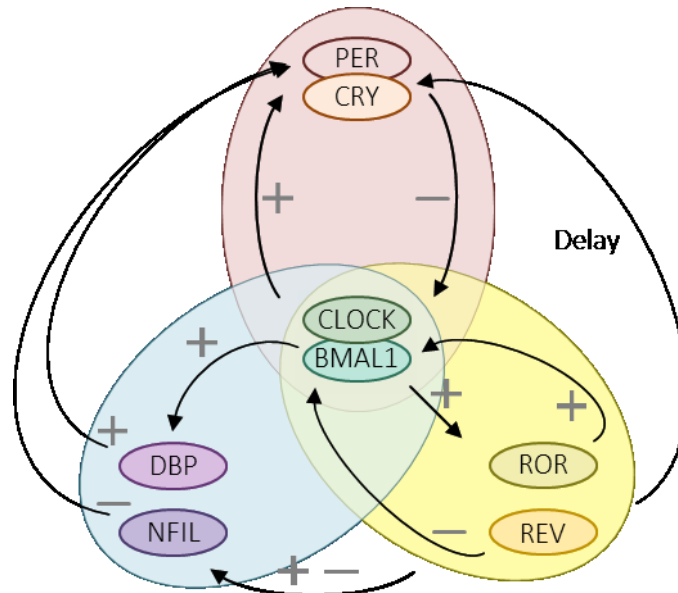


Figure 2-4: Components and interactions of the molecular clock

Heterodimer BMAL1:CLOCK positively regulates the transcription of clock controlled genes like *Per*, *Cry* (forming the heterodimer PER:CRY), *Dbp*, *Ror* and *Nr1d1/2* (REV-ERBs; REV). PER:CRY and REV-ERBs negatively regulate *Bmal1*, whereas RORs positively influence *Bmal1* transcription. DBP positively and NFIL3 negatively regulate PER transcription and are modulated by ROR/REV-ERB. These also delay the expression of *Cry* mRNA. Other abbreviations can be found in the text.

The REV-ERB – ROR feedback loop

The second transcription-translation feedback loop is generated by the clock controlled transcription factors retinoid-related orphan receptors (ROR α , β , γ) and REV-ERBs (α , β ; encoded as *Nr1d1* and *Nr1d2*) [257, 258]. While RORs generally activate the transcription of BMAL1, REV-ERBs decrease the transcription rate of *Bmal1* by binding to orphan receptor elements (ROREs) in its promoter region in a competitive fashion. This connects the first and second loop and fine tunes the *Bmal1* transcription rate [259]. Furthermore, the REV-ERB/ROR feedback loop delays *Cry1* mRNA expression, which is critical for correct circadian timing [260] (**Figure 2-4**).

The DBP – NFIL3 feedback loop

The third transcription-translation feedback loop comprises the albumin D-box binding protein (DBP), directly regulated by BMAL1 (loop 1), and repressor nuclear factor interleukin 3 (NFIL3; also known as E4BP4), regulated via RORE elements (loop 2). Together, they act by binding to D-box elements and modulating the transcription of for example *Per*, where NFIL3 acts inhibitory and DBP stimulating [242] (**Figure 2-4**).

This tripartite system is pivotal for a functional clock with a 24h periodicity. Mutations in clock genes, such as *PER2* (S662G), can lead to diseases and malfunctions in humans [261]. Moreover, disruption of the clock due to abnormal lighting or feeding behavior can induce pathological changes. As an example, shift work is associated with an increased risk of cancer, metabolic disorders and cardiovascular diseases [262-264].

2.5.2 Synergy of clocks and entrainment

The major entrainment factor or *Zeitgeber* (from the German ‘time giver’) for the SCN is light. The eye is a light receptor in mammals. The SCN needs to transform this light information into neuronal signals and transmit it to peripheral clocks. This is possible owing to connections between the SCN and the hypothalamus-pituitary-adrenal (HPA) axis and autonomic nervous system (ANS). In turn, glucocorticoids as well as temperature act as internal *Zeitgebers* to orchestrate peripheral clocks in e.g. immune cells and vessels [238, 243, 265]. Albeit the humoral entrainment, feeding-related metabolic cues for clock synchronization are now recognized as being crucial to circadian rhythms as well. One example that is heavily influenced by food-uptake is the liver [266, 267]. Currently discussed other entrainment factors for leukocytes are reactive oxygen species (ROS) as well as the microbiota [268-270]. Studies have shown the influence of systemic cues on clocks within blood vessels and leukocytes [243, 271]; however the entrainment of the skin, whether by neuronal, thermal or microbial factors, remains elusive.

2.5.2.1 Circadian terminologies

In order to fully understand the research of circadian rhythms in immunity, one needs to be aware of different terminologies. For a biological process to be truly circadian with an approximately 24h period, meaning the time from peak to peak, it is required to be entrainable by external stimuli and enduring in constant conditions, such as permanent darkness.

In chronobiology, researchers are interested in the amplitude of oscillations, difference between mean and peak values, as well as the acrophase, time of the peak value, and the trough/nadir, time of the lowest value. To transform the environmental timing, for example light and darkness, into internal timing, the term '*Zeitgeber* time' (ZT) is used. ZT contains the timing of an entrainment stimulus, such as light. Therefore, ZT0 is regarded as the onset of light and ZT6 is 6h post light onset. Consequently, it easily allows for comparison of different chronobiological investigations and settings across studies. An oscillation in biological pathways between different ZTs is described as diurnal. However, if external stimuli do not change, e.g. constant darkness, the term '*circadian time*' (CT) is used, as it reflects the subjective time of an organism without external cues.

Thus, under light/darkness conditions, ZTs are used to represent timing of external cues (e.g. ZT12 = onset of light in a 12h:12h light/darkness schedule in an animal house), whereas under darkness/darkness conditions, CTs are used (e.g. CT12 = the start of the subjective night, when the lights would have switched off).

2.5.3 Circadian rhythms in immunity

Already around 60 years ago diurnal rhythmicity in host responses to lethal infections and endotoxins were demonstrated [272]. Likewise, susceptibility to pneumococcal infection shows periodicity that is dependent on light/darkness and rhythmic adrenocortical secretions [273]. Nevertheless, it is only recently, that research has identified molecular clocks in various leukocyte populations and described their role in trafficking of immune cells, host-pathogen interactions as well as activation of both innate and adaptive immunity [242, 274]. Every leukocyte population examined provides a functional molecular clock, including neutrophils [275], monocytes and macrophages [276-278], T cells [279, 280], B cells [278], and DCs [278]. Their development is influenced by the molecular clock. For example, NFIL3 controls the

development of ILC lineages and lymphocytes like IL-17-producing CD4⁺ T helper (T_H17) cells and *Bmal1*^{-/-} animals show defects in B cell development [279, 281-283]. However, general CD4⁺ and CD8⁺ T cells are not affected in their development by the clock.

The molecular clock may help shaping the immune responses to maximize their efficiency but at the same time reduce metabolic costs. First, it temporarily limits innate immunity, to prevent synchronous and potentially over-reactive activation. This is translated into different peaks and troughs in expression and release of complement factors, antimicrobial peptides, cytokines and chemokines as well as activation of phagocytes such as DCs [276, 284-286]. For example, TLR9 expression is oscillating in mice and peaking at ZT10 in macrophages and ZT16 in B cells whereas in DCs, no rhythmicity was found [284]. Rhythmic regulation of TLRs in turn is immune-protective against harmful events such as sepsis [287]. Secondly, due to temporal expression of inflammatory genes, the immune cell clock might control the length of inflammatory responses to find a compromise between fast activation and over-activation of immune compartments. For example, genetic deletion of *Bmal1* or *Nr1d1* does not alter the peak but alleviates the trough of LPS-induced inflammatory responses in macrophages [288]. As another example, it was shown that CRY proteins can directly modulate the inflammatory NF-κB pathway [289]. On the contrary, microbial products such as LPS also disrupt the phase, period and amplitude of immune cell clocks, shifting basal oscillations of genes towards pathogen-associated transcriptional programs [276, 290].

In conclusion, the circadian machinery influences every arm of immunity of various organisms. One important aspect is rhythmic immune cell trafficking, which will be explained in more detail.

2.5.3.1 Circadian leukocyte trafficking

Another way to control the efficiency of immune responses may be to direct the localization of immune cells. In the past years, multiple studies have established a strong impact of the molecular clock on immune cell distribution and locomotion. For instance, numbers of leukocytes in blood show oscillations throughout the day, with leukocytes leaving the blood and entering tissue at the behavioral rest phase of an organism (ZT13 in mice and inverted in humans) [56]. This time-of-day difference can be abolished by genetic ablation of *Bmal1*, thus linking phenotype and molecular clock [56, 243, 291]. To date, there is no study published showing circadian rhythms in lymphatic leukocyte trafficking from skin to the dLN, however,

many other tissues experience rhythms in homing and egress of leukocytes from the innate and adaptive immune system.

In general, leukocytes cross the endothelial wall of veins at different times, e.g. the evening in mice. Indeed, genes involved in the trafficking cascade like *Icam1*, *Vcam1*, *Sele*, *Selp*, *Cxcl1*, *Cxcl2* and *Ccl2* as well as their proteins ICAM1, VCAM1, E-SELECTIN and P-SELECTIN show rhythmic variation across the day [271]. He and colleagues could show that circadian rhythms in leukocyte trafficking in the blood system are heterogeneous across organs, with a unique mosaic of trafficking molecules being expressed in organ-specific BECs and leukocytes. Albeit the organ-specific differences, homing to organs via the blood stream is generally elevated at ZT13 and depends both on the clock from the microenvironment as well as the intrinsic immune cell clock [56].

Specifically, chemokines seem to be strongly regulated by the clock machinery, as this has been shown for different organs and cell types. Neutrophil trafficking across the organism is highly influenced by circadian rhythms, as their recruitment to the lung and sites of parasite infections as well as their overall location is temporally gated by rhythmic expression of the chemokines CXCL5, CXCL12 and CXCL2 [275, 290, 292]. Likewise, CXCR4 or CCL2 regulate the migration of inflammatory monocytes from blood to BM and sites of infection in a time-of-day dependent fashion [276, 293]. Oscillations of T cells in human blood have been linked to oscillations in CXCR4 and CX₃CR1, again indicating chemokine levels to be a key output of circadian immune control [294]. Druzd and colleagues could prove that the cellularity of LNs exhibits strong circadian oscillations, with highest lymphocyte numbers at the onset of the night in mice [291]. This was due to time-of-day dependent homing and egress of lymphocytes to and from the LN. Two of the key regulatory elements found were CCL21 (tested on high-endothelial venules) and its receptor CCR7 (tested on T cells and B cells), both showing a peak in their expression at around ZT7 and suggesting molecular control by *Bmal1* since CCR7 rhythmicity was ablated in T cell specific *Bmal1*^{-/-} mice. Both the microenvironment of the organ and the cell intrinsic clock promote rhythms in trafficking. Lymphocyte egress via efferent LVs from LNs is highly rhythmic, with highest counts in lymph observed at around ZT9 due to rhythmicity in the expression of *S1pr1*, a key gene involved in egress of lymphocytes [291, 295]. Thus, chemokines are a target of the molecular clock and seem to be strongly affected. Rhythms in trafficking molecules including chemokines are summarized in **Table 2-3**.

Although it was demonstrated that DCs own a molecular clock, a lot of research is lacking about how the molecular clock regulates DC-specific immune aspects. DCs play a major role in rhythmic immune responses as recently shown in parasitic worm infections. DC-specific

Bmal1^{-/-} mice lost the circadian rhythmicity of humoral immune response with a dampened immunoglobulin production at night [296]. Additionally, circadian variations in responses to antigens have been observed in mice and since DCs are the major APCs in the immune system, this might suggest circadian control mechanisms in DC biology [297]. DCs might also play a role in circadian variation in vaccination and disease as highlighted in the next paragraphs.

Protein / Gene	Origin	AP	Ref
CCL2	Serum, art & ven BECs, brain	CT12, ZT1, 7, 6	[271, 288, 298]
CCL21	LN HEV	9	[291]
CCL5	Serum	CT12	[288]
CCR1	B, eos, IM	N/A	[56]
CCR10	CD4 ⁺	N/A	[56]
CCR2	CD8 ⁺ , NIM	N/A	[56]
CCR3	Eos	N/A	[56]
CCR4	CD8 ⁺	N/A	[56]
CCR6	B	N/A	[56]
CCR7	B, CD4 ⁺ , CD8 ⁺	13	[56, 291]
CD11a	N, B, CD4 ⁺ , CD8 ⁺ , eos, IM	N/A	[56]
CD11b	NIM	N/A	[56]
CD18	CD4 ⁺ , CD8 ⁺	N/A	[56]
CD29	N, IM	N/A	[56]
CD44	Skin & SI BECs, B, CD4 ⁺ , CD8 ⁺ , eos, IM, NIM	N/A	[56]
CD49d	N, B, CD4 ⁺ , CD8 ⁺ , eos	7, 9, 9, 9, 13	[56]
CD49e	IM, NIM	N/A	[56]
CD49f	CD8 ⁺	N/A	[56]
CD62L	N	1	[299]
CX3CR1	IM, NIM	N/A	[56]
CXCL1	Serum, art & ven BECs	CT12, ZT1, 7	[271, 288]
CXCL12	BM fluid, Plasma	21, 17	[299, 300]
<i>Cxcl2</i>	Art & ven BECs	1,17	[271]
CXCR2	N	N/A, 13-21	[56, 299]
CXCR3	CD4 ⁺ , eos, NIM	N/A	[56]
CXCR4	N, B, CD4 ⁺ , CD8 ⁺ , NK, eos, IM, NIM, HSC	13/17, 13, 13, 13, 9, 13, 13, 13, 13	[56, 286, 291, 301]
CXCR5	B, CD8 ⁺	N/A	[56]
E-SELECTIN	Liver BECs, BM, ven BECs	N/A, 13	[56, 243, 271]
ICAM1	Splenic, LN, liver, SI, PPs, muscle, art & ven BECs	∅ 13, 1/7, 17	[56, 243, 271]
ICAM2	Thymic, liver, gut, PPs BECs	∅ 13	[56]
L-SELECTIN	N, B, CD4 ⁺ , CD8 ⁺ , eos	1, 13, 13, 17, 17	[56]
MADCAM	LN BECs	N/A	[56]
PNAd	SI BECs	N/A	[56]

Protein / Gene	Origin	AP	Ref
P-selectin	BM, thymic, splenic, ven BECs	13, N/A, 17	[56, 243, 271]
PSGL-1	N, B, CD4 ⁺ , CD8 ⁺ , NK, eos, IM, NIM	N/A	[56]
<i>S1pr1</i>	LN tissue	5	[291]
<i>S1pr3</i>	LN tissue	5	[291]
<i>S1pr4</i>	LN tissue	1	[291]
<i>S1pr5</i>	LN tissue	1	[291]
VCAM1	Thymic, splenic, LN, lung, PPs, BM, art & ven BECs	∅ 13, 1, 17	[56, 243, 271]

Table 2-3: Rhythms in murine trafficking molecules & chemokines

Comparative list of rhythmic trafficking molecules and chemokines in mice. Exact acrophases (Aps) of respective proteins are mentioned if stated in the publication. *Italic* indicates mRNA. AP shown in ZT as otherwise indicated. N= neutrophils, B= B cells, CD4⁺ & CD8⁺= T cells, NK= natural killer cells, eos= eosinophils, IM= inflammatory monocytes, NIM= non-inflammatory monocytes, HSC= hematopoietic stem cell, LN= lymph node, PPs= Peyer's patches, SI= small intestine, BM= bone marrow, art= arterial, ven= venular, BEC= blood endothelial cell, HEV= high endothelial venule. PSGL-1= P-selectin glycoprotein ligand-1, other abbreviations explained in text. ∅ = no organ-specific ZTs but only averages are given in the publication.

2.5.3.2 Circadian rhythms in skin

To date, there is no study examining the molecular clock of skin LECs or DCs under steady state. Although literature covering circadian rhythms in skin is scarce, there are studies showing that skin is heavily influenced by environmental factors. Mouse skin contains a functional molecular clock that is controlled by the SCN and feeding time [98, 302, 303]. One regulator of dermal clocks is melatonin [304]. It is secreted by the pineal gland in a rhythmic fashion, being high during the behavioral rest phase and low during the active phase [305]. Melatonin has been associated with suppression of skin UV damage, hair growth, wound healing and antitumor effects [304-306]. Collectively, this allows for the assumption that the immune landscape of the skin might be under circadian control.

Although it was already shown about two decades ago that the skin expresses clock genes [307], time-of-day influence on the skin's immune system is only now starting to be uncovered. Transcriptome analysis of total mouse skin harvested every 4h for 48h revealed a circadian regulation of more than 1400 genes including chemokines, pro- and anti-inflammatory cytokines as well as anti-microbial peptides, with the majority peaking during the onset of the resting phase [302, 308]. Moreover, skin permeability in the *stratum corneum* is higher in the onset of the behavioral rest phase as AQUAPORIN 3 is regulated by the clock [309], which in turns promotes rhythms in dermal itch [310]. Generally, the epidermis harbors

more proliferating keratinocytes during the resting phase [311]. Finally, clock genes heavily influence the nature of hair follicles, even during missing influence of the SCN [312].

Various skin immune diseases like psoriasis disease show circadian variability [313, 314] and genetic clock ablation might even enhance pathological skin reactions [315]. This has also been observed in humans, for which night-shift work increases the incidence of psoriatic lesions due to misalignment of clocks in the skin [316]. Another study has shown that abolishment of circadian rhythms changes the trafficking of APCs in skin and impaired hypersensitivity reactions [317]. In addition to that, researchers applied imiquimod, a TLR7 agonist, to murine skin to dampen the rhythmicity of skin inflammation and thereby could show circadian control of IFN-sensitive gene expression in skin [318].

Uncovering and examining the molecular clock of skin immune cells and vessels might aid in chronotherapy and timed vaccination strategies, as the skin is one of the major sites for vaccinations.

2.5.4 Chronotherapy and the benefit of rhythms in immunity

Scientists currently try to decipher how genetic or environmental disruption of the clock can translate into or exacerbate pathological conditions as outlined in many animal models and human studies [313, 316, 319-321]. It is well known in humans that diseases like asthma, rheumatoid arthritis, acute myocardial infarction and ventricular arrhythmias as well as acute coronary syndrome show time-of-day variation in occurrence, symptoms and disease markers [322-326]. Many studies investigating chrono-immunotherapy are arising from this, e.g. administration of drugs at specific times during the day. Notably, numerous drugs used in treatment of inflammatory, metabolic, neurologic and cancerous diseases influence clock controlled targets [327].

More and more studies are initiated testing the timed delivery of vaccines. For vaccination, a functional lymphatic system and trafficking of dermal DCs are required. One study revealed that morning vaccination yields an enhanced antibody-response in comparison with afternoon vaccination in a cluster-randomized human trial [328]. Another recent study testing the anti-tuberculosis vaccine Bacillus Calmette-Guérin pointed towards higher effectivity of vaccination in the morning. This circadian influence on vaccination efficacy could even be extended to very preterm infants and non-mammalian animals [329, 330]. Less knowledge exists on how the immune system creates such time-of-day differences. CD8⁺ T cells seem to

be heavily involved as administration of vaccine during the day leads to a stronger and more efficient activation as well as proliferation during the day compared to the night [331]. Unfortunately, there are no circadian vaccination studies available surveying the skin DC trafficking.

Taken together, a better understanding of the molecular clock of DCs and the lymphatic system would be of great benefit for the chronotherapeutic targeting of diseases as well as novel approaches such as timed vaccination and therapies.

2.6 Objective & aims

Within this thesis, I aim to decipher how the molecular clock of the lymphatic system and to lesser extent of the dermal DCs are influencing rhythmic dermal lymphatic leukocyte trafficking. This is accomplished by the following aims:

1. Establishment of *ex-vivo* crawl-in trafficking assays as well as visualization of LECs and DCs.
2. Demonstration of rhythmic DC trafficking into initial skin lymphatic capillaries.
3. Assessment of the dermal LEC intrinsic clock by measuring rhythmic RNA and protein expression in LECs.
4. Analysis of the dermal DC intrinsic clock functionality.
5. Survey of functional rhythmic trafficking molecules and chemokine micro-patterning in skin.
6. Establishment of genetic clock ablation and scrutinizing the molecular link between DC clock, LEC clock and rhythmic trafficking in skin.

3 Materials and Methods

3.1 Materials

3.1.1 Buffers and media

Buffer / medium	Supplements	Application
R10 – RPMI 1640	10% FCS (heat-inactivated) 20mM penicillin & Streptomycin 2mM L-glutamine 50µM β-mercaptoethanol	Bone marrow-derived dendritic cell culture, staining buffer, crawl-in & crawl-out assay
R10 + HEPES – Phenol-red free RPMI 1640	10% FCS (heat-inactivated) 20mM penicillin & Streptomycin 2mM L-glutamine 50µM β-mercaptoethanol 10mM HEPES	Live-imaging of crawl-in assays
FACS buffer (PEB)	PBS 0.02M EDTA 20% FCS (heat-inactivated)	FACS
50x tris-EDTA (TE) buffer	2M tris 50mM EDTA	gDNA isolation
50x tris-acetate-EDTA (TAE) buffer	2M tris 50mM EDTA 1M acetic acid	Gel electrophoresis
Genotyping digestion buffer	0.5mM EDTA 0.1M tris 0.2% SDS 0.2M NaCl (pH = 8.5)	gDNA isolation

Table 3-1: Buffers and media

3.1.2 Kits

Kit	Application	Supplier	Location
GM-CSF Quantikine ELISA Kit	GM-CSF producing hybridoma cell culture	R&D systems	Wiesbaden, Germany
Streptavidin / biotin blocking kit	IF	Vector Laboratories Inc.	Burlingame CA, USA

Table 3-2: Kits

3.1.3 Primers

All primers were designed using the PCR primer design tool and purchased at Eurofins (Munich, Germany). F= forward, R= reverse, MT= mutant, C= common, WT= wild type.

Primer	Sequence (5' → 3')
Generic CRE F	GCG GTC TGG CAG TAA AAA CTA TC
Generic CRE R	GTG AAA CAG CAT TGC TGT CAC TT
<i>Bmal1 flox</i> F	ACT GGA AGT AAC TTT ATC AAA CTG
<i>Bmal1 flox</i> R	CTG ACC AAC TTG CTA ACA ATT A
<i>Clec9acre</i> C	AAA AGT TCC ACT TTC TGG ATG ATG A
<i>Clec9acre</i> WT	TCA CTT ACT CCT CCA TGC TGA CG
<i>Clec9acre</i> MT	GGC TCT CTC CCC AGC ATC CAC A
<i>Prox1cre</i> WT F	GTG GAA AGG AGC GTA CAC TGA
<i>Prox1cre</i> C	CAC ACA CAC ACA CGC TTG C
<i>Prox1cre</i> MT F	GCC AGA GGC CAC TTG TGT AG

Table 3-3: Genotyping primers

3.1.4 Antibodies and staining reagents

All antibodies used in this thesis target mouse proteins.

3.1.4.1 Primary antibodies

Antigen	Conj.	Dil.	Clone	Appl.	Catalog #	Supplier
ALCAM	PE	1:100	Polyclonal	IF	FAB1172P	R&D Systems Wiesbaden, Germany
B220/CD45R	PE-Cy7	1:100	RA3-6B2	FACS	103222	Biolegend London, UK
CCL21	Biotin	1:100	Polyclonal	IF	BAF457	R&D Systems Wiesbaden, Germany
CCR7 / CD197	BV786	1:25	4B12	FACS	564355	BD Biosciences Laagstraat, Belgium
CD103	FITC	1:100	2E7	IF FACS	121419	Biolegend London, UK
CD103	BV480	1:50	M290	FACS	566118	BD Biosciences Laagstraat, Belgium
CD11b	AF700	1:200	M1/70	FACS	101222	Biolegend London, UK
CD11c	PE	1:100	N418	IF FACS	117308	Biolegend London, UK
CD11c	APC/Cy7	1:400	N418	FACS	117323	Biolegend London, UK
CD11c	BV510	1:300	N418	FACS	117337	Biolegend London, UK
CD11c	APC-R700	1:200	N418	FACS	565872	BD Biosciences

Antigen	Conj.	Dil.	Clone	Appl.	Catalog #	Supplier
						Laagstraat, Belgium
CD16/32	-	1:50	93	FACS	101302	Biolegend London, UK
CD19	PE-Cy5	1:200	eBio 1D3	FACS	2025768	Thermo Fisher Munich, Germany
CD205	PE-Cy7	1:200	205yekta	FACS	25-2051- 43	Biolegend Luzern, Switzerland
CD3	PE-Cy5	1:200	17A2	FACS	2132345	Thermo Fisher Munich, Germany
CD301b	PerCP- Cy5.5	1:200	URA-1	FACS	146810	Biolegend Luzern, Switzerland
CD31/PECAM-1	APC	1:100	390	IF FACS	102410	Biolegend London, UK
CD31/PECAM-1	AF488	1:100	390	IF	102413	Biolegend London, UK
CD4	BV605	1:100	RM4-5	FACS	100548	Biolegend London, UK
CD40	BUV737	1:200	3/23	FACS	741749	BD Biosciences Laagstraat, Belgium
CD45	PE-Dazzle 594	1:500	30-F11	FACS	103145	Biolegend London, UK
CD45	AF488	1:500	30-F11	FACS	103122	Biolegend London, UK
CD45	BV421	1:400	30-F11	FACS	563890	BD Bioscience Heidelberg, Germany
CD45	BUV395	1:300	30-F11	FACS	565967	Biolegend London, UK
CD80	BUV605	1:200	16-10A1	FACS	563052	BD Biosciences Laagstraat, Belgium
CD86	BUV395	1:200	GL1	FACS	564199	BD Biosciences Laagstraat, Belgium
CD8a	APC-Cy7	1:100	53-6.7	FACS	100713	Biolegend London, UK
CD99	PE	1:100	Polyclonal	IF	FAB3905P	Novusbio Wiesbaden, Germany
EPCAM/CD326	AF647	1:1000	G8.8	FACS	118212	London, UK
EPCAM/CD326	PE	1:200	G8.8	FACS	563477	BD Biosciences Laagstraat, Belgium
E-SELECTIN	PE	1:100	10E9.6	IF	553751	BD Bioscience

Antigen	Conj.	Dil.	Clone	Appl.	Catalog #	Supplier
						Heidelberg, Germany
GOLPH4/GPP130	-	1:100	Polyclonal	IF	Ab28049	Abcam Cambridge, UK
GP38/PODOPLA NIN	PE	1:100 1:200	8.1.1.	IF FACS	127407	Biolegend London, UK
ICAM1	PE	1:100	YNI.7.4	IF	116108	Biolegend London, UK
JAM-A/CD321	PE	1:100	H202-106	IF	B100- 65340PE	Novusbio Wiesbaden, Germany
JAM-A/CD321	FITC	1:200	REA854	FACS	51910285 95	Miltenyi Biotech Bergisch Gladbach, Germany
JAM-C/CD323	APC	1:100	209628	IF	-	Internal gift Geneva, Switzerland
JAM-C/CD323	APC	1:100	209628	IF FACS	209628	R&D Systems Wiesbaden, Germany
KI67	PE	1:100	16A8	IF	652403	Biolegend London, UK
L1CAM	PE	1:100	555	IF	FAB5674P	R&D Systems Wiesbaden, Germany
LAMININ	-	1:100	Polyclonal	IF	L9393- 100UL	Sigma-Aldrich Taufkirchen, Germany
LANGERIN	AF647	1:100	929F3.01	IF	DDX0362 A647-5	Origene (Acris) Herford, Germany
Ly6C	PE	1:100	HK1.4	FACS	128007	Biolegend London, UK
Ly6G	PerCP- Cy5.5	1:100	1A8	FACS	127615	Biolegend London, UK
LYVE-1	AF488	1:100	ALY7	IF	53-0443- 82	eBioscience Munich, Germany
LYVE-1	DL405	1:100	ALY7	IF	NBP1- 43411V	Novusbio Wiesbaden, Germany
LYVE-1	-	1:100	223322	IF	MAB2125- SP	R&D Systems Wiesbaden, Germany
MHCII/I-A/I-E	BV711	1:300	M5/114.1 5.2	FACS	107643	Biolegend London, UK
MHCII/I-A/I-E	PE/Cy7	1:1000	M5/114.1 5.2	FACS	107629	Biolegend London, UK
MHCII/I-A/I-E	AF700	1:300	M5/114.1	FACS	107621	Biolegend

Antigen	Conj.	Dil.	Clone	Appl.	Catalog #	Supplier
			5.2			London, UK
MHCII/I-A/I-E	PE/Cy5	1:1000	M5/114.1 5.2	FACS	107611	Biolegend London, UK
MHCII/I-A/I-E	BV650	1:2000	M5/114.1 5.2	FACS	107641	Biolegend Luzern, Switzerland
MMR1	PE	1:100	Polyclonal	IF	FAB2535P	Novusbio Wiesbaden, Germany
NEUROFILIN	PE	1:100	3E12	IF	145204	Biolegend London, UK
PROX-1	APC	1:100	5G10	IF	NBP1- 30045APC	Novusbio Wiesbaden, Germany
SEMA3A	PE	1:100	215803	IF	IC1250P	R&D Systems Wiesbaden, Germany
VCAM1	PE	1:100	429 (MVCAM. A)	IF	105714	Biolegend London, UK
VE-CADHERIN	PE	1:100	BV13	IF	NBP1- 43348PE	Novusbio Wiesbaden, Germany

Table 3-4: Primary antibodies

3.1.4.2 Secondary antibodies and streptavidin

Target	Host	Conj.	Dilution	Clone	Catalog #	Supplier
Rabbit	Goat	FITC	1:100	Polyclonal	111-095-144	Jackson Immuno Cambridge, UK
Rabbit	Goat	Cy3	1:700	Polyclonal	111-165-144	Jackson Immuno Cambridge, UK
Rat	Donkey	AF488	1:500	Polyclonal	712-546-150	Jackson Immuno Cambridge, UK
Biotin	Streptavidin	PE	1:500	-	S866	Invitrogen Schwerte, Germany
Biotin	Streptavidin	AF647	1:400	-	019-600-084	Jackson Immuno Cambridge, UK

Table 3-5: Secondary antibodies and streptavidin

3.1.4.3 Isotype antibodies

Isotype	Conj.	Dil.	Clone	Appl.	Catalog #	Supplier
Goat IgG	Biotin	1:100	Polyclonal	IF	BAF108	R&D Systems Wiesbaden, Germany
Goat IgG	PE	1:100	Polyconal	IF	IC108P	Novusbio Wiesbaden, Germany
Hamster IgG2, κ	BV605	1:200	B81-3	FACS	563012	BD Biosciences Laagstraat, Belgium
Human IgG1	FITC	1:200	RTK2758	FACS	130-113- 437	Miltenyi Biotech Bergisch Gladbach, Germany
Human IgG1	APC	1:200	REA-293	FACS	130-113- 434	Miltenyi Biotech Bergisch Gladbach, Germany
Rat IgG1, κ	PE	1:100	E3-34 (RUO)	IF	553925	BD Biosciences Heidelberg, Germany
Rat IgG2a	BV786	1:25	R35-95	FACS	563335	BD Biosciences Laagstraat, Belgium
Rat IgG2a, κ	PE	1:100	RTK2758	IF	400508	Biologend London, UK
Rat IgG2a, κ	BUV395	1:200	R35-95	FACS	563556	BD Biosciences Laagstraat, Belgium
Rat IgG2a, κ	BUV737	1:200	R35-95	FACS	612760	BD Biosciences Laagstraat, Belgium
Rat IgG2a, κ	PE-Cy7	1:200	R35-95	FACS	552784	BD Biosciences Laagstraat, Belgium
Rat IgG2a, λ	PerCP- Cy5.5	1:200	R35-95	FACS	552784	BD Biosciences Laagstraat, Belgium
Rat IgG2b, κ	PE	1:100	RTK4530	IF	400608	Biologend London, UK

Table 3-6: Isotype control antibodies

3.1.4.4 Neutralization antibodies

Target	Host	IG	Conc.	Clonality	Catalog #	Supplier
CCL21	Goat	IgG	20µg/ml	Polyclonal	AF457	R&D Systems Wiesbaden, Germany
Isotype control	Goat	IgG	20µg/ml	Polyclonal	AB-108-C	R&D Systems Wiesbaden, Germany
CD99	Rabbit	IgG	30µg/ml	Polyclonal	Gift from Dietmar Vestweber	MPI Molecular Biomedicine, Münster, Germany
Isotype control	Rabbit	IgG	30µg/ml	Polyclonal	AB-105-C	R&D Systems Wiesbaden, Germany
JAM-A/CD321	Rat	IgG2b	30µg/ml	BV1	MABT128	Sigma-Aldrich Taufkirchen, Germany
Isotype control	Rat	IgG2b	30µg/ml	141945	MAB0061	R&D Systems Wiesbaden, Germany
JAM-C	Rat	IgG2a	30µg/ml	H33	Gift from Prof. Beat Imhof	University of Geneva, Geneva, Switzerland
Isotype control	Rat	IgG2a	30µg/ml	54447	MAB006	R&D Systems Wiesbaden, Germany
LYVE-1	Rat	IgG2A	30µg/ml	22322	MAB2125- 100	R&D Systems Wiesbaden, Germany
Isotype control	Rat	IgG2A	30µg/ml	54447	MAB006	R&D Systems Wiesbaden, Germany
CD31	Rat	IgG2A	30µg/ml	MEC13.3	NB600- 1475	Novusbio, Wiesbaden, Germany
Isotype control	Rat	IgG2A	30µg/ml	54447	MAB006	R&D Systems Wiesbaden, Germany

Table 3-7: Neutralization antibodies

All neutralization bodies are NA/low for endotoxin.

3.1.5 Chemicals and reagents

Chemical / reagent	Supplier	Location
5x GoTaq Flexi	Promega	Madison WI, USA
Agarose	Biozym Scientific	Oldendorf, Germany
Buprenorphine / Temgesic	Indivior UK Limited	Hull, UK
CellTrace Violet	ThermoFisher	Darmstadt, Germany
Collagenase IV	Sigma-Aldrich	Taufkirchen, Germany
Corn oil	Sigma-Aldrich	Taufkirchen, Germany
CountBright™ absolute counting beads	Life Technologies	Darmstadt, Germany
DAPI	Biolegend	London, UK
dATP, dCTP, dGTP, dTTP nucleotides	Promega	Madison WI, USA
Dispase II	Sigma-Aldrich	Taufkirchen, Germany
DNase I Ambion™	Life Technologies	Darmstadt, Germany
EDTA	Life Technologies	Darmstadt, Germany
Absolute ethanol for molecular Biology	AppliChem	Darmstadt, Germany
FastGene 11bp DNA Marker	Nippon Genetics	Düren, Germany
FastGene Optima PCR HotStart	Nippon Genetics	Düren, Germany
FCS	Life Technologies	Darmstadt, Germany
GoTaq Hot Start	Promega	Madison WI, USA
Heparinase II & IV	Sigma-Aldrich	Taufkirchen, Germany
HyPure™ Molecular Biology Grad Water (nuclease-free)	GE Healthcare LifeSciences	South Logan, Utah, USA
Isoflurane	CP-Pharma	Burgdorf, Germany
Isopropanol (Propan-2-ol)	Applichem	Darmstadt, Germany
Ketamine	Medistar	Munich, Germany
L-glutamine	Sigma-Aldrich	Taufkirchen, Germany
Lipopolysaccharide (LPS) from Escherichia coli	Sigma-Aldrich	Taufkirchen, Germany
Magnesium Chloride (MgCl ₂)	Promega	Madison WI, USA
mCCL21	Peprotech	Hamburg, Germany
Murine GM-CSF	In house produced	Martinsried, Germany
Midori Green Advance	Nippon Genetics	Düren, Germany
Normal Goat Serum	Sigma-Aldrich	Taufkirchen, Germany
OCT compound	Sakura Finetek	Alphen aan den Rijn, Germany
Paraformaldehyde solution 4% in PBS (PFA)	ChemCruz	Heidelberg, Germany
PBS	Apotheke Klinikum Universität München	Munich, Germany
Pen/Strep	Sigma-Aldrich	Taufkirchen, Germany
Proteinase K	Life Technologies	Darmstadt, Germany
RPMI	Gibco	Darmstadt, Germany
SDS 10%	Sigma-Aldrich	Taufkirchen, Germany
Sodium Chloride (NaCl ₂)	Sigma-Aldrich	Taufkirchen, Germany
Tamoxifen	Sigma-Aldrich	Taufkirchen, Germany

Chemical / reagent	Supplier	Location
Tris	AppliChem	Darmstadt, Germany
Triton-X100	Sigma-Aldrich	Taufkirchen, Germany
Trizol-LS	Qiagen	Hilden, Germany
Xylazine / Rompun	Bayer vital GmbH	Leverkusen, Germany
β -mercaptoethanol (β -me)	Gibco	Darmstadt, Germany

Table 3-8: Chemicals and reagents

3.1.6 Utilities

Utility	Supplier	Location
24-well plates	Thermo Fisher Scientific	Darmstadt, Germany
Petri dish (4cm, 6cm and 10cm)	Corning	Kaiserslautern, Germany
Surgery utilities	Fine Science Tools	Heidelberg, Germany
Modelling Clay	Städtler	Nürnberg, Germany
Cover glass	Thermo Scientific	Darmstadt, Germany
Tissue Slide	Thermo Scientific	Darmstadt, Germany
1.5ml & 2ml microfuge tubes	Eppendorf	Hamburg, Germany
1ml, 2ml and 10ml syringes	BBraun and Terumo	Melsungen, Germany and Shibuya City, Japan
15ml and 50ml Polypropylene conical centrifuge (falcon) tube	Falcon / Fisherscientific	Darmstadt, Germany
Needles for injection	BD Microlance	Heidelberg, Germany
40 μ m and 70 μ m strainer	Fisherbrand	Darmstadt, Germany
1ml, 200 μ l, 20 μ l and 2.5 μ l pipette tips	Starlab	Hamburg, Germany
Cryomold	Tissue Tek Sakura	Staufen, Germany
S35 microtome blade	Feather / Cellpath Ltd	Newtown, UK
Cell culture filter 50ml and 500ml	Sigma-Aldrich	Taufkirchen, Germany
5ml FACS tubes w/o filter	Falcon	Darmstadt, Germany
Cryotubes	Thermo Fisher Scientific	Darmstadt, Germany

Table 3-9: Utilities and materials

3.1.7 Machines

Machine	Supplier	Location
Gallios flow cytometer	Beckmann Coulter	Krefeld, Germany
Light / Darkness cabinet (small)	Parkbio	Gaveland, MA, USA
Light / Darkness cabinet (large)	Tecniplast	Buguggiate, Italy
Mastercycler Egradient S	Eppendorf	Munich, Germany
NanoDrop TM 2000	Life Technologies	Darmstadt, Germany
Coulter Z2 (cell counter)	Beckmann Coulter	Krefeld, Germany
PowerPac Basic (for gel electrophoresis)	BioRad	Munich, Germany
Electrophoresis chamber	BioRad	Munich, Germany
ThermoMixer F1.5	Eppendorf	Munich, Germany
Vortex Genie 2	Scientific Industries	Munich, Germany
UVP Minidizer Oven	AnalyticJena	Jena, Germany

Machine	Supplier	Location
Heraeus Multifuge X3R	Thermo Fisher Scientific	Munich, Germany
Cryotom CM3050 S	Leica	Wetzlar, Germany
Cell culture incubator Galaxy 170S	New Brunswick (Eppendorf)	Munich, Germany
Bright-field microscope (cell culture)	Leica	Wetzlar, Germany
Gel imaging chamber	INTAS Science Imaging	Göttingen, Germany
Mastercycler nexus	Eppendorf	Munich, Germany
Minicentrifuge	Eppendorf	Munich, Germany
Spinning disk confocal microscope	Zeiss	Jena, Germany
LSRFortessa	BD	Heidelberg, Germany
Gallios flow-cytometer	Beckmann Coulter	Munich, Germany
FACSAriaIIIu	BD	Heidelberg, Germany
Isoflurane chamber	Groppler Medizintechnik	Deggendorf, Germany

Table 3-10: Machines

3.1.7.1 Microscope & flow-cytometer configurations

Flow-cytometer	Excitation laser [nm]	Fluorescence channel	Default filter	Filter range [nm]
Gallios flow-cytometer	405	9	450/50	425-475
		10	550/40	530-570
	488	1	525BP	xxx-550
		2	575BP/26	562-588
		3	620/30	606-635
		4	695/30	680-710
		5	755LP	>755
	633	6	660BP	650-670
7		725/20	715/735	
8		755/LP	>755	
BD LSR Fortessa flow-cytometer LMU Munich core-facility and BD LSR Fortessa flow-cytometer Geneva core facility (diverging default filter & filter range are	355	1	450/50	425-475
		1	380/30	365-395
		1	379/08	375-383
		2	530/30	515-545
	405	2	740/35	723-757
		3	450/40	430-470
		4	525/50	500-550
		5	610/20	600-620
488	6	660/20	650-670	
	7	710/50	685-735	
	8	780/60	750/810	
	9	530/30	515-545	
	10	710/50	685-735	
	561	11	586/15	579-593
12		610/20	600-620	
13		670/30	655-685	
14		710/50	685-735	
15		780/60	750-810	

Flow-cytometer	Excitation laser [nm]	Fluorescence channel	Default filter	Filter range [nm]
shown in dark green)	640	16	670/14	663-677
		17	730/45	708-752
		18	780/60	750-810
FACSriaIIIu (cell sorter)	405	1	450/40	430-470
		2	525/50	500-550
		3	610/20	600-620
		4	660/20	650-670
		5	710/50	685-735
		6	780/60	750/810
	488	7	530/30	515-545
		8	695/40	675-715
	561	9	582/15	575-589
		10	610/20	600-620
		11	780/60	750-810
	640	12	660/20	650-670
		13	730/45	708-752
		14	780/60	750-810

Table 3-11: Flow-cytometer configurations

Microscope	Objectives	Numerical aperture	Excitation laser [nm]	Default filter	Filter range [nm]
Upright Zeiss Axio Examiner.Z1 confocal spinning disk microscope	5x (n-plan)	0.15	405	387/11	382-391
	10x (w-plan)	0.3	488	485/20	475-495
	20x (w-plan)	1.0	561	560/25	552-572
	63x (w-plan)	1.0	640	650/13	644-656
10x ocular – (<i>magnification = ocular x objective</i>)					

Table 3-12: Microscope configurations

3.1.8 Softwares

The Matlab licence was kindly provided by the group of Dr. Tobias Bonhoeffer at the Max-Planck Institute for Neurobiology Martinsried, Germany.

Software	Version	Supplier	Location
ImageJ / Fiji	1.51n	Open-Source	USA
Slidebook	6.0	3i – Intelligent Imaging Innovations	USA
Matlab	R2018b	Mathworks	USA
Prism	7.0	GraphPad	USA
Excel	2010/2017	Microsoft	USA
Galaxy, storage platform	-	LAFUGA Gene Center	LMU Munich, Germany

Table 3-13: Softwares

3.2 Methods

3.2.1 Animals

All animals referred to as wild type animals (WT) in this doctoral thesis were male C57BL6/6N mice aged 6-8 weeks (or otherwise indicated) and purchased from either Charles River Laboratories (Sulzfeld, Germany) or Janvier labs (Le Genest-Saint-Isle, France). Genetically modified animals used in this work include: *Cdh5-creER^{T2}-Bmal1^{flox/flox}* (referred to as EC-*Bmal1^{-/-}*), *Prox1-creER^{T2}-Bmal1^{flox/flox}* (referred to as LEC-*Bmal1^{-/-}*), *EYFP;Clec9acre-Bmal1^{flox/flox}* (referred to as DC-*Bmal1^{-/-}*), *Cd99^{-/-}* and *Myd88^{-/-}* mice. *Cdh5-creER^{T2}* mice (B6) were previously obtained as a kind gift from Dr. Ralf Adams (Max-Planck-Institute for Molecular Biomedicine Münster, Germany) and crossbred with B6 *Bmal1^{flox/flox}* mice obtained from Jackson Laboratories (Sulzfeld, Germany; as previously used in [56]) to be able to target blood and lymphatic ECs. B6 *Prox1-creER^{T2}* mice (purchased at Jackson Laboratories Sulzfeld, Germany) were crossbred with *Bmal1^{flox/flox}* mice to obtain *Prox1-creER^{T2}-Bmal1^{flox/flox}* mice to specifically target LECs. B6 *EYFP;Clec9acre* mice were a kind gift from Dr. Barbara Schraml (LMU Munich, Germany) and were crossbred with *Bmal1^{flox/flox}* at ENVIGO (Milano, Italy) to solely target cDC1 & cDC2. B6 *Cd99^{-/-}* mice were a kind gift from Dr. Dietmar Vestweber (Max-Planck-Institute for Molecular Biomedicine Münster, Germany, which was also the site of the experiments) and *Myd88^{-/-}* mice were purchased from Jackson Laboratories.

3.2.1.1 Housing & animal law regulations

All animals except *CD99^{-/-}* mice (14h:10h) were housed under a 12h:12h light:dark schedule with *ad libitum* access to water and food in the Core Facility Animal Models at the Biomedical Centre (CAM; LMU, Germany). Animals were supervised by multiple care takers and veterinarians. Upon each shipment, animals were given seven days to adjust to the new environment before experiments. All experiments were performed using age- and sex-matched groups. All animal procedures and experiments were in accordance with the ministry of animal welfare of the region of Oberbayern and with the German law of animal welfare. Mice were always euthanized using an isoflurane chamber (>5% isoflurane) with subsequent dislocation of the neck.

3.2.1.2 Light / darkness (LD) experiments

For each experiment, animals were either removed from the animal facility and directly used at time points indicated or placed into time shifted light cabinets to facilitate simultaneous experiments at different time points of the day. For each shift of 1h, animals were placed in a cabinet at least 1 day prior to the experiment (e.g., animals for experiments at ZT19, 2am, were harvested at 2pm and were thus placed into a +/- 12h shifted cycle 12 days prior to the experiment).

For constant darkness experiments (to obtain information without rhythmic light influence), mice were kept under constant darkness conditions in red cages for at least 24h prior to experiments. As mice cannot perceive red light information [332], this simulated complete darkness. These animals were euthanized under red light.

3.2.1.3 Tamoxifen treatment

Cre/lox-directed gene knockout is based on the 'floxing' of an essential exon of the gene of interest with two loxP sites with ensuing expression of a recombinase Cre to excise the flanked exon, thus generating a null allele (or dysfunctional protein) in all cells where cre is active. The ligand-dependent chimeric CRE recombinases (CreER) consist of a CRE fused to mutated hormone-binding domains of the estrogen receptor which inhibits the release and function of CRE. CreER recombinases can be activated by the synthetic estrogen receptor ligand 4-hydroxitamoxifen (henceforth referred to as tamoxifen), allowing for temporal release and activation of CRE. The CreER^{T2} specifically contains a triple mutation (G400V/M543A/L544A) and is currently the best tool in the CreER utility box [333].

To induce CRE expression, animals were given intraperitoneal (i.p.) tamoxifen injections for 5 consecutive days at the age of 6 weeks. Prior to the injection, each mouse was weighed. For each 20g of mouse, 1mg of tamoxifen was injected (0.02 g/mL). Fresh tamoxifen was dissolved in corn oil under sterile conditions, sterile filtrated and directly used for injection using a 25G x 5/8 needle attached to a 1ml syringe. Each day, the site of injection was altered to avoid further injuries and every injection was performed at the same time of day. Animals were given a recovery period of 3 weeks until the final experiment.

3.2.1.4 DNA isolation

To obtain the genotype of *Cdh5-creERT2-Bmal1^{flox/flox}*, *Prox1-creERT2-Bmal1^{flox/flox}* and *EYFP;Clec9acre-Bmal1^{flox/flox}* mice, ear clips were harvested by animal caretakers and used for genotyping. Biopsies were digested overnight in 200µl genotyping lysis buffer (Table 3-1) together with 1µl proteinase K (in total 1.5 U per sample) at 55°C while shaking at 700rpm. The next day, samples were thoroughly mixed, centrifuged at 4°C for 10min at 18,000 x g and its supernatant was transferred to a new tube containing 500µl isopropanol. Tubes were inverted multiple times to let the DNA precipitate and spun down at 4°C for 10min at 18,000 x g. The supernatant was removed and the DNA pellet was dissolved in 100µl TE-buffer (Table 3-1) while being slowly shaken for 1h at 300rpm and 37°C. Either samples were directly used for polymerase chain reaction (PCR) or frozen and stored at -20°C.

3.2.1.5 Genotyping PCR

Cdh5cre & *Bmal1*, *Prox1cre* & *Clec9acre* genotyping had an individual PCR protocol. Consistently, 1µl of extracted DNA in TE-buffer was used. The primer concentration used was 10µM (Table 3-3). DNA was added to the reaction mix (Table 3-14) and amplified according to PCR programs (Table 3-15) on a Mastercycler Eppgradient S.

Reagent	1x solution (19µl reaction vol.) [µl]
<i>Cdh5cre</i> and <i>Bmal1</i> reaction	
Nuclease-free H ₂ O	8
2x Fast gene buffer	10
10µM F primer (1:10)	0.5
10µM R primer (1:10)	0.5
<i>Prox1cre</i> reaction	
Nuclease-free H ₂ O	6,36
5x Green buffer goTaqflif	4
25 mM MgCl ₂	1.6
1mM dNTP	4
WT primer (1:10)	1
Common primer (1:10)	1
Mutant primer (1:10)	1
GoTaq	0.04

<i>Clec9acre</i> reaction	
Nuclease-free H ₂ O	7,875
5x Green buffer goTaqflx	4
25 mM MgCl ₂	1.5
1mM dNTP	4
WT primer (1:10)	0.5
Common primer (1:10)	0.5
Mutant primer (1:10)	0.5
GoTaq	0.125

Table 3-14: Genotyping PCR master mix

Temperature [°C]	Time	Reaction
<i>Cdh5cre</i> reaction		
95	3 mins	Initial denaturation
Start cycle		
95	20 sec	Denaturation
62	30 sec	Primer annealing
72	30 sec	Polymerization
End cycle – repeat 38x		
72	10 mins	Final extension
<i>Bmal1</i> reaction		
94	3 mins	Initial denaturation
Start cycle		
94	30 sec	Denaturation
55	30 sec	Primer annealing
72	30 sec	Polymerization
End cycle – repeat 35x		
72	2 mins	Final extension
<i>Prox1cre</i> reaction		
94	3 mins	Initial denaturation
Start cycle		
94	15 sec	Denaturation
61.4	15 sec	Primer annealing
72	10 sec	Polymerization
End cycle – repeat 35x		
72	2 mins	Final extension
<i>Clec9acre</i> reaction		
94	3 mins	Initial denaturation
Start cycle		
94	30 sec	Denaturation
61.4	30 sec	Primer annealing
72	40 sec	Polymerization
End cycle – repeat 35x		
72	10 mins	Final extension

Table 3-15: Genotyping PCR reactions

3.2.1.6 Genotyping gel electrophoresis

For visualization, 1% agarose gels including Midori Green (1:25,000) were used. 10µl of the PCR product were added to the agarose gel. DNA samples ran for around 30-50min (depending on the product) at 200V together with a 100bp DNA ladder marker (**Table 3-8**). The gel was imaged using ultraviolet light on an UV transilluminator. The respective PCR products and examples of genotypes can be seen below (**Table 3-16** and **Figure 3-1**). Only mice that express CRE in a hetero/hemizygotic fashion (abbreviated as CRE+) or WT were used, as hemizygotic CRE expression is sufficient for *Bmal1* excision. For *Bmal1*, only mice homozygotic for flox (fl/fl) were used. Cre negative mice were used as control mice.

Product	Size [bp]	Reaction
CRE band	324	Cdh5cre
Flox band	431	Bmal1 fl/fl
WT band	327	Bmal1 fl/fl
CRE band	160	Prox1cre
WT band	280	Prox1cre
CRE band	597	Clec9acre
WT band	407	Clec9acre

Table 3-16: Genotyping PCR product sizes

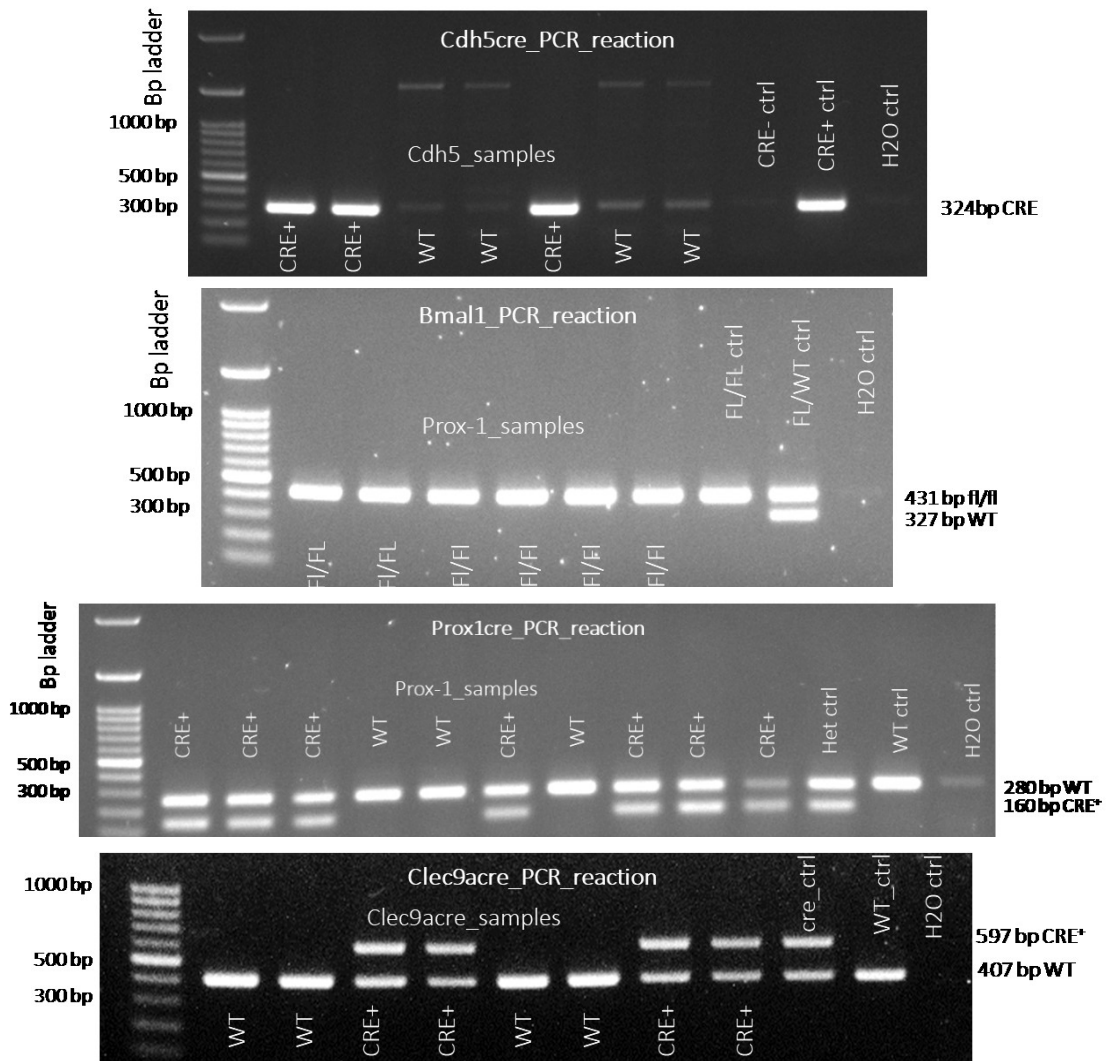


Figure 3-1: Genotyping gel electrophoresis

From top to bottom: *Cdh5cre*, *Bmal1*, *Prox1cre* and *Clec9acre* reactions. Bands were size matched and based on this, genotypes were created. Numbers on the left indicate the size of the DNA marker. Results of the respective reactions can be seen in Table 3-16.

3.2.2 Organ harvest & surgeries

3.2.2.1 Ear harvest

Once the mouse was euthanized (see 3.2.1), the ears were freed from loose hair using 70% ethanol and cut off at the transition from ear to head (seen by a color change of the skin, dark to bright). Ear sheets were then separated into dorsal and ventral sides using blunt forceps. The ear was placed ventral side up and held down with one pair of forceps. The other pair of

forceps then carefully and slowly pulled off the almost transparent uppermost layer of the skin. Both layers contain epidermis and dermis, the ventral side contains less cartilage and was always used.

3.2.2.2 Bone harvest for bone marrow-derived dendritic cell isolation

To harvest femur and tibia for experiments, the mouse was euthanized as described beforehand (see 3.2.1). Legs were released from the pelvic bone by cutting the surrounding skin. A straight pair of scissors was used to cut major ligaments and muscle strands. Reverse rotations of the bone then separated the femur from the tibia. Intact bones were further cleaned with tissue paper and a scalpel and immersed in 70% EtOH.

3.2.2.3 Superior cervical ganglionectomy

The superior cervical ganglionectomy (SCGx) surgery was performed by Dr. Chien-Sin Chen (LMU Munich, Germany). Prior to the surgery, mice were anaesthetized by intraperitoneal (i.p.) injection of ketamine (100mg/kg) and xylazine (20mg/kg). Skin on the ventral neck area was depilated and the whole surgery was commenced as described in [243, 334]. Briefly, a ventral incision of the skin was performed from the anterior tip of the sternum to the chin to expose the mandibular glands. These were then separated by carefully tearing apart the connective tissues. After separation, the carotid bifurcation of the internal and external carotid arteries was exposed. This bifurcation was flipped outwards to the side using a fine suturing thread to expose the SCG, which was then gently removed by dissection with sharp forceps. The incision was then closed by using fine suture threads. Animals were given a 2 weeks recovery period until the final experiment and received pain medication (buprenorphine, 0.1 mg/kg, subcutaneously) twice a day for 4 consecutive days.

3.2.3 Cell culture

Cells cultured and used for experiments in this thesis include WT and CCR7^{-/-} bone marrow-derived dendritic cells (BMDCs) as well as hybridoma cells for producing murine granulocyte-macrophage colony-stimulating factor (GM-CSF).

3.2.3.1 Bone marrow-derived dendritic cell culture

To culture BMDCs, femur and tibia were harvested from euthanized mice as described above (see 3.2.2.2). Single cell suspensions were isolated from femur and tibia using a 21G needle attached to a small 1 mL syringe filled with PBS, quantified on a cell counter and used for plating 2.75×10^6 BM cells. BMDCs were cultured using full R10 medium (Table 3-1) supplemented with 20ng/ml GM-CSF.

Depending on whether BMDCs were used for ex-vivo crawl-in live imaging or endpoint analysis, cells were cultured for 9 or 10 days, respectively, at 37°C and 5% CO₂. On day 3, 10ml of R10 medium supplemented with 20ng/ml GM-CSF were added. On day 6 and 8, 10ml medium of the cell culture were exchanged with 10ml fresh R10 medium supplemented with 20ng/ml GM-CSF. At day 9 or 10, all non- and semi-adherent cells were harvested and plated on a 6cm petri dish in R10 medium supplemented with 10ng/ml GM-CSF and stimulated with 100ng/ml LPS for 24h.

Viability and purity of BMDCs was tested before every experiment measuring the expression of MHCII and CD11c on DAPI⁺ BMDCs. For this purpose, 1×10^6 BMDCs were first Fc receptor blocked with anti-mouse CD16/32 for 5min at RT and subsequently stained with fluorescence-conjugated antibodies (Table 3-4 and Table 3-17) for 30min at 4°C. DAPI (0.3µM) was added to the cells, whose purity and viability were then analysed by flow-cytometry using a Gallios Flow Cytometer (Figure 3-2, Table 3-11 and Table 3-17). Viability and purity of cells were always greater than 94% and 80%, respectively, in every experiment.

Antigen	Fluorophore	Machine
MHCII	PE/Cy5	Gallios Flow Cytometer
CD11c	APC/Cy7	

Table 3-17: Viability and purity check of bone marrow-derived dendritic cells

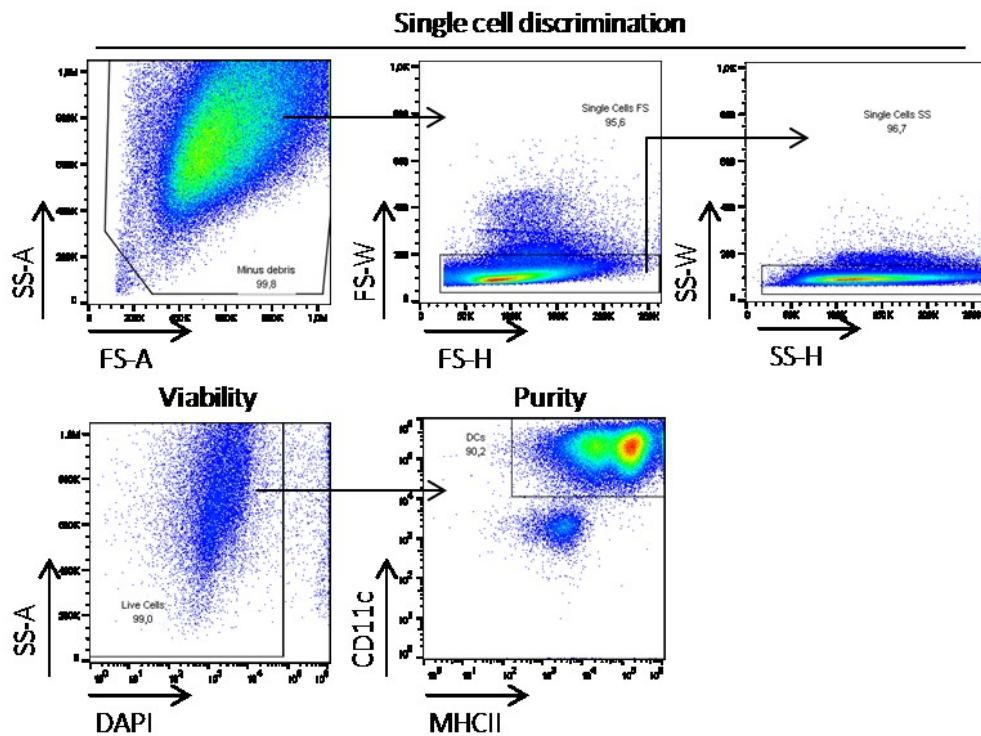


Figure 3-2: Bone marrow-derived dendritic cell culture viability and purity

1×10^6 bone marrow-derived dendritic cells (BMDCs) were cultured for 10 days and lipopolysaccharide (LPS) activated for 24h. Cells were then stained and analysed on a flow-cytometer. After single cell discrimination, viability and purity of $CD11c^+MHCII^+$ BMDCs were checked. In each experiment, viability and purity were always greater than 94% and 80% respectively.

3.2.3.2 CellTrace Violet bone marrow-derived dendritic cell stain

After maturation and stimulation (see 3.2.3.1), the BMDCs were stained with CellTrace Violet (CTV). CTV dye was added to 1×10^6 cells (working concentration of $5 \mu M$, diluted in PBS) and incubated for 20min at $37^\circ C$ in the dark, followed by 2x5min washes (300 x g and RT) using R10 medium. The cell concentration was then adjusted to 500,000 or 750,000 cells/ml and used for exogenous crawl-in assays.

3.2.3.3 Granulocyte-macrophage colony-stimulating factor producing hybridoma cell culture

GM-CSF producing hybridoma cells were a kind gift of Dr. Cornelia Halin. Frozen hybridoma cells were washed and then resuspended in 5ml R10 (day 0). Here, R10 was not supplemented with β -me. On day 3, 10ml of R10 were added to the cells. On day 6, cells were

transferred to a larger cell culture flask and medium with 150ml R10 (3 days incubation time each). On the final day, hybridoma cells were harvested and spun down at 300 x g for 5min at RT and the supernatant was collected. GM-CSF in the supernatant was quantified using a GM-CSF ELISA kit according to the manufacturer's instructions (Table 3-2). GM-CSF was then sterile filtered, aliquoted and frozen until further usage.

3.2.4 Crawl-in assays (cell trafficking assays)

3.2.4.1 Exogenous crawl-in assay (end-point)

To identify and examine the time-of-day dependent difference in lymphatic leukocyte trafficking, an exogenous crawl-in assay was utilized.

For the *ex-vivo* mouse ear sheet crawl-in migration assay (here referred to as exogenous crawl-in assay), mice were euthanized as described above (see 3.2.1). The initial protocol was based on [178] and then adapted for rhythmic analyses. Ears were quickly harvested (see 3.2.2.1) and rinsed in R10 medium (Table 3-1). The ear halves were then placed in custom built imaging chambers and immobilized (Figure 3-3A). Around 25,000-37,500 labelled BMDCs (exact numbers depending on the assay) were added on top of the open ears which were placed in 37°C, 5% CO₂ for 10-30min (WT BMDCs were incubated for 15min, CCR7^{-/-} BMDCs and controls for 30min). During this incubation, BMDCs attach to the dermal tissue. After washing off any unbound BMDCs with PBS, the ears were completely covered with R10 medium and incubated for 3h at 37°C, 5% CO₂. Within this incubation time, BMDCs migrate towards LVs.

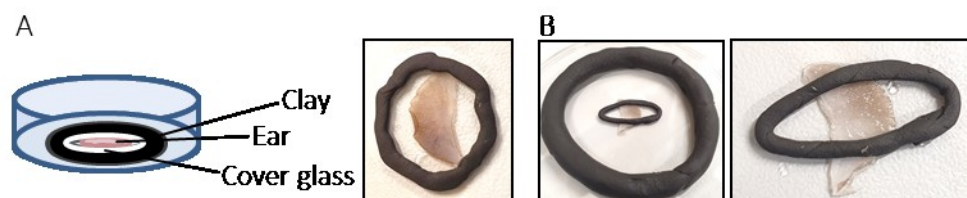


Figure 3-3: Imaging chamber for ear whole mounts

Imaging chambers were always assembled the day before the experiment.

(A) The glass on top of the open ear ensures even flattening of the ear half and thus massively improves the imaging quality. Except for live imaging and initial incubation of added bone marrow-derived dendritic cells (BMDCs), the cover slip was always added for every skin whole mount.

(B) For live imaging and initial incubation time of BMDCs, the ear was flattened using clay in an ellipsoid shape. The central part was then filled with R10 medium.

Ear sheets were then stained with different combinations of LYVE-1, CD31 or PDPLN (Table 3-4) for 30min at RT and subsequently fixed for 1h in 4% PFA. For the end point analyses, staining was performed after the migration incubation, to reduce any effects of protein staining and possibly blocking of BMDC migration. After placing ear sheets in the custom build image chamber (Figure 3-3B), images were obtained using a Zeiss Axio Examiner.Z1 confocal spinning disk microscope (Figure 3-4 and Table 3-12).

At least 8 images / ear sheet were taken from LVs (pre-collecting and capillaries) using a 20x magnification. For analysis, the number of cells outside or inside the vessels was counted using 3D visualization tools in Fiji and Slidebook 6.0 as well as orthogonal views and optical slicing (Figure 3-4). This number was then normalized to the calculated volume of the vessels. To calculate the volume of the vessels, an ellipsoid structure of the vessels was assumed.

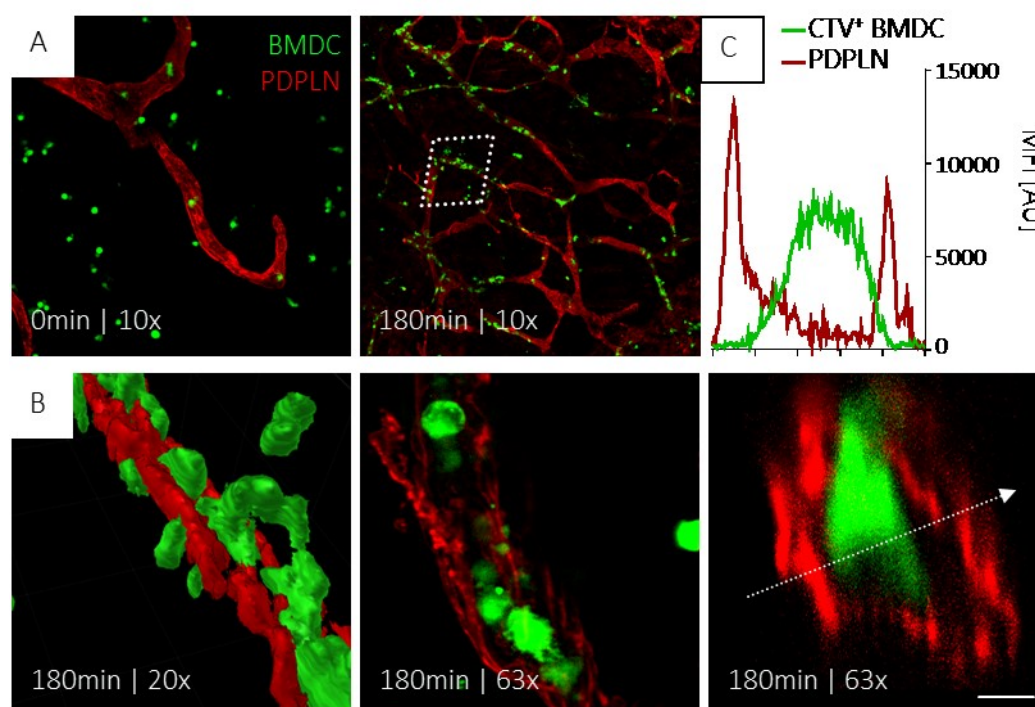


Figure 3-4: Exogenous bone marrow-derived dendritic cell crawl-in assay

(A) 25,000 CellTrace Violet⁺ bone marrow-derived dendritic cells (BMDCs) were added onto split ears & incubated for 180min at 37°C and 5% CO₂. After 180min, BMDCs have localized inside the lumen of PODOPLANIN⁺ (PDPLN) vessels as exemplified with a 10x objective.

(B) Higher magnification and 3D rendering visualizes BMDCs migrating into lymphatic capillaries.

(C) Mean-fluorescence-intensity (MFI) profiling of BMDCs enables a clear separation of BMDCs inside and outside of vessels. Scale bar = 100 / 50 / 10µm.

3.2.4.2 Endogenous crawl-in assay

To analyse and better understand the time-of-day difference in endogenous dermal DC trafficking through LVs, an endogenous crawl-in assay was designed. For the endogenous skin DC mobilization and crawl-in migration assay (in this thesis referred to as endogenous crawl-in assay), mice were euthanized and ear halves harvested as described above (see 3.2.1 and 3.2.2.1). After a 15min wash in R10 medium, ear sheets were stored on R10 medium dermis facing down at 37°C 5% CO₂ for 6h or 24h in 24-well cell culture plates. During the incubation period, dermal DCs become mobilized and migrate towards lymphatic capillaries (see Figure 3-5). Afterwards, ear sheets were fixed for 2h in 4% PFA and stained for CD11c and either LYVE-1 or CD31 for 30min at RT (Table 3-4). The number of cells in and outside the vessels as well as the vessel volume was then analysed as before (see 3.2.4.1, Figure 3-4B&C and Figure 3-5).

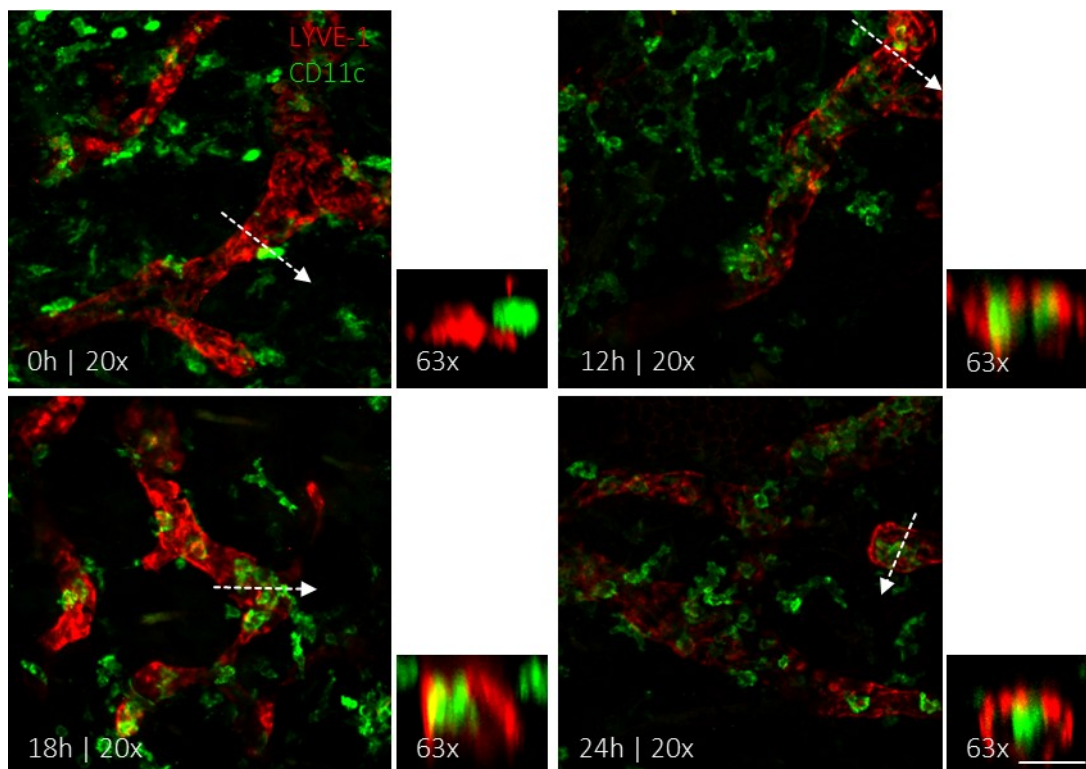


Figure 3-5: Endogenous crawl-in assay

Ears were harvested, split and cultured dermis facing down for 0h, 12, 18h or 24h and stained for LYVE-1 and CD11c. The longer ears were incubating on medium, the more CD11c⁺ dendritic cells migrated into LYVE-1⁺ lymphatic capillaries as shown using 20x and 63x magnification. Scale bars= 10 / 50μm.

3.2.4.3 Live imaging of exogenous crawl-in assays

For live-imaging of the exogenous crawl-in assay, mice were euthanized and ear halves were harvested as described above (see **3.2.1** and **3.2.2.1**).

Ear sheets were then stained for LAMININ with a primary antibody for 45min in R10 medium at RT, followed by a secondary FITC conjugated antibody for another 45min at RT in R10 medium (**Table 3-5**) prior to the assay. Ear sheets were placed in custom built imaging chambers (**Figure 3-3**), immobilized and 50,000 BMDCs in R10 medium were added on top. After 10min incubation at 37°C 5% CO₂, unbound BMDCs were washed off with R10 medium and ear halves were immersed in phenol-red free R10 supplemented with 10 mM HEPES (**Table 3-1**). Imaging in a 5% CO₂ chamber at 37°C was then commenced with one 30-40µm deep 3D image per 120 seconds for around 60min using either 10x or 20x objectives.

3.2.4.4 Short crawl-in assays with zone segmentation

To decipher the role of time-of-day dependent differences in the CCL21 chemokine gradient, short crawl-ins with zone segmentation of the dermal interstitium were employed. Mice were euthanized and ears harvested as described above (see **3.2.1** and **3.2.2.1**).

37,500 BMDCs in R10 medium were cultured for 10 days, LPS activated for 24h and then added to the opened & immobilized ear sheets for 15min at 37°C and 5% CO₂. After a wash in R10, sheets were incubated in either 0min, 10min, 20min, 30min, 40min, 50min or 60min. Immediately after the assay, sheets were washed in PBS and stained for CD31-488 at RT for 30min. After another wash, sheets were fixed in 4% PFA for 1h and mounted for imaging using custom-built imaging chambers (**Figure 3-3**). 5 3D (20x objective) with 30-40µm depth were acquired / sheet and transformed into maximum z-projections. In each projection, the LVs were manually outlined and a binary mask and distance dependent map was generated with distance zones as shown in **Figure 3-6** using algorithms (see **7.2**). CTV⁺ BMDCs were counted and visualized as parts of total CTV⁺ BMDCs.

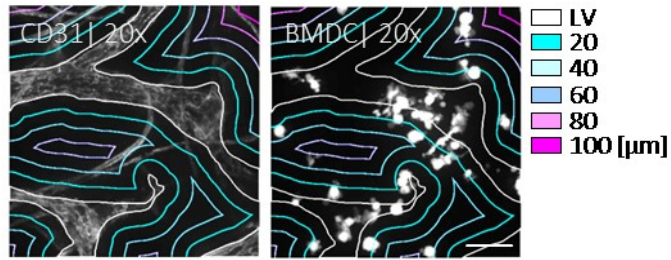


Figure 3-6: Zone segmentation of the lymphatic interstitium

Segmentation of the interstitium of lymphatic vessels (LV) was performed using Matlab. A region of interest was drawn based on CD31 signal resembling LVs. An algorithm then segmented the space into 20µm contours that were used for analysis. Cells in the LV were excluded from the analysis. The code can be found in the appendix (see 7.2). Legend on the right is shown in µm. Scale bar = 50µm.

3.2.5 Flow cytometry

3.2.5.1 Crawl-out assay and ear cellularity quantification

To quantify and phenotype the ear cellularity and how well dermal DCs can emigrate the skin into medium, ears were harvested from euthanized mice as described beforehand (see 3.2.2.1 and 3.2.1.1), weighed and placed onto R10 medium (Table 3-1) dermis facing down for 1h to wash.

After incubation, ear halves were stored on fresh R10 medium for 24h which was either plain or supplemented with 1µg/ml mCCL21 (henceforth described as crawl-out assay). 24h later, ear halves were harvested, pooled and gently digested for 20min at 37°C with collagenase IV (1mg/ml), DNase (0.2mg/ml) and dispase II (0.2mg/ml). If no crawl-out but direct quantification or phenotyping of the ear cellularity was desired, ear halves were quickly washed in PBS after harvest and directly digested. After digestion, cells were filtered through a 70µm cell strainer, washed in PBS (5min, 300 x g at RT) and resuspended in FACS buffer (Table 3-1). Simultaneously, the medium containing emigrated DCs was harvested, pooled, washed with PBS (5min, 300 x g at RT) and both the ear cell suspension and medium cell suspension were first Fc receptor blocked with anti-mouse CD16/32 for 5min at RT and subsequently stained with fluorescence-conjugated antibodies for 30min at 4°C (Table 3-4 and Table 3-18). DAPI (0.3µM) and full-bright counting beads were added to the cells, which were then analysed by flow-cytometry using either a Gallios Flow Cytometer or LSRTFortessa flow-cytometer at the LMU Munich or University of Geneva (Table 3-11 and Figure 3-7 for the gating strategy).

Antigen	Fluorophore	Experiment	Machine
CD103	FITC	Ear cellularity WT animals, crawl-out +/- mCCL21	Gallios flow cytometer
Ly6C	PE		
CD45	PE/dzI594		
Ly6G	PerCP/Cy5.5		
MHCII	PE/Cy7		
EPCAM	AF647		
CD11b	AF700		
CD11c	APC/Cy7		
CD45	BUV395	MyD88 and SCGx ear cellularity & crawl-outs	LSRFortessa flow-cytometer LMU core facility
MHCII	BV711		
CD11c	BV510		
EpCAM	AF647		
CD103	FITC		
CD11b	AF700		
Ly6C	PE		
Ly6G	PerCP-Cy5.5		
B220	PE-Cy7		
CD4	BV605		
CD8	APC-Cy7	Ear skin DC phenotyping	LSR Fortessa flow-cytometer University of Geneva core facility
CD86	BUV395		
CD40	BUV737		
CD45	BV421		
CD103	BV480		
CD80	BV605		
MHCII	BV650		
CCR7	BV786		
CD321	FITC		
CD301b	PerCP-Cy5.5		
EpCAM	PE		
CD3	PE-Cy5		
CD19	PE-Cy5		
CD205	PE-Cy7		
CD11c	APC-R700		

Table 3-18: Staining panels for crawl-outs, ear cellularity and phenotyping

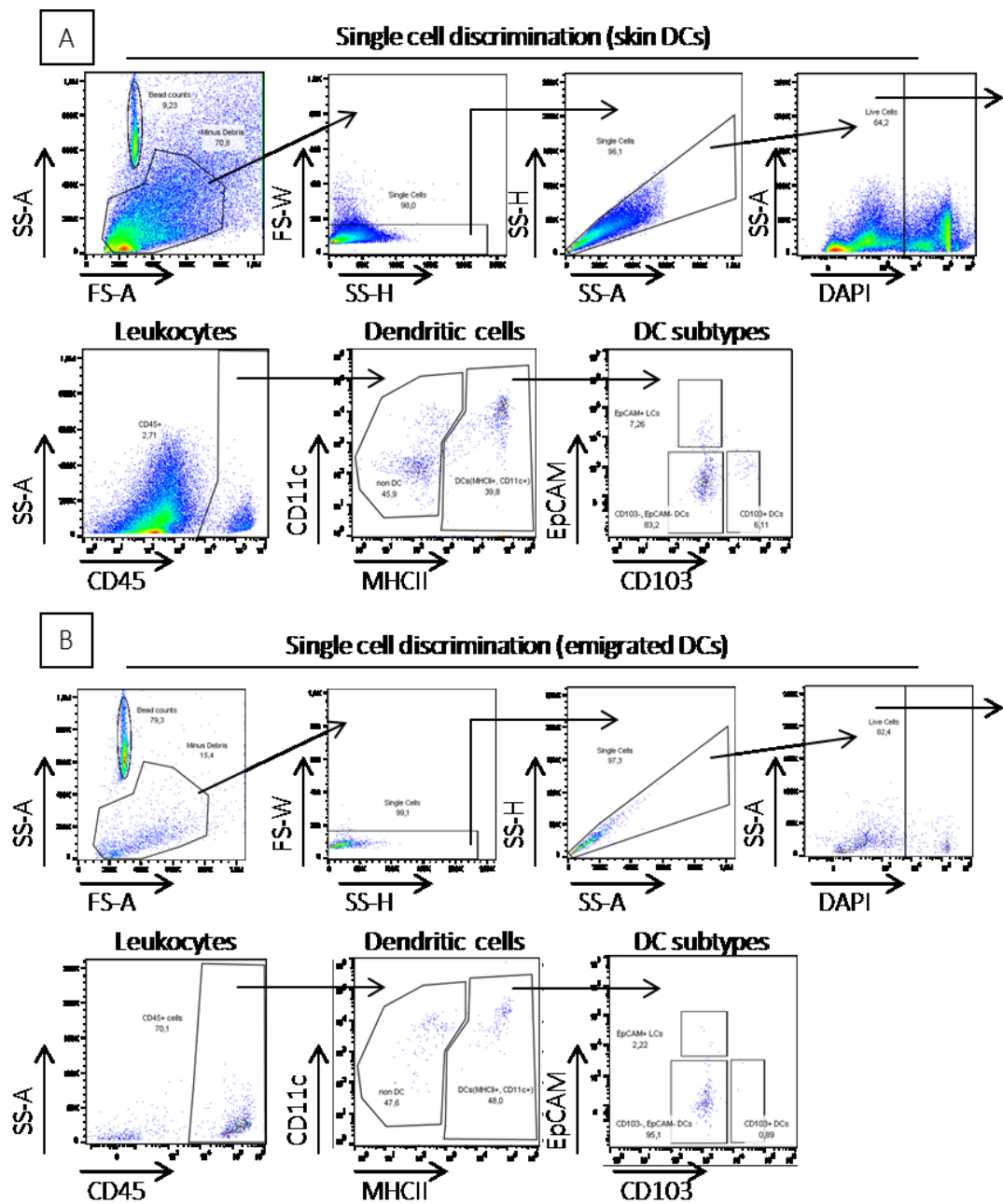


Figure 3-7: Skin dendritic cell & crawl-out assay gating strategy

(A) For flow-cytometric analysis of ear cellularity & phenotyping, ears of mice were harvested and directly digested and stained.

(B) To quantify the amount of emigrated skin dendritic cells (DCs; crawl-out assay), ears were cultured on R10 medium for 24h. Medium was then harvested, pooled and cells were stained.

DCs were gated as $CD45^+CD11c^+MHCII^+$ and can be classified as either Langerhans cells (LC; $EPCAM^+CD103^-$), conventional DC 1 (cDC1; $EPCAM^-CD103^+$) or cDC2 ($EPCAM^-CD103^-$). Counting beads and DAPI were always added for quantification of absolute cell numbers and viability check.

3.2.5.2 Sorting of skin LECs

To sort murine skin LECs for RNA sequencing, 4 ears from two mice were harvest, digested as described above (see 3.2.4.1 and 3.2.5.1) and pooled per biological replicate and time point. Harvesting of ears was always done at 8am using light/darkness cabinets to minimize side effects. After isolation, the cell suspensions were prepared solely on ice for sorting on a BD FACSAriaIIIu (Table 3-11). The cell fraction was stained with fluorescence-conjugated antibodies for 30min at 4°C (Table 3-4 and Table 3-19). Immediately before the sort, DAPI (0.3µM) was added to the cells. Live PDPLN⁺CD31⁺ LECs were sorted directly into 350µl Trizol-LS at 4°C using a 100µm nozzle and with a purity > 90% as determined after every sort (Figure 3-8). The cell numbers sorted ranged between 3000 and 5000 cells / two pooled ear pairs (see 3.2.8 for exact numbers). Directly after sorting, the samples were shock-frozen on dry-ice.

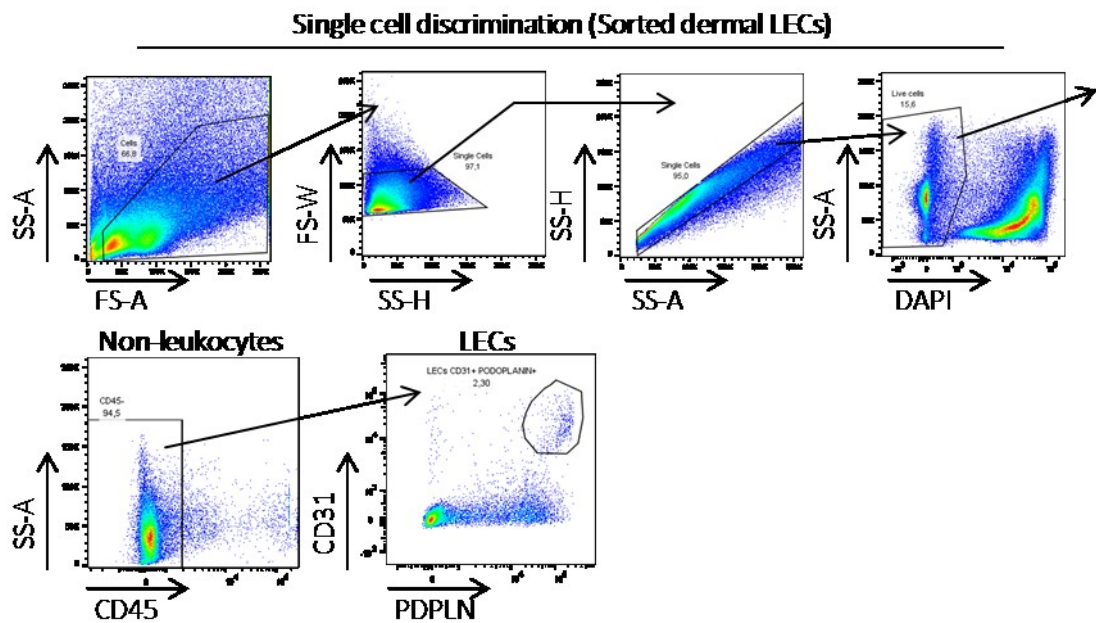


Figure 3-8: Gating strategy of sorted lymphatic endothelial cells

Ears were harvested, split, digested and stained to discriminate live CD45⁻CD31⁺PODOPLANIN⁺(PDPLN⁺) lymphatic endothelial cells (LECs). LECs were sorted on a FACSAriaIIIu with 1 70µm nozzle and purity >90%.

Antigen	Fluorophore	Experiment	Machine
PODOPLANIN	PE	LEC sort	FACSAriaIIIu
CD45	PE/dz1594		
CD31	APC		

Table 3-19: Staining panel for lymphatic endothelial cell sort

3.2.6 Functional neutralization of proteins and chemokine gradient disturbance

To investigate the functional relevance of proteins involved in rhythmic dermal DC trafficking, neutralization antibodies or chemokine disturbances were utilized. Split ears used for exogenous crawl-in assays were incubated with R10 medium containing diluted neutralization antibodies prior to the cell migration assay for 1h at RT (**Table 3-7**). In case of the endogenous crawl-in assay, neutralization antibodies or reagents were directly added to the R10 medium for 24h. In general, isotype antibodies of neutralization antibodies were used as controls (**Table 3-7**). Endogenous and exogenous crawl-in assays were further performed as described above (*see 3.2.4*).

For disturbing the extracellular CCL21 gradient in the skin, ear halves were incubated with either heparinase II and IV (100 mIU) at 37°C for 1h or placed in PBS containing 0.1% BSA and 0.6µg/ml CCL21 at 4°C for 90min prior to the endogenous crawl-in (**Table 3-8**). After heparinase incubation, ear halves were thoroughly washed to remove any remaining CCL21. Ear halves were then stored on R10 for 24h and the endogenous crawl-in assay was performed as described above (*see 3.2.4.2*).

3.2.7 Immunofluorescence staining

All immunofluorescence stainings were imaged using a Zeiss Axio Examiner.Z1 confocal spinning disk microscope. In general, ear whole mounts were imaged using a custom-built imaging chamber (**Figure 3-3**).

3.2.7.1 Quantitative immunofluorescence staining

To measure the expression levels of trafficking molecules in LECs, mice were euthanized as previously described (*see 3.2.1*) and organs (ear, inguinal LN, lung and small intestine (cleaned)) were harvested, placed in OCT, shock frozen on dry ice and stored at -80°C. The next day, organs were shifted to -20°C and sectioned at a thickness of 10µm on a cryostat to ensure only having one layer of cells on a glass slide (organs were given 1h to warm up to -20 before cutting). Tissue sections were thawed to RT and encircled with a hydrophobic alcohol-

resistant pen. Sections were then fixed with cold methanol (100%) for 10 min at RT followed by a 5min wash in PBS at RT and blocked and permeabilized in PBS containing Triton-X100 (0.5%) and normal goat serum (20%). Sections were always stained for LYVE-1-AF488 in combination with the proteins of interest labelled with either PE or APC o/n at 4°C (**Table 3-4**). For quantification and as negative controls, isotype stains (**Table 3-6**) were employed. On the next day, samples were washed with PBS for 2x5min in PBS at RT and imaged.

For staining intracellular CCL21 in sections using a biotinylated anti-CCL21 antibody, the tissue slides were fixed for 10min using cold methanol (100%) and blocked and permeabilized in PBS containing triton-X100 (0.5%), normal goat serum (20%) and avidin (20%; **Table 3-2**). After a wash for 10min in PBS at RT and incubation in PBS containing 20% biotin, the sections were stained for LYVE-1 and CCL21 o/n at 4°C (**Table 3-4**). On the next day, samples were 3x5min washed with PBS, incubated in streptavidin-PE (2.5µg/slice) at RT for 15min (**Table 3-5**) and washed again for 3x5min using PBS for.

2D images were obtained using a 20x objective with at least 5 pictures of the region of interest. For quantification, 5 images of one slice were averaged and counted as one biological replicate. Automated thresholding was applied to identify LYVE-1⁺ capillaries and create a mask, which was then applied to the fluorescent signal of the protein of interest (**Figure 3-9**).

The average mean-fluorescence intensity of 5 isotype stains was then deducted from the mean fluorescence intensity of the protein of interest. It was always made sure, that the LYVE-1⁺ area size did not differ significantly between samples within one type of organ.

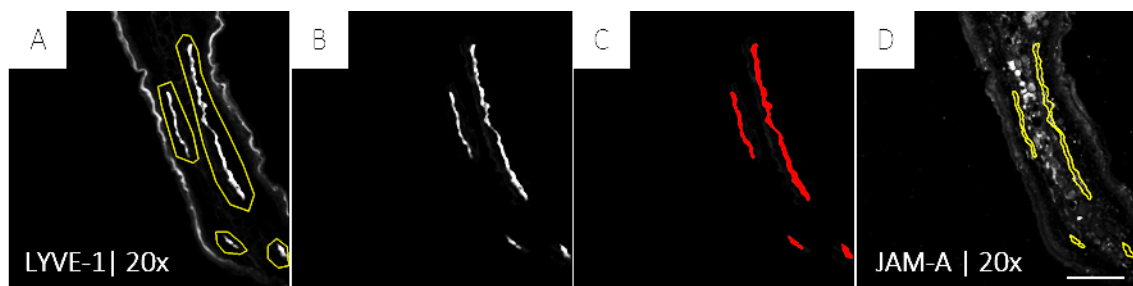


Figure 3-9: Quantitative immunofluorescence analysis

(A) 10µm skin sections were stained for LYVE-1 and JAM-A o/n. LYVE-1⁺ lymphatic vessels were selected with a region of interest (ROI; shown in yellow).

(B) Images were cleared for any fluorescent signal outside the ROI.

(C) Using automated thresholding, only the LYVE-1⁺ capillary was selected (shown in red).

(D) The ROI (shown in yellow) of the automated thresholding was applied to the JAM-A fluorescent signal to measure its intensity. Scale bar = 50µm.

3.2.7.2 Whole mount immuno-fluorescence staining

To better understand the 3D architecture of proteins expressed on LVs or cellular structures in the skin, ears were collected as described beforehand (see 3.2.1 and 3.2.2.1). In general for whole-mount staining of skin, split ears were either 4% PFA fixed for 1h before or after staining of proteins with fluorescence-conjugated and primary/ secondary antibodies or biotin and streptavidin (see 3.1.4). In case of staining for CD31 or PROX-1, fixation was done after staining. If staining for LYVE-1, PODOPLANIN, LAMININ, CCL21, JAM-A, JAM-C, CD99, VE-CADHERIN, CD11c, CD103, LAMININ, KI67 and GOLPH4, split ears were fixed before staining. For proteins expressed on the surface of cells, split ears were blocked in R10 medium for 2h at RT. Split ears were then placed in the staining solution for either 30min at RT or o/n at 4°C. After 3x15min wash in PBS at RT, the whole mounts were ready to image.

3.2.7.3 Intracellular whole mount staining of CCL21, GOLPH4, PROX-1 and KI67

To image intracellular proteins in skin whole mounts, harvested ears were first fixed in 4% PFA at RT for 1h and then blocked and permeabilized in R10 medium containing 0.3% triton-X100 for 1h. Ear halves were further (without washing) incubated in R10 medium supplemented with primary or in the case of PROX-1 and KI67 staining fluorescence-conjugated antibodies o/n at 4°C (Table 3-4). Ears were washed for 2x15min in PBS at RT and either directly imaged (PROX-1 + DAPI (0.3µM)) or incubated in R10 containing secondary antibodies and streptavidin (Table 3-5). After 3x15min wash in PBS at RT, DAPI (if needed; 0.3µM) was added to the cells and whole mounts were imaged.

To analyse the intracellular amounts of golgi- and vesicular CCL21 in LYVE-1⁺ LECs in skin, 5 different regions of lymphatic capillaries were imaged. Maximum z-projections of 30-40µm deep z-stacks were then taken for analysis in FIJI. A makro (see 7.2) was used to minimize any human bias. The makro first created a ROI based on LYVE-1 expression and automatically excluded non-lymphatics and lymphatic-membrane regions, so that only the nucleus and cytoplasm of LECs were left. CCL21 was then first quantified in GOLPH4^{high} regions, resembling the golgi apparatus (regarded as golgi CCL21). The golgi area was then deducted from the cellular compartment, and CCL21 in the remaining GOLPH4^{low} staining was quantified (regarded as vesicular CCL21). MFIs from 5 different regions from one ear were averaged and

the isotype MFI signal from GOLPH4^{high} and GOLPH4^{low} regions was deducted (analysis is based on the example shown in **Figure 3-9**)

3.2.7.4 CCL21 whole mount staining and gradient analysis

To visualize and analyse the extracellular CCL21 gradient, ears from euthanized mice were harvested as described above (see **3.2.1** and **3.2.2.1**) and directly fixed for 1h in 4% PFA. After blocking in R10 medium containing avidin (20%) for 1h at RT, leaving split ears in PBS and Biotin (20%) for 30min, split ears were stained for LYVE-1 and CCL21 (Biotin) o/n at 4°C (**Table 3-4**). Next day, ears were incubated in streptavidin-PE for 3h at 4°C in the dark (**Table 3-5**). After washing for 3x15min in PBS at RT, split ears were mounted and imaged.

Images used to quantify the average intensities of interstitial CCL21 chemokine signal were maximum intensity projections ranging between 30-40µm Z-stacks with a z-step size of 1µm. Within an area of 512x512 pixels (341.33µm x 341.33µm), LV capillaries were manually outlined based on LYVE-1 staining, converted into binary masks and transformed into distance maps (via Matlab, see **7.2**). The average intensity images of CCL21 staining were then integrated into distance-dependent fluorescence intensities (Figure 3-10). 5 average distance-dependent fluorescence intensities from different locations within one mouse ear were averaged and counted as one biological replicate. All samples from ZT7 and ZT19 were normalized to the highest average fluorescence intensity of ZT7. Isotype stains were taken as negative controls.

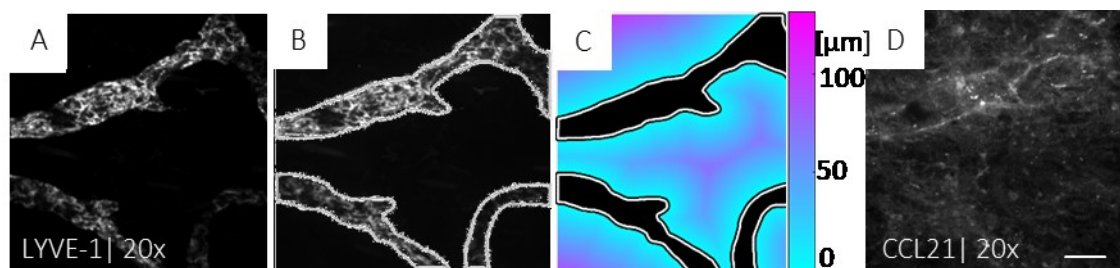


Figure 3-10: Extracellular CCL21 gradient analysis

(A) Ear sheets were stained for LYVE-1 and CCL21 o/n and subjected to analysis.

(B) LYVE-1⁺ capillaries were outlined to create a region of interest. Based on this, the image was transformed into a binary mask.

(C) The image was converted into a distance map which was applied to (D) to measure the averaged intensity at every distance from the binary mask. The algorithm can be seen in the appendix (see **7.2**). Scale bar = 50µm.

3.2.8 RNA sequencing of lymphatic endothelial cells

Shock frozen, sorted LECs (see 3.2.5.2) were stored at -80°C and then given to Dr Julia Phillipou-Massier in the Laboratory for Functional Genome Analysis (LAFUGA; Gene Center LMU, Germany), which performed the RNA isolation, cDNA reverse transcription, gene bank generation as well as the RNA sequencing. The analyses were partly done by Julia Philippou-Massier and Stephan Holtkamp. The methods description was provided by Julia Philippou-Massier.

Zeitgeber Time	# Cells	Purity [%]	RNA conc. [ng/μl]	RIN value
1.1	3544	91	Not provided by Core Facility	Not provided by Core Facility
1.2	3627	94		
1.3	3448	96		
1.4	3791	93		
1.5	3217	95		
7.1	4355	96		
7.2	4894	97		
7.3	5595	91		
7.4	5599	91		
7.5	3847	92		
13.1	3449	94		
13.2	3807	95		
13.3	3424	93		
13.4	3906	95		
13.5	3398	97		
19.1	6819	96		
19.2	3538	95		
19.3	5684	92		
19.4	5465	91		
19.5	5659	92		

Table 3-20: Cell counts of sorted lymphatic endothelial cells

Briefly, RNA of cells harvested in TriZol LS was purified using Direct-zol RNA mini Prep Kit (ZymoResearch) following manufacturer's instructions. Isolated RNA was quantified using the Nanodrop (ThermoFisher) and analyzed on a Bioanalyzer (Agilent) using the RNA 6000 Nano or Pico Kit (Agilent). Next, 75 ng of eluted total RNA was digested with DNase (ThermoFisher) to remove DNA contaminations. An additional purification step with RNAClean XP Beads (Agencourt) was performed. The purified, bead bounded RNA was directly used as input in the SMART-Seq v4 Ultra Low Input RNA Kit (TaKaRa Bio). Full-length cDNA was generated following manufacturer's instructions. Full-length cDNA was quantified using the Qubit dsDNA

HS Assay Kit (Invitrogen) with the Qubit fluorometer. Finally, sequencing libraries were generated using 500 pg full-length cDNA following the NexteraXT protocol (Illumina). Briefly, in a single tube enzymatic reaction cDNA is simultaneously tagmented and tagged with Illumina sequencing adapters before the obtained sequencing libraries are amplified. Finally, sequencing libraries were quantified on a Bioanalyzer (Agilent) using the DNA 1000 Kit (Agilent) and sequenced on a HiSeq1500 system (Illumina) with a readlength of 100 nt, single-end mode.

For data processing, obtained transcriptome profiles were processed on a Galaxy web interface [335] hosted by LAFUGA, Gene Center, Munich. After demultiplexing and recommended trimming data was mapped against the mouse genome (mm10) using RNA-STAR mapper (Galaxy Version 2.5.2b-0). Abundant reads were counted using HTSeq-count (Galaxy Version 1.0.0). Afterwards gene expression analysis to detect differentially expressed genes was performed using DESeq2 (Galaxy Version 2.11.40.6) setting the FDR <0.05.

Shown RNA counts in the results section were normalized to gene length and presented as either log₂ or raw values. Heat maps of genes were generated using GraphPad Prism 7.0.

3.2.9 Statistical analysis

Statistical analyses were performed using GraphPad Prism 7.0. All data are represented as mean ± SEM. For comparison of two groups, either an unpaired student's *t*-test or a Mann-Whitney test was performed. One-way ANOVA followed by Tukey's post hoc test, two-way ANOVA followed by a Šidák correction or a Kruskal-Wallis test were executed if three or more groups were analysed.

In order to examine the oscillations and rhythmicity of data, a cosinor-based rhythmometry/statistical technique was employed [336]. The more a fitting curve lining through the data of different time points mirrors the shape of a cosinor's curve, the lower the *p*-value and more significant the oscillation of the data is. Statistical significance was assessed as **p*<0.05, ***p*<0.01, ****p*<0.001 and *****p*<0.0001.

4 Results

4.1 Visualization of lymphatic vessels

The study was commenced by establishing the visualization of LECs in skin, LN, small intestine and lung using quantitative immunofluorescence imaging and a spinning disk confocal microscope.

First, 10 μ m sections of these four organs were stained for LYVE-1, PDPLN and CD31. Imaged sections of the skin revealed large triple positive LVs (**Figure 4-1A**). Notably, the depicted central large vessel is marked with an arrow, and surrounded by small, blind-ended LYVE-1⁺ capillaries (**Figure 4-1A**). LN LECs were triple positive for LYVE-1, PDPLN and CD31 as well, with LYVE-1 showing the strongest signal intensity. This triple positivity extended to all lymphatic sub-regions, the SCS, CS and MS (**Figure 4-1B**).

Captured small intestine sections presented LYVE-1⁺ lacteals and outer small intestinal submucosal LVs (SMLVs). This LYVE-1⁺ signal overlapped with PDPLN⁺ and CD31⁺ signals, forming a triple positivity for these biomarkers as well (**Figure 4-1C**).

Finally, stained lung sections displayed a dense vascular network, in which evenly distributed small LYVE-1⁺ vessels could be observed. These LVs were double positive for CD31 and PDPLN. Additionally, BECs from this network express LYVE-1 and PDPLN as well but to a lower extent (**Figure 4-1D**).

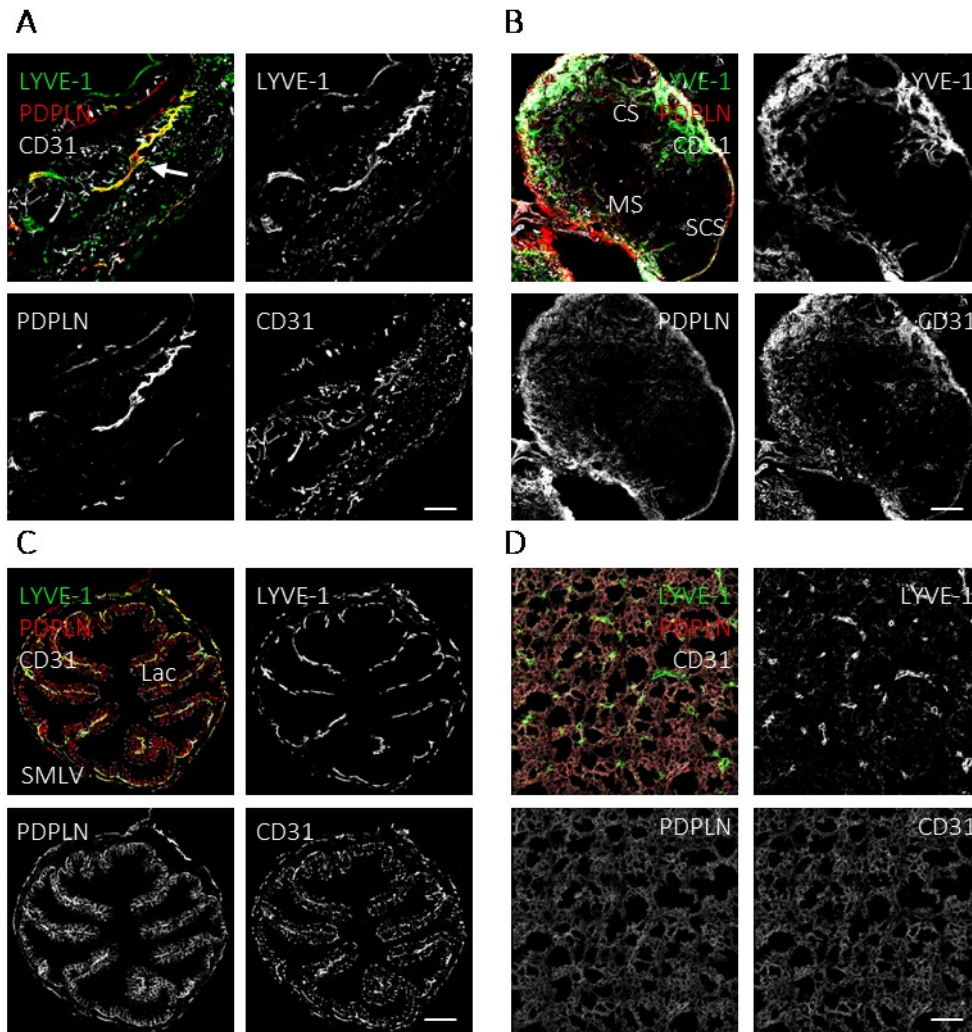


Figure 4-1: 2D Fluorescence microscopy of lymphatic biomarkers

Fixed and permeabilized 10 μ m slices of sectioned ears **(A)**, inguinal lymph node **(B)**, small intestine **(C)** and lung **(D)** were stained for LYVE-1, PODOPLANIN (PDPLN), and CD31. Each image contains 4 patched images to facilitate a greater view.

(A) Arrow directs at a large lymphatic vessel. Scale bar = 70 μ m

(B) Scale bar = 100 μ m. SCS = subcapsular sinus, CS = cortical sinus, MS = medullary sinus.

(C) Scale bar = 100 μ m. Lac = lacteal, SMLV = submucosal lymphatic vessel.

(D) Scale bar = 70 μ m.

I then moved from 2D visualization to 3D visualization allowing for a better understanding of the 3D lymphatic architecture. For this purpose, a whole mount staining technique for the skin and small intestine was set up (see 3.2.7.2).

Similar to 2D images, 3D images of stained whole-mounted ears showed LYVE-1^{high} capillaries merging into LYVE-1^{low} pre-collecting vessels. These vessels were also positive for PDPLN, CD31 and LAMININ. Since CD31 and LAMININ stain other cellular structures as well, LVs in the respective images are highlighted with an arrow (**Figure 4-2A**). Higher magnification visualized an accumulation of LYVE-1 and CD31 in cell to cell contact regions (junctions), whereas PDPLN was evenly dispersed on the LEC surface and LAMININ on the basal membrane (**Figure 4-2A**).

This was visualized with a Slidebook 3D software tool at higher magnification, confirming LYVE-1 to be expressed on LEC junctions and that PDPLN was evenly distributed on the LEC membrane (**Figure 4-2B**). 3D visualization of lacteals in the small intestine exposed a singular LYVE-1⁺ LV, which is engrafted into an intertwined CD31⁺ small capillary network (**Figure 4-2C**). Lacteals flow into outer SMLVs, that were LYVE-1⁺ and CD31⁺ (**Figure 4-2C**).

Based on these results, I decided to make use of LYVE-1, CD31 and PDPLN for visualizing LVs in all following experiments.

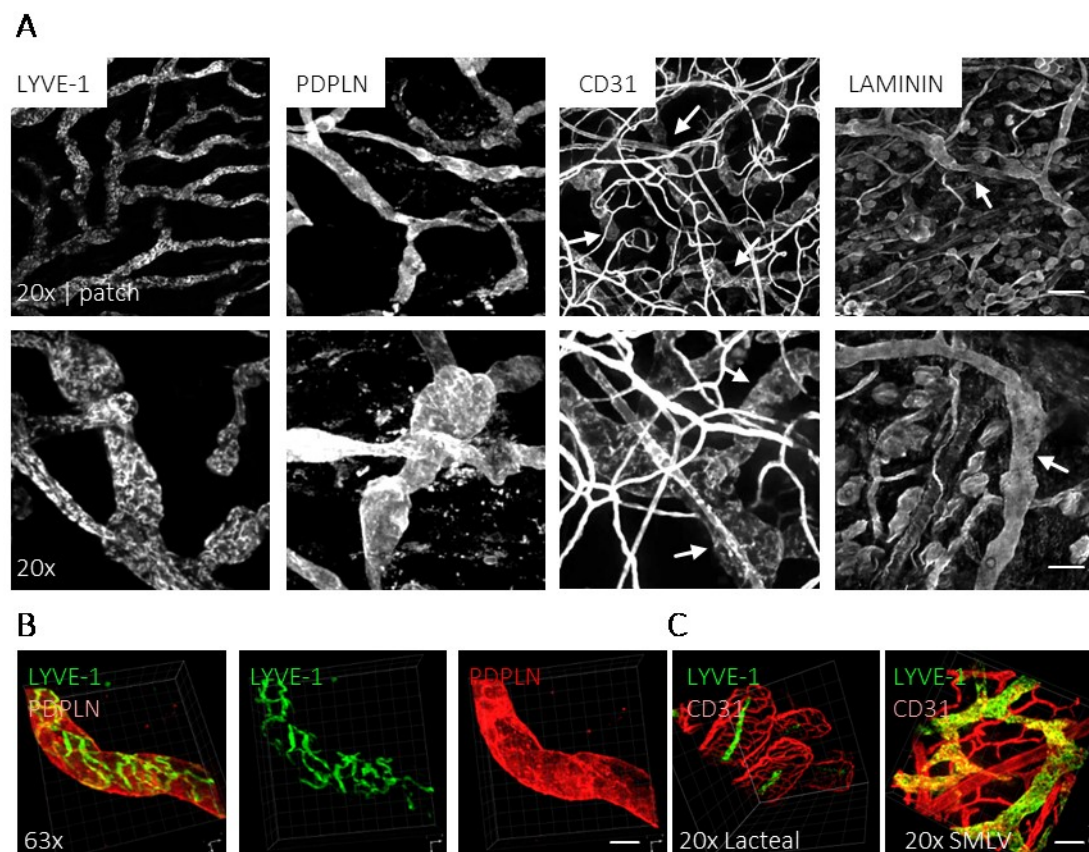


Figure 4-2: 3D Lymphatic whole mounts of biomarkers in skin and small intestine

(A) Split ears were stained for LYVE-1, PODOPLANIN (PDPLN), CD31 or LAMININ. Upper pictures consist of 4 patched images of skin whole mounts; lower pictures show a higher magnification. Arrows indicate lymphatic vessels. Scale bar = 70 / 50 μ m.

(B) Split ears were stained for LYVE-1 and PDPLN and visualized with the Slidebook 3D visualization tool. Scale bar = 10 μ m.

(C) Small intestines were cut, cleaned, and stained for LYVE-1 and CD31. Both the lacteal and submucosal lymphatic vessel (SMLV) regions were visualized with the Slidebook 3D visualization tool. Scale bar = 50 μ m.

4.2 Demonstration of rhythmic dendritic cell migration into dermal lymphatic capillaries

I then moved on to design two complementing trafficking assays, exogenous and endogenous crawl-in assays (see 3.2.4). Using these approaches, it was tried to assess the migratory properties of either dermal DCs or exogenous BMDCs in the skin with respect to the time of day.

First, an *ex-vivo* mouse ear crawl-in migration assay using cultured BMDCs was adapted for circadian experiments as this allowed a survey of the initial steps in an immune response and conclusions with respect to the micro-environment. Fresh BM cells were isolated and differentiated into BMDCs. BMDCs were then stained with CTV and subsequently added onto split ears harvested from mice at four different times of the day. In the first experiment, ears from different time points received their own batch of cells (**Figure 4-3A**). Surprisingly, BMDC migration into lymphatic capillaries and pre-collecting vessels was highly dependent on the time the ear was harvested. BMDCs migrated into lymphatic capillaries with a rhythm, peaking at ZT7 and troughing at ZT19, with a significantly higher ratio of cells being located within the lymphatics compared to cells located on the outside (**Figure 4-3B**). Neither were differences seen between overall transferred BMDC cell counts present in the ear after the assay, nor were differences observed in the analyzed vascular volume (**Figure 4-3C**). Since using different batches of cells might compromise the comparability between different ZTs, I further harvested ears at the same time from phase-shifted mice allowing us to simultaneously transfer the same batch of BMDCs onto different ears (**Figure 4-3D**). The data generated in this manner were almost identical to the previous experiment with BMDCs predominantly migrating into afferent lymphatics at ZT7 compared to other time points (**Figure 4-3E**). As before, LV volume and the amount of overall transferred CTV⁺ BMDCs did not differ between time points (**Figure 4-3F**). This rhythmic behavior is shown as an example in skin whole mounts, indicating a higher percentage of BMDCs within PDPLN⁺ vessels at ZT7 compared to ZT19 (**Figure 4-3G**). Viability and purity of transferred BMDCs in both experiments were not lower than 92% and 70%, respectively, and did not vary between cells (see 3.2.3.1 for gating strategy and exemplary flow-cytometry plots; data shown in **Figure 4-3H**). These data thus demonstrated the ear micro-environment to govern a rhythmic migration capacity of BMDCs into lymphatics.

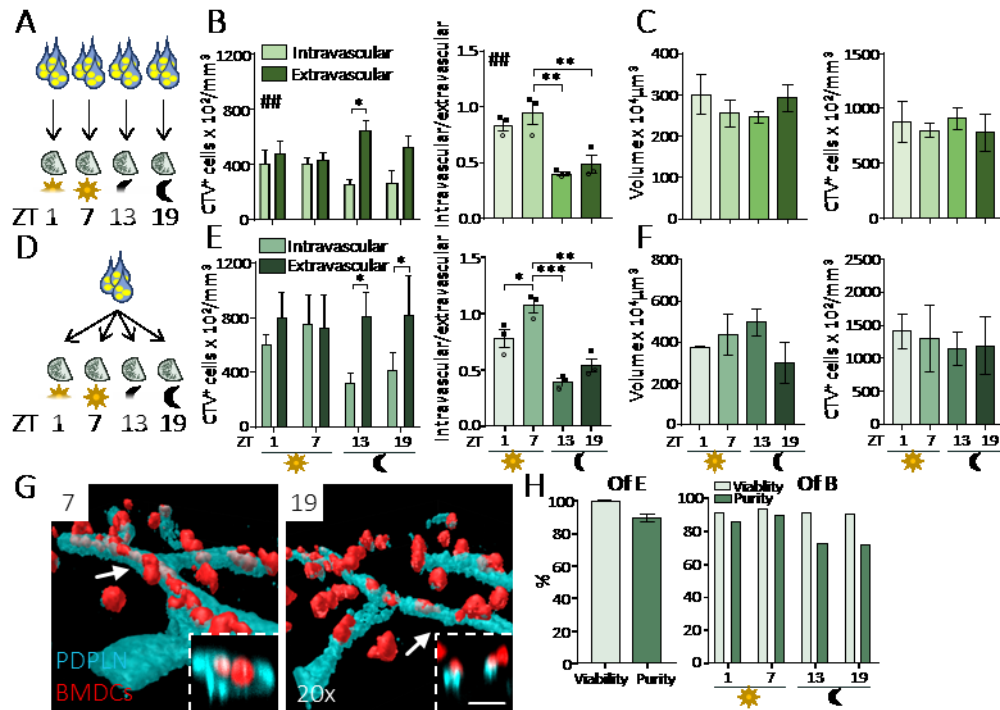


Figure 4-3: Higher trafficking capacity during the day in dermal lymphatic vessels

(A/D) Schematic overviews of exogenous crawl-in setups. Numbers represent *Zeitgeber* time (ZT) of ear harvest.

(B) Individual bone marrow-derived dendritic cell (BMDC) batches were used for different crawl-ins. Left: numbers of Celltrace Violet (CTV⁺) BMDCs intralymphatic or extralymphatic normalized to lymphatic vessel (LV) volume (# = two-way ANOVA, * = Šidák's multiple comparisons test); right: ratio of intravascular versus extravascular BMDCs (# = one-way ANOVA, * = Tukey's multiple comparisons test). N = 3 mice across 4 time points measured each.

(C/F) Left: LV volume; right: absolute number of imaged CTV⁺ BMDCs normalized to LV volume (C refers to B and F refers to E).

(E) One BMDC batch was used for different ZTs. Statistical testing and arrangement equal to B. N = 3 mice across 4 time points measured each.

(G) Exemplary whole mount staining of split ears for PODOPLANIN (PDPLN) containing migrated CTV⁺ BMDCs after exogenous crawl-in assays. Arrows point at orthogonal views. Scale bar = 50 / 10µm.

(H) Flow-cytometric analyses of BMDC viability and purity used for crawl-in assays in E (left) and B (right); **p*<0.05, ***p*<0.01, ****p*<0.001. All data are represented as mean ± SEM.

I subsequently assessed whether endogenous dermal DCs located within ears exhibit this rhythmic trafficking pattern as well, by measuring their ability to migrate into lymphatic capillaries of the skin. Split ears were cultured with the dermis facing down for 6h and stained for endogenous DCs (CD11c⁺) and lymphatic capillaries and finally the number of DCs within or outside LVs was tracked (Figure 4-4A). Due to the small trauma induced by the ear sheet separation, dermal DCs slowly become activated and migrate towards lymphatic capillaries allowing for scrutiny of the initial step of an immune response.

In close analogy to the migration assays using *ex-vivo* generated BMDCs, site-specific dermal DCs showed elevated numbers inside the lymphatic capillaries at ZT7 compared to ZT19 after 6h incubation (Figure 4-4B). The volume of analyzed LVs as well as total imaged CD11c⁺ cell numbers did not differ between time points (Figure 4-4C). I additionally performed

endogenous crawl-in assays with 24h incubation of ears harvested at the peak and trough times observed thus far (ZT7 and ZT19, respectively), as 6h incubation time might be too short for the majority of DCs to become activated and migrate into LVs (**Figure 4-4D**). After 24h incubation, an even more pronounced migration difference was observed between ZT7 and ZT19, with ZT7 presenting a ratio of 1.8 and ZT19 a ratio of 0.5 (**Figure 4-4E**). Again, no differences in either imaged DC counts or LV volume were found (**Figure 4-4F**). These data indicated, that even after a longer incubation period, the time point at ZT19 was insufficient in catching up with the ZT7 time point. Indeed, examination of both ratios of intravascular versus extravascular DCs after 6h and 24h incubation revealed only a mere increase in ears harvest at ZT19, whereas at ZT7, the ratio had more than doubled (**Figure 4-4B/E**). This difference is exemplified in **Figure 4-4H**, in which the majority of DCs is associated with LVs at ZT7.

Diurnal DC trafficking through lymphatic capillaries can only be termed circadian, if the oscillation persists under constant conditions. I thus performed LD/DD/DL experiments to allow the conclusion of circadian rhythmicity and regulation via intrinsic clocks. While DC trafficking in mice housed under LD and DD condition peaked at ZT7 and had its nadir at ZT19, DC trafficking in mice housed under DL (jetlag) condition exhibited an inversed rhythm (**Figure 4-4G**). Consequently, mice exhibit a circadian rhythmicity in dermal DC trafficking, peaking during the behavioral rest phase, which might be under the control of the circadian clocks.

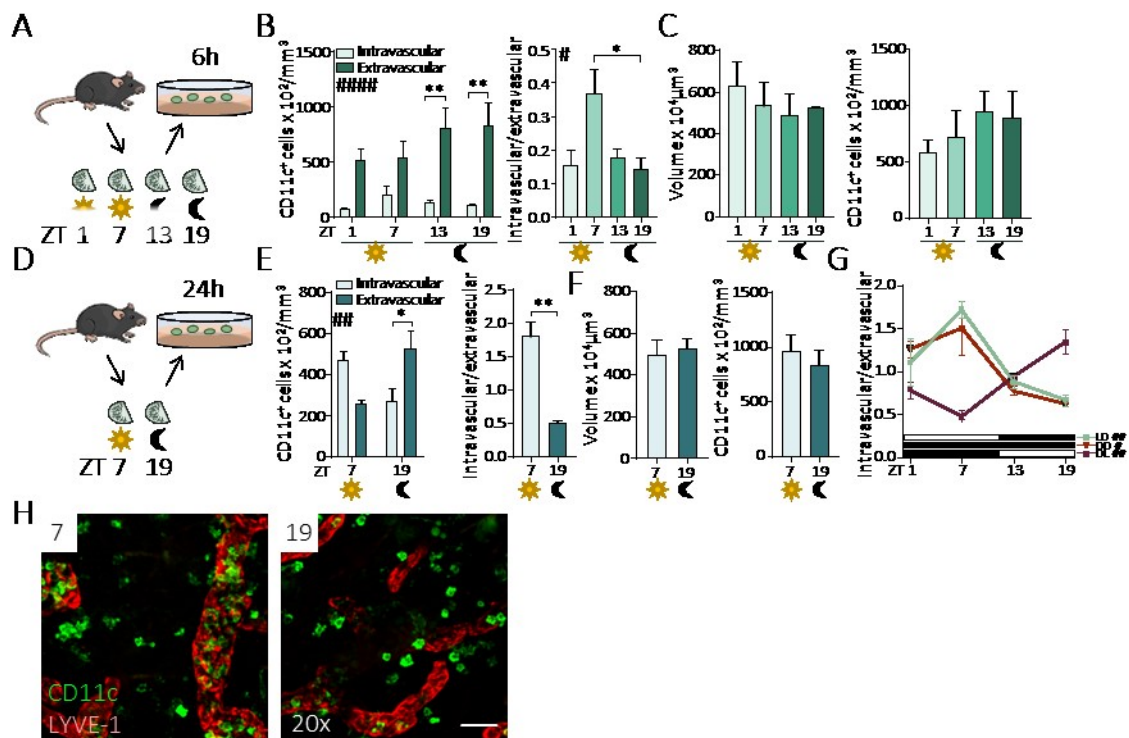


Figure 4-4: Circadian rhythm in dermal dendritic cell migration into lymphatic vessels

(A/D) Schematic overviews of endogenous crawl-in setups. Numbers represent *Zeitgeber* time (ZT) of ear harvest.

(B/E) 6h (B) or 24h (E) endogenous crawl-in assays. Left: number of dermal CD11c⁺ dendritic cells (DCs) normalized to lymphatic vessel (LV) volume (# = two-way ANOVA, * = Šidák's multiple comparisons test); right: ratio of intravascular versus extravascular DCs (# = one-way ANOVA, * = Tukey's multiple comparisons test for B and * = unpaired student's *t*-test for E). N = 3 mice across 4 (B) or two (E) time points measured each.

(C/F) Left: LV volume; right: absolute number of imaged CD11c⁺ DCs normalized to LV volume (C refers to B and F refers to E).

(G) 24h endogenous crawl-in assay performed with animals kept in Light (L): Dark (D), DD or DL conditions. # = one-way ANOVA. N = 3 mice across all time points measured each.

(H) Exemplary whole mount staining of split ears harvested at ZT7 or ZT19 for CD11c and LYVE-1 after a 24h endogenous crawl-in assay. Scale bar = 50µm; **p*<0.05, ***p*<0.01. All data are represented as mean ± SEM.

4.3 Rhythmic protein and RNA levels in lymphatic endothelial cells

In my initial experiments different timing of the dermal environment impacted changes in BMDC and dermal DC migration. Thus, I investigated whether molecules, essential for DC adhesion and transmigration, on tissue-specific LECs oscillate over the course of 24h during steady-state conditions. I performed quantitative immunofluorescence profiling on non-inflamed, sectioned ears, lungs, small intestines and inguinal LNs harvested over four time points of the day (see 3.2.7.1). In detail, I examined dermal lymphatic capillaries, overall lung LVs, lacteals and SMLV of small intestines and SCS, CS and MS of inguinal LNs using LYVE-1 as biomarker (Figure 4-5A). Surprisingly, this method yielded a mosaic of temporally expressed

proteins with a marked tissue-specificity (**Figure 4-5AB**). The skin shows strong rhythmicity for LYVE-1, JAM-A, CD99 and JAM-C on capillaries, while other markers were either present but not oscillatory or not expressed. Every marker except JAM-A peaked at ZT1, whereas JAM-A peaked at ZT7 (**Figure 4-5E**). In lung, LYVE-1 (peaking ZT1), ICAM1 (peaking ZT7), ALCAM (peaking ZT1) and CD99 (peaking ZT7) showed rhythmicity in expression (**Figure 4-5F**). The other two investigated lymphatic structures and respective sub-regions presented a high heterogenic temporal expression of trafficking markers. For instance, on small intestinal lacteals LYVE-1 (peaking ZT1), MMR1 (peaking ZT1), L1CAM (peaking ZT7), ICAM1 (peaking at ZT7), JAM-A (peaking ZT7), JAM-C (peaking ZT7), CD99 (peaking ZT7) and E-SELECTIN (peaking ZT1) displayed an oscillatory expression. However, on SMLVs, only LYVE-1 (peaking ZT1), L1CAM (peaking ZT7), ICAM1 (peaking ZT1) and E-SELECTIN (peaking ZT1) exhibited rhythmic expression. Remarkably, ICAM1 peaks at different time points although examined LVs are situated in the same organ (**Figure 4-5G**). Similar phenotypes were observed in different regions of the LN (**Figure 4-5H**). In all tissues analyzed, the averaged, integrated expression of rhythmic proteins revealed a peak in expression between ZT1 and ZT7 and nadir at ZT19 (**Figure 4-5C**). This was also true for integration of dermal-only protein expression data (**Figure 4-5D**). To better understand the expression of JAM-A, JAM-C and CD99 on LVs in the skin, whole mount staining of each molecule using LYVE-1 as biomarker was performed. JAM-A and JAM-C were expressed evenly on the LEC surface comparable with PDPLN, and CD99 is expressed on LECs in the fashion of CD31 or LYVE-1 (**Figure 4-5I/J/K**).

These data might be responsible for the strong circadian influence of the micro environment on rhythmic DC trafficking as shown in the crawl-in assays. Moreover, they point towards site-specific regulation of proteins by LEC intrinsic clocks, highlighting the importance of heterogeneity between LVs.

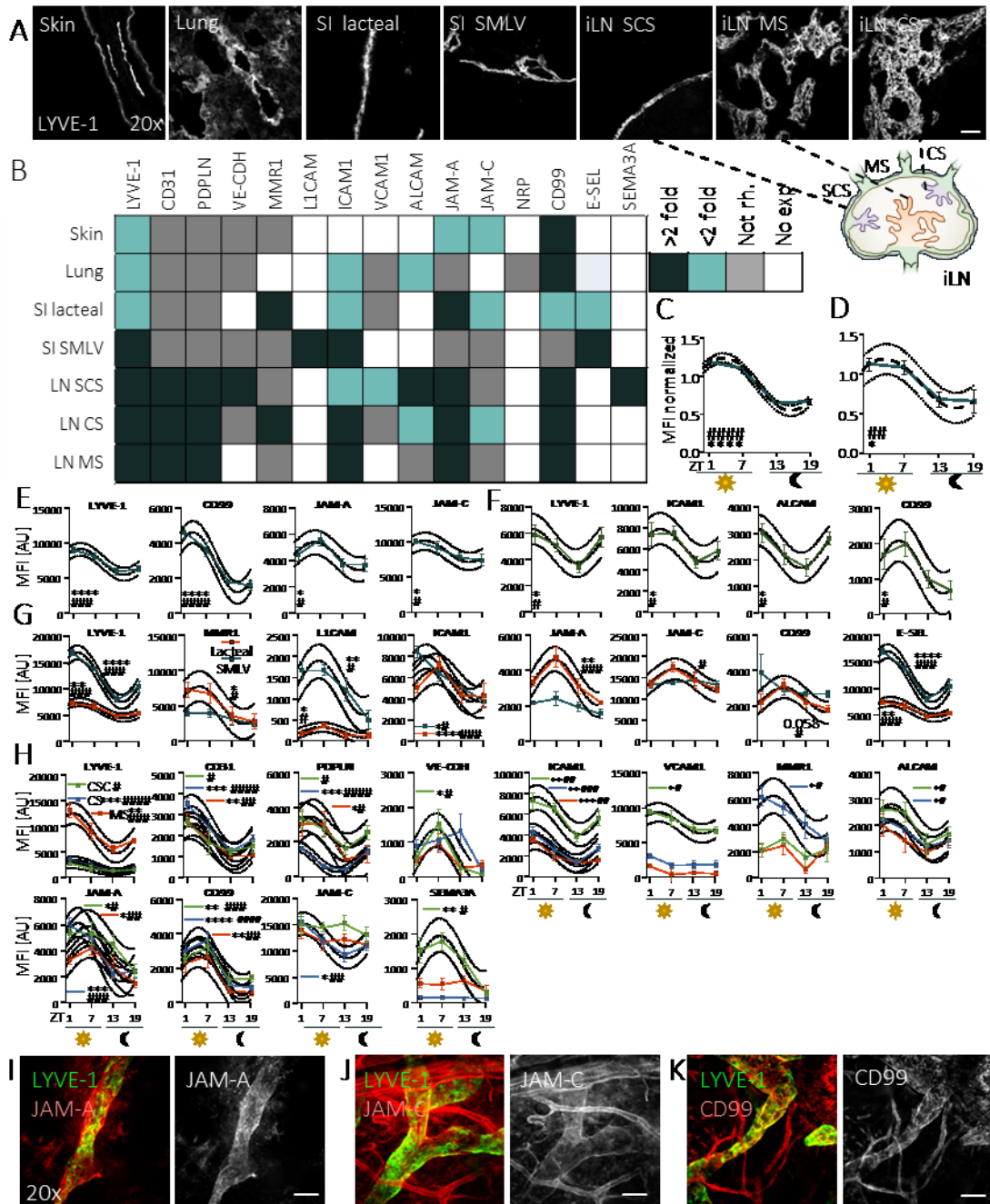


Figure 4-5: Tissue-specific oscillations in lymphatic adhesion and transmigration molecules

(A) LYVE-1 expression on 10µm slices from sectioned ears (skin), lung, small intestine (SI) lacteals, SI submucosal lymphatic vessels (SMLV) and inguinal lymph node (iLN) subcapsular sinus (SCS), medullary sinus (MS) and cortical sinus (CS). Scale bar = 50µm.

(B) Quantitative immuno-fluorescence microscopy protein screen of LYVE-1⁺ lymphatic vessels (LVs) using 10µm organ sections. Dark green = >2 fold significant difference in expression between *Zeitgeber* times (ZTs), light green = <2 fold difference in expression, grey = no rhythmic expression (Not rh.) and white = no expression (No exp.) as mean fluorescence intensity (MFI) <1.5% of max MFI. For calculations, isotype MFIs were subtracted beforehand. N = 5 mice with 4 ZTs measured each.

(C-D) Integration of all rhythmically expressed molecules over all organs **(C)** or skin **(D)** across 4 time points and normalized to ZT1 or ZT7 values. * = one-way ANOVA, # = cosinor analysis. N = 5 mice with 4 ZTs measured each. Dotted line represents SD, dashed line represents fit curve.

(E-H) MFI profiles of screened molecules on LVs in skin **(E)**, lung **(F)**, SI **(G)** and LN **(H)** from **B**. Isotype MFIs were deducted from shown MFIs. * = one-way ANOVA, # = cosinor analysis. Dotted line represents SD, dashed line represents fit curve.

(I-K) Whole mount staining of split ears for LYVE-1 with JAM-A **(I)**, JAM-C **(J)** or CD99 **(K)**. Scale bars = 50µm; **p*<0.05, ***p*<0.01, ****p*<0.001, *****p*<0.0001. All other data are represented as mean ± SEM.

Besides adhesion and transmigration, chemotactic cues and their guidance through the interstitial space are integral parts of dermal lymphatic DC trafficking. Different chemokines were screened and the focus was set on CCL21, as it is not only the best described but also most important chemokine in dermal lymphatic trafficking (see 2.4.2).

As an initial experiment, I stained and quantified the expression of CCL21 within LYVE-1⁺ areas in sectioned skin (Figure 4-6A). Quantification of the signal intensity uncovered a peak of CCL21 expression on LECs at ZT7 (Figure 4-6B). To generate further insight into the intracellular CCL21 architecture in LECs, whole mount staining of permeabilized LVs in the skin was performed and stained for LYVE-1 and CCL21 (see 3.2.7.2). The majority of intracellular CCL21 was confined to a small region, less CCL21 was evenly dispersed in the cell (Figure 4-6C). Skin whole mount staining of the Golgi apparatus using the biomarker GOLPH4 unveiled CCL21 and GOLPH4 double-positive regions in LYVE-1⁺ capillary LECs (Figure 4-6D). To further dissect the temporal regulation of the intracellular CCL21 quantity, I evaluated the CCL21⁺ signal in either GOLPH4^{high} (resembling the Golgi apparatus) or GOLPH4^{low} regions (resembling small vesicles within the cell) employing LYVE-1 mask algorithms (see 3.2.7.4 for methods and Figure 4-6E for data) [199]. In both examined regions, the CCL21 fluorescence intensity was maximal at ZT7 and lowest at ZT19. Although the highest CCL21⁺ signal intensity was found in the Golgi apparatus (GOLPH4^{high}), the difference between ZT7 and ZT19 was most striking in GOLPH4^{low} regions, pointing towards higher vesicular trafficking and possibly release of CCL21 at ZT7 (Figure 4-6F).

Taken together, temporal expression of various molecules involved in lymphatic leukocyte adhesion and transmigration as well as chemotactic guidance was found. Not only does this hint at a functional intrinsic clock of LECs, but could also explain the elevated migration capacity of DCs at ZT7 shown in both crawl-in assays (Figure 4-3 and Figure 4-4).

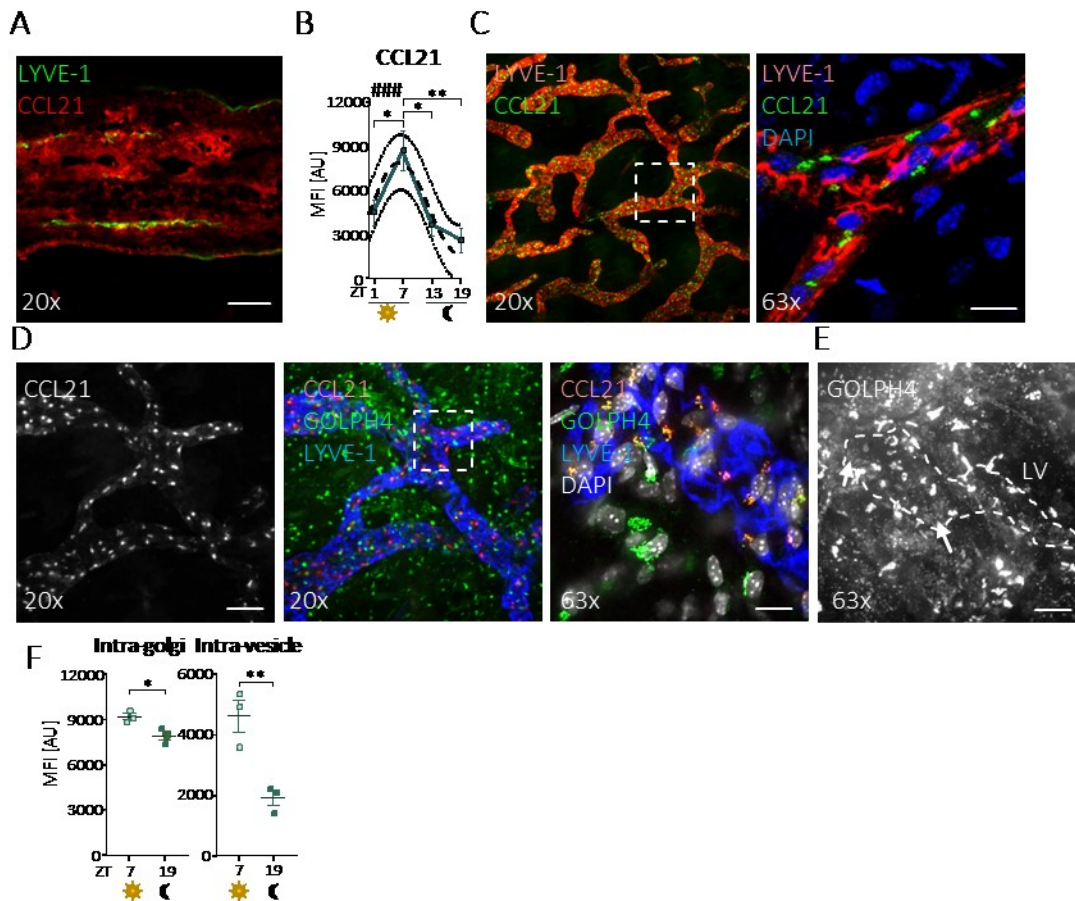


Figure 4-6: Elevated expression, storage and traffic of intracellular CCL21 in dermal lymphatic endothelial cells

(A) Representative 2D immuno-fluorescence microscopy staining of CCL21 and LYVE-1 in 10 μ m skin slices. Scale bar = 50 μ m.

(B) Quantitative immuno-fluorescence microscopy profiling of the CCL21 mean fluorescence intensity (MFI) on LYVE-1⁺ lymphatic vessels (LVs) in 10 μ m skin sections. * = one-way ANOVA, # = cosinor analysis. N = 5 mice with 4 *Zeitgeber* times (ZTs) measured each. Dotted line represents SD, dashed line represents fit curve.

(C) Whole mount staining of split and permeabilized ears for LYVE-1, CCL21 and DAPI. Left: picture contains 4 patched images. Scale bar = 70 / 10 μ m.

(D) Representative whole mount staining of split and permeabilized ears for CCL21, GOLPH4, LYVE-1, and DAPI. Left: CCL21 staining, 20x objective; center: CCL21, GOLPH4 and LYVE-1 staining, 20x objective; right: CCL21, GOLPH4, LYVE-1 and DAPI staining, scale bars = 50 / 10 μ m.

(E) Representative whole mount staining of split and permeabilized ears for GOLPH4. Arrows indicate GOLPH4^{low} regions, resembling small intracellular vesicles. Scale bar = 10 μ m.

(F) Quantitative immuno-fluorescence microscopy profiling of the CCL21 MFI in LYVE-1⁺ lymphatic endothelial cells (LECs) in whole-mounted, permeabilized and split ears. Left: CCL21 MFI in the GOLPH4^{high} area (intra-golgi); right: CCL21 MFI in GOLPH4^{low} area (intra-vesicle). N = 3 mice ZT7 and ZT19 measured each, * = unpaired student's *t*-test; **p*<0.05, ***p*<0.01. All other data are represented as mean \pm SEM.

Given the strong oscillatory protein expression in LECs, I next sought to elucidate how LECs adapt to environmental changes on a broader molecular level in a time-of-day-dependent manner. Dermal CD31⁺PDPLN⁺ LECs were sorted at four different time points to perform RNA-sequencing analyses. Every sort (with purities > 90%) was performed at the same time of day using phase-shifted mice to minimize side-effects. Isolated RNA of LECs had sufficient quality

and amounts for performing RNA sequencing (see **Figure 3-8** for LEC gating strategy and **3.2.5.2** and **3.2.8** for experimental procedures).

Robust expression of dermal LEC-specific marker genes *Lyve-1*, *Flt4*, *Prox-1*, *Pdpln*, *Pecam1* and *Reelin* (*Reln*) ensured high purity of samples used for sequencing. On the contrary, the dermal BEC-, leukocyte- or stromal cell-specific markers *Integrin subunit alpha 2b* (*Itga2b*), *Flt1*, *Notch receptor 4* (*Notch4*), *Neuropilin 1* (*Nrp1*), *Von willebrand factor* (*Vwf*), *E-selectin* (*Sele*; encoding for E-SELECTIN), *Protein tyrosine phosphatase receptor type C* (*Cd45/Ptprc*), *Fibulin 1* (*Fbln1*) and *Procollagen C-endopeptidase enhancer* (*Pcolce*) were not expressed (**Figure 4-7A**). Notably, *Esele* is only upregulated in dermal LVs under inflammatory conditions, demonstrating the non-activated state of examined LECs. Interestingly, the two markers *Prox-1* and *Reln* displayed a peak in expression at ZT1 (**Figure 4-7G**).

Principal-component analysis (PCA) could not entirely cluster sequenced samples according to time of harvest. However, samples harvested at ZT1 and ZT19 give an indication of grouping in opposite directions (**Figure 4-7B**). Importantly, PCA analyses are relying on strong differences between sample groups and rhythmic gene expression often fails to provide high amplitudes. Indeed, gene overlap analysis revealed 265 differentially expressed genes between ZT1 and ZT19, as represented by the outer arc of the circos plot. Likewise, ZT13:ZT19 comprise 163 and ZT1:ZT7 155 differentially expressed genes, respectively (**Figure 4-7C**). Moreover, overlapping genes which appear in multiple sample comparisons (for example gene A is significantly different between time points ZT1:19 and ZT7:19) and genes that were unique to one gene comparison and do not appear in other comparisons (gene A is only significantly different in ZT1:19 and not in ZT7:19) were illustrated in the inner arc of the plot. Strikingly, the majority of genes was not connected with other comparisons (inner arc) and thus found to be unique to the ZT1 and ZT19 comparison (**Figure 4-7C**). In general, gene expression analyzed at ZT19 was most distinct compared to other time points (**Figure 4-7C**). I then continued with further analyses considering that samples harvested at ZT1 and ZT19 provided uniquely altered transcriptional regulation.

Since ZT1:ZT19 had by far the most significant targets based on the DeSeq2 analysis, I decided to further dissect transcriptional alterations (**Figure 4-7D**). All significant genetic comparisons were clustered into functionally related groups based on gene ontology. Enriched gene ontology clustering, however, did not reveal differences between ZT1/ZT7 and ZT19 with respect to adhesion. ZT1:ZT13 provided differences for adhesion, extracellular matrix organization, ZT7:ZT13 variation in water homeostasis and ZT13:19 change in cell motility regulation. Many other gene ontologies were enriched that were not the main topic of this thesis (**Figure 4-7E/H**).

Given LECs present oscillatory, transcriptional alterations in several pathways, initial targets for further analysis were molecular clock genes. Indeed, *Bmal1* (peak at ZT1/19), *Clock* (peak at ZT1), *Per2* (peak at ZT13), *Per3* (peak at ZT13), *Dbp* (peak at ZT7), *Nr1d1* (peak at ZT7) and *Nr1d2* (peak at ZT7/13) show significant differences in their expression across 24h. This demonstrated that components of the circadian clock were expressed in a rhythmic manner and proved a good quality control for the experiment, given that these were peaking at the expected times. *Per1* and *Cry2* expression levels did not exhibit statistically significant oscillation (**Figure 4-7F**). In summary, RNA sequencing of sorted LECs exposed major transcriptional differences between ZT1 and ZT19. Moreover, RNA sequencing uncovered robust rhythms in molecular clock gene expression, potentially regulating genes involved in adhesion and migration.

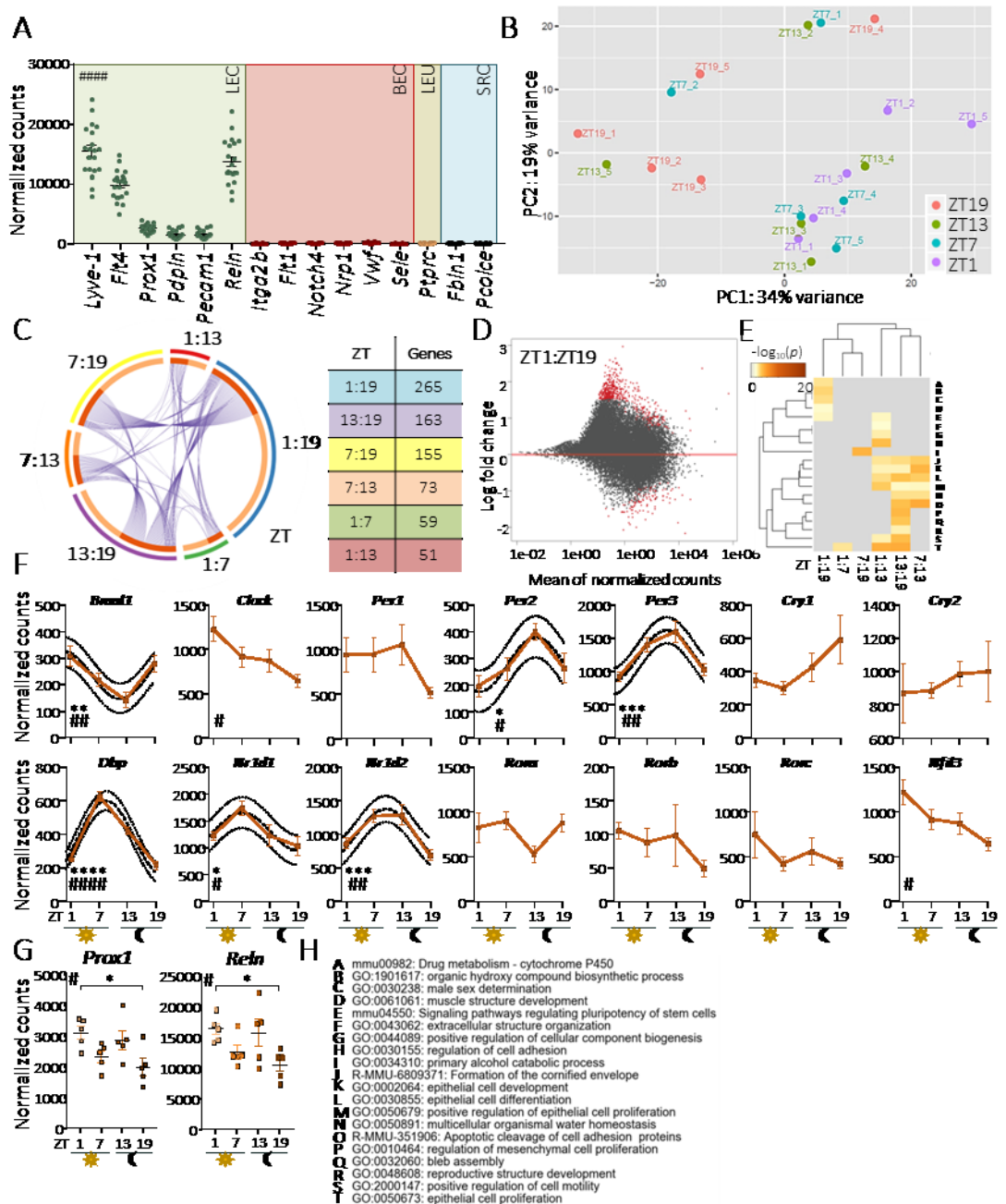


Figure 4-7: Lymphatic endothelial cells express a molecular clock and are transcriptionally most distinct between ZT1 and ZT19

(A) Expression of lymphatic endothelial cell (LEC-), blood endothelial cell (BEC-, leukocyte (LEU-) and stromal cell (SRC-) -specific genes as measure for the high purity of sorted and sequenced skin LECs. N = 20 mice, # = one-way ANOVA.

(B) Principal component analysis (PCA) of sequenced cDNA from sorted LECs based on all genes. N = 5 across 4 different *Zeitgeber* times (ZT) each.

(C) Gene overlap analysis depicted as a circos plot (left) and corresponding table of overlapping genes (right). Each ZT contains the average of 5 biological replicates. The inner arc highlights the overlapping genes which appear in multiple sample comparisons in dark orange and genes in light orange are unique to one gene comparison and do not appear in other comparisons.

(D) MA plot visualizing the transformed values of 'M' (log ratio) and 'A' (mean average) ZT1 and ZT19.

(E/H) Enriched ontology cluster cumulating hierarchically enriched terms/pathways based on sequencing data between different ZTs (E). $-\log_{10}$ of *p* values shown to express significance. List of terms/ GO pathways shown in H.

(F) Molecular clock gene expression profile of sorted LECs. * = one-way ANOVA, # = cosinor analysis. N = 5 mice across 4 ZTs measured each. Dotted line represents SD, dashed line represents fit curve.

(G) Visualization of LEC specific genes from A across 4 ZTs. # = one-way ANOVA, * = Tukey's multiple comparisons test. N= 5 mice with 4 time points measured each; **p*<0.05, ***p*<0.01, ****p*<0.001, *****p*<0.0001. All other data are represented as mean \pm SEM.

Considering the clear expression profile of the molecular clock components and required high amplitudes for successful principal-component and DeSeq2 analysis, an overlooked temporal regulation of adhesion genes was estimated. Analyses of adhesion genes listed in the ontology cluster 'cell adhesion' (GO:0007155) were performed and each gene was tested for its rhythmic expression using one-way ANOVA statistics. A list of rhythmic adhesion genes (121 expressed adhesion genes experienced a peak in expression once during 24h) was compiled in a structured heat map, showing the gene with the highest counts at ZT1 first and the gene with the lowest counts at ZT1 last. Interestingly, a great majority of genes peaking at ZT1 was downregulated at ZT19 and vice versa (**Figure 4-8A**). Of note, a large fraction of these genes was not significant in the DeSeq2 analysis as their amplitudes between time points tested were too little. Nevertheless, this supports the initially reported difference in temporal transcriptional regulation between ZT1 and ZT19 (**Figure 4-7B-D**).

I thereafter grouped genes of interest based on their role in migration and activation, the cytoskeleton, neuronal influence and voltage gated channels, permeability and extracellular matrix in a second heat map (**Figure 4-8B**). Integration of all rhythmic adhesion genes (except *Ackr4*, see 5.2) uncovered a peak in expression at ZT1 and a trough at ZT19 (**Figure 4-8C**). Integration of classified adhesion genes illustrated the transcriptional upregulation of migration and activation, as well as cytoskeletal genes at ZT1 (**Figure 4-8D**). In comparison with the protein screen in **Figure 4-5**, *Lyve1*, *Ccl21*, *Cd99*, *F11r/Jam1* and *Jam2* could either not be sequenced or were not found to be rhythmically transcribed.

However, other enriched targets from the sequencing include interleukins and receptor components such as *Il20r*, *Il2r* and *Il6*, chemotaxis genes *Cxcl12* and *Ackr4*, neuronal receptor *Adrb2*, and several genes involved in permeability and the cytoskeleton regulation, such as *Myoc*, *Cdh5* and *Fbn1* (values are shown in the appendix).

Together these data provide novel temporal adaptation of adhesion gene expression according to the time of day in dermal LECs. Adhesion genes were upregulated at ZT1, coinciding with a higher trafficking capacity as previously shown (**Figure 4-3** and **Figure 4-4**). Moreover these results hint at rhythmic neuronal control of LECs and rhythms in lymphangiogenesis.

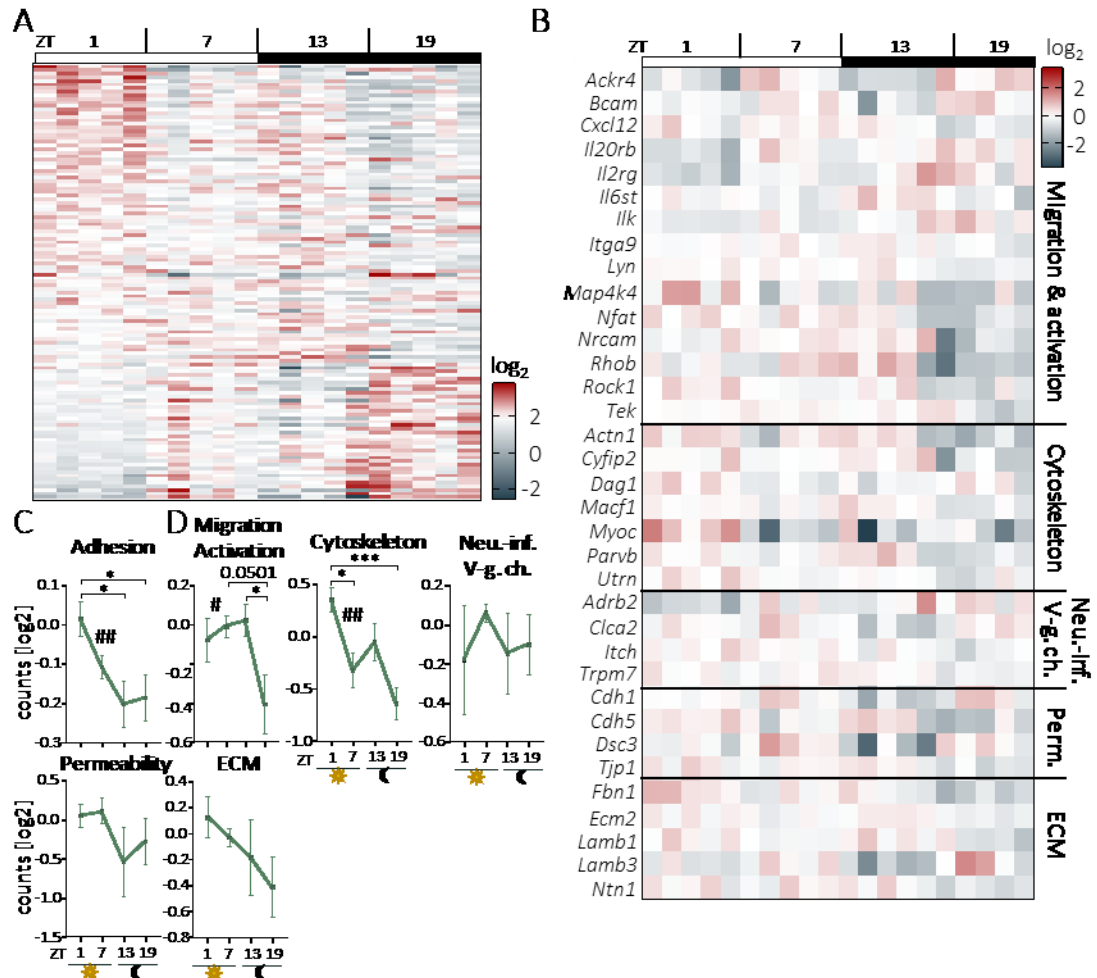


Figure 4-8: Rhythmic adhesion gene signature in lymphatic endothelial cells

(A) Heat map of rhythmic adhesion genes (Gene ontology (GO):0007155) based on one-way ANOVA testing in sorted and sequenced lymphatic endothelial cells (LECs). Normalized gene counts shown as binary logarithm. N = 5 mice across 4 different time points measured each. ZT = *Zeitgeber* time.

(B) Grouping of selected adhesion genes from A into migration and activation, cytoskeleton, neuronal influence (Neu.-inf.) and voltage-gated channels (V-g. ch.), permeability (Perm.) and extracellular matrix (ECM). Normalized counts shown as binary logarithm.

(C-D) Integration of all rhythmic adhesion genes from A (C) or selected genes from B (D). Normalized counts shown as binary logarithm. # = one-way ANOVA, * = Tukey's multiple comparisons test; * $p < 0.05$, ** $p < 0.01$, *** $p < 0.001$. All data are represented as mean \pm SEM.

4.4 Evaluation of migratory behavior and chemotaxis ability amongst dendritic cell subtypes

Transcriptome and protein signatures of dermal LECs seemed to be strongly influenced by the time of day. I next searched for possible consequences of rhythmic regulation in skin under steady-state conditions. Specifically, I further dissected the influence of biological rhythms on dermal DC subtypes.

Ears from phase-shifted mice were harvested at four different time points and the amount of dermal DCs and respective subtypes was quantified using flow-cytometry (see **Figure 3-7** for gating strategy and **3.2.5.1** for methods). Importantly, the weight of collected ears did not vary across time points tested (**Figure 4-9A**). Surprisingly, the number of assayed CD45⁺ leukocytes oscillated, peaking at ZT7 and troughing at ZT19. Likewise, CD11c⁺MHCII⁺ DC cell numbers increased at ZT7 and were lowest at night and onset of day. This extended to EPCAM⁺ LCs and EPCAM⁻CD103⁻ cDC2s but not CD103⁺ cDC1s with highest numbers at ZT7 (**Figure 4-9B**). Apart from rhythmic egress being a likely contributor for the oscillatory count, I speculated whether a higher turnover of cells may also be caused by varying proliferation states of DCs within the skin. For this purpose the marker KI67 was utilized, which is associated with cellular proliferation [337], and whole mount staining of KI67 in skin to visualize proliferating cells was established (**Figure 4-9C**). Interestingly, the amount of KI67 in CD11c⁺ cells as well as relative numbers of KI67⁺ CD11c⁺ cells varied throughout the day, peaking at ZT7 (**Figure 4-9D**). This might represent a possible mechanism in the temporal regulation of cellularity in skin and could be important in the regulation of immune responses.

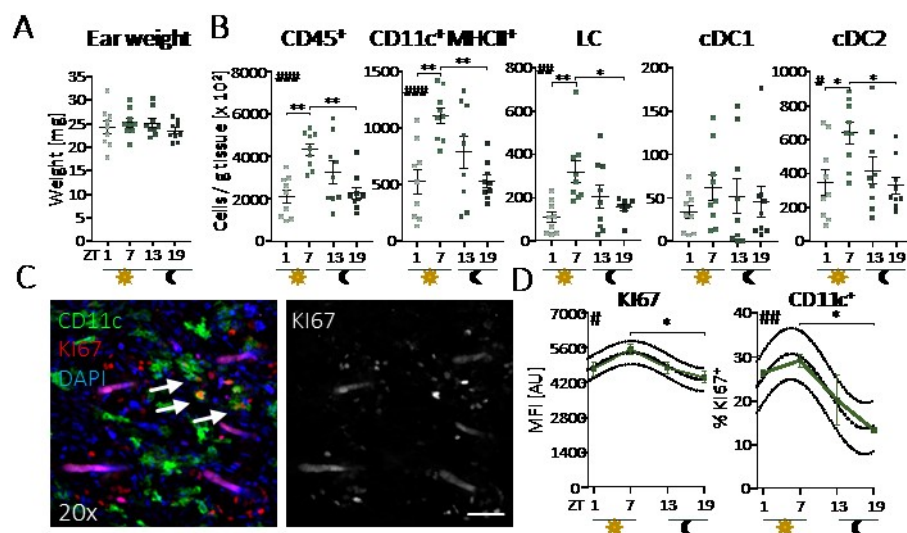


Figure 4-9: Diurnal rhythmicity in skin cellularity

(A) Weight of harvested ears in milligrams (mg). N = 9 mice at 4 different *Zeitgeber* times (ZT) each.

(B) Flow-cytometric analyses of cellularity normalized to tissue weight from harvested ears. LC = Langerhans cell, cDC1/2 = conventional dendritic cell 1/2. # = one-way ANOVA, * = Tukey's multiple comparisons test. N = 9 mice across 4 time points measured each.

(C) Representative whole mount staining of CD11c, KI67 and DAPI in permeabilized, split ears. Scale bar = 50µm.

(D) Left: mean fluorescence intensity (MFI) profile of KI67 signal in CD11c⁺ DCs from skin whole mounts. Right: relative number of imaged KI67⁺ CD11c⁺ cells in skin whole mounts. # = one-way ANOVA and cosinor analysis, * = Tukey's multiple comparisons test. Dotted line represents SD, dashed line represents fit curve. N = 3 mice across 4 time points measured each; **p*<0.05, ***p*<0.01. All other data are represented as mean ± SEM.

Quantity and migration capacity of dermal DCs vary throughout the day as shown by several crawl-in assays and flow-cytometric profiling of the skin. I was wondering if by splitting ears and performing crawl-in assays, dermal DCs also emigrate into the incubation medium in a time-of-day dependent manner. Thus, I designed a crawl-out assay, in which split ears were cultured on plain or supplemented medium for 24h. During these 24h the majority of DCs remain in the ear within the LVs. However, a small fraction emigrates into the medium, which was quantified by FACS (see 3.2.5.1 for methods and **Figure 3-7** for gating strategies). By reason of altering total numbers of DCs in the ear, I decided to analyze the number of emigrated DCs in relation to remaining DCs. After 24h incubation, 22% of total DCs (the sum of ear and medium cellularity) emigrated the ear at ZT7 compared to 15% at ZT19. This difference could be extended to LCs (only a tendency) and cDC2s, but not cDC1s (**Figure 4-10A-C**). On the one hand this secured that the majority of DCs remains in the ear, justifying the used crawl-in cell migration assays. On the other hand, this implied differences in transitory migration behavior between DC subtypes.

I expanded my endogenous crawl-in assay to explore, which DC subtype is migrating into the lymphatic capillaries. First, I established the whole-mount staining of LANGERIN and CD103 in the epidermis and dermis. Under steady-state conditions, the great majority of LANGERIN⁺ DCs (LCs) resides in the epidermis, whereas cDC1s and cDC2s populate the dermis (**Figure 4-10D**). In light of low cDC1 numbers and lack of rhythmicity in the crawl-out assay, I excluded them from the experiment. Split ears from phase-shifted mice were cultured for 24h and subsequently examined. The total and relative numbers of imaged DCs did not differ between the time points (**Figure 4-10E**). Analysis of intravascular versus extravascular LCs and cDC2s revealed a marked increase in migration of both subtypes at ZT7 compared to ZT19. Interestingly, this difference was slightly more pronounced in LCs (**Figure 4-10F/G**). Together, these differences pinpoint heterogeneity between different dermal DCs in terms of migration and activation throughout the course of a day, potentially exerted by DC-specific molecular clocks. This might be especially of relevance for pathogen-specific immune responses and the positioning of LCs in the epidermis.

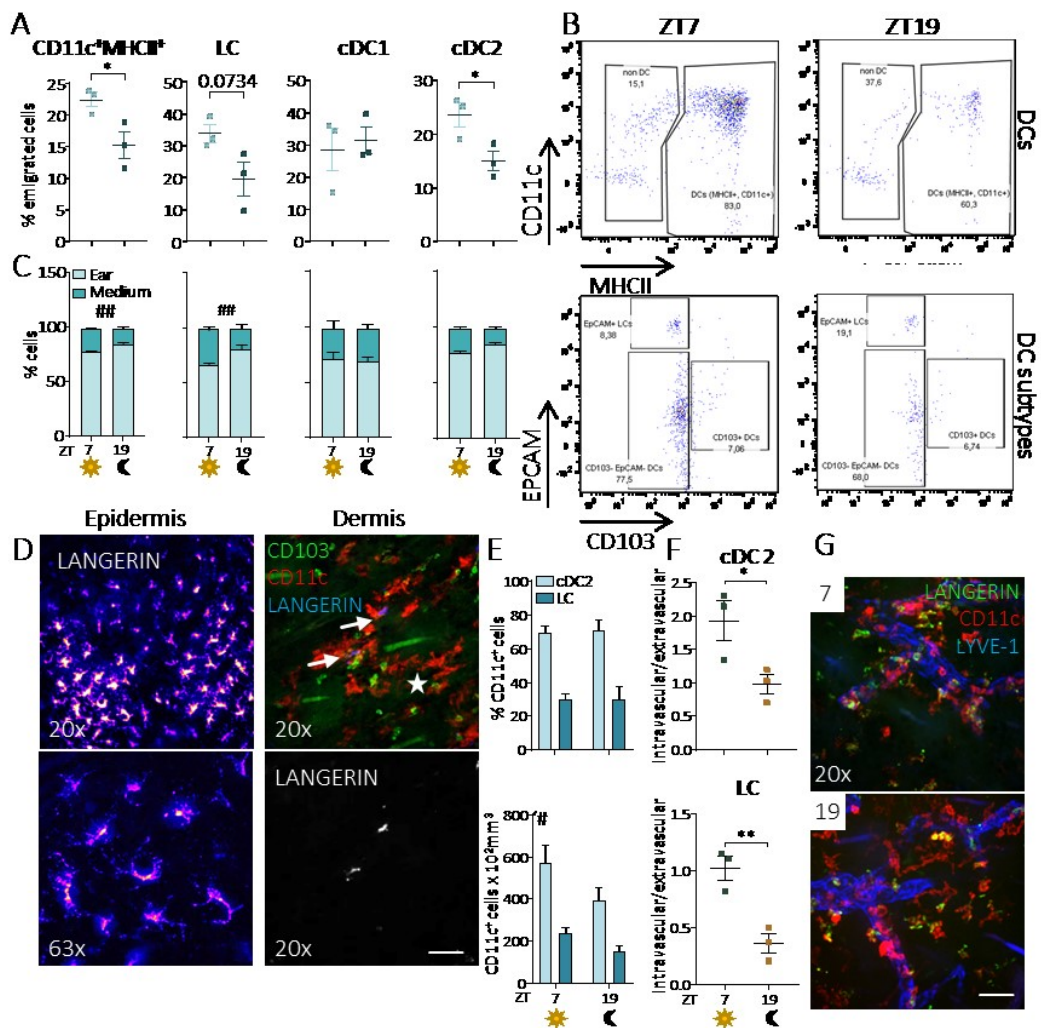


Figure 4-10: Dermal dendritic cell subtype-specific rhythms in migration

(A) Flow-cytometric analyses of emigrated CD11c⁺MHCII⁺ dendritic cells (DCs) from cultured, split ears (crawl-out assay) into medium. Values shown as fraction of total DCs, the sum of ear and medium DCs. LC = Langerhans cell, cDC1/2 = conventional DC 1/2. N = 3 mice across Zeitgeber Time (ZT) 7 and ZT19 measured each. * = unpaired student's *t*-test.

(B) Representative flow-cytometry plots of DCs (top) and DC subtypes (bottom) using EPCAM and CD103 for differentiation at ZT7 and ZT19.

(C) Ratio of DCs that either emigrated or remained inside the ear tissue. N = 3 mice across ZT7 and ZT19 measured each. # = two-way ANOVA.

(D) Representative whole mount staining of epidermis (left) and dermis (right) of permeabilized, split ears for Langerin, CD103 and CD11c during steady state. Arrows point at LCs, star shows cDC1. Scale bar = 50 / 10μm.

(E) 24h endogenous crawl-in assays of CD11c⁺ DCs divided into Langerin⁺ LCs and Langerin⁻ cDC2s. Top: relative amount of CD11c⁺ DCs that are LCs or cDC2s. Bottom: absolute number of CD11c⁺ cells imaged normalized to the lymphatic vessel volume. # = two-way ANOVA. N = 3 mice across ZT7 and ZT19 measured each.

(F) Ratio of intravascular versus extravascular cDC2s (top) or LCs (bottom) after 24h endogenous crawl-in assays. N = 3 mice across ZT7 and ZT19 measured each. * = unpaired student's *t*-test.

(G) Representative images stained for Langerin, CD11c and LYVE-1. Scale bar = 50μm; **p*<0.05, ***p*<0.01. All data are represented as mean ± SEM.

This potential heterogeneity within dermal DCs was subjected to further analysis. First, I assayed the individual chemotaxis abilities of DCs regarding CCL21 by combining a crawl-out with a chemotaxis assay. Ears from phase-shifted mice were simultaneously harvested, split and cultured dermis facing down onto medium supplemented with CCL21 at ZT7 and ZT19. During the 24h crawl-out assay, dermal DCs were activated by exogenous CCL21 and migrated towards the extracellular chemokine source to localize inside the medium. Interestingly, at ZT7 around 65% of total (sum of ear and medium cellularity) dermal DCs emigrated whereas at ZT19 only 37% left the ear. Specifically, LCs and cDC2s, but not cDC1s, presented significant differences in migratory behavior between time points (**Figure 4-11A-C**). Collectively, this suggests a transitory upregulation of trafficking molecules such as CCR7 on the DC surface concomitant with an elevated global alertness and better migration of DCs at ZT7.

Because of this, Coline Barnoud (University of Geneva, Switzerland) phenotyped non-activated, homeostatic LCs, cDC1s and cDC2s isolated from harvested ears at four time points across the day using flow-cytometric quantitative immunofluorescence profiling. She quantified activation markers (CD80, CD86, CD40, CD201, CD301b) as well as molecules involved in the trafficking cascade (CCR7, JAM-A) on respective DC subsets. This approach yielded a temporal expression map for dendritic cell molecules that seemed to be DC subtype-specific (**Figure 4-11D**). LCs probed during the onset of the day show higher expression levels of CCR7, CD86 as well as JAM-A and cDC2s higher expression levels of CD86 and CD40 (**Figure 4-11E-F**). These findings support the idea of an elevated global alertness and chemotaxis ability of steady state DCs during the day and corroborate the trafficking data obtained earlier (**Figure 4-3** and **Figure 4-4**).

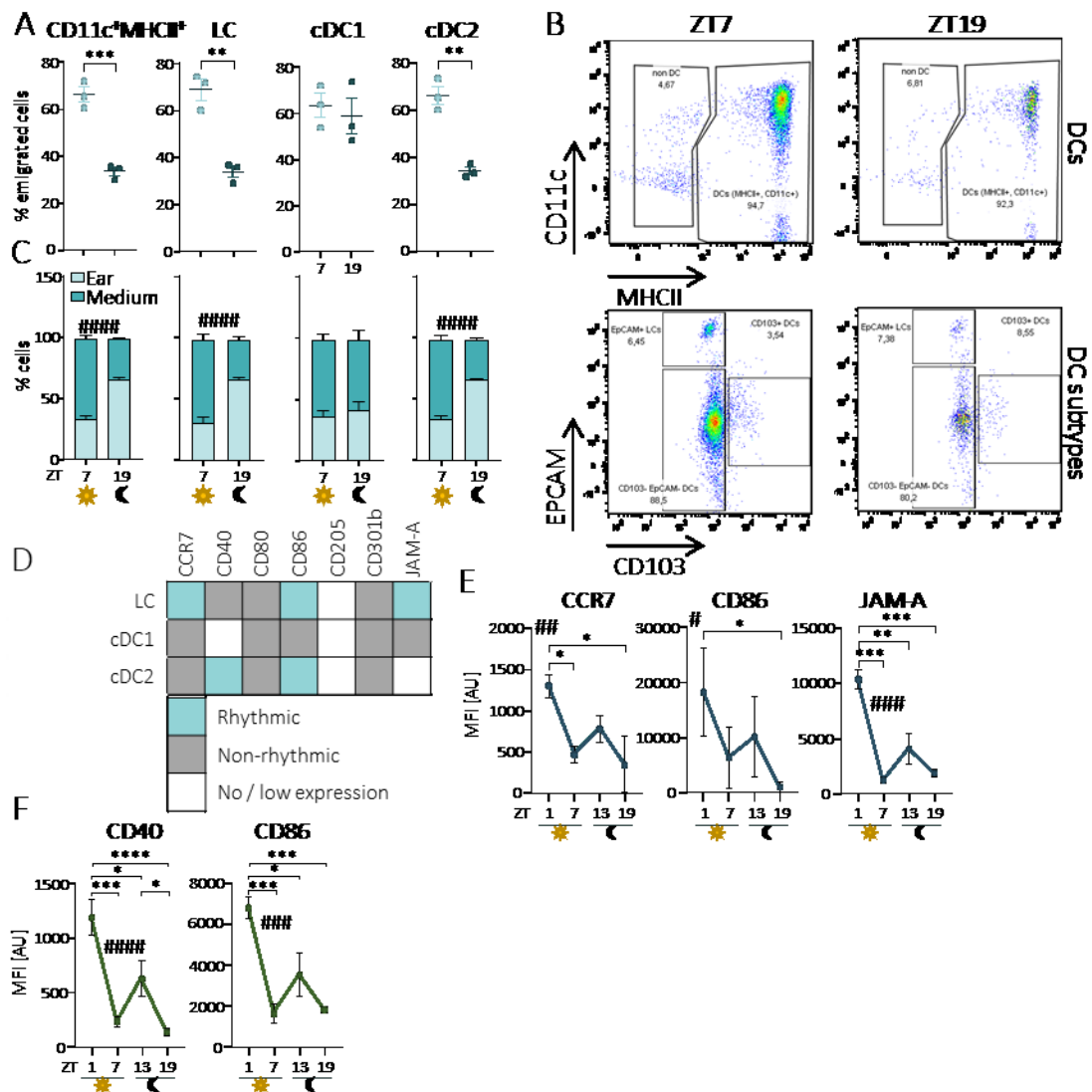


Figure 4-11: Elevated activation and chemotaxis of dendritic cells during the day

(A) Flow-cytometric analyses of emigrated CD11c⁺MHCII⁺ dendritic cells (DCs) from cultured, split ears (crawl-out assay) into medium. Values shown as fraction of total DCs, the sum of ear and medium DCs. Ears were cultured on culture medium supplemented with 100ng/ μ l CCL21. LC = Langerhans cell, cDC1/2 = conventional DC 1/2. N = 3 mice across *Zeitgeber* time (ZT) 7 and ZT19 measured each. * = unpaired student's *t*-test.

(B) Representative flow-cytometry plots of Dcs (top) and DC subtypes (bottom) using EPCAM and CD103 for discrimination at ZT7 and ZT19.

(C) Ratio of DCs that either emigrated or remained in the skin tissue. N = 3 mice across ZT7 and ZT19 measured each. # = two-way ANOVA.

(D) Flow-cytometric quantitative analyses of activation markers and trafficking molecules across 4 different time points on the surface of LCs, cDC1s and cDC2s. Blue = rhythmic expression validated by one-way ANOVA testing. Grey = non-rhythmic expression. White = not expressed as mean-fluorescence intensity (MFI) < 1.5% of max MFI. N = 5 mice across 4 different time points measured each.

(E-F) MFI profile of screened LCs (E) or cDC2s (F) from D. * = one-way ANOVA and # = Tukey's multiple comparisons test; **p*<0.05, ***p*<0.01, ****p*<0.001, *****p*<0.0001. All data are represented as mean \pm SEM.

4.5 Assessment of diurnal CCL21 gradient micro-patterning, adhesion and transmigration

Both, LECs and DCs together govern rhythms in dermal DC trafficking. Further, LCs and cDC2s were shown to better migrate towards an external CCL21 source and upregulate pro-migratory factors during the day. Based on this, I sought to delineate the functional relevance of molecules partaking in the multi-faceted cascade of lymphatic trafficking with respect to the time of day.

Since adhesion and transmigration of dermal DCs heavily rely on functional chemotaxis, I studied the spatio-temporal gating of dermal chemotactic gradients first. I determined CCL21 to be the perfect candidate for investigation due to its rhythmicity in the intracellular compartment and importance for trafficking (**Figure 4-6**). For this purpose, I employed quantitative immunofluorescence imaging to quantify the naturally built-up gradient. Staining for CCL21 and LYVE-1 in non-permeabilized, whole-mounted ear sheets revealed a chemokine gradient that is concentrating in close proximity to lymphatic capillaries (**Figure 4-12A**). By adopting distance-dependent fluorescence maps of CCL21⁺ signal in LYVE-1⁺ capillary environments, I was able to quantify the exponential CCL21 gradient. Interestingly, gradients varied according to the time of the day with ZT7 presenting a higher concentration at close proximity to LVs which is why statistical analysis was only significant for a total distance of around 50 μ m (**Figure 4-12B/C**). These findings highly support the rhythmicity observed in crawl-in assays as a more pronounced chemotaxis at ZT7 might enhance interstitial DC migration.

The intralymphatic space harbors low numbers of DCs for induction of self-tolerance and T cell communication. In order to quantify the intralymphatic amount of DCs under steady-state conditions, ears were harvested from phase-shifted mice at four different time points of the day, split, stained and directly imaged. Quantification of the intravascular versus extravascular ratio of DCs uncovered an increased cellularity within the lymphatic space during the day compared to night time points (**Figure 4-12D**). Thus, rhythmic CCL21 gradients functionally influence the intradermal distribution of DCs under steady state.

Additionally, I designed short exogenous BMDC crawl-in assays ranging from 0-60min, allowing me to delineate the physiological relevance of rhythmic gradients for DC migration. For the analysis, interstitial space between LVs was segregated into five different zones (see 3.2.4.4 and Figure 3-6). Next, the number of cells was counted in the respective zones at ZT7 and ZT19 from exogenous crawl-in assays. Throughout the course of 60min, more DCs accumulated within 20 μ m distance to the LV at ZT7, whereas in ZT19, the increase was much lower (Figure 4-12E).

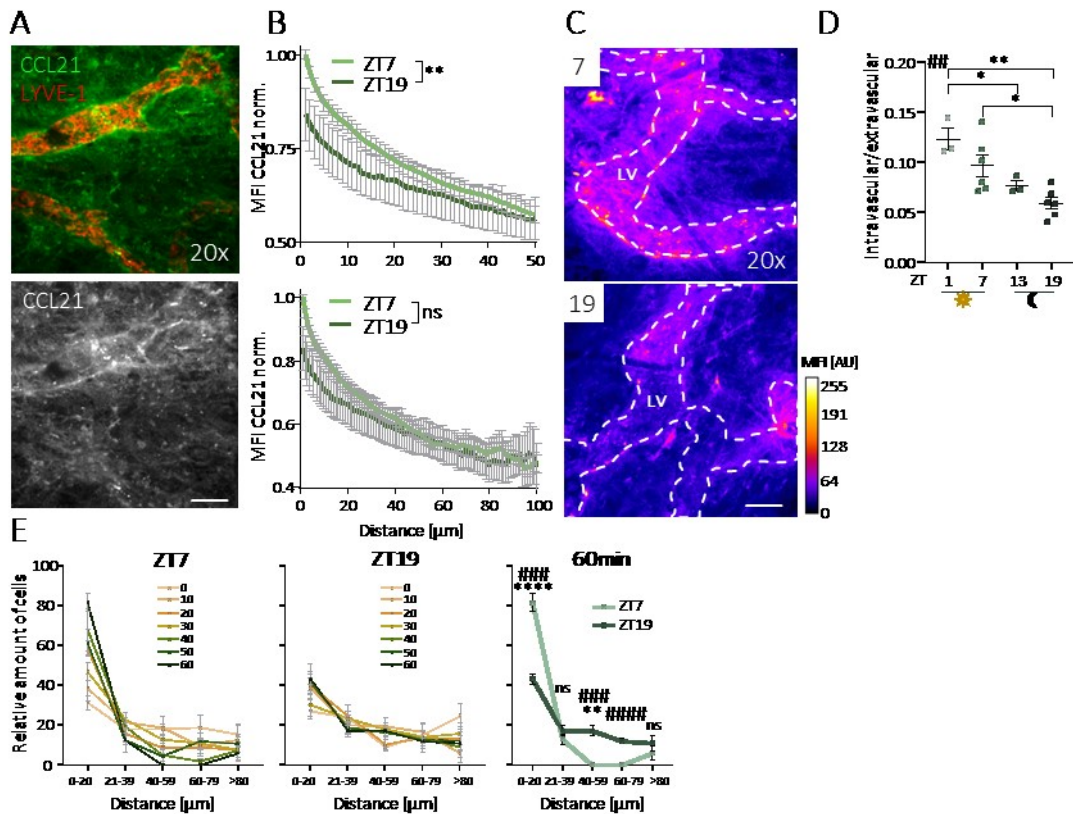


Figure 4-12: Rhythmic CCL21 micro-patterning influences dermal dendritic cell distribution

(A) Representative whole mount staining of split, non-permeabilized ears for CCL21 and LYVE-1. Scale bar = 50 μ m.

(B) Normalized (to highest value at ZT7) and averaged mean fluorescence intensity (MFI) profile of CCL21 in specific distances to lymphatic vessels (LVs). Top displays a maximum distance of 50 μ m, bottom a maximum distance of 100 μ m. N = 5 mice at *Zeitgeber* time (ZT) 7 and ZT19 measured each. * = Mann-Whitney U test.

(C) Exemplary whole mount staining of CCL21 in split and non-permeabilized ears at ZT7 or ZT19. LVs are indicated with a dotted line (based on LYVE-1 staining). Scale bar = 50 μ m.

(D) Cumulative distance distribution of CD11c⁺ cells in relation to LYVE-1⁺ LVs in split ears under steady state conditions. N = 3 mice at ZT7 and ZT19 measured each.

(E) Relative number of bone-marrow derived dendritic cells (BMDCs) after 0-60min (indicated by colored lines) crawl-in assays in specific distances to CD31⁺ LVs. Left: all time points; right: 60min crawl-in assay for ZT7 and ZT19. * = Tukey's multiple comparisons test, # = unpaired student's *t*-test. N= 1 mouse across all incubation and *Zeitgeber* times measured each; **p*<0.05, ***p*<0.01, ****p*<0.001, *****p*<0.0001. All other data are represented as mean \pm SEM.

Following this, I explored the consequences of disturbing CCL21 gradients in the skin at ZT7 and ZT19. I either masked, by adding exogenous CCL21, or completely ablated, using heparinase digestion or antibody blockade, the extracellular gradient of CCL21 while performing endogenous and/or exogenous crawl-in assays (see 3.2.6).

For antibody-mediated blockade of CCL21, ears from different ZTs were simultaneously harvested, incubated in blocking or isotype antibodies and subjected to trafficking assays using time-shifted mice. In the exogenous assay, chrono-pharmacological inhibition of CCL21 led to a 2.5-fold decrease of DC trafficking at ZT7, while no change was seen at ZT19 (**Figure 4-13A**). Similarly, targeting CCL21 in endogenous crawl-in assays, I noticed a 4.5-fold decrease in DC migration only at ZT7 (**Figure 4-13B**). Importantly, isotype antibody administration did not interfere with the diurnal trafficking phenotype in both experiments. Antibody-mediated neutralization of CCL21 led to a loss of DC orientation, as they appeared to be randomly distributed in the interstitial space and less directed towards LVs compared to isotype controls (**Figure 4-13C**).

Heparinase cleaves the heparin sulfate at the linkage between hexosamines and CCL21, thus releasing the bound CCL21 from the ECM and disturbing the naturally built-up gradient (**Figure 4-13D**). Digestion of the CCL21 gradient using heparinase caused a 1.5-fold decrease in DC trafficking at ZT7 compared to ZT19 and controls (**Figure 4-13E**).

Applied exogenous CCL21 binds to hexosamine structures on the ECM of the skin, leading to accumulation of CCL21 and thereby masking the natural gradient (**Figure 4-13F**). Correspondingly, adding exogenous CCL21 led to a 2.2-fold reduced DC trafficking solely at ZT7 (**Figure 4-13G**).

To confirm the neutralization of CCL21, I employed genetically modified BMDCs lacking CCR7 expression. CCR7-KO BMDCs are not able to sense CCL21 or CCL19 gradients and are thus blind to the stimulus. After culture and activation, CCR7 KO or WT BMDCs were added to split ears from time-shifted mice for exogenous crawl-in assays. The migratory behavior of CCR7 KO BMDCs was almost completely ablated as they failed to migrate towards LVs. ZT7 ears containing CCR7-KO BMDCs present a 16-fold, whereas ZT19 ears containing CCR7-KO BMDCs a 5-fold decrease in migration compared to WT levels (**Figure 4-13H**).

These results suggest a fundamental role for diurnal dermal CCL21 gradients to promote lymphatic trafficking of DCs during the day.

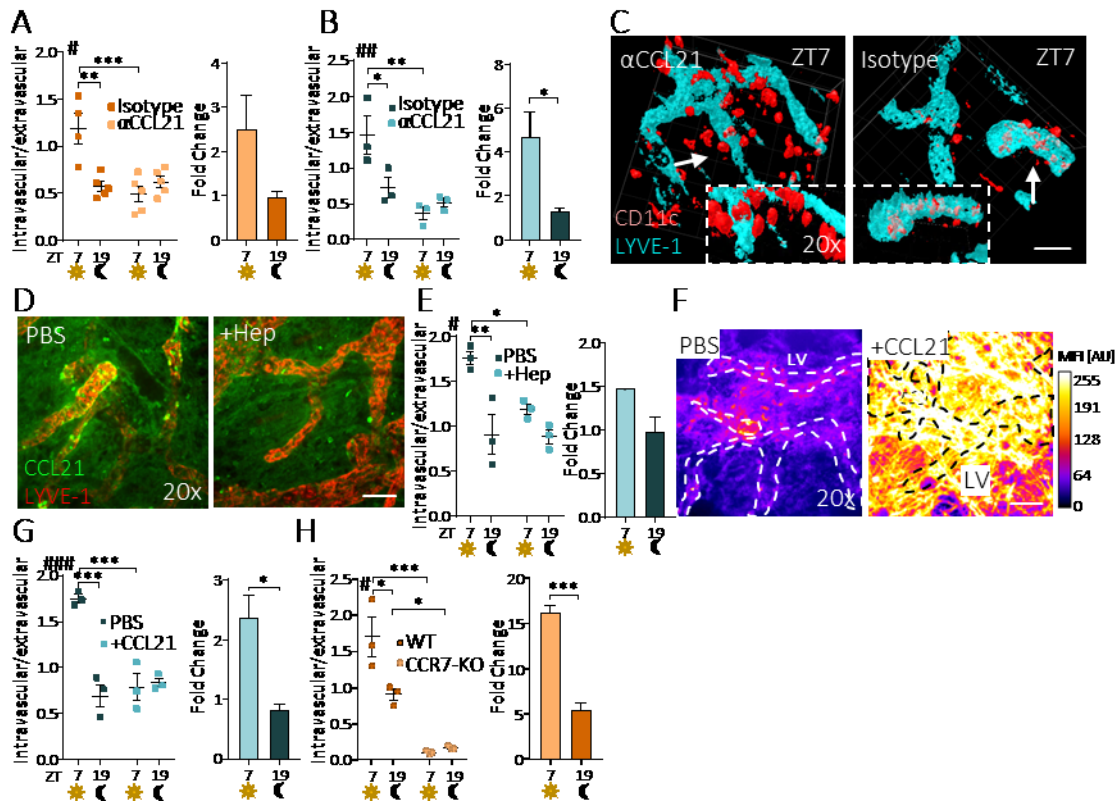


Figure 4-13: Manipulation of the CCL21 gradient leads to dysfunctional dendritic cell migration during the day

(A-B) Exogenous (A) or endogenous (B) crawl-in assays using α CCL21 or isotype antibody-treated ears. Left shows the ratio of intravascular versus extravascular bone marrow-derived dendritic cells (BMDCs) or dermal CD11c⁺ DCs, respectively, in LYVE-1⁺ lymphatic vessels (LVs; # = two-way ANOVA, * = Šidák's multiple comparisons test); right displays the fold change of antibody blockade in comparison with isotype controls (* = unpaired student's *t*-test). N = 4-5 (A) or 3 (B) mice across Zeitgeber Time (ZT) 7 and ZT19 measured each.

(C) Exemplary whole mount staining of split ears for CD11c and LYVE-1 after 24h incubation of an endogenous crawl-in using α CCL21 or isotype antibodies at ZT7. Arrows direct at higher magnifications. Scale bar = 50 / 10 μ m.

(D) Exemplary whole mount staining of CCL21 and LYVE-1 in non-permeabilized, split ears after heparinase or PBS treatment. Scale bar = 50 μ m.

(E) Endogenous crawl-in using heparinase or PBS treated ears. Arrangement and statistical tests equal to B. N = 3 mice across ZT7 and ZT19 measured each.

(F) Exemplary whole mount staining of CCL21 and LYVE-1 of non-permeabilized, split ears after addition of PBS or exogenous CCL21. Dotted lines resemble LVs (aligned with LYVE-1 staining). Scale bar = 50 μ m.

(G) Endogenous crawl-in using ears treated with exogenous CCL21 or PBS. Arrangement and statistical tests equal to B. N = 3 mice across ZT7 and ZT19 measured each. MFI = mean fluorescence intensity.

(H) Exogenous crawl-in using WT or CCR7 KO BMDCs. Arrangement and statistical tests equal to B. N = 3 mice across ZT7 and ZT19 measured each; **p*<0.05, ***p*<0.01, ****p*<0.001. All data are represented as mean \pm SEM.

After interstitial migration DCs adhere and transmigrate into the lumen of LVs. Previously, I described factors involved in these two steps to be rhythmically expressed. Consequently, I performed endogenous and exogenous crawl-in assays and neutralized molecules involved in adhesion and transmigration via antibody-mediated blockade together with employing isotype-matched controls. Specifically, I decided to target LYVE-1, CD99, JAM-A and JAM-C as

they showed strong oscillations in expression across the day during homeostasis and have been implicated in DC adhesion and transmigration before (**Table 2-2**).

In exogenous crawl-in assays, targeting LYVE-1 (3-fold reduction), JAM-A (2.2-fold reduction) and CD99 (1.5-fold reduction) reduced DC trafficking at ZT7, whereas at ZT19 these effects were not detected (**Figure 4-14A/D/G**). I then tried to reproduce the effects of LYVE-1, JAM-A, and CD99 neutralization in endogenous crawl-in assays. Similarly, targeting LYVE-1 led to a 3-fold reduction, JAM-A led to a 1.7-fold and CD99 led to a 2.0-fold reduction in DC migration at ZT7 (**Figure 4-14B/E/H**). Close observations of whole-mount staining of LVs and CD11c⁺ DCs after blockade unveiled that DCs manage to arrive at LVs in each of these scenarios, however they seemed to be immobilized on the LV wall and transmigrate at lower rate compared to isotype controls (**Figure 4-14C/F/I**). Due to strong oscillations of CD99 expression in LECs (**Figure 4-5**), I used genetically modified mice lacking CD99 expression. In an endogenous crawl-in setting using CD99^{-/-} ears, DC trafficking was markedly reduced at ZT7 compared to expected WT values, whereas at ZT19 only a slight reduction was noted (**Figure 4-14J**).

Neutralizing JAM-C in an endogenous crawl-in setting did not reduce DC migration in a statistically significant manner (**Figure 4-14K**). Since the effect of blockage was low, I did not follow up on the functional role of JAM-C with an exogenous crawl-in assay.

Moreover, CD31 was not found to be rhythmic in skin and thus, neutralization should decrease trafficking both at ZT7 and ZT19 serving as a control experiment. Endogenous crawl-in assays of CD31-blocked or isotype-stained ears led to a strong reduction in DC trafficking at both time points (**Figure 4-14L**).

In summary, these data highlight the relevance of rhythms in adhesion and transmigration molecules on LECs. Malfunction of targeted molecules led to dysfunctional migration of DCs into the lumen of LVs. This functionality, together with diurnal micro-patterning of CCL21 gradients, might prove a valuable insight into timing of vaccination as well as infection times.

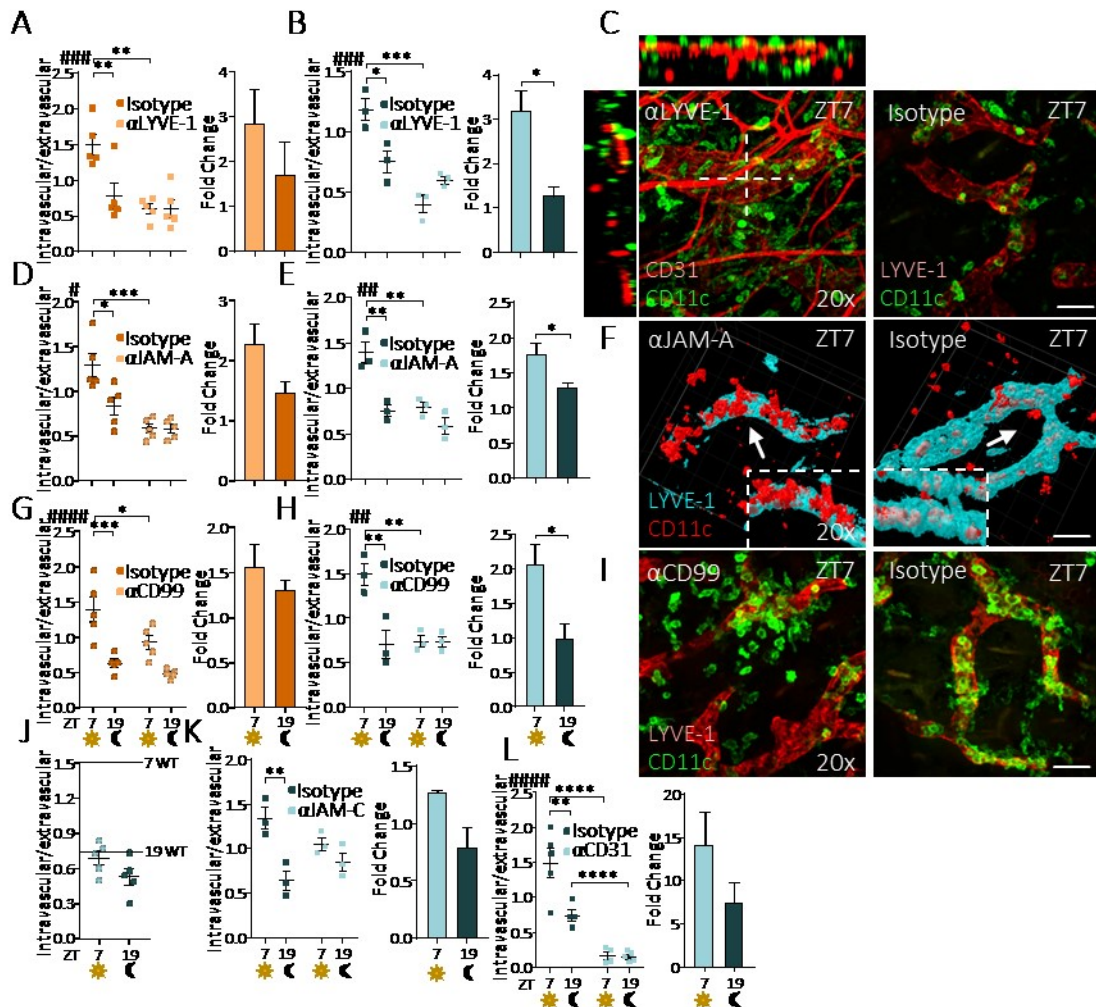


Figure 4-14: Chrono-pharmacological block of adhesion and transmigration reduces dendritic cell migration during the day

(A-B) Exogenous (A) or endogenous (B) crawl-in using α LYVE-1 or isotype antibody-treated ears. Left shows the ratio of intravascular versus extravascular bone marrow-derived dendritic cells (BMDCs) or dermal CD11c⁺ DCs, respectively, in CD31⁺/LYVE-1⁺ lymphatic vessels (LVs; # = two-way ANOVA, * = Šidák's multiple comparisons test); right displays the fold change of antibody blockade in comparison with isotype controls (* = unpaired student's *t*-test). N = 5 (A) or 3 (B) mice across Zeitgeber time (ZT) 7 and ZT19 measured each.

(C/F/I) Exemplary whole mount stainings of split ears for CD11c and CD31/LYVE-1 from 24h endogenous crawl-in assays using α LYVE-1 (C), α JAM-A (F) or α CD99 (I), or respective isotype antibodies at ZT7. Dotted lines (cross) and arrows facilitate magnifications and orthogonal views. Scale bars = 50 / 30 μ m.

(D-E) Exogenous (D) or endogenous (E) crawl-in assays using either α JAM-A or isotype antibody-treated ears. Arrangement and statistical tests equal to A-B. N = 5 (D) or 3 (E) mice across ZT7 and ZT19 measured each. All data are represented as mean \pm SEM.

(G-H) Exogenous (G) or endogenous (H) crawl-in assays using either α CD99 or isotype antibody-treated ears. Arrangement and statistical tests equal to A-B. N = 5 (G) or 3 (H) mice across ZT7 and ZT19 measured each.

(J) Endogenous crawl-in assay using WT or CD99-KO ears. Dotted lines resemble expected WT levels at different ZTs. N = 5 mice at ZT7 and ZT19 measured each.

(K-L) Endogenous crawl-in assay using α JAM-C (K) or α CD31 (L) and respective isotype antibody-treated ears. Arrangement and statistical tests equal to B. N = 3 (K) and 4-5 (L) mice across ZT7 and ZT19 measured each; **p*<0.05, ***p*<0.01, ****p*<0.001, *****p*<0.0001. All data are represented as mean \pm SEM.

4.6 Effects of lineage-specific clock deficiency on lymphatic dendritic cell migration

In previous experiments, I could link oscillations in pro-migratory molecules with rhythmic trafficking behavior and tried to uncover their functionality in the context of time-of-day dependent trafficking. However, for drawing conclusions to intrinsic clocks as initiator of rhythmic trafficking, a definite molecular link was yet to be uncovered.

For this purpose, I generated genetically modified mice lacking a functional molecular clock in key cell subsets to explore the link between rhythmic trafficking and the intrinsic clock machinery. In detail, together with my research group I generated mice deficient in the circadian clock gene *Bmal1* specifically in ECs using two different models, inducible *Cdh5cre^{ERT2}* mice, targeting both BECs and LECs and inducible *Prox1cre^{ERT2}* only targeting LECs. As tested in whole-mount staining of the skin, biomarkers PROX-1 and VE-CADHERIN are strongly expressed in dermal LECs and thus are eligible promoters for *Cre* expression in LECs (**Figure 4-15A/B**). I then performed exogenous (3h) and endogenous (6h and 24h) crawl-in assays to appraise the migration capacity of LVs using WT or KO ears. Interestingly, compared to control animals, *Cdh5cre-Bmal1^{-/-}* and *Prox1cre-Bmal1^{-/-}* mice failed to exhibit a rhythm in the immigration capacity of DCs into lymphatic capillaries at ZT7 in all migration assays tested with no significant differences between the two genetic models (**Figure 4-15C/D/F/G**). DCs required more time to arrive at the LVs concomitant with slower transmigration ability as shown in exemplary whole mount images (**Figure 4-15E/H**). These experiments implied LEC-specific *Bmal1* as a key player for rhythmic lymphatic DC trafficking and a molecular link between the previously observed phenotypes and the clock machinery.

In line with my previous experiment, I additionally investigated the DC molecular clock. For this, my research group generated mice deficient in the clock gene *Bmal1* using *Cre* expression within the promoter of *Clec9a* (*Clec9acre-Bmal1^{-/-}* mice). cDC1s and cDC2s in the skin both express *Clec9a* during their development whereas LCs have a different, macrophage origin and do not express *Clec9a*. As a consequence, *Bmal1* is not expressed in the cDCs of these mice. I decided to use a cDC *Bmal1* KO model, since cDC2s were the most abundant DC cell type measured in skin and showed strong rhythmicity in trafficking behavior and they were readily available in the lab (**Figure 4-9** and **Figure 4-10**). I performed 24h endogenous crawl-in assays to examine to what extent the DC intrinsic clock contributes to rhythms in lymphatic DC trafficking. Surprisingly, the migration of DCs was only reduced in *Clec9acre-Bmal1^{-/-}* mice tested at ZT7 in comparison with control animals (**Figure 4-15I**). Likewise, the majorities of DCs in KO ears failed to arrive at LVs, indicating a reduced interstitial migration

capacity (**Figure 4-15J**). In comparison with data from *Cdh5cre-Bmal1^{-/-}* and *Prox1cre-Bmal1^{-/-}* mice, *Clec9acre-Bmal1^{-/-}* mice yielded a slightly lower reduction at ZT7.

Together these data for the first time link both lymphatic vasculature and cDC clocks with rhythmic cDC migration within the skin. Interstitial migration as well as transmigration of the lymphatic endothelium was markedly reduced in *Bmal1* KO animals. Both the LEC and DC clock partially influenced the rhythmic behavior and both cellular clocks were required to facilitate a functional rhythm. These findings should be helpful in exploring the consequences of jetlag, shiftwork and other disruptions of the clock.

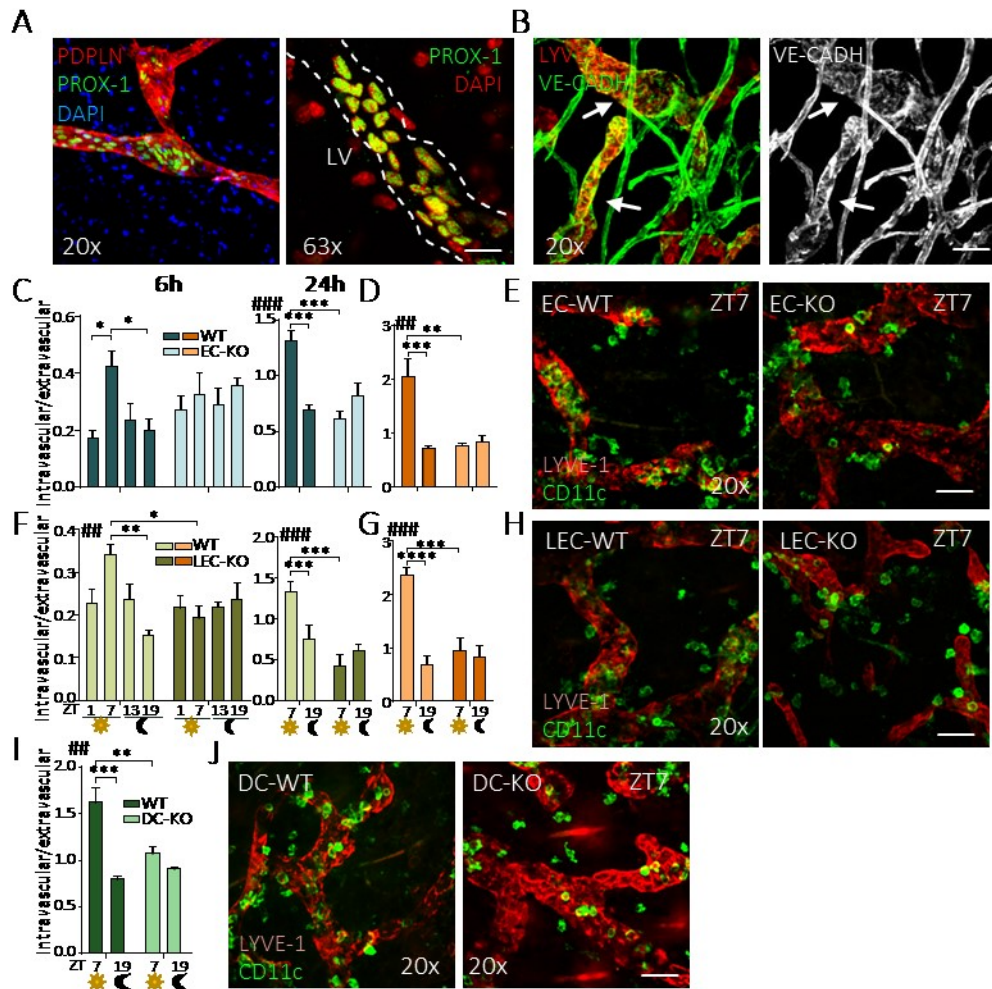


Figure 4-15: Lineage-specific clock deficiency leads to dysfunctional dermal dendritic cell trafficking

(A-B) Whole mount staining of split, permeabilized ears for PODOPLANIN (PDPLN), PROX-1 and DAPI (A) or for LYVE-1 and VE-CADHERIN (VE-CADH; B). Arrows point towards and dashed line outlines lymphatic vessels (LV). Scale bars = 50 / 10 μ m.

(C-D) Ratio of intravascular versus extravascular dermal CD11c⁺ dendritic cells (DCs) or bone marrow-derived DCs (BMDCs) in endogenous (C; left 6h, right 24h) or exogenous crawl-in (D) assays, respectively, using *Cdh5cre-Bmal1*^{-/-} (EC-KO) or WT ears. # = two-way ANOVA, * = Šidák's multiple comparisons test. N = 5-7 (C) or 5-6 (D) mice across 4 or two time points measured each. Zeitgeber time = ZT.

(E/H/J) Exemplary wholemount staining of split ears for CD11c and LYVE-1 after 24h endogenous crawl-in assays using *Cdh5cre-Bmal1*^{-/-} (EC-KO; E), *Prox1cre-Bmal1*^{-/-} (LEC-KO; H), or *Clec9acre-Bmal1*^{-/-} (DC-KO; J) and WT animals at ZT7. Scale bars = 50 μ m.

(F-G) Ratio of intravascular versus extravascular dermal CD11c⁺ DCs or BMDCS in endogenous (F; left 6h, right 24h) or exogenous (G) crawl-in assays, respectively, using *Prox1cre-Bmal1*^{-/-} (LEC-KO) or WT ears. Statistical tests equal to C-D. N = 4-6 (F) or 4-5 (G) mice across 4 or two time points measured each.

(I) Ratio of intravascular versus extravascular dermal CD11c⁺ DCs in exogenous crawl-in assays using *Clec9acre-Bmal1*^{-/-} (DC-KO) or WT ears. Statistical testing equal to C-D. N = 4-5 across ZT7 and ZT19 measured each; **p*<0.05, ***p*<0.01, ****p*<0.001, *****p*<0.0001. All data are represented as mean \pm SEM.

Since mice lacking *Bmal1* in LECs exhibit defects in DC migration, I further wanted to investigate the connection between the molecular clock and rhythmic migration. For this purpose, I repeated the quantitative immune-fluorescence profiling of chemokines, adhesion and transmigration proteins in sectioned skin samples from both *Cdh5cre-Bmal1^{-/-}* and *Prox1cre-Bmal1^{-/-}* as well as control animals. Loss of *Bmal1* reduced levels of previously described rhythmic proteins LYVE-1, JAM-A, JAM-C, CD99 and intracellular CCL21 at ZT7 but not ZT19 in comparison to WT controls (**Figure 4-16A/B**). As expected, non-rhythmic CD31 levels were not affected in both genetic models (**Figure 4-16A/B**).

To further shed light on the link between the molecular clock and chemokine micro-patterning I analyzed the extracellular CCL21 in *Prox1cre-Bmal1^{-/-}* and control animals. By employing the same algorithm used in **Figure 4-12**, I visualized the CCL21 gradient in the dermal capillary environment. Surprisingly, the CCL21 gradient analyzed in *Prox1cre-Bmal1^{-/-}* mice at ZT7 presented dramatically lower concentration and loss of diurnal upregulation compared to gradients in WT ZT7 as well as WT ZT19 and KO ZT19 ears (**Figure 4-16C**). Genetic ablation of *Bmal1* also reduced the shape of the CCL21 gradient (**Figure 4-16C/D**) possibly owing to reduced production or release in KO mice.

These data create a strong link between regulation of DC trafficking and intrinsic molecular clocks. In particular, the LEC clock influences chemotaxis, adhesion and transmigration of dermal DCs within the skin.

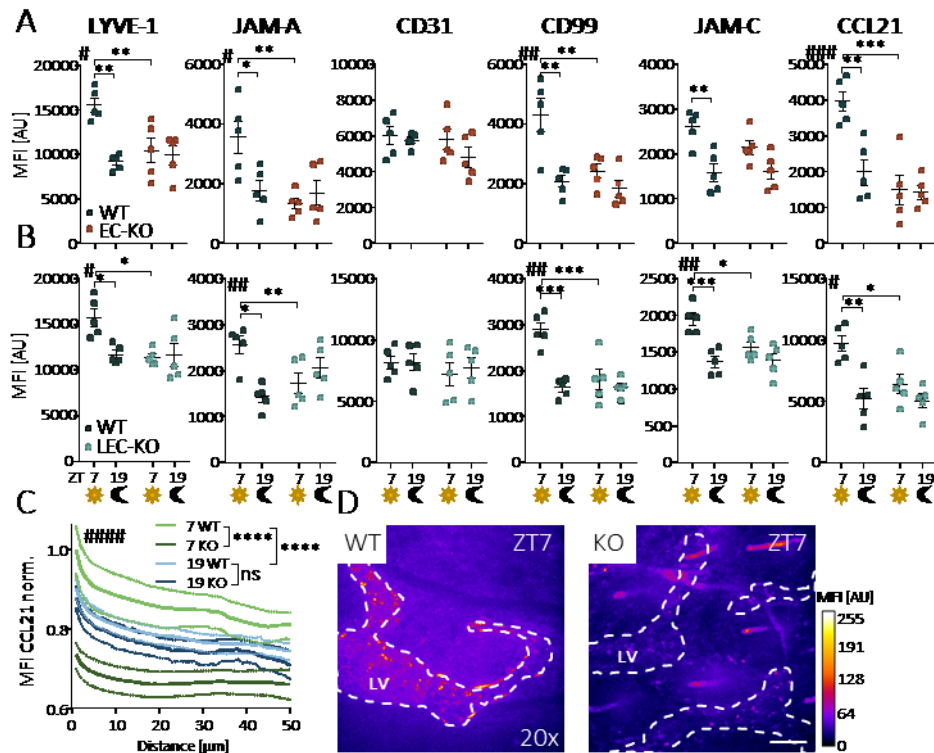


Figure 4-16: Loss of Bmal1 in lymphatic endothelial cells leads to downregulation of trafficking factors and chemokine micro-patterning

(A-B) Mean fluorescence intensity (MFI) profile of trafficking molecules measured by quantitative immuno-fluorescence microscopy in 10 μ m ear sections from WT and *Cdh5cre-Bmal1*^{-/-} (EC-KO; A) or *Prox1cre-Bmal1*^{-/-} (LEC-KO; B) mice at Zeitgeber time (ZT) 7 or ZT19.

(C) Normalized (to highest value of WT ZT7) and averaged MFI profile of CCL21 in specific distances around the lymphatic vessel (LV) using either WT or *Prox1cre-Bmal1*^{-/-} (KO) ears. N = 5 mice at ZT7 and ZT19 measured each. * = Dunn's correction for multiple comparisons, # = Kruskal-Wallis test. Dotted line represents SEM.

(D) Exemplary whole mount stainings of split and non-permeabilized ears for CCL21 at ZT7 from either WT or *Prox1cre-Bmal1*^{-/-} (KO) animals. LVs are indicated with a dashed line (based on LYVE-1 staining). Scale bar = 50 μ m. LEC = lymphatic endothelial cell; **p*<0.05, ***p*<0.01, ****p*<0.001, *****p*<0.0001. All data are represented as mean \pm SEM.

In a final approach, I sought to further scrutinize the consequence of genetic ablation of *Bmal1* in LECs. I surveyed the DC cellularity of *Cdh5cre-Bmal1^{-/-}* and WT ears across four different time points using flow-cytometry. Strikingly, the previously observed rhythm in DC cell numbers in KO animals was abolished compared to WT control animals, especially at ZT7 (**Figure 4-17A**). Specifically, LC and cDC2 oscillations were ablated (**Figure 4-17A**). This could point towards a functional role of BVs and LVs and their respective clocks in the regulation of ear cellularity.

I further assessed the emigration capacity of dermal DCs employing crawl-out assays since an altered CCL21 gradient and less lymphatic trafficking in KO animals might lead to increased lymphatic vessel-independent emigration of DCs, as shown by Förster and colleagues [191]. Whilst in WT animals, only a low number of DCs emigrated the ear and reproduced the results depicted in **Figure 4-10**, in *Cdh5cre-Bmal1^{-/-}* animals, a greater absolute number of DCs emigrated the ear at ZT7 and ZT19 (**Figure 4-17B**). In detail, cDC2s showed significant differences between KO and WT animals and harvest times specifically in KO animals. On the contrary LCs and cDC1s gave a trend but no significant differences in emigration tested. Importantly, the increase in emigration was more pronounced at ZT7 compared to ZT19 (**Figure 4-17B**). This might be partially explained by an altered or reduced CCL21 gradient, leading to loss of orientation and elevated emigration of DCs. However, this needs to be confirmed in *Prox1cre-Bmal1^{-/-}* mice, as this model is tailored to solely LECs.

Irrespectively, the loss of *Bmal1* clearly alters the ability of DCs to migrate to LVs and modifies the ear cellularity.

Together, these genetic KO data create a strong link between the observed rhythmic processes and the molecular clock. Both the LEC and DC clock seem to either be capable to influence the rhythmic behavior and both cellular clocks are required to facilitate a functional rhythm.

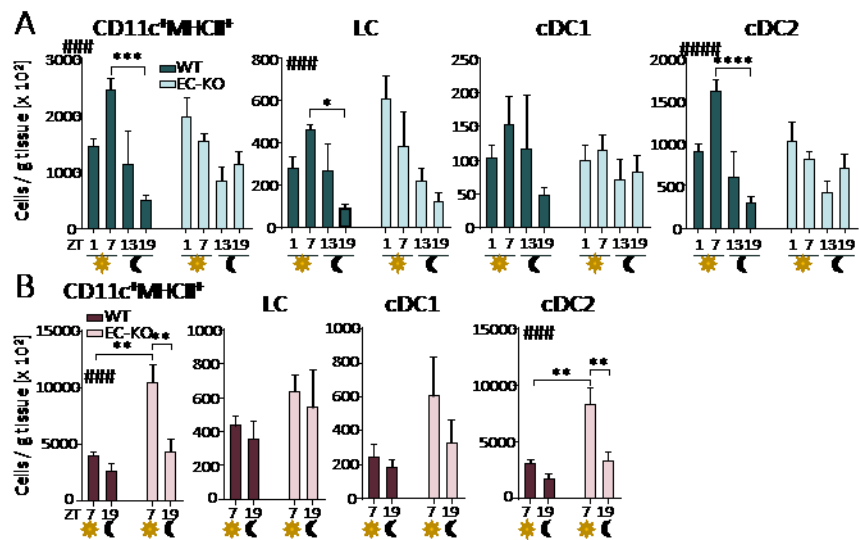


Figure 4-17: Genetic ablation of *Bmal1* leads to alteration in ear cellularity and increased dendritic cell emigration

(A) Flow-cytometric analyses of ear CD11c⁺MHCII⁺ dendritic cell (DC) cellularity normalized to ear weight from either WT or *Cdh5cre-Bmal1*^{-/-} (EC-KO) mice. LC = Langerhans cell, cDC1/2 = conventional DC 1/2. # = two-way ANOVA, * = Tukey's multiple comparisons test. N = 9 mice across 4 *Zeitgeber* times (ZT) measured each.

(B) Flow-cytometric analyses of emigrated DCs from cultured, split ears (crawl-out assay) from either WT or *Cdh5cre-Bmal1*^{-/-} (EC-KO) mice normalized to ear weight. Statistical testing equal to **A**. N = 4-5 mice across ZT7 and ZT19 measured each; **p*<0.05, ***p*<0.01, ****p*<0.001, *****p*<0.0001. All data are represented as mean ± SEM.

5 Discussion and future perspectives

In the past years, the circadian clock has been identified as an elemental modulator of the immune system. Various components of immunity are under the control of the molecular clock [338-340], but we only just commenced understanding the molecular circuits. Very little is known about how the lymphatic system, an important component of the immune system, is shaped by environmental factors throughout the day. This study provides first evidence for rhythmic lymphatic immune cell migration, temporal regulation of protein and RNA expression within LECs and sheds light on tissue-specific loss of the molecular clock and its consequences on dermal immune cell trafficking.

In this final chapter of the work, rhythmic leukocyte trafficking of dermal DCs into lymphatics and its potential future investigation are discussed.

5.1 Circadian rhythms in lymphatic dendritic cell migration

Ex-vivo ear migration assays using dermal DCs or BMDCs revealed a circadian migration capacity, peaking during the behavioral resting phase of the mouse at ZT7 (**Figure 4-3** and **Figure 4-4**). The endogenous and exogenous crawl-in assays address different questions. The exogenous assay gives a clear indication about the influence of the microenvironment, as cultured BMDCs do not display a synchronized clock during typical culture conditions [331]. Individual BMDCs express all clock components, but on average, the population as a whole does not show a rhythm in expression across 24h. On the contrary, the endogenous crawl-in assay only allows for the assumption of general rhythms in lymphatic DC migration. Additionally, examined CD11c⁺ cells in the endogenous assay comprise all dermal DC subtypes, which were previously described owning distinct differences in their migratory behavior (*see 4.4* and [108]). Moreover, BMDCs are transcriptionally and evolutionary distinct from dermal (especially cDC1 and cDC2) DCs and thus, differing activation state, cytoskeletal components as well as expression of chemokine receptors and trafficking molecules might influence the outcome of the trafficking assay. A study by Helft and colleagues could reveal differences amongst BMDCs which adds another level of complexity to the reasons presented above [341]. Another culture method, e.g. Flt3L culture rather than GM-CSF or a pre-sort between culture and crawl-in assay could be employed here. Nonetheless, during both migration assays, trafficking was highest during the day. The difference observed in the

strength of immigration into lymphatics is likely being explained by the higher activation status of LPS-derived BMDCs compared to non-activated tissue-resident cells.

Reported oscillations in dermal DC cell numbers (**Figure 4-9**) could not be observed in total CD11c⁺ DC numbers per field of view analyzed in the endogenous crawl-in assay (**Figure 4-4**). Due to physical reasons, spinning disk confocal microscopy of dermal explants is not able to visualize and quantify the whole ear cellularity (owing to limiting imaging depth). Additionally, DCs do not only arrange in close proximity to LVs, they also reside in dermal segments directly underneath the epidermis and thus are missed during image acquisition. This is why the cellularity shown in **Figure 4-4** is only used as a control for even distribution of cell numbers amongst different groups to ascertain comparability.

Collectively, both cell migration assays strongly support the hypothesis of rhythmic DC trafficking across lymphatics. Velocity, directionality towards LVs and other migration parameters were not assessed but are currently being investigated in real-time assays. In contrast to end point analyses, live imaging of migrating BMDCs allows further resolution of rhythmic migration [178], especially in the context of the rhythmic CCL21 gradient and the consequence of genetic *Bmal1* ablation. Preliminary data show that the method *per se* is working and data can be readily generated in the future (see appendix **Figure 7-1**).

What could be the functional importance of an increased migration capacity during the behavioral rest phase? Herein, migration capacities of dermal DCs were highest at ZT7, whereas in other studies, leukocytes show an elevated migratory state and enter organs at ZT13, and DCs peaked in migration in mesenteric LNs at around ZT9 [56, 291]. Migration regulation of different leukocytes and ECs by the circadian clock seems to be tissue-specific. This was also reported in a study by Druzd *et al.*, in which the egress rate of lymphocytes via efferent LVs from the LN was assessed. This rate was highest between ZT7 and ZT9, revealing a pro-migratory state of efferent LVs during the behavioral rest phase of mice due to temporal upregulation of *S1pr1*, a receptor binding the factor S1P promoting lymphocyte egress [291]. Conversely, LN BVs adopt a pro-migratory protein signature and homing of lymphocytes to the LN via BVs was highest at ZT13 [56, 291]. Diversity in rhythmic leukocyte trafficking allows for flexibility and a balanced immunity. Complete concentration of immune effectivity at one time point during the day would increase the risk of immune overreaction during that time and susceptibility to pathogens at other times of the day. Thus, differing peaks in migration enhance the flexibility and secure adequate immune reactions. Another explanation could be found in increased LN lymphocyte numbers at the onset of the active phase [291]. During the active phase, organisms capture antigens of all kinds on the surface of the skin. Afterwards, antigen capture, activation, initial migration to LVs as well as re-localization to dLNs of DCs

requires multiple hours. Consequently, DCs are likely to arrive at the dLN after several hours, coinciding with a higher cellularity and an increasing chance of antigen cross-presentation to T cells. By maximizing the efficiency of immune responses, metabolic costs are reduced, which may be one of the main reasons why the immune system temporally changes its reactivity and activity [339].

5.2 The role of oscillations in lymphatic protein and RNA expression

Quantitative immuno-fluorescence profiling of organ sections and RNA sequencing of sorted dermal LECs at different times of the day unveiled a rhythmic expression map of proteins and genes (see 4.3). Rhythmic pro-migratory proteins investigated peak at ZT1 or ZT7, coinciding with an upregulation of adhesion genes at ZT1 (**Figure 4-5**, **Figure 4-6**, **Figure 4-7**, **Figure 4-8**).

The protein screen employed a LYVE-1 based mask of the region of interesting, in which the target protein was then quantified. Interestingly, LYVE-1 exhibited a rhythm in expression, which could lead to varying mask sizes through the analysis. The algorithm generating the mask (see appendix 7.2) is based on relative fluorescence intensities. Consequently, absolute changes in LYVE-1 MFIs do not alter the mask size, unless LYVE-1 is changing its distribution pattern on the surface of the cell. Although this was not investigated, differing distribution patterns should only negligibly alter the mask size. Irrespectively, approaching distribution patterns of proteins of interest could be important for time-of-day dependent cargo-transport of proteins to the cell surface, especially for released chemokines such as CCL21.

Similar to differences in leukocyte trafficking, regulation of trafficking factors seems to be differing between BVs and LVs. Under steady-state conditions, dermal LECs maintain unique expression patterns of migratory factors when compared to inflammation, during which they acquire a BEC-like phenotype by up-regulating integrin ligands such as ICAM-1 [206]. In BVs, organ- and site-specific BECs up-regulate pro-migratory factors at the onset of the active phase (e.g. ZT13; **Table 2-3**) [55, 243, 271]. Tissue-specific LECs contrarily display augmented expression of pro-migratory factors during the resting phase (ZT1/ZT7; **Figure 4-5**). The question remains, how heterogeneity between different ECs and within organ-specific LECs can be established by the circadian clock. In the following, multiple reasons are discussed.

Temporal regulation of clock controlled genes relies on genetic regulatory elements, such as E-boxes and ROR elements, as well as post-transcriptional modifications [338]. An evolutionary reason for this might be the multiplication of diversity in gene regulation and a flexible metabolism and immune system. As an example, REV-ERB is a potent regulator of

CCL2 in human and murine macrophages as proven by pharmacological activation (REV-ERB ligand GSK4112) of REV-ERB α and chromatin immunoprecipitation (ChIP) assays, in which REV-ERB α binds to a proximal ROR element in the promoter region [288, 342]. At the same time the cognate receptor of *CCL2*, CCR2, is regulated by PER1 together with the nuclear receptor peroxisome proliferator-activated receptor gamma (PPAR γ) [343]. Additionally, ROR α opposes REV-ERB α in its regulation and positively influences the *Ccl2* expression via binding to ROR elements, whereas BMAL1 promotes methylation of *Ccl2* together with reducing its expression using E-boxes at ZT7 in peritoneal macrophages [276, 342].

Despite the complexity of E-box- and ROR-mediated gene regulation, differences between cell types also heavily depend on individual interactions with hormone signals. Hormones are an essential internal entrainment factor [243] and their receptors are expressed on cells in a tissue-specific manner. For example, adrenaline and noradrenaline are important neurotransmitters and hormones in the periphery and are able to entrain the circadian clock via numerous adrenoceptors including α_{1A} , α_{1B} , α_{1D} , $\alpha_{2A/D}$, α_{2B} , α_{2C} , β_1 , β_2 , and β_3 receptors [243, 344, 345]. Tissue-specific BECs or myocytes provide different signatures of these receptors to maximize the flexibility in physiological function. For instance, in humans adrenaline consistently reduces renal and skin blood flow because α -adrenoceptors are predominant, whereas in skeletal muscle and splanchnic vasculature adrenaline acts mainly via β -adrenoceptors and induces vasodilatation [345]. As another example, β_2 adrenergic receptor agonists cause a dilatation of smooth muscles in the lung leading to opening of the airways, although in large arteries and heart tissue their binding enhances myocyte contraction [346, 347]. The functional role of the autonomic nervous system on LECs under physiological conditions was only recently described by Bachmann *et al.*, demonstrating functional expression of α_1 (contraction) and β_2 (dilatation) adrenoceptors on flank collector LVs *in-vivo*, whereas lacteals express β_2 adrenoceptors only [348]. Furthermore, RNA-sequencing of sorted dermal LECs performed here could reveal an oscillation in the β_2 receptor subunit, pointing at a possible entrainment of LECs by the peripheral nervous system (**Figure 4-8**). Although more research is required to disentangle the role of the nervous system on regulating LECs, distinctive humoral signals might increase tissue-specificity and generate differences observed in this thesis.

Epigenetic changes in chromatin accessibility of different cell types or methylation processes regulating transcription of clock-controlled genes might contribute to the observed heterogeneity. For example, CLOCK functions as histone acetyl transferase (HAT) regulating glucocorticoid receptors [349]. Furthermore, polycomb repressive complexes (PRC) such as PRC2 can be induced by BMAL1 and bind to methylated regions to repress gene expression in

a rhythmic manner [276]. Finally, recent *in-vivo* quantification of circadian phosphorylation in the liver suggests a crucial role for phosphorylation-dependent circadian tuning of molecular pathways as well [350].

Accordingly, circadian regulation of target genes is depending on numerous factors and could explain differences between cell types. This complex regulation might lead to differences in protein expression within organ-specific LEC subtypes, such as ICAM1 expression levels in lacteal and SMLV LECs (**Figure 4-4**).

Results from the protein and RNA screen can only be interpreted to a certain extent as the direct molecular link, how clock genes regulate respective lymphatic genes is yet to be discovered. Localization of E-boxes and other regulatory elements in the promoter region of genes of interest together with promoter binding assays of BMAL1 or other transcription factors such as REV-ERB α could be a first step linking rhythmic expression with the binding of transcription factors of the circadian clock family. An overview of proposed binding regions for the clock genes *Bmal1*, *Dbp*, *Nfil3* and ROR-binding clock genes *Rora* and *Nr1d1/Nr1d2* in promoters of genes relevant for this thesis is provided in **Table 5-1** and appendix **7.3**. Based on the results from the promoter database, *F11r* and *Jam3* (JAM-A and JAM-C, respectively), *Ackr4* and *Cd86* might be directly regulated via ROR-binding clock proteins, whereas *Reln* could be under the direct control of Bmal1. Other genes such as *Ccl21-a*, *Ccl21-c* or *Lyve-1* yield elements for a more complex regulation (**Table 5-1** and appendix **7.3**). Importantly, loss of Bmal1 in ECs led to a downregulation of target proteins LYVE-1, JAM-A, JAM-C, CD99 and CCL21, pointing towards a direct molecular link between the circadian clock and pro-migratory molecules in lymphatics (**Figure 4-16**). BMAL1 or REV-ERB α could be possible candidates in LECs, as they have been involved in chemokine expression as mentioned above and are strongly expressed at the beginning of the behavioral rest and active phase, respectively.

Transcr. factors	<i>Bmal1</i>			<i>Dbp</i>			<i>Nfil3</i>			<i>Rora</i>		
	<i>p</i> -value	0.01	0.001	0.0001	0.01	0.001	0.0001	0.01	0.001	0.0001	0.01	0.001
<i>Ccl21a</i>	29 9	4 2	1	28	2	0	34	3	0	40	5	0
<i>Ccl21c</i>	26	3	1	28	2	0	31	2	0	40	3	1
<i>Lyve1</i>	44	6	1	43	8	0	28	3	1	42	4	0
<i>Jam3</i>	22	1	0	15	0	0	21	0	0	23	3	0
<i>F11r</i>	19	0	0	9	0	0	18	1	0	47	6	0
<i>Cd99L2</i>	45	1	0	25	1	0	18	2	0	40	3	1
<i>Reln</i>	61	9	1	14	0	0	18	1	0	30	1	0
<i>Ackr4</i>	32	2	0	26	1	0	24	2	0	41	3	0
<i>Ccr7</i>	49	6	0	19	2	0	20	2	0	44	6	0
<i>Cd80</i>	32	5	0	19	0	0	26	2	0	40	2	0
<i>Cd86</i>	37	0	0	22	1	0	20	3	0	31	2	0
<i>Cd40</i>	32	2	0	10	1	0	8	2	0	37	4	0

Table 5-1: Number of promoter binding sites for clock genes *Bmal1*, *Dbp*, *Nfil* and *Rora*

Genes were screened using the eukaryotic promoter database provided by the Swiss Institute of Bioinformatics. Motifs were searched within -2000bp to +100bp distance in the promoter region using the JASPAR CORE 2018 vertebrates library and with different *p*-values. Canonical binding sites (CAN NTG) for *Bmal1* in the *Ccl21a* promoter region calculated in red as an example (see 7.3 for sequence). *Cd99* was not found in database; instead the closely related *Cd99L2* was presented as an example. *Jam3* = JAM-C, *F11r* = JAM-A, Transcr. = transcription. The exact sites and example of *Ccl21a* are shown in the appendix 7.3.

RNA sequencing of sorted LECs revealed oscillations in clock gene expression. Internal control of sufficient RNA quality (not provided but ensured by the sequencing core facility), high amount of detected transcripts (>10,000) with more than 35 million reads and satisfactory gene body coverage to avoid the bias of RNA degradation at the 5' / 3' end ensured a successful and well-controlled RNA sequencing (controls not shown). Besides this, confidence in the sequencing results can be built on the observed clock gene expression (Figure 4-7). Other studies have shown similar expression patterns in different cell types, including neutrophils [299], NK cells [351], eosinophils and mast cells [352], T cells and LN tissue [280, 291], large arteries and veins [271], macrophages and monocytes [277, 353], as well as B cells and DCs [278]. In LECs, *Bmal1* peaks at the transition of active to resting phase (ZT19-ZT1), and *Per2* and *Per3* peak during the trough of *Bmal1*, at the transition of active to resting phase (ZT13). *Dbp*, *Nr1d1* and *Nr1d2* peak during the active phase (ZT7 and ZT7-13 for *Nr1d2*). Consequently these results are consistent with the published literature.

Sorted LECs presented an upregulation of adhesion genes during the resting phase, as shown by DeSeq2 and one-way ANOVA statistical evaluation. *Ackr4* was excluded from the adhesion gene clustering (Figure 4-8) as it represents a negative regulator of leukocyte trafficking [202]. Studies have shown, that *Ackr4* expressed on keratinocytes sequesters chemokines such as CCL19 to prevent overreaction of the immune system and keep leukocyte trafficking within

physiological frames [202]. Expression and relevance of *Ackr4* within the LEC has not been fully understood yet, but was found to be important in the development of the lymphatic system at the embryonic day 6 and might be of similar relevance compared to ACKR4 on keratinocytes in adult mice [214]. Down-regulation of *Ackr4* at ZT1 might therefore positively influence leukocyte trafficking and is in support of this proposed role in LECs (**Figure 4-5**).

Other genes encoding rhythmic proteins of interest could not be sequenced or proven rhythmic. A complete lack of signal during sequencing could be due to RNA degradation or complexity in gene and RNA structure, e.g. by splicing. Notably, there is no published study showing the mRNA expression profile of *Ccl21b/c* in the skin.

For other genes, e.g. LYVE-1, high but non-rhythmic expression could be quantified. Nonetheless, studies by Hughes and colleagues as well as Geyfman *et al.* describe rhythmic expression of *Lyve1* in liver and epidermal tissue with a peak occurring at CT14 and ZT14 and a trough at CT3 and ZT2, respectively [308, 354]. Besides regulatory elements in promoters, the temporal regulation of CCGs is heavily dependent on post-transcriptional modifications by clock genes. In particular, a study by Kojima and colleagues could identify circadian rhythms in mouse liver mRNA poly(A) tails uncoupled from rhythmic transcription. This means that the circadian clock can regulate the post-transcriptional regulation of mRNA resulting in oscillatory protein expression irrespective of steady-state mRNA levels [355]. Consequently, the RNA expression profile does not necessarily have to reflect the rhythmic pattern in order for its protein product to be rhythmically expressed. Nevertheless, a second proof of diurnal protein expression by quantitative flow-cytometric screening and quantitative real-time PCR of RNA could aid in clarification. Targets should include *Ccl21* and *Lyve1* to not only validate the previous results but also gain further insight into mRNA abundance.

Collectively, these data support the hypothesis that up-regulation of pro-migratory factors heavily contributes to rhythmic trafficking of DCs within the skin and might be under the control of the molecular clock.

5.3 Temporal chemokine patterning during steady state – pointing towards rhythmic tolerance induction?

CCL21 was found to be rhythmically expressed in dermal LECs, with a peak at ZT7 (**Figure 4-6**). This timed-expression of CCL21 was already published by Druzd and colleagues in the LN, in which gene (*Ccl21a*) and protein expression peaked during the day and night, respectively,

[291]. This is in line with micro-array profiling of the gene *Ccl21a* in liver tissue [354]. Profiling of CCL21 in skin whole mounts indicated that not only the storage, but specifically the release of CCL21 might be rhythmic (**Figure 4-6**). Further experiments assaying the CCL21 release capacity and RNA sequencing for rhythmic factors involved in cargo-transport are required for a better understanding of temporal CCL21 release. Several chemical compounds interfering with secretion pathways, such as brefeldin A, Exo1 or secramine B could be used to further dissect molecular mechanisms [356, 357]. Moreover, generated RNA-sequencing data could be screened for genes associated with transport of proteins. Nevertheless, an increased storage or release rate at ZT7 might be beneficial in immediate inflammatory responses and would be a novel phenomenon to be observed in rhythmic leukocyte trafficking.

Furthermore, an oscillation in dermal CCL21 micro-patterning could be visualized, which influenced the localization and migration of dermal DCs under steady-state conditions (**Figure 4-12**). Since CCL21 is rhythmically expressed and released in dermal and LN LECs under steady-state conditions [291], the question arises, whether other LEC activities important for tissue homeostasis might oscillate as well.

One possible role of steady-state rhythms in migration and chemotaxis might be the induction of self- and peripheral tolerance, which partially relies on interactions with DCs [358]. Indeed, LECs from the thymus [359, 360], LN [361] and (to a lesser extent) from colon and diaphragm [362] were demonstrated to be heavily involved in T cell- and self-tolerance. In detail, LN LECs present peripheral tissue antigens (PTA) under the control of autoimmune regulatory elements [359] and members of the SAND family such as *Deformed epidermal autoregulatory factor 1 homolog (Deaf1)* [363, 364]. They display tyrosinase antigen by MHC I molecules to activate CD8⁺ T cell proliferation, which undergo apoptosis and deletion rather than accumulation (resembling a form of extra-thymic negative selection). LN LECs additionally express a particularly high level of PD-L1 instead of co-stimulatory molecules such as OX40L, CD86, CD80, or CD70 to regulate other cells [361, 365, 366]. Finally, LECs express intermediate levels of MHC II, proposing a role in CD 4⁺ T cell tolerance that requires DC interaction [358, 367] as well as IL-7 and its receptor IL-7R α , important in T cell homeostasis and lymphatic drainage [368, 369]. Results from this thesis give compelling hints at rhythmic self-tolerance induction as described below.

First, sorted and sequenced LECs from the skin in this study strongly expressed *Deaf1*, and at lower levels *Cd274* (encoding the protein PD-L1) and *H2-ab1* (encoding the protein MHC II) with slight oscillations, peaking at ZT13/19 for *Deaf1* (not significant but indicative) and ZT7 for *Cd274* (significant) and *H2-ab1* (not significant but indicative). Data are shown in appendix

Figure 7-2 since they are not relevant for this thesis *per se* but could imply steady-state rhythms in self- and peripheral-tolerance induction.

Secondly, more DCs localized inside the LVs during steady-state conditions at ZT7 compared to ZT19, which could be a direct consequence of augmented interstitial CCL21 micro-patterns and facilitate T cell: DC communication (**Figure 4-12**).

Third, LECs displayed rhythms in a variety of genes and proteins that facilitate permeability as well as adhesion during the resting phase, possibly aiding in induction of self-tolerance, which is supported by two studies showing rhythmicity in AQUAPORIN 3 and 4 in skin and the glymphatic system in the CNS, respectively, leading to increased interstitial fluid clearance during the resting phase (**Figure 4-5**) [309, 370]. Moreover, LN LECs displayed rhythmicity in protein expression, with differences between anatomical sub-regions (**Figure 4-5**). This might be relevant as self- and peripheral-tolerance induction includes site-specificity within the LN. The fact that dermal DCs were more efficient in following an external source of CCL21 during crawl-out assays supports the hypothesis of rhythmic CCL21 chemotaxis to be essential during steady state (**Figure 4-11**). Since ears used for the crawl-out assay were not inflamed and splitting of the ears without an external CCL21 source only led to an emigration of around 22% and 15% for ZT7 and ZT19, respectively, CCL21 seems to be very potent in activating and attracting DCs during the day. The up-regulation of the cognate receptor CCR7 and several activation markers of DCs corroborate the elevated chemotaxis ability of DCs during the day (**Figure 4-11**). Notably, results from the flow-cytometric profiling require repetition as all rhythmic markers provide the exact same peaks in expression.

Although more experiments are necessary to fully clarify the role of steady-state rhythms in chemokine micro-patterning and DC migration in the skin, results in this thesis point towards rhythms in steady-state functions of LECs.

5.4 Chrono-pharmacological targeting of lymphatic leukocyte trafficking

In this study, circadian DC trafficking was abrogated by time-of-day-dependent administration of neutralization antibodies against LYVE-1, CD99, JAM-A, JAM-C and CCL21 (**Figure 4-13** and **Figure 4-14**). These effects link the oscillation of target molecules in LECs with the peak in migration capacity at ZT7. Literature showing time-of-day neutralization of leukocyte trafficking is very limited. He and colleagues for example could reduce leukocyte trafficking by timed administration of blocking antibodies [56].

LYVE-1 is involved in early adhesion of DCs onto lymphatics by binding surface HA. Although literature is scarce concerning manipulation of LYVE-1-mediated migration, Johnson and colleagues could reduce trafficking of DCs by blocking or genetically ablating LYVE-1. Employing adoptive transfer assays as well as FITC painting and crawl-out assays, they highlighted the involvement of LYVE-1 in DC migration across lymphatics [209]. Here, and in line with the presented peak in expression at ZT7, LYVE-1-mediated trafficking could only be reduced during the day (**Figure 4-5** and **Figure 4-14**). Another proof-of-concept might be found in CD44-mediated trafficking of leukocytes, since CD44 is the homologue of LYVE-1 and also binds HA [371]. CD44 supports the rolling and firm adhesion of various leukocytes [371-373] and has been implied as regulator of trans-endothelial migration and chemotaxis [142] by use of neutralization antibodies. Further studies on LYVE-1 might reveal a more defined role especially in the context of molecular clock regulation.

CD99 and CD31 are mediators of leukocyte transmigration across lymphatic endothelial barriers. Blockade of CD99 or CD31 markedly reduced trafficking, with CD99 blockade showing highest reduction at ZT7, and CD31 blockade reducing DC trafficking at both ZT7 and ZT19 (**Figure 4-14**). CD99 has been implicated in lymphatic transmigration of human DCs. Torzicky *et al.* could quantify the expression of CD99 on cultured human LECs and skin LECs and could impair reverse transmigration of monocyte-derived DCs *in vitro* and *in situ* by manipulating CD99 [218]. It is currently discussed, whether CD31 acts ahead of CD99, with CD99 being higher expressed on the intra-luminal side of LECs, whereas CD31 is found rather on the extra-luminal side of the cellular junctions [374, 375], similar to what has been described for BECs [376]. Nevertheless, more research is required on CD99 and its role in lymphatic trafficking. This evokes the question, to what degree transmigration of DCs in dermal LVs might be influenced by time. Blocking data shown here indicate control of CD99 but not CD31, as CD31 was neither rhythmically expressed, nor did its neutralization show time-of-day dependent effects. The study of Torzicky *et al.* revealed comparable results for CD31 blockade, consequently showing that both CD31 and CD99 are required for DC trafficking into LVs [218]. Notably, here the effect of CD31 blockage is unexpectedly strong, hence further experiments are required for validation.

Two other molecules involved in the transmigration of leukocytes are the tight junctional adhesion molecules JAM-A and JAM-C. Block of each reduced DC trafficking across dermal LVs especially at ZT7, with JAM-A showing a stronger effect (**Figure 4-14**). JAM-A is expressed on multiple leukocytes, including DCs, whereas in mice, JAM-C – with respect to leukocyte migration – is restricted to endothelial and stromal cells [377-380]. So far, JAM-A has received relatively little attention in terms of involvement in the lymphatic transmigration process.

JAM-A can either engage in homotypic *cis* interactions, regulating the tight junctional stabilization or simultaneously perform *trans* interactions, allowing the modulation of tight junctions to support leukocyte migration as shown in BVs [21]. In the only published study to date, endothelial specific deletion of JAM-A did not result in significant impairment in DC trafficking *in vivo*. On the contrary, cultured JAM-A^{-/-} DCs displayed increased transmigration through JAM-A^{+/+} LEC monolayers *in vitro* and an elevated migration capacity *in vivo* when adoptively transferred into WT mice under inflammatory conditions [221]. The results obtained here seem contradictory. However, both studies used different models of leukocyte trafficking in addition to steady state and inflammation. Thus, comparability of both studies is compromised and requires further experiments. It is known that lymphatics alter their transcriptional landscape during inflammation and consequently, a bipartite system could be possible, since in BVs antibody-mediated neutralization of JAM-A led to a significant reduction in neutrophil transmigration *in-vitro* under inflammatory conditions [381]. Notably, it is possible that the culture of JAM-A^{-/-} DCs caused compensatory mechanisms as they will lose their clock synchrony that could change their migration in an unexpected manner.

JAM-C interacts with JAM-B and can simultaneously bind the integrin $\alpha_M\beta_2$ [382]. Neutralization of JAM-C leads to reduced JAM-B binding and subsequent redistribution of JAM-C on the endothelial surface [383]. Lamagna and colleagues neutralized JAM-C and subsequently observed an increase in adhesion of neutrophils and monocytes on BECs. In a more recent study by Ballet *et al.*, neutralization of JAM-C increased trafficking of leukocytes including dermal DCs, monocyte-derived DCs as well as neutrophils in an infection model of *Leishmania major*. The effect of blockade here contradicts the results of the previously mentioned study. Although experiments in this thesis were performed under almost steady-state conditions, a repetition of JAM-C and JAM-A blockade should lead to clarification if blockade of respective molecules is different under steady-state compared to inflammatory conditions. For this purpose a repetition with the same conditions together with a repetition under inflammatory condition is necessary since JAMs could be pro-migratory in steady-state but inhibitory in inflammation.

In all neutralization experiments, including various modes of CCL21 blockade, trafficking could not be reduced below a certain baseline. Remarkably, no neutralization (except for the CCR7^{-/-} BMDC and CD31 neutralization experiment) alone could completely abrogate DC trafficking (**Figure 4-13** and **Figure 4-14**). This might be due to pro-migratory factors compensating for the loss of a single factor. Hence, a multi-blockade approach might be necessary, if other molecules compensate the “loss of functionality” of one molecule. One hint that supports this hypothesis is the KO of CD99, as the DC trafficking was only partly ablated. It is likely that

CD31 alone meets the requirements to facilitate successful transmigration. On the other hand, loss of CCR7 completely abolished BMDC trafficking, possibly owing to an inability of cells to detect the CCL21 gradient within the tissue.

Many other interesting targets were not screened in this study, but might be a subject in the future, such as ACKR4 (important in embryonic development of lymphatics and expressed on LECs [214]) or REELIN, which was recently shown to be of importance in CNS leukocyte trafficking during autoimmune encephalomyelitis [49] and was strongly and rhythmically expressed in dermal LECs in this study (**Figure 4-7**). One of the pitfalls of pharmacological intervention via antibodies is the missing guarantee for complete neutralization of antigenicity, which might explain the different results obtained between loss of CCR7 and CCL21 blockade. Of note, although endotoxin levels of commercially available antibodies are advertised as being low, small traces of sodium azide or endotoxins are sufficient to damage the sensitive dermis. Moreover, a FC-block during a crawl-in assay should be performed, as FC-receptors on both LECs and DCs could also oscillate throughout the day and might thus additionally influence the neutralization experiments.

Nonetheless, neutralization of oscillatory proteins validates the concept of time-of-day dependent administration of antibodies for chrono-therapeutic targeting of diseases. As of the end of 2019, 79 therapeutic monoclonal antibodies have been approved by the United States Food and Drug Administration (US FDA) for treating various human diseases [384]. By targeting proteins such as $\alpha 4\beta 7$ integrin, P-selectin, CCR4, IL-5 or IL-17 α essential arms of the immune system are blocked to treat diseases [384]. Financially (estimated market value of monoclonal antibodies is about to be 300 billion in 2025 [384]) and from the perspective of therapy, this market is very important for research and development, which is why its optimization is of greatest interest. One relatively easy and cost-saving method is to investigate the timed administration of antibodies and other drugs. Chronotherapy has long been acknowledged in treatment of diseases, yet it remains relatively scarce in clinical trials. Theophylline was one of the first drugs for which circadian variation in pharmacokinetic parameters was proven and since then, many studies have supported the chronotherapy of medicines such as statins, antihypertensive agents and proton pump inhibitors [385]. Despite evidence received in vaccination studies (see **2.5.4**) timed administration of antibodies or antigens is not commonly pursued and this study should add valuable insight into avenues for the timed dosing of anti-migration interventions with respect to vaccinations and chronotherapy of lymphatic diseases.

5.5 Do cell type-specific intrinsic clocks govern rhythmic dermal leukocyte trafficking?

Tissue-specific genetic ablation of *Bmal1* in either LECs or DCs was sufficient to ablate oscillations in DC migration and cellularity (**Figure 4-15** and **Figure 4-17**). Moreover, loss of *Bmal1* perturbed oscillations of pro-migratory trafficking molecules (**Figure 4-16**). The protein screen indicated that the daily rhythms in migration were driven (at least in part) by the LEC clock. Molecules such as dermal CCL21 were starkly decreased in their expression at ZT7 in LEC specific *Bmal1*^{-/-} mice, which points at a possible direct regulation. This effect was also reported for BECs using the model of *Cdh5cre-Bmal1*^{fl/fl}, in which ICAM-1 levels were significantly reduced in liver BECs [56]. Knocking out other components of the clock such as *Per2* or *Nr1d1/Nr1d2*, could further shine light on which pro-migratory factor is regulated by which clock protein in LECs. For this purpose, a mouse harboring floxed *Nr1d1* and *Nr1d2* loci would be beneficial, which was recently generated for metabolic research by Dierickx and colleagues [386]. Another faster method would be ChIP-sequencing to survey regulatory sites for molecular clock components. The list of binding motifs provided in **Table 5-1** and appendix **7.3** also offers possible sites for the introduction of targeted mutations, which could lead to a down-regulation of respective proteins and thus create a strong mechanistic link between immune cell clocks and rhythms in protein expression. Collectively, these experiments could give compelling evidence of molecular clock regulation.

Skin circadian clocks have already been implicated as regulators of immune cellularity, as described in human epidermal stem cells [387]. Here, flow-cytometric analysis of ears revealed a diurnal rhythm in ear cellularity (**Figure 4-9**). In addition, time-of-day dependent proliferation of CD11c⁺ cells using KI67 as marker could be shown. Although this is an interesting first indication of rhythmic dermal cellularity, further experiments are required to validate time-of-day dependent proliferation. Intra-cellular flow-cytometric analysis of KI67 together with another model such as 5-ethynyl-2'-deoxyuridine (EdU) or bromodeoxyuridine (BrdU) staining could give further insights into the proliferative state of immune cells. Of note, EdU would be favored as its incorporation is not influenced by steric hindrance of double-stranded DNA [388]. This association of dermal clock genes and cell cycle was already shown early on in 2001 [389]. Other cells such as keratinocytes in the epidermis were also indicated to be rhythmic (circadian rhythms in the G2-M phase of the cell cycle) [311], and thus, a complete 24h overview of immune cell demographics in the skin would be of high interest.

For the DC intrinsic clock, data presented using *Clec9acre-Bmal1*^{-/-} mice can only give limited conclusion about its functional role in migration (**Figure 4-15**). All trafficking assays used in this

study do not allow assumptions to what degree the DC clock influences the observed phenotypes. The screening of activation markers and receptors involved in trafficking as well as the DC-specific KO indicates that the DC clock might be involved. However, for a more profound understanding, further experiments are required. BMDC synchronization might be a possible experiment to regard the influence of the DC intrinsic clock on the phenotype observed during crawl-in assays [331]. Secondly, further *in-vitro* chemotaxis assays using sorted DCs from phase-shifted mice could identify chemotaxis abilities of different DCs. Use of other cell type-specific *Bmal1* KOs would also be important, such as *Langerin*-Cre or *CD11c*-Cre mice. Although *Cd11c*-Cre mice will also affect macrophages and monocytes, it will cover all DCs. In the literature, a molecular link between leukocyte specific clocks and migratory behavior and immune function could be shown in BMDCs, (*Cd11c*-Cre [296]) T cells (*Cd4*-Cre [279, 291] and *Lck*-Cre [291]), B cells (*Cd19*-Cre [56, 291] and *Mb1*-Cre [279]), macrophages/monocytes and neutrophils (*Lyz2*-Cre / *LysM*-Cre [56, 276, 288, 390] and hMRP8-Cre [299]) and site-specific immune cells, such as microglia in the CNS (*Cd11b*-Cre [391]) or club cells in the lung (*Ccsp*-iCre [292]). Yet, the study by Hopwood and colleagues does not address the migration of DCs, and thus, the molecular link between the circadian clock and DCs, especially dermal DCs, remains elusive [296]. Nevertheless, given the long list of cell-specific effects of *Bmal1* in leukocytes, a direct link between immune function and migratory capacity in dermal DCs can be assumed and should be the subject to future investigations.

5.6 Outlook

WIn this study, it was shown that LECs governed rhythmic DC trafficking into lymphatic capillaries. Future experiments (**Figure 5-1**) should dissect how the molecular clock of LECs regulates respective pro-migratory components, since a direct molecular link was not established in this study. For this purpose, ChIP sequencing might be a perfect candidate to understand which pro-migratory genes harbor regulatory elements of clock genes (**Table 5-1** and appendix **7.3**). Moreover, other KO models of various clock genes can further specify which transcription factor is modulating the expression of pro-migratory factors. A special focus should lie on CCL21, as it is by far the most promising candidate to regulate lymphatic leukocyte trafficking.

Further studies are required to understand the link between the circadian clock and DCs on a cell type-specific level. Using synchronized BMDCs (for example by horse serum shock) in exogenous crawl-in assays will give an estimate to what degree the DC clock influences the observed phenotype. To further differentiate the differences between dermal DCs, other cell type-specific *Bmal1* KO mice are necessary. A combination of *Cd11c* (targeting all DCs), *Langerin* (to target LCs only) and possibly *Cd103* (only cDC1) mediated CRE expression will allow complete differentiation between LCs, cDC1s and cDC2s. Additionally this could be used to investigate if dermal DCs influence each other in their rhythm in migration, for example by releasing chemokines such as CCL17 [392]. Furthermore, RNA-sequencing of genetically modified LECs and DCs is required to understand the impact of loss of the clock on a more global level.

As already alluded in the introduction, microbiota and the nervous system heavily influence circadian rhythms, as they are entrainment factors [340]. Consequently, the observed phenotype might be altered during loss of microbial or neuronal influence.

To analyze the involvement of the autonomic nervous system, various methodologies can be employed. SCGx (see 3.2.2.3) or adrenoceptor KO mice could be used to gather a first glimpse into the impact of loss of neuronal influence onto the clock of LECs.

Recently rhythms in the microbiota and the closely related topic of intestinal microbiota tolerance were receiving more attention. For example, restricted feeding influences the intestinal microbiome-epithelial-immune homeostasis in the intestine [393]. To investigate the role of the microbiota in the skin on circadian leukocyte trafficking, *Myd88*^{-/-} or germ-free mice together with mice treated with antibiotics (erasing the microbiota of the skin) could be utilized. Early experiments performed by me and my colleague Chien-Sin Chen (LMU, Munich) of ear cellularity and crawl-out assays showed ablated or inverse rhythmic immune cell cellularity in *Myd88*^{-/-} mice (see appendix **Figure 7-3**). Likewise, local sympathetic tone in SCGx mice perturbed time-of-day dependent differences in ear cellularity (see appendix **Figure 7-3**). Other cells like T cells and neutrophils might be an interesting target, as they also migrate through LVs. For this purpose, single-cell RNA-sequencing of the whole leukocyte populations could be employed to gain a complete overview of the immune cell landscape in the skin. Additionally, quantitative immunofluorescence of respective cell types and crawl-in assays can be performed to possibly reveal other rhythms in leukocyte trafficking.

This study opens up potential future projects regarding dermal leukocyte trafficking, dermal immunity and vaccination studies. These and other ideas are again summarized in **Figure 5-1**.

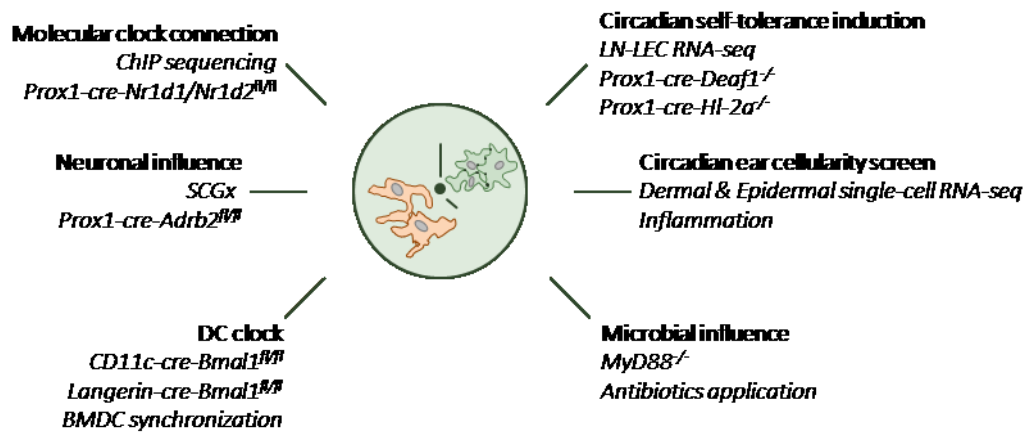


Figure 5-1: Future directions and arising projects

Many possible experiments and projects can arise from this thesis. By investigating the molecular clock connection, neuronal and microbial influence on the dermis, dendritic cell (DC) clock involvement on trafficking as well as a general cellularity screen and self-tolerance induction, a more profound understanding of how circadian clocks influence the immune system of the skin and its draining lymph nodes (LN) can be gained. LEC = lymphatic endothelial cell, ChIP = chromatin immunoprecipitation, SCGx = superior cervical ganglionectomy, BMDC = bone marrow-derived DC.

5.7 Conclusion

Migration of DCs through LVs is an integral part of immune responses, induction of self-tolerance, as well as inflammatory processes. By employing *ex-vivo* trafficking assays using split ear halves and spinning disk confocal microscopy, I showed that migration of dermal DCs into LVs is time-of-day dependent, experiencing a peak during the day and a trough at night. This oscillation was facilitated by temporal up-regulation of trafficking factors in dermal LECs, such as LYVE-1, CCL21 and CD99. In addition, rhythmic micro-patterning of CCL21 heavily contributed to time-of-day differences in DC migration, with a more pronounced CCL21 gradient found in close proximity to lymphatic capillaries during the day. Dermal DCs could follow this gradient better during the day as they transiently up-regulated the cognate receptor (CCR7), along with a subset of activation markers.

Pharmacological neutralization of the rhythmic CCL21 gradient or the oscillatory proteins such as LYVE-1 and CD99 abrogated time-of-day dependent trafficking only during the day. The circadian migration of DCs as well as the up-regulation of trafficking factors might be under the control of the circadian clock, since tissue-specific genetic ablation of the core clock component *Bmal1* led to a reduction in trafficking and loss of rhythms in pro-migratory factors. The results are summarized in a graphical abstract shown in **Figure 5-2**.

This study reveals a novel understanding of lymphatic trafficking, as the molecular clock comes into play as a new regulator. This study underlines the importance of circadian rhythm in regulating immunity. Moreover, results point to the importance of maintaining healthy biological rhythms to regulate immune tolerance. This regulation could be used for future experiments dissecting the timing of self- and peripheral-tolerance induction, vaccination, cancer metastasis and metabolic disorders that are influenced by the lymphatic system.

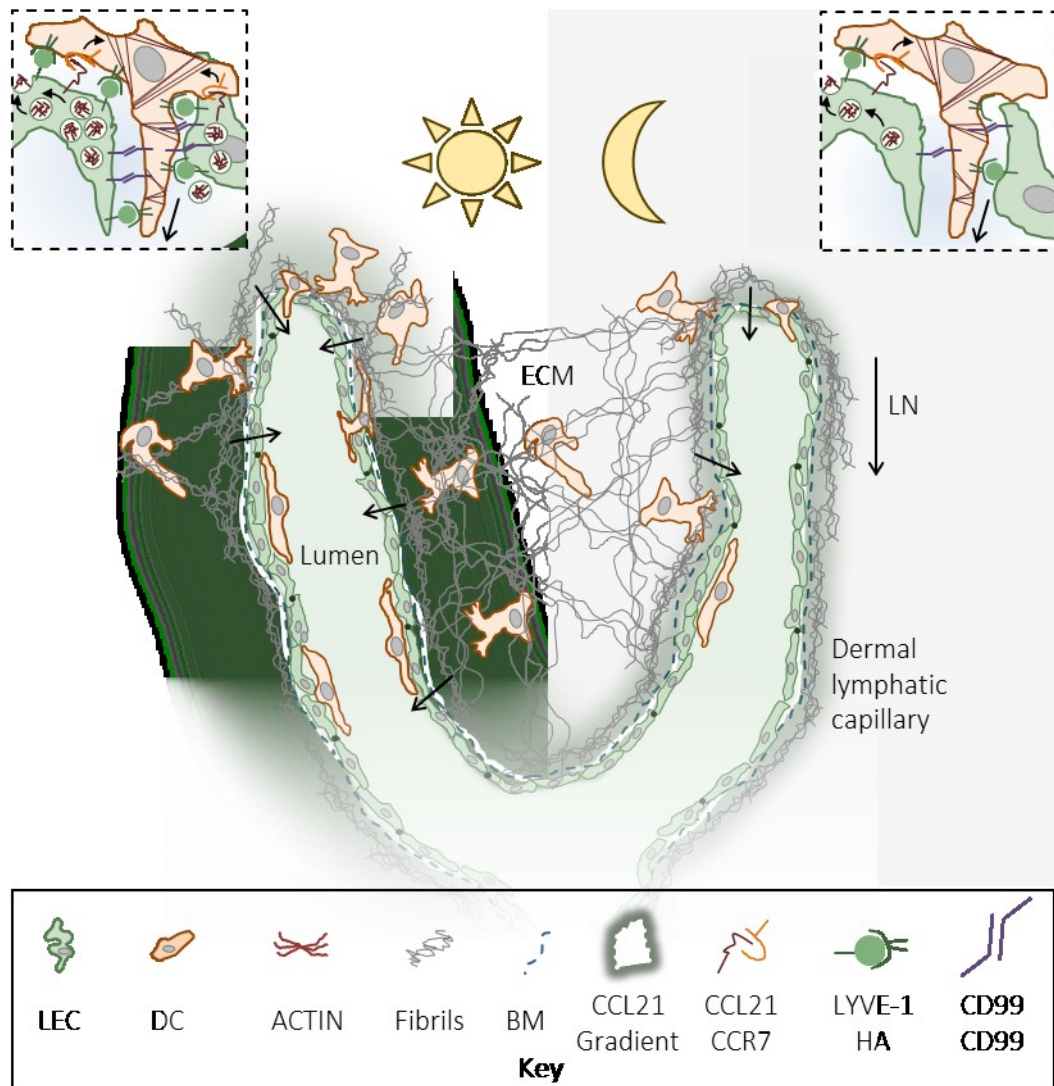


Figure 5-2: Time-of-day dependent trafficking of leukocytes across lymphatics

During the day, more dermal DCs migrate into the lymphatic vessels (LVs) due to a stronger extracellular CCL21 gradient and up-regulation of trafficking factors such as LYVE-1, CCR7, CD99 and intracellular / surface CCL21 in both lymphatic endothelial cells (LECs) and dendritic cells (DCs). Collectively, this allows for higher motility, interstitial migration, adhesion and transmigration of DCs into LVs.

At night, these factors are downregulated and a lower migratory state is induced. Consequently, less DCs are found within the lymphatic capillaries since interstitial migration, adhesion and transmigration are reduced. ECM = extracellular matrix, BM = basal membrane, LN = lymph node.

6 Bibliography

1. Paul, W.E., *Fundamental Immunology*, ed. W.L. Lippincott, W. Vol. 7. 2012.
2. Puntì, J., *Immunology*. Macmillan Education, 2019. **8**.
3. Abbas, A., K., *Cellular and molecular immunology*. Elsevier, 20018. **9**: p. 565.
4. Lynskey, N.N., et al., *Rapid Lymphatic Dissemination of Encapsulated Group A Streptococci via Lymphatic Vessel Endothelial Receptor-1 Interaction*. PLoS Pathog, 2015. **11**(9): p. e1005137.
5. Hunter, M.C., A. Teijeira, and C. Halin, *T Cell Trafficking through Lymphatic Vessels*. Front Immunol, 2016. **7**: p. 613.
6. Loukas, M., et al., *The lymphatic system: a historical perspective*. Clin Anat, 2011. **24**(7): p. 807-16.
7. Ambrose, C.T., *Immunology's first priority dispute--an account of the 17th-century Rudbeck-Bartholin feud*. Cell Immunol, 2006. **242**(1): p. 1-8.
8. Rubin, C.E., *O Nova exercitatio anatomica exhibens ductus hepaticos aquosos et vasa glandularum serosa, nune primum inventa, aeneifque figuris delineata*. Arosiae. [Västerås]: Eucharius Lauringer, 1653.
9. Schmid-Schonbein, G.W., *Microlymphatics and lymph flow*. Physiol Rev, 1990. **70**(4): p. 987-1028.
10. Webb, R.L., *Observations on the propulsion of lymph through the mesenteric lymphatic vessels of the living rat*. Anat Rec, 1933. **57**: p. 345–350.
11. Zawieja, D.C., von der Weid P. Y., Gashev A. A., *Microlymphatic Biology In: Handbook of Physiology: Microcirculation, edited by Tuma RF, Duran WN, and Ley K. San Diego, CA. Academic Press - Elsevier, 2008: p. 125–158.*
12. Choi, I., et al., *Visualization of lymphatic vessels by Prox1-promoter directed GFP reporter in a bacterial artificial chromosome-based transgenic mouse*. Blood, 2011. **117**(1): p. 362-5.
13. Fuller, K.M. and R.R. Munro, *Lymphatic Drainage of Bone Marrow*. Aust N Z J Surg, 1964. **34**: p. 11-4.
14. Baluk, P., et al., *Pathogenesis of persistent lymphatic vessel hyperplasia in chronic airway inflammation*. J Clin Invest, 2005. **115**(2): p. 247-57.
15. Cursiefen, C., et al., *Time course of angiogenesis and lymphangiogenesis after brief corneal inflammation*. Cornea, 2006. **25**(4): p. 443-7.
16. Aspelund, A., et al., *A dural lymphatic vascular system that drains brain interstitial fluid and macromolecules*. J Exp Med, 2015. **212**(7): p. 991-9.
17. Hammersen F, a.H.E., *On the fine structure of lymphatic capillaries In: The Initial Lymphatics, edited by Bollinger A, Partsch H, and Wolfe JHN. Georg Thieme Verlag, 1985.*
18. Lynch, P.M., F.A. Delano, and G.W. Schmid-Schonbein, *The primary valves in the initial lymphatics during inflammation*. Lymphat Res Biol, 2007. **5**(1): p. 3-10.
19. Mendoza, E. and G.W. Schmid-Schonbein, *A model for mechanics of primary lymphatic valves*. J Biomech Eng, 2003. **125**(3): p. 407-14.
20. Kriehuber, E., et al., *Isolation and characterization of dermal lymphatic and blood endothelial cells reveal stable and functionally specialized cell lineages*. J Exp Med, 2001. **194**(6): p. 797-808.
21. Baluk, P., et al., *Functionally specialized junctions between endothelial cells of lymphatic vessels*. J Exp Med, 2007. **204**(10): p. 2349-62.
22. Pflücke, H. and M. Sixt, *Preformed portals facilitate dendritic cell entry into afferent lymphatic vessels*. J Exp Med, 2009. **206**(13): p. 2925-35.

23. Kurtz, K.H., et al., *Rho kinase enhances contractions of rat mesenteric collecting lymphatics*. PLoS One, 2014. **9**(4): p. e94082.
24. Yao, L.C., et al., *Plasticity of button-like junctions in the endothelium of airway lymphatics in development and inflammation*. Am J Pathol, 2012. **180**(6): p. 2561-75.
25. Cliff, W.J. and P.A. Nicoll, *Structure and function of lymphatic vessels of the bat's wing*. Q J Exp Physiol Cogn Med Sci, 1970. **55**(2): p. 112-31.
26. Mazzoni, M.C., T.C. Skalak, and G.W. Schmid-Schonbein, *Structure of lymphatic valves in the spinotrapezius muscle of the rat*. Blood Vessels, 1987. **24**(6): p. 304-12.
27. Mislin, H., [*Experimental detection of autochthonous automatism of lymph vessels*]. Experientia, 1961. **17**: p. 29-30.
28. H., Z., *Morphology and Physiology of Lymphatic Endothelial Cells In: Microvasculature Research: Biology and Pathology*, edited by Shepro D, and D'Amore PA. Elsevier Academic Press, 2006: p. 535–544.
29. Moore, J.E., Jr. and C.D. Bertram, *Lymphatic System Flows*. Annu Rev Fluid Mech, 2018. **50**: p. 459-482.
30. Yoffey, J.M., and Courtice, F.C., *Lymphatics, Lymph and the Lymphomyeloid Complex*. London: Academic Press, 1970.
31. Riquet, M., et al., *Thoracic duct tributaries from intrathoracic organs*. Ann Thorac Surg, 2002. **73**(3): p. 892-8; discussion 898-9.
32. Adair, T.H. and A.C. Guyton, *Modification of lymph by lymph nodes. II. Effect of increased lymph node venous blood pressure*. Am J Physiol, 1983. **245**(4): p. H616-22.
33. Knox, P. and J.J. Pflug, *The effect of the canine popliteal node on the composition of lymph*. J Physiol, 1983. **345**: p. 1-14.
34. Srinivasan, R.S., et al., *Lineage tracing demonstrates the venous origin of the mammalian lymphatic vasculature*. Genes Dev, 2007. **21**(19): p. 2422-32.
35. Wigle, J.T. and G. Oliver, *Prox1 function is required for the development of the murine lymphatic system*. Cell, 1999. **98**(6): p. 769-78.
36. Wigle, J.T., et al., *An essential role for Prox1 in the induction of the lymphatic endothelial cell phenotype*. EMBO J, 2002. **21**(7): p. 1505-13.
37. Jussila, L., et al., *Lymphatic endothelium and Kaposi's sarcoma spindle cells detected by antibodies against the vascular endothelial growth factor receptor-3*. Cancer Res, 1998. **58**(8): p. 1599-604.
38. Pajusola, K., et al., *Signalling properties of FLT4, a proteolytically processed receptor tyrosine kinase related to two VEGF receptors*. Oncogene, 1994. **9**(12): p. 3545-55.
39. Jeltsch, M., et al., *Hyperplasia of lymphatic vessels in VEGF-C transgenic mice*. Science, 1997. **276**(5317): p. 1423-5.
40. Kaipainen, A., et al., *Expression of the fms-like tyrosine kinase 4 gene becomes restricted to lymphatic endothelium during development*. Proc Natl Acad Sci U S A, 1995. **92**(8): p. 3566-70.
41. Banerji, S., et al., *LYVE-1, a new homologue of the CD44 glycoprotein, is a lymph-specific receptor for hyaluronan*. J Cell Biol, 1999. **144**(4): p. 789-801.
42. Lutter, S., et al., *Smooth muscle-endothelial cell communication activates Reelin signaling and regulates lymphatic vessel formation*. J Cell Biol, 2012. **197**(6): p. 837-49.
43. Wang, X.N., et al., *A three-dimensional atlas of human dermal leukocytes, lymphatics, and blood vessels*. J Invest Dermatol, 2014. **134**(4): p. 965-974.
44. Mouta Carreira, C., et al., *LYVE-1 is not restricted to the lymph vessels: expression in normal liver blood sinusoids and down-regulation in human liver cancer and cirrhosis*. Cancer Res, 2001. **61**(22): p. 8079-84.
45. Breiteneder-Geleff, S., et al., *Podoplanin, novel 43-kd membrane protein of glomerular epithelial cells, is down-regulated in puromycin nephrosis*. Am J Pathol, 1997. **151**(4): p. 1141-52.

46. Breiteneder-Geleff, S., et al., *Angiosarcomas express mixed endothelial phenotypes of blood and lymphatic capillaries: podoplanin as a specific marker for lymphatic endothelium*. *Am J Pathol*, 1999. **154**(2): p. 385-94.
47. Acton, S.E., et al., *Dendritic cells control fibroblastic reticular network tension and lymph node expansion*. *Nature*, 2014. **514**(7523): p. 498-502.
48. Sabine, A., et al., *FOXC2 and fluid shear stress stabilize postnatal lymphatic vasculature*. *J Clin Invest*, 2015. **125**(10): p. 3861-77.
49. Calvier, L., et al., *Reelin depletion protects against autoimmune encephalomyelitis by decreasing vascular adhesion of leukocytes*. *Sci Transl Med*, 2020. **12**(556).
50. Bianchi, R., et al., *A transgenic Prox1-Cre-tdTomato reporter mouse for lymphatic vessel research*. *PLoS One*, 2015. **10**(4): p. e0122976.
51. Hong, M., et al., *Efficient Assessment of Developmental, Surgical and Pathological Lymphangiogenesis Using a Lymphatic Reporter Mouse and Its Embryonic Stem Cells*. *PLoS One*, 2016. **11**(6): p. e0157126.
52. Jang, J.Y., et al., *Conditional ablation of LYVE-1+ cells unveils defensive roles of lymphatic vessels in intestine and lymph nodes*. *Blood*, 2013. **122**(13): p. 2151-61.
53. Onder, L., et al., *A novel bacterial artificial chromosome-transgenic podoplanin-cre mouse targets lymphoid organ stromal cells in vivo*. *Front Immunol*, 2011. **2**: p. 50.
54. Chavkin, N.W. and K.K. Hirschi, *Single Cell Analysis in Vascular Biology*. *Front Cardiovasc Med*, 2020. **7**: p. 42.
55. He, L., et al., *Single-cell RNA sequencing of mouse brain and lung vascular and vessel-associated cell types*. *Sci Data*, 2018. **5**: p. 180160.
56. He, W., et al., *Circadian Expression of Migratory Factors Establishes Lineage-Specific Signatures that Guide the Homing of Leukocyte Subsets to Tissues*. *Immunity*, 2018. **49**(6): p. 1175-1190 e7.
57. Jambusaria, A., et al., *Endothelial heterogeneity across distinct vascular beds during homeostasis and inflammation*. *Elife*, 2020. **9**.
58. Takeda, A., et al., *Single-Cell Survey of Human Lymphatics Unveils Marked Endothelial Cell Heterogeneity and Mechanisms of Homing for Neutrophils*. *Immunity*, 2019. **51**(3): p. 561-572 e5.
59. Baluk, P., et al., *Preferential lymphatic growth in bronchus-associated lymphoid tissue in sustained lung inflammation*. *Am J Pathol*, 2014. **184**(5): p. 1577-92.
60. Lauweryns, J.M., *Stereomicroscopic funnel-like architecture of pulmonary lymphatic valves*. *Lymphology*, 1971. **4**(4): p. 125-32.
61. Lauweryns, J.M. and J.H. Baert, *Alveolar clearance and the role of the pulmonary lymphatics*. *Am Rev Respir Dis*, 1977. **115**(4): p. 625-83.
62. Ohtani, O. and Y. Ohtani, *Organization and developmental aspects of lymphatic vessels*. *Arch Histol Cytol*, 2008. **71**(1): p. 1-22.
63. Mori, M., et al., *Increased number and altered phenotype of lymphatic vessels in peripheral lung compartments of patients with COPD*. *Respir Res*, 2013. **14**: p. 65.
64. Willrodt, A.H., et al., *ALCAM Mediates DC Migration Through Afferent Lymphatics and Promotes Allospecific Immune Reactions*. *Front Immunol*, 2019. **10**: p. 759.
65. Pappenheimer, J.R. and C.C. Michel, *Role of villus microcirculation in intestinal absorption of glucose: coupling of epithelial with endothelial transport*. *J Physiol*, 2003. **553**(Pt 2): p. 561-74.
66. Unthank, J.L. and H.G. Bohlen, *Lymphatic pathways and role of valves in lymph propulsion from small intestine*. *Am J Physiol*, 1988. **254**(3 Pt 1): p. G389-98.
67. Bernier-Latmani, J. and T.V. Petrova, *Intestinal lymphatic vasculature: structure, mechanisms and functions*. *Nat Rev Gastroenterol Hepatol*, 2017. **14**(9): p. 510-526.
68. Azzali, G., *Transendothelial transport of lipids in the absorbing lymphatic vessel*. *Experientia*, 1982. **38**(2): p. 275-7.

69. Azzali, G., *The ultrastructural basis of lipid transport in the absorbing lymphatic vessel*. J Submicrosc Cytol, 1982. **14**(1): p. 45-54.
70. Florey, H., *Observations on the contractility of lacteals: Part II*. J Physiol, 1927. **63**(1): p. 1-18.
71. Florey, H., *Observations on the contractility of lacteals: Part I*. J Physiol, 1927. **62**(3): p. 267-72.
72. Schulte-Merker, S., A. Sabine, and T.V. Petrova, *Lymphatic vascular morphogenesis in development, physiology, and disease*. J Cell Biol, 2011. **193**(4): p. 607-18.
73. Norrmen, C., et al., *Liprin (beta)1 is highly expressed in lymphatic vasculature and is important for lymphatic vessel integrity*. Blood, 2010. **115**(4): p. 906-9.
74. Cerovic, V., et al., *Intestinal CD103(-) dendritic cells migrate in lymph and prime effector T cells*. Mucosal Immunol, 2013. **6**(1): p. 104-13.
75. Worbs, T., et al., *Oral tolerance originates in the intestinal immune system and relies on antigen carriage by dendritic cells*. J Exp Med, 2006. **203**(3): p. 519-27.
76. Mackley, E.C., et al., *CCR7-dependent trafficking of RORgamma(+) ILCs creates a unique microenvironment within mucosal draining lymph nodes*. Nat Commun, 2015. **6**: p. 5862.
77. Jalkanen, S. and M. Salmi, *Lymphatic endothelial cells of the lymph node*. Nat Rev Immunol, 2020.
78. Gray, E.E. and J.G. Cyster, *Lymph node macrophages*. J Innate Immun, 2012. **4**(5-6): p. 424-36.
79. Grigorova, I.L., M. Panteleev, and J.G. Cyster, *Lymph node cortical sinus organization and relationship to lymphocyte egress dynamics and antigen exposure*. Proc Natl Acad Sci U S A, 2010. **107**(47): p. 20447-52.
80. Li, W., R.N. Germain, and M.Y. Gerner, *Multiplex, quantitative cellular analysis in large tissue volumes with clearing-enhanced 3D microscopy (Ce3D)*. Proc Natl Acad Sci U S A, 2017. **114**(35): p. E7321-E7330.
81. Cyster, J.G. and S.R. Schwab, *Sphingosine-1-phosphate and lymphocyte egress from lymphoid organs*. Annu Rev Immunol, 2012. **30**: p. 69-94.
82. Malhotra, D., et al., *Transcriptional profiling of stroma from inflamed and resting lymph nodes defines immunological hallmarks*. Nat Immunol, 2012. **13**(5): p. 499-510.
83. Berendam, S.J., et al., *Comparative Transcriptomic Analysis Identifies a Range of Immunologically Related Functional Elaborations of Lymph Node Associated Lymphatic and Blood Endothelial Cells*. Front Immunol, 2019. **10**: p. 816.
84. Scudamore, C.L., *A practical guide to the histology of the mouse*. Vol. 1. 2014: Wiley.
85. Ross, A.A., A. Rodrigues Hoffmann, and J.D. Neufeld, *The skin microbiome of vertebrates*. Microbiome, 2019. **7**(1): p. 79.
86. Oh, J., et al., *Temporal Stability of the Human Skin Microbiome*. Cell, 2016. **165**(4): p. 854-66.
87. Nakatsuji, T., et al., *Antimicrobials from human skin commensal bacteria protect against Staphylococcus aureus and are deficient in atopic dermatitis*. Sci Transl Med, 2017. **9**(378).
88. Zipperer, A., et al., *Human commensals producing a novel antibiotic impair pathogen colonization*. Nature, 2016. **535**(7613): p. 511-6.
89. Wanke, I., et al., *Skin commensals amplify the innate immune response to pathogens by activation of distinct signaling pathways*. J Invest Dermatol, 2011. **131**(2): p. 382-90.
90. Schade, H.a.M.A., *Der Säuremantel der Haut (nach Gaskettenmessungen; in German)*. Klin. Wochenschr., 1928. **7**(12).
91. Ali, S.M. and G. Yosipovitch, *Skin pH: from basic science to basic skin care*. Acta Derm Venereol, 2013. **93**(3): p. 261-7.

92. Basler, K. and J.M. Brandner, *Tight junctions in skin inflammation*. Pflugers Arch, 2017. **469**(1): p. 3-14.
93. Egawa, G. and K. Kabashima, *Multifactorial skin barrier deficiency and atopic dermatitis: Essential topics to prevent the atopic march*. J Allergy Clin Immunol, 2016. **138**(2): p. 350-358 e1.
94. Eyerich, S., et al., *Cutaneous Barriers and Skin Immunity: Differentiating A Connected Network*. Trends Immunol, 2018. **39**(4): p. 315-327.
95. Merad, M., F. Ginhoux, and M. Collin, *Origin, homeostasis and function of Langerhans cells and other langerin-expressing dendritic cells*. Nat Rev Immunol, 2008. **8**(12): p. 935-47.
96. Gaiser, M.R., et al., *Cancer-associated epithelial cell adhesion molecule (EpCAM; CD326) enables epidermal Langerhans cell motility and migration in vivo*. Proc Natl Acad Sci U S A, 2012. **109**(15): p. E889-97.
97. Merad, M., et al., *The dendritic cell lineage: ontogeny and function of dendritic cells and their subsets in the steady state and the inflamed setting*. Annu Rev Immunol, 2013. **31**: p. 563-604.
98. Wang, Y., et al., *Nonredundant roles of keratinocyte-derived IL-34 and neutrophil-derived CSF1 in Langerhans cell renewal in the steady state and during inflammation*. Eur J Immunol, 2016. **46**(3): p. 552-9.
99. Fainaru, O., et al., *Runx3 regulates mouse TGF-beta-mediated dendritic cell function and its absence results in airway inflammation*. EMBO J, 2004. **23**(4): p. 969-79.
100. Tang, A., et al., *Adhesion of epidermal Langerhans cells to keratinocytes mediated by E-cadherin*. Nature, 1993. **361**(6407): p. 82-5.
101. Ouwehand, K., et al., *CXCL12 is essential for migration of activated Langerhans cells from epidermis to dermis*. Eur J Immunol, 2008. **38**(11): p. 3050-9.
102. Griffiths, C.E., et al., *Cytokines and Langerhans cell mobilisation in mouse and man*. Cytokine, 2005. **32**(2): p. 67-70.
103. Antonopoulos, C., et al., *Functional caspase-1 is required for Langerhans cell migration and optimal contact sensitization in mice*. J Immunol, 2001. **166**(6): p. 3672-7.
104. Cumberbatch, M., et al., *Interleukin (IL)-18 induces Langerhans cell migration by a tumour necrosis factor-alpha- and IL-1beta-dependent mechanism*. Immunology, 2001. **102**(3): p. 323-30.
105. Eaton, L.H., et al., *Skin sensitization induced Langerhans' cell mobilization: variable requirements for tumour necrosis factor-alpha*. Immunology, 2015. **144**(1): p. 139-48.
106. Salvermoser, J., et al., *Clec9a-Mediated Ablation of Conventional Dendritic Cells Suggests a Lymphoid Path to Generating Dendritic Cells In Vivo*. Front Immunol, 2018. **9**: p. 699.
107. Schraml, B.U., et al., *Genetic tracing via DNDR-1 expression history defines dendritic cells as a hematopoietic lineage*. Cell, 2013. **154**(4): p. 843-58.
108. Tamura, T., et al., *IFN regulatory factor-4 and -8 govern dendritic cell subset development and their functional diversity*. J Immunol, 2005. **174**(5): p. 2573-81.
109. Edelson, B.T., et al., *Peripheral CD103+ dendritic cells form a unified subset developmentally related to CD8alpha+ conventional dendritic cells*. J Exp Med, 2010. **207**(4): p. 823-36.
110. Henri, S., et al., *CD207+ CD103+ dermal dendritic cells cross-present keratinocyte-derived antigens irrespective of the presence of Langerhans cells*. J Exp Med, 2010. **207**(1): p. 189-206.
111. Rizzitelli, A., et al., *The proliferative response of CD4 T cells to steady-state CD8+ dendritic cells is restricted by post-activation death*. Int Immunol, 2006. **18**(3): p. 415-23.

112. Cruz, F.M., et al., *The Biology and Underlying Mechanisms of Cross-Presentation of Exogenous Antigens on MHC-I Molecules*. Annu Rev Immunol, 2017. **35**: p. 149-176.
113. Allan, R.S., et al., *Epidermal viral immunity induced by CD8alpha+ dendritic cells but not by Langerhans cells*. Science, 2003. **301**(5641): p. 1925-8.
114. Bedoui, S., et al., *Cross-presentation of viral and self antigens by skin-derived CD103+ dendritic cells*. Nat Immunol, 2009. **10**(5): p. 488-95.
115. Belz, G.T., et al., *CD8alpha+ dendritic cells selectively present MHC class I-restricted noncytolytic viral and intracellular bacterial antigens in vivo*. J Immunol, 2005. **175**(1): p. 196-200.
116. Smith, C.M., et al., *Cutting edge: conventional CD8 alpha+ dendritic cells are preferentially involved in CTL priming after footpad infection with herpes simplex virus-1*. J Immunol, 2003. **170**(9): p. 4437-40.
117. Dorner, B.G., et al., *Selective expression of the chemokine receptor XCR1 on cross-presenting dendritic cells determines cooperation with CD8+ T cells*. Immunity, 2009. **31**(5): p. 823-33.
118. Tamoutounour, S., et al., *Origins and functional specialization of macrophages and of conventional and monocyte-derived dendritic cells in mouse skin*. Immunity, 2013. **39**(5): p. 925-38.
119. Haniffa, M., et al., *Human tissues contain CD141hi cross-presenting dendritic cells with functional homology to mouse CD103+ nonlymphoid dendritic cells*. Immunity, 2012. **37**(1): p. 60-73.
120. Gerner, M.Y., et al., *Histo-cytometry: a method for highly multiplex quantitative tissue imaging analysis applied to dendritic cell subset microanatomy in lymph nodes*. Immunity, 2012. **37**(2): p. 364-76.
121. Lubber, C.A., et al., *Quantitative proteomics reveals subset-specific viral recognition in dendritic cells*. Immunity, 2010. **32**(2): p. 279-89.
122. Edwards, A.D., et al., *Toll-like receptor expression in murine DC subsets: lack of TLR7 expression by CD8 alpha+ DC correlates with unresponsiveness to imidazoquinolines*. Eur J Immunol, 2003. **33**(4): p. 827-33.
123. Proietto, A.I., et al., *Differential production of inflammatory chemokines by murine dendritic cell subsets*. Immunobiology, 2004. **209**(1-2): p. 163-72.
124. Dudziak, D., et al., *Differential antigen processing by dendritic cell subsets in vivo*. Science, 2007. **315**(5808): p. 107-11.
125. Tatsumi, N.I., A.; Kumamoto, Y., *Antigen presentation by CD301b+ dermal dendritic cells dictates CD4+ T cell fate*. Journal of Immunology, 2019. **202**(1).
126. Cepek, K.L., et al., *Adhesion between epithelial cells and T lymphocytes mediated by E-cadherin and the alpha E beta 7 integrin*. Nature, 1994. **372**(6502): p. 190-3.
127. Ahrens, S., et al., *F-actin is an evolutionarily conserved damage-associated molecular pattern recognized by DNGR-1, a receptor for dead cells*. Immunity, 2012. **36**(4): p. 635-45.
128. Tan, S.M., et al., *Effect of integrin beta 2 subunit truncations on LFA-1 (CD11a/CD18) and Mac-1 (CD11b/CD18) assembly, surface expression, and function*. J Immunol, 2000. **165**(5): p. 2574-81.
129. Stoitzner, P. and N. Romani, *Langerin, the "Catcher in the Rye": an important receptor for pathogens on Langerhans cells*. Eur J Immunol, 2011. **41**(9): p. 2526-9.
130. Murata, Y., et al., *The CD47-SIRPalpha signalling system: its physiological roles and therapeutic application*. J Biochem, 2014. **155**(6): p. 335-44.
131. Lin, H.H., et al., *F4/80: the macrophage-specific adhesion-GPCR and its role in immunoregulation*. Adv Exp Med Biol, 2010. **706**: p. 149-56.
132. Lee, M., et al., *Tissue-specific Role of CX3CR1 Expressing Immune Cells and Their Relationships with Human Disease*. Immune Netw, 2018. **18**(1): p. e5.

133. Kashem, S.W., M. Haniffa, and D.H. Kaplan, *Antigen-Presenting Cells in the Skin*. *Annu Rev Immunol*, 2017. **35**: p. 469-499.
134. Askew, D. and C.V. Harding, *Antigen processing and CD24 expression determine antigen presentation by splenic CD4+ and CD8+ dendritic cells*. *Immunology*, 2008. **123**(3): p. 447-55.
135. Shrimpton, R.E., et al., *CD205 (DEC-205): a recognition receptor for apoptotic and necrotic self*. *Mol Immunol*, 2009. **46**(6): p. 1229-39.
136. Yu, Y.-H.L.K.-I., *Advances in Immunology*. Chapter Two - Factors That Regulate the Generation of Antibody-Secreting Plasma Cells. Vol. 131. 2016: Elsevier.
137. Jameson, J.M., et al., *A keratinocyte-responsive gamma delta TCR is necessary for dendritic epidermal T cell activation by damaged keratinocytes and maintenance in the epidermis*. *J Immunol*, 2004. **172**(6): p. 3573-9.
138. Adams, E.J., S. Gu, and A.M. Luoma, *Human gamma delta T cells: Evolution and ligand recognition*. *Cell Immunol*, 2015. **296**(1): p. 31-40.
139. MacLeod, A.S., et al., *Dendritic epidermal T cells regulate skin antimicrobial barrier function*. *J Clin Invest*, 2013. **123**(10): p. 4364-74.
140. Cruz, M.S., et al., *Human alphabeta and gammadelta T Cells in Skin Immunity and Disease*. *Front Immunol*, 2018. **9**: p. 1304.
141. Steinert, E.M., et al., *Quantifying Memory CD8 T Cells Reveals Regionalization of Immunosurveillance*. *Cell*, 2015. **161**(4): p. 737-49.
142. Khan, T.N., et al., *Local antigen in nonlymphoid tissue promotes resident memory CD8+ T cell formation during viral infection*. *J Exp Med*, 2016. **213**(6): p. 951-66.
143. Schenkel, J.M., et al., *T cell memory. Resident memory CD8 T cells trigger protective innate and adaptive immune responses*. *Science*, 2014. **346**(6205): p. 98-101.
144. Park, C.O., et al., *Staged development of long-lived T-cell receptor alphabeta TH17 resident memory T-cell population to *Candida albicans* after skin infection*. *J Allergy Clin Immunol*, 2018. **142**(2): p. 647-662.
145. Nestle, F.O., et al., *Skin immune sentinels in health and disease*. *Nat Rev Immunol*, 2009. **9**(10): p. 679-91.
146. Albanesi, C., et al., *Keratinocytes in inflammatory skin diseases*. *Curr Drug Targets Inflamm Allergy*, 2005. **4**(3): p. 329-34.
147. Mohammed, J., et al., *Stromal cells control the epithelial residence of DCs and memory T cells by regulated activation of TGF-beta*. *Nat Immunol*, 2016. **17**(4): p. 414-21.
148. Kobayashi, T., R.R. Ricardo-Gonzalez, and K. Moro, *Skin-Resident Innate Lymphoid Cells - Cutaneous Innate Guardians and Regulators*. *Trends Immunol*, 2020. **41**(2): p. 100-112.
149. Kobayashi, T., et al., *Homeostatic Control of Sebaceous Glands by Innate Lymphoid Cells Regulates Commensal Bacteria Equilibrium*. *Cell*, 2019. **176**(5): p. 982-997 e16.
150. Nagao, K., et al., *Stress-induced production of chemokines by hair follicles regulates the trafficking of dendritic cells in skin*. *Nat Immunol*, 2012. **13**(8): p. 744-52.
151. Liu, Z., et al., *Visualization of T Cell-Regulated Monocyte Clusters Mediating Keratinocyte Death in Acquired Cutaneous Immunity*. *J Invest Dermatol*, 2018. **138**(6): p. 1328-1337.
152. Yanez, D.A., et al., *The role of macrophages in skin homeostasis*. *Pflugers Arch*, 2017. **469**(3-4): p. 455-463.
153. Nguyen, A.V. and A.M. Soulika, *The Dynamics of the Skin's Immune System*. *Int J Mol Sci*, 2019. **20**(8).
154. Theilgaard-Monch, K., et al., *The transcriptional activation program of human neutrophils in skin lesions supports their important role in wound healing*. *J Immunol*, 2004. **172**(12): p. 7684-93.

155. Christoffersson, G., et al., *VEGF-A recruits a proangiogenic MMP-9-delivering neutrophil subset that induces angiogenesis in transplanted hypoxic tissue*. *Blood*, 2012. **120**(23): p. 4653-62.
156. Alitalo, K., *The lymphatic vasculature in disease*. *Nat Med*, 2011. **17**(11): p. 1371-80.
157. Kerjaschki, D., *The lymphatic vasculature revisited*. *J Clin Invest*, 2014. **124**(3): p. 874-7.
158. Forster, R., A. Braun, and T. Worbs, *Lymph node homing of T cells and dendritic cells via afferent lymphatics*. *Trends Immunol*, 2012. **33**(6): p. 271-80.
159. Kubik S, a.M.M., *Anatomy of the lymph capillaries and precollectors of the skin In: The Initial Lymphatics*, ed. P.H. Bollinger A, and Wolfe JHN. 1985, Stuttgart, Germany: Georg Thieme Verlag.
160. Bollinger, A., et al., *Fluorescence microlymphography*. *Circulation*, 1981. **64**(6): p. 1195-200.
161. Makinen, T., et al., *PDZ interaction site in ephrinB2 is required for the remodeling of lymphatic vasculature*. *Genes Dev*, 2005. **19**(3): p. 397-410.
162. Bellman, S. and B. Oden, *Experimental micro-lymphangiography*. *Acta radiol*, 1957. **47**(4): p. 289-307.
163. Schuster, C., et al., *Development of Blood and Lymphatic Endothelial Cells in Embryonic and Fetal Human Skin*. *Am J Pathol*, 2015. **185**(9): p. 2563-74.
164. Hall, J.G. and B. Morris, *The output of cells in lymph from the popliteal node of sheep*. *Q J Exp Physiol Cogn Med Sci*, 1962. **47**: p. 360-9.
165. Sokolowski, J., E. Jakobsen, and J.V. Johannessen, *Cells in peripheral leg lymph of normal men*. *Lymphology*, 1978. **11**(4): p. 202-7.
166. Olszewski, W.L., et al., *Immune cell traffic from blood through the normal human skin to lymphatics*. *Clin Dermatol*, 1995. **13**(5): p. 473-83.
167. Tomura, M., et al., *Activated regulatory T cells are the major T cell type emigrating from the skin during a cutaneous immune response in mice*. *J Clin Invest*, 2010. **120**(3): p. 883-93.
168. Mackay, C.R., W.L. Marston, and L. Dudler, *Naive and memory T cells show distinct pathways of lymphocyte recirculation*. *J Exp Med*, 1990. **171**(3): p. 801-17.
169. Yawalkar, N., et al., *Human afferent lymph from normal skin contains an increased number of mainly memory / effector CD4(+) T cells expressing activation, adhesion and co-stimulatory molecules*. *Eur J Immunol*, 2000. **30**(2): p. 491-7.
170. Ikebuchi, R., et al., *A rare subset of skin-tropic regulatory T cells expressing Il10/Gzmb inhibits the cutaneous immune response*. *Sci Rep*, 2016. **6**: p. 35002.
171. Zhang, N., et al., *Regulatory T cells sequentially migrate from inflamed tissues to draining lymph nodes to suppress the alloimmune response*. *Immunity*, 2009. **30**(3): p. 458-69.
172. Tomura, M., et al., *Tracking and quantification of dendritic cell migration and antigen trafficking between the skin and lymph nodes*. *Sci Rep*, 2014. **4**: p. 6030.
173. Tomura, M., et al., *Monitoring cellular movement in vivo with photoconvertible fluorescence protein "Kaede" transgenic mice*. *Proc Natl Acad Sci U S A*, 2008. **105**(31): p. 10871-6.
174. Abolins, S., et al., *The comparative immunology of wild and laboratory mice, Mus musculus domesticus*. *Nat Commun*, 2017. **8**: p. 14811.
175. Schineis, P., P. Runge, and C. Halin, *Cellular traffic through afferent lymphatic vessels*. *Vascul Pharmacol*, 2019. **112**: p. 31-41.
176. Clark, R.A., et al., *The vast majority of CLA+ T cells are resident in normal skin*. *J Immunol*, 2006. **176**(7): p. 4431-9.
177. Lammermann, T., et al., *Rapid leukocyte migration by integrin-independent flowing and squeezing*. *Nature*, 2008. **453**(7191): p. 51-5.

178. Weber, M., et al., *Interstitial dendritic cell guidance by haptotactic chemokine gradients*. Science, 2013. **339**(6117): p. 328-32.
179. Russo, E., et al., *Intralymphatic CCL21 Promotes Tissue Egress of Dendritic Cells through Afferent Lymphatic Vessels*. Cell Rep, 2016. **14**(7): p. 1723-1734.
180. Dixon, J.B., et al., *Lymph flow, shear stress, and lymphocyte velocity in rat mesenteric prenodal lymphatics*. Microcirculation, 2006. **13**(7): p. 597-610.
181. Dixon, J.B., et al., *Measuring microlymphatic flow using fast video microscopy*. J Biomed Opt, 2005. **10**(6): p. 064016.
182. Renkawitz, J., et al., *Adaptive force transmission in amoeboid cell migration*. Nat Cell Biol, 2009. **11**(12): p. 1438-43.
183. Renkawitz, J., et al., *Nuclear positioning facilitates amoeboid migration along the path of least resistance*. Nature, 2019. **568**(7753): p. 546-550.
184. Lammermann, T. and R.N. Germain, *The multiple faces of leukocyte interstitial migration*. Semin Immunopathol, 2014. **36**(2): p. 227-51.
185. Nitschke, M., et al., *Differential requirement for ROCK in dendritic cell migration within lymphatic capillaries in steady-state and inflammation*. Blood, 2012. **120**(11): p. 2249-58.
186. Sen, D., et al., *Selective and site-specific mobilization of dermal dendritic cells and Langerhans cells by Th1- and Th2-polarizing adjuvants*. Proc Natl Acad Sci U S A, 2010. **107**(18): p. 8334-9.
187. Tal, O., et al., *DC mobilization from the skin requires docking to immobilized CCL21 on lymphatic endothelium and intralymphatic crawling*. J Exp Med, 2011. **208**(10): p. 2141-53.
188. Sallusto, F., et al., *Rapid and coordinated switch in chemokine receptor expression during dendritic cell maturation*. Eur J Immunol, 1998. **28**(9): p. 2760-9.
189. Nakano, H. and M.D. Gunn, *Gene duplications at the chemokine locus on mouse chromosome 4: multiple strain-specific haplotypes and the deletion of secondary lymphoid-organ chemokine and EBI-1 ligand chemokine genes in the plt mutation*. J Immunol, 2001. **166**(1): p. 361-9.
190. Johnson, L.A. and D.G. Jackson, *Inflammation-induced secretion of CCL21 in lymphatic endothelium is a key regulator of integrin-mediated dendritic cell transmigration*. Int Immunol, 2010. **22**(10): p. 839-49.
191. Forster, R., et al., *CCR7 coordinates the primary immune response by establishing functional microenvironments in secondary lymphoid organs*. Cell, 1999. **99**(1): p. 23-33.
192. Ohl, L., et al., *CCR7 governs skin dendritic cell migration under inflammatory and steady-state conditions*. Immunity, 2004. **21**(2): p. 279-88.
193. Saeki, H., et al., *Cutting edge: secondary lymphoid-tissue chemokine (SLC) and CC chemokine receptor 7 (CCR7) participate in the emigration pathway of mature dendritic cells from the skin to regional lymph nodes*. J Immunol, 1999. **162**(5): p. 2472-5.
194. Bao, X., et al., *Endothelial heparan sulfate controls chemokine presentation in recruitment of lymphocytes and dendritic cells to lymph nodes*. Immunity, 2010. **33**(5): p. 817-29.
195. de Paz, J.L., et al., *Profiling heparin-chemokine interactions using synthetic tools*. ACS Chem Biol, 2007. **2**(11): p. 735-44.
196. Benvenuti, F., et al., *Requirement of Rac1 and Rac2 expression by mature dendritic cells for T cell priming*. Science, 2004. **305**(5687): p. 1150-3.
197. Luther, S.A., et al., *Coexpression of the chemokines ELC and SLC by T zone stromal cells and deletion of the ELC gene in the plt/plt mouse*. Proc Natl Acad Sci U S A, 2000. **97**(23): p. 12694-9.

198. Vassileva, G., et al., *The reduced expression of 6Ckine in the plt mouse results from the deletion of one of two 6Ckine genes*. J Exp Med, 1999. **190**(8): p. 1183-8.
199. Vaahtomeri, K., et al., *Locally Triggered Release of the Chemokine CCL21 Promotes Dendritic Cell Transmigration across Lymphatic Endothelia*. Cell Rep, 2017. **19**(5): p. 902-909.
200. Schumann, K., et al., *Immobilized chemokine fields and soluble chemokine gradients cooperatively shape migration patterns of dendritic cells*. Immunity, 2010. **32**(5): p. 703-13.
201. Britschgi, M.R., S. Favre, and S.A. Luther, *CCL21 is sufficient to mediate DC migration, maturation and function in the absence of CCL19*. Eur J Immunol, 2010. **40**(5): p. 1266-71.
202. Bryce, S.A., et al., *ACKR4 on Stromal Cells Scavenges CCL19 To Enable CCR7-Dependent Trafficking of APCs from Inflamed Skin to Lymph Nodes*. J Immunol, 2016. **196**(8): p. 3341-53.
203. Hansen, M., et al., *Autocrine CCL19 blocks dendritic cell migration toward weak gradients of CCL21*. Cytotherapy, 2016. **18**(9): p. 1187-96.
204. Johnson, L.A. and D.G. Jackson, *The chemokine CX3CL1 promotes trafficking of dendritic cells through inflamed lymphatics*. J Cell Sci, 2013. **126**(Pt 22): p. 5259-70.
205. Kabashima, K., et al., *CXCL12-CXCR4 engagement is required for migration of cutaneous dendritic cells*. Am J Pathol, 2007. **171**(4): p. 1249-57.
206. Vigl, B., et al., *Tissue inflammation modulates gene expression of lymphatic endothelial cells and dendritic cell migration in a stimulus-dependent manner*. Blood, 2011. **118**(1): p. 205-15.
207. Vestweber, D., *How leukocytes cross the vascular endothelium*. Nat Rev Immunol, 2015. **15**(11): p. 692-704.
208. Xu, H., et al., *The role of ICAM-1 molecule in the migration of Langerhans cells in the skin and regional lymph node*. Eur J Immunol, 2001. **31**(10): p. 3085-93.
209. Johnson, L.A., et al., *Dendritic cells enter lymph vessels by hyaluronan-mediated docking to the endothelial receptor LYVE-1*. Nat Immunol, 2017. **18**(7): p. 762-770.
210. Lawrence, W., et al., *Binding of Hyaluronan to the Native Lymphatic Vessel Endothelial Receptor LYVE-1 Is Critically Dependent on Receptor Clustering and Hyaluronan Organization*. J Biol Chem, 2016. **291**(15): p. 8014-30.
211. Dubacheva, G.V., et al., *Superselective targeting using multivalent polymers*. J Am Chem Soc, 2014. **136**(5): p. 1722-5.
212. Banerji, S., et al., *Homodimerization of the Lymph Vessel Endothelial Receptor LYVE-1 through a Redox-labile Disulfide Is Critical for Hyaluronan Binding in Lymphatic Endothelium*. J Biol Chem, 2016. **291**(48): p. 25004-25018.
213. Hou, W.H., et al., *CRSBP-1/LYVE-1 ligands disrupt lymphatic intercellular adhesion by inducing tyrosine phosphorylation and internalization of VE-cadherin*. J Cell Sci, 2011. **124**(Pt 8): p. 1231-44.
214. McKimmie, C.S., et al., *An analysis of the function and expression of D6 on lymphatic endothelial cells*. Blood, 2013. **121**(18): p. 3768-77.
215. Iolyeva, M., et al., *Novel role for ALCAM in lymphatic network formation and function*. FASEB J, 2013. **27**(3): p. 978-90.
216. Qu, C., et al., *Role of CCR8 and other chemokine pathways in the migration of monocyte-derived dendritic cells to lymph nodes*. J Exp Med, 2004. **200**(10): p. 1231-41.
217. Teijeira, A., et al., *CD137 on inflamed lymphatic endothelial cells enhances CCL21-guided migration of dendritic cells*. FASEB J, 2012. **26**(8): p. 3380-92.
218. Torzicky, M., et al., *Platelet endothelial cell adhesion molecule-1 (PECAM-1/CD31) and CD99 are critical in lymphatic transmigration of human dendritic cells*. J Invest Dermatol, 2012. **132**(4): p. 1149-57.

219. Teijeira, A., et al., *Lymphatic endothelium forms integrin-engaging 3D structures during DC transit across inflamed lymphatic vessels*. *J Invest Dermatol*, 2013. **133**(9): p. 2276-85.
220. Ballet, R., et al., *Blocking junctional adhesion molecule C enhances dendritic cell migration and boosts the immune responses against Leishmania major*. *PLoS Pathog*, 2014. **10**(12): p. e1004550.
221. Cera, M.R., et al., *Increased DC trafficking to lymph nodes and contact hypersensitivity in junctional adhesion molecule-A-deficient mice*. *J Clin Invest*, 2004. **114**(5): p. 729-38.
222. Maddaluno, L., et al., *The adhesion molecule L1 regulates transendothelial migration and trafficking of dendritic cells*. *J Exp Med*, 2009. **206**(3): p. 623-35.
223. Del Prete, A., et al., *Regulation of dendritic cell migration and adaptive immune response by leukotriene B4 receptors: a role for LTB4 in up-regulation of CCR7 expression and function*. *Blood*, 2007. **109**(2): p. 626-31.
224. Robbiani, D.F., et al., *The leukotriene C(4) transporter MRP1 regulates CCL19 (MIP-3beta, ELC)-dependent mobilization of dendritic cells to lymph nodes*. *Cell*, 2000. **103**(5): p. 757-68.
225. Ratzinger, G., et al., *Matrix metalloproteinases 9 and 2 are necessary for the migration of Langerhans cells and dermal dendritic cells from human and murine skin*. *J Immunol*, 2002. **168**(9): p. 4361-71.
226. Yen, J.H., T. Khayrullina, and D. Ganea, *PGE2-induced metalloproteinase-9 is essential for dendritic cell migration*. *Blood*, 2008. **111**(1): p. 260-70.
227. Marttila-Ichihara, F., et al., *Macrophage mannose receptor on lymphatics controls cell trafficking*. *Blood*, 2008. **112**(1): p. 64-72.
228. Linehan, S.A., et al., *Endogenous ligands of carbohydrate recognition domains of the mannose receptor in murine macrophages, endothelial cells and secretory cells; potential relevance to inflammation and immunity*. *Eur J Immunol*, 2001. **31**(6): p. 1857-66.
229. Acton, S.E., et al., *Podoplanin-rich stromal networks induce dendritic cell motility via activation of the C-type lectin receptor CLEC-2*. *Immunity*, 2012. **37**(2): p. 276-89.
230. Czeloth, N., et al., *Sphingosine-1-phosphate mediates migration of mature dendritic cells*. *J Immunol*, 2005. **175**(5): p. 2960-7.
231. Takamatsu, H., et al., *Semaphorins guide the entry of dendritic cells into the lymphatics by activating myosin II*. *Nat Immunol*, 2010. **11**(7): p. 594-600.
232. Swartz, M.A., D.A. Berk, and R.K. Jain, *Transport in lymphatic capillaries. I. Macroscopic measurements using residence time distribution theory*. *Am J Physiol*, 1996. **270**(1 Pt 2): p. H324-9.
233. Berk, D.A., et al., *Transport in lymphatic capillaries. II. Microscopic velocity measurement with fluorescence photobleaching*. *Am J Physiol*, 1996. **270**(1 Pt 2): p. H330-7.
234. Kerjaschki, D., et al., *Lymphatic neoangiogenesis in human kidney transplants is associated with immunologically active lymphocytic infiltrates*. *J Am Soc Nephrol*, 2004. **15**(3): p. 603-12.
235. Bell-Pedersen, D., et al., *Circadian rhythms from multiple oscillators: lessons from diverse organisms*. *Nat Rev Genet*, 2005. **6**(7): p. 544-56.
236. Menet, J.S., et al., *Nascent-Seq reveals novel features of mouse circadian transcriptional regulation*. *Elife*, 2012. **1**: p. e00011.
237. Panda, S., et al., *Coordinated transcription of key pathways in the mouse by the circadian clock*. *Cell*, 2002. **109**(3): p. 307-20.
238. Dibner, C., U. Schibler, and U. Albrecht, *The mammalian circadian timing system: organization and coordination of central and peripheral clocks*. *Annu Rev Physiol*, 2010. **72**: p. 517-49.

239. O'Neill, J.S. and A.B. Reddy, *Circadian clocks in human red blood cells*. *Nature*, 2011. **469**(7331): p. 498-503.
240. Milev, N.B., et al., *Analysis of the redox oscillations in the circadian clockwork*. *Methods Enzymol*, 2015. **552**: p. 185-210.
241. Bass, J. and J.S. Takahashi, *Circadian integration of metabolism and energetics*. *Science*, 2010. **330**(6009): p. 1349-54.
242. Curtis, A.M., et al., *Circadian clock proteins and immunity*. *Immunity*, 2014. **40**(2): p. 178-86.
243. Scheiermann, C., et al., *Adrenergic nerves govern circadian leukocyte recruitment to tissues*. *Immunity*, 2012. **37**(2): p. 290-301.
244. Edgar, R.S., et al., *Peroxiredoxins are conserved markers of circadian rhythms*. *Nature*, 2012. **485**(7399): p. 459-64.
245. Kang, T.H., et al., *Circadian control of XPA and excision repair of cisplatin-DNA damage by cryptochrome and HERC2 ubiquitin ligase*. *Proc Natl Acad Sci U S A*, 2010. **107**(11): p. 4890-5.
246. Mohawk, J.A. and J.S. Takahashi, *Cell autonomy and synchrony of suprachiasmatic nucleus circadian oscillators*. *Trends Neurosci*, 2011. **34**(7): p. 349-58.
247. Buhr, E.D., S.H. Yoo, and J.S. Takahashi, *Temperature as a universal resetting cue for mammalian circadian oscillators*. *Science*, 2010. **330**(6002): p. 379-85.
248. Ko, C.H. and J.S. Takahashi, *Molecular components of the mammalian circadian clock*. *Hum Mol Genet*, 2006. **15 Spec No 2**: p. R271-7.
249. Schibler, U. and P. Sassone-Corsi, *A web of circadian pacemakers*. *Cell*, 2002. **111**(7): p. 919-22.
250. Balsalobre, A., F. Damiola, and U. Schibler, *A serum shock induces circadian gene expression in mammalian tissue culture cells*. *Cell*, 1998. **93**(6): p. 929-37.
251. Huang, N., et al., *Crystal structure of the heterodimeric CLOCK:BMAL1 transcriptional activator complex*. *Science*, 2012. **337**(6091): p. 189-94.
252. Busino, L., et al., *SCFFbxl3 controls the oscillation of the circadian clock by directing the degradation of cryptochrome proteins*. *Science*, 2007. **316**(5826): p. 900-4.
253. Siepka, S.M., et al., *Circadian mutant Overtime reveals F-box protein FBXL3 regulation of cryptochrome and period gene expression*. *Cell*, 2007. **129**(5): p. 1011-23.
254. Godinho, S.I., et al., *The after-hours mutant reveals a role for Fbxl3 in determining mammalian circadian period*. *Science*, 2007. **316**(5826): p. 897-900.
255. Lee, H.M., et al., *The period of the circadian oscillator is primarily determined by the balance between casein kinase 1 and protein phosphatase 1*. *Proc Natl Acad Sci U S A*, 2011. **108**(39): p. 16451-6.
256. Partch, C.L., et al., *Posttranslational regulation of the mammalian circadian clock by cryptochrome and protein phosphatase 5*. *Proc Natl Acad Sci U S A*, 2006. **103**(27): p. 10467-10472.
257. Sato, T.K., et al., *A functional genomics strategy reveals Rora as a component of the mammalian circadian clock*. *Neuron*, 2004. **43**(4): p. 527-37.
258. Preitner, N., et al., *The orphan nuclear receptor REV-ERB α controls circadian transcription within the positive limb of the mammalian circadian oscillator*. *Cell*, 2002. **110**(2): p. 251-60.
259. Cho, H., et al., *Regulation of circadian behaviour and metabolism by REV-ERB- α and REV-ERB- β* . *Nature*, 2012. **485**(7396): p. 123-7.
260. Ukai-Tadenuma, M., et al., *Delay in feedback repression by cryptochrome 1 is required for circadian clock function*. *Cell*, 2011. **144**(2): p. 268-81.
261. Toh, K.L., et al., *An hPer2 phosphorylation site mutation in familial advanced sleep phase syndrome*. *Science*, 2001. **291**(5506): p. 1040-3.

262. McHill, A.W. and K.P. Wright, Jr., *Role of sleep and circadian disruption on energy expenditure and in metabolic predisposition to human obesity and metabolic disease*. *Obes Rev*, 2017. **18 Suppl 1**: p. 15-24.
263. Qian, J. and F. Scheer, *Circadian System and Glucose Metabolism: Implications for Physiology and Disease*. *Trends Endocrinol Metab*, 2016. **27**(5): p. 282-293.
264. Reitz, C.J. and T.A. Martino, *Disruption of Circadian Rhythms and Sleep on Critical Illness and the Impact on Cardiovascular Events*. *Curr Pharm Des*, 2015. **21**(24): p. 3505-11.
265. Dickmeis, T., *Glucocorticoids and the circadian clock*. *J Endocrinol*, 2009. **200**(1): p. 3-22.
266. Stokkan, K.A., et al., *Entrainment of the circadian clock in the liver by feeding*. *Science*, 2001. **291**(5503): p. 490-3.
267. Bass, J. and M.A. Lazar, *Circadian time signatures of fitness and disease*. *Science*, 2016. **354**(6315): p. 994-999.
268. Zhao, Y., et al., *Uncovering the mystery of opposite circadian rhythms between mouse and human leukocytes in humanized mice*. *Blood*, 2017. **130**(18): p. 1995-2005.
269. Parkar, S.G., A. Kalsbeek, and J.F. Cheeseman, *Potential Role for the Gut Microbiota in Modulating Host Circadian Rhythms and Metabolic Health*. *Microorganisms*, 2019. **7**(2).
270. Frazier, K. and E.B. Chang, *Intersection of the Gut Microbiome and Circadian Rhythms in Metabolism*. *Trends Endocrinol Metab*, 2020. **31**(1): p. 25-36.
271. de Juan, A., et al., *Artery-Associated Sympathetic Innervation Drives Rhythmic Vascular Inflammation of Arteries and Veins*. *Circulation*, 2019. **140**(13): p. 1100-1114.
272. Halberg, F., et al., *Susceptibility rhythm to E. coli endotoxin and bioassay*. *Proc Soc Exp Biol Med*, 1960. **103**: p. 142-4.
273. Shackelford, P.G. and R.D. Feigin, *Periodicity of susceptibility to pneumococcal infection: influence of light and adrenocortical secretions*. *Science*, 1973. **182**(4109): p. 285-7.
274. Labrecque, N. and N. Cermakian, *Circadian Clocks in the Immune System*. *J Biol Rhythms*, 2015. **30**(4): p. 277-90.
275. Ella, K., R. Csepanyi-Komi, and K. Kaldi, *Circadian regulation of human peripheral neutrophils*. *Brain Behav Immun*, 2016. **57**: p. 209-221.
276. Nguyen, K.D., et al., *Circadian gene Bmal1 regulates diurnal oscillations of Ly6C(hi) inflammatory monocytes*. *Science*, 2013. **341**(6153): p. 1483-8.
277. Keller, M., et al., *A circadian clock in macrophages controls inflammatory immune responses*. *Proc Natl Acad Sci U S A*, 2009. **106**(50): p. 21407-12.
278. Silver, A.C., et al., *Circadian expression of clock genes in mouse macrophages, dendritic cells, and B cells*. *Brain Behav Immun*, 2012. **26**(3): p. 407-13.
279. Hemmers, S. and A.Y. Rudensky, *The Cell-Intrinsic Circadian Clock Is Dispensable for Lymphocyte Differentiation and Function*. *Cell Rep*, 2015. **11**(9): p. 1339-49.
280. Bollinger, T., et al., *Circadian clocks in mouse and human CD4+ T cells*. *PLoS One*, 2011. **6**(12): p. e29801.
281. Yu, X., et al., *The basic leucine zipper transcription factor NFIL3 directs the development of a common innate lymphoid cell precursor*. *Elife*, 2014. **3**.
282. Xu, W., et al., *NFIL3 orchestrates the emergence of common helper innate lymphoid cell precursors*. *Cell Rep*, 2015. **10**(12): p. 2043-54.
283. Sun, Y., et al., *MOP3, a component of the molecular clock, regulates the development of B cells*. *Immunology*, 2006. **119**(4): p. 451-60.
284. Silver, A.C., et al., *The circadian clock controls toll-like receptor 9-mediated innate and adaptive immunity*. *Immunity*, 2012. **36**(2): p. 251-61.

285. Mauvoisin, D., et al., *Circadian clock-dependent and -independent rhythmic proteomes implement distinct diurnal functions in mouse liver*. Proc Natl Acad Sci U S A, 2014. **111**(1): p. 167-72.
286. Casanova-Acebes, M., et al., *Rhythmic modulation of the hematopoietic niche through neutrophil clearance*. Cell, 2013. **153**(5): p. 1025-35.
287. Rittirsch, D., M.A. Flierl, and P.A. Ward, *Harmful molecular mechanisms in sepsis*. Nat Rev Immunol, 2008. **8**(10): p. 776-87.
288. Gibbs, J.E., et al., *The nuclear receptor REV-ERB α mediates circadian regulation of innate immunity through selective regulation of inflammatory cytokines*. Proc Natl Acad Sci U S A, 2012. **109**(2): p. 582-7.
289. Narasimamurthy, R., et al., *Circadian clock protein cryptochrome regulates the expression of proinflammatory cytokines*. Proc Natl Acad Sci U S A, 2012. **109**(31): p. 12662-7.
290. Haspel, J.A., et al., *Circadian rhythm reprogramming during lung inflammation*. Nat Commun, 2014. **5**: p. 4753.
291. Druzd, D., et al., *Lymphocyte Circadian Clocks Control Lymph Node Trafficking and Adaptive Immune Responses*. Immunity, 2017. **46**(1): p. 120-132.
292. Gibbs, J., et al., *An epithelial circadian clock controls pulmonary inflammation and glucocorticoid action*. Nat Med, 2014. **20**(8): p. 919-26.
293. Chong, S.Z., et al., *CXCR4 identifies transitional bone marrow premonocytes that replenish the mature monocyte pool for peripheral responses*. J Exp Med, 2016. **213**(11): p. 2293-2314.
294. Besedovsky, L., J. Born, and T. Lange, *Endogenous glucocorticoid receptor signaling drives rhythmic changes in human T-cell subset numbers and the expression of the chemokine receptor CXCR4*. FASEB J, 2014. **28**(1): p. 67-75.
295. Suzuki, K., et al., *Adrenergic control of the adaptive immune response by diurnal lymphocyte recirculation through lymph nodes*. J Exp Med, 2016. **213**(12): p. 2567-2574.
296. Hopwood, T.W., et al., *The circadian regulator BMAL1 programmes responses to parasitic worm infection via a dendritic cell clock*. Sci Rep, 2018. **8**(1): p. 3782.
297. Fortier, E.E., et al., *Circadian variation of the response of T cells to antigen*. J Immunol, 2011. **187**(12): p. 6291-300.
298. Gagnidze, K., et al., *Nuclear receptor REV-ERB α mediates circadian sensitivity to mortality in murine vesicular stomatitis virus-induced encephalitis*. Proc Natl Acad Sci U S A, 2016. **113**(20): p. 5730-5.
299. Adrover, J.M., et al., *A Neutrophil Timer Coordinates Immune Defense and Vascular Protection*. Immunity, 2019. **51**(5): p. 966-967.
300. Mendez-Ferrer, S., et al., *Haematopoietic stem cell release is regulated by circadian oscillations*. Nature, 2008. **452**(7186): p. 442-7.
301. Lucas, D., et al., *Mobilized hematopoietic stem cell yield depends on species-specific circadian timing*. Cell Stem Cell, 2008. **3**(4): p. 364-6.
302. Plikus, M.V., et al., *The circadian clock in skin: implications for adult stem cells, tissue regeneration, cancer, aging, and immunity*. J Biol Rhythms, 2015. **30**(3): p. 163-82.
303. Tanioka, M., et al., *Molecular clocks in mouse skin*. J Invest Dermatol, 2009. **129**(5): p. 1225-31.
304. Kleszczynski, K., L.H. Hardkop, and T.W. Fischer, *Differential effects of melatonin as a broad range UV-damage preventive dermato-endocrine regulator*. Dermatoendocrinol, 2011. **3**(1): p. 27-31.
305. Schernhammer, E.S., et al., *Rotating night shifts and risk of breast cancer in women participating in the nurses' health study*. J Natl Cancer Inst, 2001. **93**(20): p. 1563-8.

306. Ozler, M., et al., *Comparison of the effect of topical and systemic melatonin administration on delayed wound healing in rats that underwent pinealectomy*. Scand J Clin Lab Invest, 2010. **70**(6): p. 447-52.
307. Zanello, S.B., D.M. Jackson, and M.F. Holick, *Expression of the circadian clock genes clock and period1 in human skin*. J Invest Dermatol, 2000. **115**(4): p. 757-60.
308. Geyfman, M., et al., *Brain and muscle Arnt-like protein-1 (BMAL1) controls circadian cell proliferation and susceptibility to UVB-induced DNA damage in the epidermis*. Proc Natl Acad Sci U S A, 2012. **109**(29): p. 11758-63.
309. Matsunaga, N., et al., *24-hour rhythm of aquaporin-3 function in the epidermis is regulated by molecular clocks*. J Invest Dermatol, 2014. **134**(6): p. 1636-1644.
310. Patel, T., Y. Ishiujji, and G. Yosipovitch, *Nocturnal itch: why do we itch at night?* Acta Derm Venereol, 2007. **87**(4): p. 295-8.
311. Frenzt, G., et al., *On circadian rhythms in human epidermal cell proliferation*. Acta Derm Venereol, 1991. **71**(1): p. 85-7.
312. Al-Nuaimi, Y., et al., *A meeting of two chronobiological systems: circadian proteins Period1 and BMAL1 modulate the human hair cycle clock*. J Invest Dermatol, 2014. **134**(3): p. 610-619.
313. Ando, N., et al., *Circadian Gene Clock Regulates Psoriasis-Like Skin Inflammation in Mice*. J Invest Dermatol, 2015. **135**(12): p. 3001-3008.
314. Nakamura, Y., et al., *Inhibition of IgE-mediated allergic reactions by pharmacologically targeting the circadian clock*. J Allergy Clin Immunol, 2016. **137**(4): p. 1226-1235.
315. Takita, E., et al., *Biological clock dysfunction exacerbates contact hypersensitivity in mice*. Br J Dermatol, 2013. **168**(1): p. 39-46.
316. Li, W.Q., et al., *Rotating night-shift work and risk of psoriasis in US women*. J Invest Dermatol, 2013. **133**(2): p. 565-7.
317. Prendergast, B.J., et al., *Impaired leukocyte trafficking and skin inflammatory responses in hamsters lacking a functional circadian system*. Brain Behav Immun, 2013. **32**: p. 94-104.
318. Greenberg, E.N., et al., *Circadian control of interferon-sensitive gene expression in murine skin*. Proc Natl Acad Sci U S A, 2020. **117**(11): p. 5761-5771.
319. Castanon-Cervantes, O., et al., *Dysregulation of inflammatory responses by chronic circadian disruption*. J Immunol, 2010. **185**(10): p. 5796-805.
320. Pagel, R., et al., *Circadian rhythm disruption impairs tissue homeostasis and exacerbates chronic inflammation in the intestine*. FASEB J, 2017. **31**(11): p. 4707-4719.
321. Nojkov, B., et al., *The impact of rotating shift work on the prevalence of irritable bowel syndrome in nurses*. Am J Gastroenterol, 2010. **105**(4): p. 842-7.
322. Durrington, H.J., et al., *The circadian clock and asthma*. Thorax, 2014. **69**(1): p. 90-2.
323. Olsen, N.J., R.H. Brooks, and D. Furst, *Variability of immunologic and clinical features in patients with rheumatoid arthritis studied over 24 hours*. J Rheumatol, 1993. **20**(6): p. 940-3.
324. Perry, M.G., et al., *Overnight variations in cortisol, interleukin 6, tumour necrosis factor alpha and other cytokines in people with rheumatoid arthritis*. Ann Rheum Dis, 2009. **68**(1): p. 63-8.
325. Takeda, N. and K. Maemura, *Circadian clock and the onset of cardiovascular events*. Hypertens Res, 2016. **39**(6): p. 383-90.
326. Culic, V., *Daylight saving time transitions and acute myocardial infarction*. Chronobiol Int, 2013. **30**(5): p. 662-8.
327. Zhang, R., et al., *A circadian gene expression atlas in mammals: implications for biology and medicine*. Proc Natl Acad Sci U S A, 2014. **111**(45): p. 16219-24.
328. Long, J.E., et al., *Morning vaccination enhances antibody response over afternoon vaccination: A cluster-randomised trial*. Vaccine, 2016. **34**(24): p. 2679-85.

329. Gottlob, S., C. Gille, and C.F. Poets, *Randomized Controlled Trial on the Effects of Morning versus Evening Primary Vaccination on Episodes of Hypoxemia and Bradycardia in Very Preterm Infants*. *Neonatology*, 2019. **116**(4): p. 315-320.
330. Guerra-Santos, B., et al., *Daily rhythms after vaccination on specific and non-specific responses in Nile tilapia (*Oreochromis niloticus*)*. *Chronobiol Int*, 2018. **35**(9): p. 1305-1318.
331. Nobis, C.C., et al., *The circadian clock of CD8 T cells modulates their early response to vaccination and the rhythmicity of related signaling pathways*. *Proc Natl Acad Sci U S A*, 2019. **116**(40): p. 20077-20086.
332. Peirson, S.N., et al., *Light and the laboratory mouse*. *J Neurosci Methods*, 2018. **300**: p. 26-36.
333. Kim, H., et al., *Mouse Cre-LoxP system: general principles to determine tissue-specific roles of target genes*. *Lab Anim Res*, 2018. **34**(4): p. 147-159.
334. Savastano, L.E., et al., *A standardized surgical technique for rat superior cervical ganglionectomy*. *J Neurosci Methods*, 2010. **192**(1): p. 22-33.
335. Afgan, E., et al., *The Galaxy platform for accessible, reproducible and collaborative biomedical analyses: 2016 update*. *Nucleic Acids Res*, 2016. **44**(W1): p. W3-W10.
336. Cornelissen, G., *Cosinor-based rhythmometry*. *Theor Biol Med Model*, 2014. **11**: p. 16.
337. Miller, I., et al., *Ki67 is a Graded Rather than a Binary Marker of Proliferation versus Quiescence*. *Cell Rep*, 2018. **24**(5): p. 1105-1112 e5.
338. Hergenhan, S., S. Holtkamp, and C. Scheiermann, *Molecular Interactions Between Components of the Circadian Clock and the Immune System*. *J Mol Biol*, 2020. **432**(12): p. 3700-3713.
339. Man, K., A. Loudon, and A. Chawla, *Immunity around the clock*. *Science*, 2016. **354**(6315): p. 999-1003.
340. Scheiermann, C., et al., *Clocking in to immunity*. *Nat Rev Immunol*, 2018. **18**(7): p. 423-437.
341. Helft, J., et al., *GM-CSF Mouse Bone Marrow Cultures Comprise a Heterogeneous Population of CD11c(+)MHCII(+) Macrophages and Dendritic Cells*. *Immunity*, 2015. **42**(6): p. 1197-211.
342. Sato, S., et al., *A circadian clock gene, Rev-erb α , modulates the inflammatory function of macrophages through the negative regulation of Ccl2 expression*. *J Immunol*, 2014. **192**(1): p. 407-17.
343. Wang, T., et al., *PER1 prevents excessive innate immune response during endotoxin-induced liver injury through regulation of macrophage recruitment in mice*. *Cell Death Dis*, 2016. **7**: p. e2176.
344. Scheiermann, C., Y. Kunisaki, and P.S. Frenette, *Circadian control of the immune system*. *Nat Rev Immunol*, 2013. **13**(3): p. 190-8.
345. Guimaraes, S. and D. Moura, *Vascular adrenoceptors: an update*. *Pharmacol Rev*, 2001. **53**(2): p. 319-56.
346. Proskocil, B.J. and A.D. Fryer, *Beta2-agonist and anticholinergic drugs in the treatment of lung disease*. *Proc Am Thorac Soc*, 2005. **2**(4): p. 305-10; discussion 311-2.
347. Billington, C.K., R.B. Penn, and I.P. Hall, *beta2 Agonists*. *Handb Exp Pharmacol*, 2017. **237**: p. 23-40.
348. Bachmann, S.B., et al., *A Distinct Role of the Autonomic Nervous System in Modulating the Function of Lymphatic Vessels under Physiological and Tumor-Draining Conditions*. *Cell Rep*, 2019. **27**(11): p. 3305-3314 e13.
349. Nader, N., G.P. Chrousos, and T. Kino, *Circadian rhythm transcription factor CLOCK regulates the transcriptional activity of the glucocorticoid receptor by acetylating its hinge region lysine cluster: potential physiological implications*. *FASEB J*, 2009. **23**(5): p. 1572-83.

350. Robles, M.S., S.J. Humphrey, and M. Mann, *Phosphorylation Is a Central Mechanism for Circadian Control of Metabolism and Physiology*. *Cell Metab*, 2017. **25**(1): p. 118-127.
351. Arjona, A. and D.K. Sarkar, *Circadian oscillations of clock genes, cytolytic factors, and cytokines in rat NK cells*. *J Immunol*, 2005. **174**(12): p. 7618-24.
352. Baumann, A., et al., *The circadian clock is functional in eosinophils and mast cells*. *Immunology*, 2013. **140**(4): p. 465-74.
353. Hayashi, M., S. Shimba, and M. Tezuka, *Characterization of the molecular clock in mouse peritoneal macrophages*. *Biol Pharm Bull*, 2007. **30**(4): p. 621-6.
354. Hughes, M.E., et al., *Harmonics of circadian gene transcription in mammals*. *PLoS Genet*, 2009. **5**(4): p. e1000442.
355. Kojima, S., E.L. Sher-Chen, and C.B. Green, *Circadian control of mRNA polyadenylation dynamics regulates rhythmic protein expression*. *Genes Dev*, 2012. **26**(24): p. 2724-36.
356. Chardin, P. and F. McCormick, *Brefeldin A: the advantage of being uncompetitive*. *Cell*, 1999. **97**(2): p. 153-5.
357. Mishev, K., W. Dejonghe, and E. Russinova, *Small molecules for dissecting endomembrane trafficking: a cross-systems view*. *Chem Biol*, 2013. **20**(4): p. 475-86.
358. Dubrot, J., et al., *Lymph node stromal cells acquire peptide-MHCII complexes from dendritic cells and induce antigen-specific CD4(+) T cell tolerance*. *J Exp Med*, 2014. **211**(6): p. 1153-66.
359. Anderson, M.S., et al., *Projection of an immunological self shadow within the thymus by the aire protein*. *Science*, 2002. **298**(5597): p. 1395-401.
360. Derbinski, J., et al., *Promiscuous gene expression in medullary thymic epithelial cells mirrors the peripheral self*. *Nat Immunol*, 2001. **2**(11): p. 1032-9.
361. Cohen, J.N., et al., *Lymph node-resident lymphatic endothelial cells mediate peripheral tolerance via Aire-independent direct antigen presentation*. *J Exp Med*, 2010. **207**(4): p. 681-8.
362. Cohen, J.N., et al., *Tolerogenic properties of lymphatic endothelial cells are controlled by the lymph node microenvironment*. *PLoS One*, 2014. **9**(2): p. e87740.
363. Johnnidis, J.B., et al., *Chromosomal clustering of genes controlled by the aire transcription factor*. *Proc Natl Acad Sci U S A*, 2005. **102**(20): p. 7233-8.
364. Fletcher, A.L., et al., *Lymph node fibroblastic reticular cells directly present peripheral tissue antigen under steady-state and inflammatory conditions*. *J Exp Med*, 2010. **207**(4): p. 689-97.
365. Tewalt, E.F., et al., *Lymphatic endothelial cells induce tolerance via PD-L1 and lack of costimulation leading to high-level PD-1 expression on CD8 T cells*. *Blood*, 2012. **120**(24): p. 4772-82.
366. Nichols, L.A., et al., *Deletional self-tolerance to a melanocyte/melanoma antigen derived from tyrosinase is mediated by a radio-resistant cell in peripheral and mesenteric lymph nodes*. *J Immunol*, 2007. **179**(2): p. 993-1003.
367. Rouhani, S.J., et al., *Roles of lymphatic endothelial cells expressing peripheral tissue antigens in CD4 T-cell tolerance induction*. *Nat Commun*, 2015. **6**: p. 6771.
368. Onder, L., et al., *IL-7-producing stromal cells are critical for lymph node remodeling*. *Blood*, 2012. **120**(24): p. 4675-83.
369. Iolyeva, M., et al., *Interleukin-7 is produced by afferent lymphatic vessels and supports lymphatic drainage*. *Blood*, 2013. **122**(13): p. 2271-81.
370. Hablitz, L.M., et al., *Circadian control of brain glymphatic and lymphatic fluid flow*. *Nat Commun*, 2020. **11**(1): p. 4411.
371. McDonald, B. and P. Kubers, *Interactions between CD44 and Hyaluronan in Leukocyte Trafficking*. *Front Immunol*, 2015. **6**: p. 68.

372. DeGrendele, H.C., et al., *CD44 and its ligand hyaluronate mediate rolling under physiologic flow: a novel lymphocyte-endothelial cell primary adhesion pathway*. J Exp Med, 1996. **183**(3): p. 1119-30.
373. Nandi, A., P. Estess, and M. Siegelman, *Bimolecular complex between rolling and firm adhesion receptors required for cell arrest; CD44 association with VLA-4 in T cell extravasation*. Immunity, 2004. **20**(4): p. 455-65.
374. Mamdouh, Z., A. Mikhailov, and W.A. Muller, *Transcellular migration of leukocytes is mediated by the endothelial lateral border recycling compartment*. J Exp Med, 2009. **206**(12): p. 2795-808.
375. Schenkel, A.R., et al., *CD99 plays a major role in the migration of monocytes through endothelial junctions*. Nat Immunol, 2002. **3**(2): p. 143-50.
376. Pasello, M., M.C. Manara, and K. Scotlandi, *CD99 at the crossroads of physiology and pathology*. J Cell Commun Signal, 2018. **12**(1): p. 55-68.
377. Scheiermann, C., et al., *Junctional adhesion molecule-C mediates leukocyte infiltration in response to ischemia reperfusion injury*. Arterioscler Thromb Vasc Biol, 2009. **29**(10): p. 1509-15.
378. Scheiermann, C., et al., *Expression and function of junctional adhesion molecule-C in myelinated peripheral nerves*. Science, 2007. **318**(5855): p. 1472-5.
379. Kummer, D. and K. Ebnet, *Junctional Adhesion Molecules (JAMs): The JAM-Integrin Connection*. Cells, 2018. **7**(4).
380. Steinbacher, T., D. Kummer, and K. Ebnet, *Junctional adhesion molecule-A: functional diversity through molecular promiscuity*. Cell Mol Life Sci, 2018. **75**(8): p. 1393-1409.
381. Ostermann, G., et al., *JAM-1 is a ligand of the beta(2) integrin LFA-1 involved in transendothelial migration of leukocytes*. Nat Immunol, 2002. **3**(2): p. 151-8.
382. Santoso, S., et al., *The junctional adhesion molecule 3 (JAM-3) on human platelets is a counterreceptor for the leukocyte integrin Mac-1*. J Exp Med, 2002. **196**(5): p. 679-91.
383. Lamagna, C., et al., *Dual interaction of JAM-C with JAM-B and alpha(M)beta2 integrin: function in junctional complexes and leukocyte adhesion*. Mol Biol Cell, 2005. **16**(10): p. 4992-5003.
384. Lu, R.M., et al., *Development of therapeutic antibodies for the treatment of diseases*. J Biomed Sci, 2020. **27**(1): p. 1.
385. Kaur, G., et al., *Timing of Administration: For Commonly-Prescribed Medicines in Australia*. Pharmaceutics, 2016. **8**(2).
386. Dierickx, P., et al., *SR9009 has REV-ERB-independent effects on cell proliferation and metabolism*. Proc Natl Acad Sci U S A, 2019. **116**(25): p. 12147-12152.
387. Janich, P., et al., *Human epidermal stem cell function is regulated by circadian oscillations*. Cell Stem Cell, 2013. **13**(6): p. 745-53.
388. Pierzynska-Mach, A., et al., *Subnuclear localization, rates and effectiveness of UVC-induced unscheduled DNA synthesis visualized by fluorescence widefield, confocal and super-resolution microscopy*. Cell Cycle, 2016. **15**(8): p. 1156-67.
389. Bjarnason, G.A., et al., *Circadian expression of clock genes in human oral mucosa and skin: association with specific cell-cycle phases*. Am J Pathol, 2001. **158**(5): p. 1793-801.
390. Sutton, C.E., et al., *Loss of the molecular clock in myeloid cells exacerbates T cell-mediated CNS autoimmune disease*. Nat Commun, 2017. **8**(1): p. 1923.
391. Nakazato, R., et al., *The intrinsic microglial clock system regulates interleukin-6 expression*. Glia, 2017. **65**(1): p. 198-208.
392. Stutte, S., et al., *Requirement of CCL17 for CCR7- and CXCR4-dependent migration of cutaneous dendritic cells*. Proc Natl Acad Sci U S A, 2010. **107**(19): p. 8736-41.
393. Tuganbaev, T., et al., *Diet Diurnally Regulates Small Intestinal Microbiome-Epithelial-Immune Homeostasis and Enteritis*. Cell, 2020.

7 Appendices

7.1 Additional data

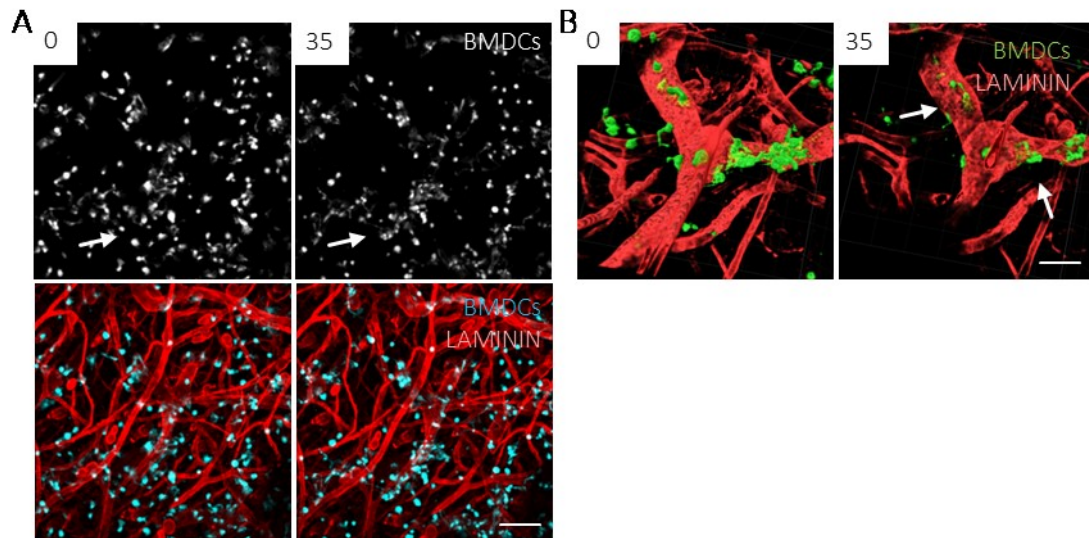


Figure 7-1: Live imaging of exogenous crawl-in assays

(A) 50,000 Activated and stained bone-marrow-derived dendritic cells (BMDCs) were added on explanted, split ear halves previously stained for LAMININ. After 35 min incubation in an imaging CO₂ chamber with 37°C, the majority of BMDCs has migrated to the lymphatic vessels (LV), as indicated by the arrows. Scale bar = 50µm.

(B) 3D views of BMDCs migrating into LAMININ⁺ LVs after 0 and 35 min. Arrows indicate transmigrating BMDCs. Scale bar = 40µm.

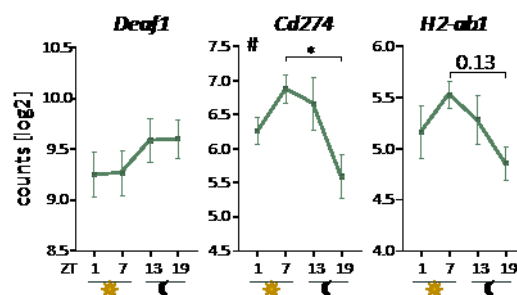


Figure 7-2: Expression of genes associated with tolerance induction

Measured expression of genes associated with self-tolerance induction in sorted dermal LECs. N = 5 mice measured for 4 time points each. # = one-way ANOVA; * = Tukey's multiple comparisons test, *p < 0.05. All data are represented as mean ± SEM.

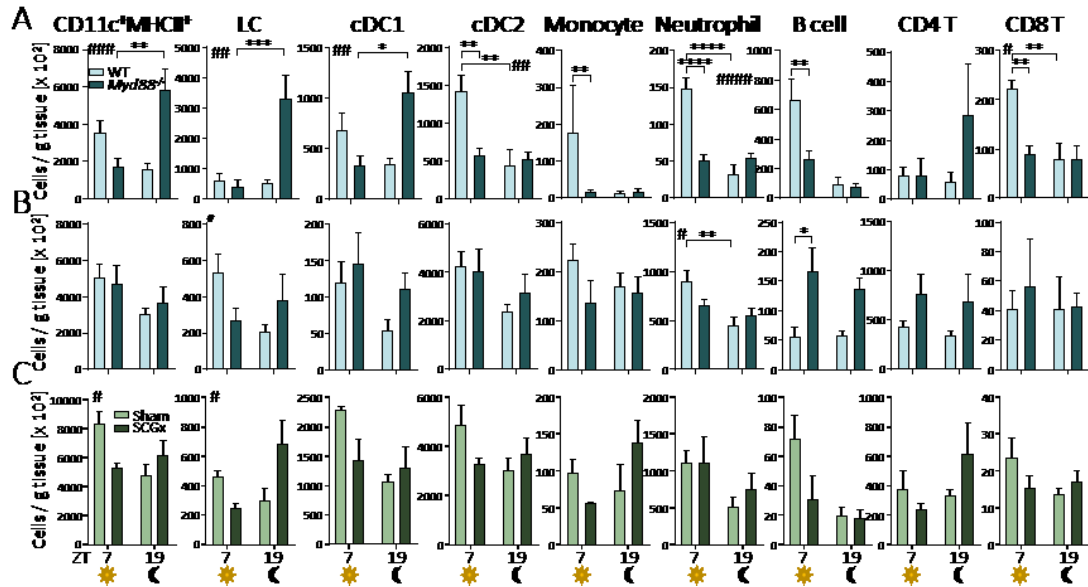


Figure 7-3: Ear cellularity and crawl-out assay using SCGx and *Myd88*^{-/-} mice

(A) Flow-cytometric analyses of cellularity normalized to tissue weight from harvested WT or *Myd88*^{-/-} ears. LC = Langerhans cell, cDC1/2 = conventional dendritic cell, T = T cell.

(B) Flow-cytometric analyses of emigrated immune cells from cultured, split ears (crawl-out assay) into medium. Cell counts normalized to tissue weight from harvested WT or *Myd88*^{-/-} ears.

(C) Flow-cytometric analyses of cellularity normalized to tissue weight from ears harvested from sham or SCGx mice. Briefly, the anterior tip of the sternum to the chin was opened and the cervical ganglion of anaesthetized mice was gently removed during a surgery, after which animals were given a 2 weeks recovery period. # = two-way ANOVA, * = Šidák's multiple comparisons test, n = 2 mice across 2 time

7.2 Codes and algorithms

LYVE-1 mask / protein screen (FIJI)

```
makeRectangle(3, 2, 506, 509);
setBackground(0, 0, 0);
run("Clear Outside", "slice");
setAutoThreshold("Otsu dark");
run("Create Selection");
roiManager("Add");
run("Next Slice [>]");
run("Measure");
close();
```

GOLPH4 mask (FIJI)

```
run("Next Slice [>]");
makeRectangle(0, 1, 512, 504);
setAutoThreshold("Triangle dark");
```

```

run("Create Selection");
setBackgroundColor(0, 0, 0);
run("Clear Outside", "stack");
resetThreshold();
run("Subtract Background...", "rolling=2 slice");
setAutoThreshold("Otsu dark");
run("Create Selection");
run("Clear", "stack");
run("Next Slice [>]");
makeLine(260, 190, 260, 190);
setAutoThreshold("IJ_IsoData dark");
run("Create Selection");
run("Next Slice [>]");
run("Measure");
run("Clear", "stack");
makeLine(227, 200, 227, 200);
setAutoThreshold("Mean dark");
run("Create Selection");
resetThreshold();
run("Measure");
close();

```

LYVE-1 dependent binary mask for further analysis (Matlab)

#1

```

function [ROI_Mask] = Stephan_LymphaticROIs(RawData_Directory,ImageName,Nr_ROIs)

% change directory
cd(RawData_Directory)

% load Lymphatic AB tiff
AB_Lymph = imread(ImageName);

% preallocate ROI structure
ROIs = cell(1,Nr_ROIs);

% draw ROIs for binary mask on lymphatic antibody picture
for i = 1:Nr_ROIs
    imshow(AB_Lymph)
    ROI = drawfreehand();
    ROIs{i} = ROI.createMask();
end

% combine all ROIs

```

```

for j = 1:Nr_ROIs
    if j == 1
        ROI_Mask = ROIs{j};
    else
        ROI_Mask = ROI_Mask + ROIs{j};
    end
end

% binarize in case of overlap
ROI_Mask(ROI_Mask > 1) = 1;
ROI_Mask = logical(ROI_Mask);

save(['ROI_Mask_' ],ROI_Mask);

```

#2

```

function Stephan_DrawSave_LymphaticROIs

close all
clear all

% select all tifs to be ROI-ed
[FileNames,~] = uigetfile('.tif','Select all images to be ROI-ed','MultiSelect','on');

% enter number of picture to be ROI-ed
Nr_Reps = length(FileNames);
clear FileNames

% draw and extract ROIs for each picture
for i = 1:Nr_Reps

    % select & load Lymphatic AB tiff
    [FileName,FilePath] = uigetfile({' .tif'},'Select an image');
    AB_Lymph = imread(strcat(FilePath,FileName));

    % define number of necessary ROIs to be drawn based on picture
    imshow(AB_Lymph)
    answer = inputdlg('Define number of necessary ROIs','Lymphatic Sample');
    Nr_ROIs = str2num(answer{1});
    clear answer
    close(gcf)

    % preallocate ROI structure
    ROIs = cell(1,Nr_ROIs);

```

```

% draw ROIs for binary mask on lymphatic antibody picture
for i = 1:Nr_ROIs
    imshow(AB_Lymph)
    ROI = drawfreehand();
    ROIs{i} = ROI.createMask();
end

% combine all ROIs
for j = 1:Nr_ROIs
    if j == 1
        ROI_Mask = ROIs{j};
    else
        ROI_Mask = ROI_Mask + ROIs{j};
    end
end

% binarize in case of overlap
ROI_Mask(ROI_Mask > 1) = 1;
ROI_Mask = logical(ROI_Mask);

% Save ROI Mask for later processing
cd(FilePath)
save(['ROI_Mask_' FileName(1:end-4) '.mat'],'ROI_Mask');
close(gcf)
end

```

CCL21 gradient analysis (Matlab)

```

function Stephan_LymphaticVessels_FluoDistance

% define number of staining protocols
answer = inputdlg('Define number of staining protocols','Lymphvessel experiments');
Nr_StainingProtocols = str2num(answer{1});
clear answer

% preallocate
DistanceStatistics = [];
for m = 1:Nr_StainingProtocols
    DistanceStatistics(m).RawDistancePixelFs = [];
    DistanceStatistics(m).NormDistancePixelFs = [];
    DistanceStatistics(m).AllNormDistancePixelFs = [];
    DistanceStatistics(m).AllRawDistancePixelFs = [];
    DistanceStatistics(m).DistanceMeans = [];
    DistanceStatistics(m).DistanceSTDs = [];
    DistanceStatistics(m).DistanceSEMs = [];
    DistanceStatistics(m).GlobalDistanceMeans = [];
    DistanceStatistics(m).GlobalDistanceSTDs = [];
    DistanceStatistics(m).GlobalDistanceSEMs = [];
    DistanceStatistics(m).normGlobalDistanceMeans = [];
    DistanceStatistics(m).normGlobalDistanceSTDs = [];
    DistanceStatistics(m).normGlobalDistanceSEMs = [];
end

tic

for k = 1:Nr_StainingProtocols

```

```

%% parameter switchboard

% select all Interstitium images
if Nr_StainingProtocols == 2
    if k == 1
        [FileNames,FilePath] = uigetfile('.tif','Select non-control Interstitium images','MultiSelect','on');
    else
        [FileNames,FilePath] = uigetfile('.tif','Select control Interstitium images','MultiSelect','on');
    end
elseif Nr_StainingProtocols == 4
    if k == 1
        [FileNames,FilePath] = uigetfile('.tif','Select non-control ZT7 Interstitium images','MultiSelect','on');
    elseif k == 2
        [FileNames,FilePath] = uigetfile('.tif','Select non-control ZT19 Interstitium images','MultiSelect','on');
    elseif k == 3
        [FileNames,FilePath] = uigetfile('.tif','Select iso-control ZT7 Interstitium images','MultiSelect','on');
    elseif k == 4
        [FileNames,FilePath] = uigetfile('.tif','Select iso-control ZT19 Interstitium images','MultiSelect','on');
    end
elseif Nr_StainingProtocols == 6
    if k == 1
        [FileNames,FilePath] = uigetfile('.tif','Select WT non-control ZT7 Interstitium images','MultiSelect','on');
    elseif k == 2
        [FileNames,FilePath] = uigetfile('.tif','Select WT non-control ZT19 Interstitium images','MultiSelect','on');
    elseif k == 3
        [FileNames,FilePath] = uigetfile('.tif','Select WT iso-control ZT7 Interstitium images','MultiSelect','on');
    elseif k == 4
        [FileNames,FilePath] = uigetfile('.tif','Select WT iso-control ZT19 Interstitium images','MultiSelect','on');
    elseif k == 5
        [FileNames,FilePath] = uigetfile('.tif','Select KO non-control ZT7 Interstitium images','MultiSelect','on');
    elseif k == 6
        [FileNames,FilePath] = uigetfile('.tif','Select KO non-control ZT19 Interstitium images','MultiSelect','on');
    end
end
Nr_files = length(FileNames);

% change directory to filepath
cd(FilePath)

% preallocate
AB_Interstitium = cell(Nr_files,1);
LymphMasks = cell(Nr_files,1);
% AB_Lymph = cell(Nr_files,1);
Pixel2Microns = NaN(Nr_files,1);

% load Interstitium images and Lymph ROIs with Pixel Conversion Factors
for i = 1:Nr_files
    FileName_temp = FileNames{i};
    AB_Interstitium{i} = double(imread(FileName_temp));
    % ImlInfo_temp = imfinfo(FileName_temp);
    % Pixel2Microns(i) = 1/ImlInfo_temp.XResolution;
    Pixel2Microns(i) = 1/1.5;
    if Nr_StainingProtocols == 2
        LymphMasks{i} = load(['ROI_Mask_' FileName_temp(1:end-10) '_LV.mat']);
    %     AB_Lymph{i} = double(imread([FileName_temp(1:end-10) '_LV.tif']));
    elseif Nr_StainingProtocols == 4
        LymphMasks{i} = load(['ROI_Mask_' FileName_temp(1:end-5) '0.mat']);
    %     AB_Lymph{i} = double(imread([FileName_temp(1:end-5) '0.tif']));
    elseif Nr_StainingProtocols == 6
        LymphMasks{i} = load(['ROI_Mask_' FileName_temp(1:end-5) '0.mat']);
    %     AB_Lymph{i} = double(imread([FileName_temp(1:end-5) '0.tif']));
    end
    clear FileName_temp
    clear ImlInfo_temp
end

%% calculate and plot Distance Mask from Lymphatic ROI

% determine longest distance from Lymph vessel from all pictures for preallocation
for h = 1:Nr_files

```

```

DistanceLength = length(unique(round(bwdist(LymphMasks{h,1}.ROI_Mask,'euclidean')*Pixel2Microns(h))));
if h == 1
    MaxDistance = DistanceLength;
elseif DistanceLength > MaxDistance
    MaxDistance = DistanceLength;
end
end

% determine longest distance from Lymph vessel from all pictures for preallocation
PixelFrequency = zeros(MaxDistance,1);
for h = 1:Nr_files
    [~,PixelFrequency_ic] = unique(round(bwdist(LymphMasks{h,1}.ROI_Mask,'euclidean')*Pixel2Microns(h))));
    PixelFrequency_temp = accumarray(PixelFrequency_ic,1);
    PixelFrequency(1:length(PixelFrequency_temp)) = PixelFrequency(1:length(PixelFrequency_temp)) + PixelFrequency_temp;
end
MaxPixelFrequency = max(max(PixelFrequency));

% preallocate
DistanceStatistics(k).AllNormDistancePixelFs = NaN(MaxPixelFrequency,MaxDistance);
DistanceStatistics(k).AllRawDistancePixelFs = NaN(MaxPixelFrequency,MaxDistance);
if k == 1
    Excel_ZT7 = NaN(MaxDistance,Nr_files);
elseif k == 2
    Excel_ZT19 = NaN(MaxDistance,Nr_files);
elseif k == 3
    Excel_isoZT7 = NaN(MaxDistance,Nr_files);
elseif k == 4
    Excel_isoZT19 = NaN(MaxDistance,Nr_files);
elseif k == 5
    Excel_KO_ZT7 = NaN(MaxDistance,Nr_files);
elseif k == 6
    Excel_KO_ZT19 = NaN(MaxDistance,Nr_files);
end

for j = 1:Nr_files

    % create distance mask around Lymph Vessel mask (round to nearest decimal)
    DistanceMask = round(bwdist(LymphMasks{j,1}.ROI_Mask,'euclidean')*Pixel2Microns(h));

    % find pixels of Lymph Vessel Mask and Perimeter
    % [ROI_IDs_Y,ROI_IDs_X] = find(LymphMasks{j,1}.ROI_Mask == 1);
    % Lymph_mask_perim = bwperim(LymphMasks{j,1}.ROI_Mask);
    % [ROIperim_IDs_Y,ROIperim_IDs_X] = find(Lymph_mask_perim);
    %
    % plot original picture and Distance Mask with ROI
    % f1 = figure('Name','Lymphatic ROI & Distance Mask','color','w','Visible','off');
    % p = uipanel('Parent',f1,'BorderType','none');
    % p.Title = 'Lymphatic ROI & Distance Mask';
    % p.TitlePosition = 'centertop';
    % p.FontSize = 12;
    % p.FontWeight = 'bold';
    %
    % subplot(1,2,1,'Parent',p);
    % imshow(AB_Lymph{j});
    % hold on
    % plot(ROIperim_IDs_X,ROIperim_IDs_Y,'r','MarkerSize',1.5)
    % title('Lymphatic ROI')
    % colormap(gca,'gray')
    % axis off
    % hold off
    %
    % subplot(1,2,2,'Parent',p);
    % imagesc(DistanceMask)
    % hold on
    % colormap(gca,'cool');
    % colorbar
    % plot(ROI_IDs_X,ROI_IDs_Y,'k')
    % plot(ROIperim_IDs_X,ROIperim_IDs_Y,'w','MarkerSize',1.5)
    % title('Distance Mask')
    % axis square
    % axis off

```

```

% hold off
%
% % save figure
% saveas(f1,[char(FileNames(j)) '_ROI_DistanceMask.fig']);
% saveas(f1,[char(FileNames(j)) '_ROI_DistanceMask.svg']);
% saveas(f1,[char(FileNames(j)) '_ROI_DistanceMask.pdf']);

%% extract distance dependent fluorescence values (normalized to F(max)) of Interstitium (relative from Lymph Vessel)

% preallocate
Fluorescence_Dist = cell(1,length(unique(DistanceMask))-1);
MEAN_FDDist = NaN(1,length(unique(DistanceMask))-1);
STD_FDDist = NaN(1,length(unique(DistanceMask))-1);
SEM_FDDist = NaN(1,length(unique(DistanceMask))-1);

% find F(max) for normalization
Fmax = max(max(AB_Interstitium{j}(~LymphMasks{j,1}.ROI_Mask)));

% extract distance dependent fluorescence values & stats
Mask_Distances = unique(DistanceMask);
for i = 1:length(Mask_Distances)
    ID = Mask_Distances(i);
    if ID > 0
        DistanceIDs = (DistanceMask == ID);
        Fluorescence_Dist{ID} = AB_Interstitium{j}(DistanceIDs);
        MEAN_FDDist(ID) = nanmean(Fluorescence_Dist{ID});
        STD_FDDist(ID) = nanstd(Fluorescence_Dist{ID});
        SEM_FDDist(ID) = nanstd(Fluorescence_Dist{ID})/sqrt(length(Fluorescence_Dist{ID}));
        clear DistanceIDs

        % save variables
        DistanceStatistics(k).RawDistancePixelFs{j,ID} = Fluorescence_Dist{ID};
        DistanceStatistics(k).NormDistancePixelFs{j,ID} = Fluorescence_Dist{ID}/Fmax;
        if j == 1
            DistanceStatistics(k).AllNormDistancePixelFs(1:length(Fluorescence_Dist{ID}),ID) = Fluorescence_Dist{ID}/Fmax;
            DistanceStatistics(k).AllRawDistancePixelFs(1:length(Fluorescence_Dist{ID}),ID) = Fluorescence_Dist{ID};
        else
            First_NaN_position = find(isnan(DistanceStatistics(k).AllNormDistancePixelFs(:,ID)) == 1, 1, 'first');
            DistanceStatistics(k).AllNormDistancePixelFs(First_NaN_position:First_NaN_position+length(Fluorescence_Dist{ID})-
1,ID) = Fluorescence_Dist{ID}/Fmax;
            DistanceStatistics(k).AllRawDistancePixelFs(First_NaN_position:First_NaN_position+length(Fluorescence_Dist{ID})-
1,ID) = Fluorescence_Dist{ID};
            clear First_NaN_position
        end
        DistanceStatistics(k).DistanceMeans(j,ID) = MEAN_FDDist(ID);
        DistanceStatistics(k).DistanceSTDs(j,ID) = STD_FDDist(ID);
        DistanceStatistics(k).DistanceSEMs(j,ID) = SEM_FDDist(ID);
        if k == 1
            Excel_ZT7(ID,j) = MEAN_FDDist(ID);
        elseif k == 2
            Excel_ZT19(ID,j) = MEAN_FDDist(ID);
        elseif k == 3
            Excel_isoZT7(ID,j) = MEAN_FDDist(ID);
        elseif k == 4
            Excel_isoZT19(ID,j) = MEAN_FDDist(ID);
        elseif k == 5
            Excel_KO_ZT7(ID,j) = MEAN_FDDist(ID);
        elseif k == 6
            Excel_KO_ZT19(ID,j) = MEAN_FDDist(ID);
        end
    end
    clear ID
end
end

% calculate Means, STDs and SEMs for each distance over all pictures (repetitions)
for i = 1:length(DistanceStatistics(k).AllNormDistancePixelFs(1,:))
    DistanceStatistics(k).GlobalDistanceMeans(i) = nanmean(DistanceStatistics(k).AllRawDistancePixelFs(:,i));
    DistanceStatistics(k).GlobalDistanceSTDs(i) = nanstd(DistanceStatistics(k).AllRawDistancePixelFs(:,i));
end

```

```

        DistanceStatistics(k).GlobalDistanceSEMs(i) =
nanstd(DistanceStatistics(k).AllRawDistancePixelFs(:,i))/sqrt(sum(~isnan(DistanceStatistics(k).AllRawDistancePixelFs(:,i))));
    end
end

%% Normalize Means, STDs and SEMs to Means (non-control) for plotting

if Nr_StainingProtocols == 2
    for m = 1:Nr_StainingProtocols
        if m == 1
            DistanceStatistics(m).normGlobalDistanceMeans =
DistanceStatistics(m).GlobalDistanceMeans/max(DistanceStatistics(m).GlobalDistanceMeans);
            DistanceStatistics(m).normGlobalDistanceSTDs =
DistanceStatistics(m).GlobalDistanceSTDs/max(DistanceStatistics(m).GlobalDistanceMeans);
            DistanceStatistics(m).normGlobalDistanceSEMs =
DistanceStatistics(m).GlobalDistanceSEMs/max(DistanceStatistics(m).GlobalDistanceMeans);
        else
            DistanceStatistics(m).normGlobalDistanceMeans = DistanceStatistics(m).GlobalDistanceMeans/max(DistanceStatistics(m-1).GlobalDistanceMeans);
            DistanceStatistics(m).normGlobalDistanceSTDs = DistanceStatistics(m).GlobalDistanceSTDs/max(DistanceStatistics(m-1).GlobalDistanceMeans);
            DistanceStatistics(m).normGlobalDistanceSEMs = DistanceStatistics(m).GlobalDistanceSEMs/max(DistanceStatistics(m-1).GlobalDistanceMeans);
        end
    end
elseif Nr_StainingProtocols == 4
    for m = 1:Nr_StainingProtocols
        if m == 1 || 2
            DistanceStatistics(m).normGlobalDistanceMeans =
DistanceStatistics(m).GlobalDistanceMeans/max(DistanceStatistics(m).GlobalDistanceMeans);
            DistanceStatistics(m).normGlobalDistanceSTDs =
DistanceStatistics(m).GlobalDistanceSTDs/max(DistanceStatistics(m).GlobalDistanceMeans);
            DistanceStatistics(m).normGlobalDistanceSEMs =
DistanceStatistics(m).GlobalDistanceSEMs/max(DistanceStatistics(m).GlobalDistanceMeans);
        elseif m == 3 || 4
            DistanceStatistics(m).normGlobalDistanceMeans = DistanceStatistics(m).GlobalDistanceMeans/max(DistanceStatistics(m-2).GlobalDistanceMeans);
            DistanceStatistics(m).normGlobalDistanceSTDs = DistanceStatistics(m).GlobalDistanceSTDs/max(DistanceStatistics(m-2).GlobalDistanceMeans);
            DistanceStatistics(m).normGlobalDistanceSEMs = DistanceStatistics(m).GlobalDistanceSEMs/max(DistanceStatistics(m-2).GlobalDistanceMeans);
        end
    end
elseif Nr_StainingProtocols == 6
    for m = 1:Nr_StainingProtocols
        if m == 1 || 2
            DistanceStatistics(m).normGlobalDistanceMeans =
DistanceStatistics(m).GlobalDistanceMeans/max(DistanceStatistics(m).GlobalDistanceMeans);
            DistanceStatistics(m).normGlobalDistanceSTDs =
DistanceStatistics(m).GlobalDistanceSTDs/max(DistanceStatistics(m).GlobalDistanceMeans);
            DistanceStatistics(m).normGlobalDistanceSEMs =
DistanceStatistics(m).GlobalDistanceSEMs/max(DistanceStatistics(m).GlobalDistanceMeans);
        elseif m == 3 || 4
            DistanceStatistics(m).normGlobalDistanceMeans = DistanceStatistics(m).GlobalDistanceMeans/max(DistanceStatistics(m-2).GlobalDistanceMeans);
            DistanceStatistics(m).normGlobalDistanceSTDs = DistanceStatistics(m).GlobalDistanceSTDs/max(DistanceStatistics(m-2).GlobalDistanceMeans);
            DistanceStatistics(m).normGlobalDistanceSEMs = DistanceStatistics(m).GlobalDistanceSEMs/max(DistanceStatistics(m-2).GlobalDistanceMeans);
        elseif m == 5 || 6
            DistanceStatistics(m).normGlobalDistanceMeans =
DistanceStatistics(m).GlobalDistanceMeans/max(DistanceStatistics(m).GlobalDistanceMeans);
            DistanceStatistics(m).normGlobalDistanceSTDs =
DistanceStatistics(m).GlobalDistanceSTDs/max(DistanceStatistics(m).GlobalDistanceMeans);
            DistanceStatistics(m).normGlobalDistanceSEMs =
DistanceStatistics(m).GlobalDistanceSEMs/max(DistanceStatistics(m).GlobalDistanceMeans);
        end
    end
end
end

```

```

%% plot distance dependent fluorescence values (normalized to F(max)) of Interstitium (relative from Lymph Vessel)

% plot mean F with SEM
if Nr_StainingProtocols == 2
    f2 = figure('Name','Distance Dependent F','color','w');
    hold on

    errorbar((1:length(DistanceStatistics(1).normGlobalDistanceMeans)),DistanceStatistics(1).normGlobalDistanceMeans,DistanceStatistics(1).normGlobalDistanceSEMs,','MarkerSize',15)

    errorbar((1:length(DistanceStatistics(2).normGlobalDistanceMeans)),DistanceStatistics(2).normGlobalDistanceMeans,DistanceStatistics(2).normGlobalDistanceSEMs,','MarkerSize',15)
    title('Distance Dependent Fluorescence');
    xlabel('Distance from LV [um]');
    ylabel('Normalized Fluorescence Intensity');
    legend('ZT7','iso control')
    xlim([0 100]);
    ylim_curr = get(gca,'ylim');
    ylim_curr(2) = 1;
    set(gca,'ylim',ylim_curr)
    hold off
elseif Nr_StainingProtocols == 4
    f2 = figure('Name','Distance Dependent F','color','w');
    hold on

    errorbar((1:length(DistanceStatistics(1).normGlobalDistanceMeans)),DistanceStatistics(1).normGlobalDistanceMeans,DistanceStatistics(1).normGlobalDistanceSEMs,','MarkerSize',15)

    errorbar((1:length(DistanceStatistics(2).normGlobalDistanceMeans)),DistanceStatistics(2).normGlobalDistanceMeans,DistanceStatistics(2).normGlobalDistanceSEMs,','MarkerSize',15)

    errorbar((1:length(DistanceStatistics(3).normGlobalDistanceMeans)),DistanceStatistics(3).normGlobalDistanceMeans,DistanceStatistics(3).normGlobalDistanceSEMs,','MarkerSize',15)

    errorbar((1:length(DistanceStatistics(4).normGlobalDistanceMeans)),DistanceStatistics(4).normGlobalDistanceMeans,DistanceStatistics(4).normGlobalDistanceSEMs,','MarkerSize',15)
    title('Distance Dependent Fluorescence');
    xlabel('Distance from LV [um]');
    ylabel('Normalized Fluorescence Intensity');
    legend('ZT7','ZT19','ZT7 iso control','ZT19 iso control')
    xlim([0 100]);
    ylim_curr = get(gca,'ylim');
    ylim_curr(2) = 1;
    set(gca,'ylim',ylim_curr)
    hold off
elseif Nr_StainingProtocols == 6
    f2 = figure('Name','Distance Dependent F','color','w');
    hold on

    errorbar((1:length(DistanceStatistics(1).normGlobalDistanceMeans)),DistanceStatistics(1).normGlobalDistanceMeans,DistanceStatistics(1).normGlobalDistanceSEMs,','MarkerSize',15)

    errorbar((1:length(DistanceStatistics(2).normGlobalDistanceMeans)),DistanceStatistics(2).normGlobalDistanceMeans,DistanceStatistics(2).normGlobalDistanceSEMs,','MarkerSize',15)

    errorbar((1:length(DistanceStatistics(3).normGlobalDistanceMeans)),DistanceStatistics(3).normGlobalDistanceMeans,DistanceStatistics(3).normGlobalDistanceSEMs,','MarkerSize',15)

    errorbar((1:length(DistanceStatistics(4).normGlobalDistanceMeans)),DistanceStatistics(4).normGlobalDistanceMeans,DistanceStatistics(4).normGlobalDistanceSEMs,','MarkerSize',15)

    errorbar((1:length(DistanceStatistics(5).normGlobalDistanceMeans)),DistanceStatistics(5).normGlobalDistanceMeans,DistanceStatistics(5).normGlobalDistanceSEMs,','MarkerSize',15)

    errorbar((1:length(DistanceStatistics(6).normGlobalDistanceMeans)),DistanceStatistics(6).normGlobalDistanceMeans,DistanceStatistics(6).normGlobalDistanceSEMs,','MarkerSize',15)
    title('Distance Dependent Fluorescence');
    xlabel('Distance from LV [um]');
    ylabel('Normalized Fluorescence Intensity');
    legend('WT ZT7','WT ZT19','WT ZT7 iso control','WT ZT19 iso control','KO ZT7','KO ZT19')

```

```

xlim([0 100]);
ylim_curr = get(gca,'ylim');
ylim_curr(2) = 1;
set(gca,'ylim',ylim_curr)
hold off
end

toc

%% save plot and data matrix

% save plot
saveas(f2,'DistanceDependentF.fig');
saveas(f2,'DistanceDependentF.svg');
saveas(f2,'DistanceDependentF.pdf');

% save data matrix
save('DistanceDependentF_ExcelMeanMatrices.mat','Excel_ZT7','Excel_ZT19','Excel_isoZT7','Excel_isoZT19')
save('DistanceDependentF_DataMatrix.mat','DistanceStatistics','-v7.3')
xlswrite('DistanceDependentF_ZT7.xlsx',Excel_ZT7);
xlswrite('DistanceDependentF_ZT19.xlsx',Excel_ZT19);
xlswrite('DistanceDependentF_isoZT7.xlsx',Excel_isoZT7);
xlswrite('DistanceDependentF_isoZT19.xlsx',Excel_isoZT19);
xlswrite('DistanceDependentF_KO_ZT7.xlsx',Excel_KO_ZT7);
xlswrite('DistanceDependentF_KO_ZT19.xlsx',Excel_KO_ZT19);

```

“Mini” crawl-in assay with interstitial segmentation (Matlab)

```

function Stephan_20MicronContourLines

%% select and load all relevant data

% select all Cell/Interstitial images
[FileNames,FilePath] = uigetfile('.tif','Select Cell images','MultiSelect','on');
Nr_files = length(FileNames);

% change directory to filepath
cd(FilePath)

% preallocate
LymphMasks = cell(Nr_files,1);
Cell_image = cell(Nr_files,1);
Lymph_image = cell(Nr_files,1);
Pixel2Microns = NaN(Nr_files,1);

% load Cell/Interstitial images and Lymph ROIs with Pixel Conversion Factors
for i = 1:Nr_files
    FileName_temp = FileNames{i};
    % ImlInfo_temp = imfinfo(FileName_temp);
    % Pixel2Microns(i) = 1/ImlInfo_temp.XResolution;
    Pixel2Microns(i) = 1/1.5;
    if exist(['ROI_Mask_' FileName_temp(1:end-10) '_LV.mat'],'file') > 0
        LymphMasks{i} = load(['ROI_Mask_' FileName_temp(1:end-10) '_LV.mat']);
    end
end

```

```

    Cell_image{i} = imread([FileName_temp(1:end-10) '_LV.tif']);
elseif exist(['ROI_Mask_' FileName_temp(1:end-5) '0.mat'],'file') > 0
    LymphMasks{i} = load(['ROI_Mask_' FileName_temp(1:end-5) '0.mat']);
    Cell_image{i} = imread([FileName_temp(1:end-5) '0.tif']);
else
    LymphMasks{i} = load(['ROI_Mask_' FileName_temp(1:end-5) '1.mat']);
    Cell_image{i} = imread(FileName_temp);
    Lymph_image{i} = imread([FileName_temp(1:end-5) '1.tif']);
end
clear FileName_temp
clear lmlInfo_temp
end

%% calculate and plot 20 microns contour lines from Lymphatic ROI for each selected image

for j = 1:Nr_files

    % create distance mask around Lymph Vessel mask (round to nearest decimal)
    DistanceMask = round(bwdist(LymphMasks{j,1}.ROI_Mask,'euclidean')*Pixel2Microns(j));

    % extract contour lines in 20 micron steps up to 100 microns
    [CL20_Y,CL20_X] = find(DistanceMask == 20);
    [CL40_Y,CL40_X] = find(DistanceMask == 40);
    [CL60_Y,CL60_X] = find(DistanceMask == 60);
    [CL80_Y,CL80_X] = find(DistanceMask == 80);
    [CL100_Y,CL100_X] = find(DistanceMask == 100);

    % find pixels of ROI and Perimeter
    Lymph_mask_perim = bwperim(LymphMasks{j,1}.ROI_Mask);
    [ROIperim_IDs_Y,ROIperim_IDs_X] = find(Lymph_mask_perim);

    % define colormap for colormap indexing
    Colormap = cool(5);

    % plot cell picture and overlay contour lines
    f1 = figure;
    imshow(Cell_image{j});
    hold on
    plot(ROIperim_IDs_X,ROIperim_IDs_Y,'.w','MarkerSize',1.5)
    plot(CL20_X,CL20_Y,'.', 'Color',[Colormap(1,:)],'MarkerSize',1.5)
    plot(CL40_X,CL40_Y,'.', 'Color',[Colormap(2,:)],'MarkerSize',1.5)
    plot(CL60_X,CL60_Y,'.', 'Color',[Colormap(3,:)],'MarkerSize',1.5)
    plot(CL80_X,CL80_Y,'.', 'Color',[Colormap(4,:)],'MarkerSize',1.5)
    plot(CL100_X,CL100_Y,'.', 'Color',[Colormap(5,:)],'MarkerSize',1.5)
    % title('20 micron contour lines')
    axis off
    hold off

```

```

% save figure
saveas(f1,[char(FileNames(j)) '_Cell_ROI_20umContour.fig']);
export_fig(f1,[char(FileNames(j)) '_Cell_ROI_20umContour.png']);
% saveas(f1,[char(FileNames(j)) '_Cell_ROI_20umContour.pdf']);

% plot lymph picture and overlay contour lines
f2 = figure;
imshow(Lymph_image{j});
hold on
plot(ROIperim_IDs_X,ROIperim_IDs_Y,'.w','MarkerSize',1.5)
plot(CL20_X,CL20_Y,'.r','Color',[Colormap(1,:)],'MarkerSize',1.5)
plot(CL40_X,CL40_Y,'.g','Color',[Colormap(2,:)],'MarkerSize',1.5)
plot(CL60_X,CL60_Y,'.b','Color',[Colormap(3,:)],'MarkerSize',1.5)
plot(CL80_X,CL80_Y,'.m','Color',[Colormap(4,:)],'MarkerSize',1.5)
plot(CL100_X,CL100_Y,'.k','Color',[Colormap(5,:)],'MarkerSize',1.5)
% title('20 micron contour lines')
axis off
hold off

% save figure
saveas(f2,[char(FileNames(j)) '_Lymph_ROI_20umContour.fig']);
export_fig(f2,[char(FileNames(j)) '_Lymph_ROI_20umContour.png']);
% export_fig(f2,[char(FileNames(j)) '_Lymph_ROI_20umContour.pdf']);
end

```

7.3 Promoter binding sites of clock genes

Ccl21a

Arntl [*p*-value = 0.01]: 83, 82, -72, -73, -86, -98, -172, -292, -293, -409, -418, -448, -449, -966, -967, -1221, -1228, -1235, -1244, -1261, -1342, -1384, -1405, -1586, -1587, -1833, -1968, -1982, -1983

Arntl [*p*-value = 0.001]: -966, -1586, -1587, -1982

Arntl [*p*-value = 0.0001]: -1586

Dbp [*p*-value = 0.01]: 49, -29, -81, -82, -299, -300, -362, -363, -399, -400, -413, -414, -565, -650, -651, -720, -721, -740, -956, -957, -1273, -1274, -1405, -1406, -1434, -1900, -1901, -1977

Dbp [*p*-value = 0.001]: -650, -651

Dbp [*p*-value = 0.0001]: none

Nfil3 [*p*-value = 0.01]: -31, -298, -301, -401, -412, -472, -564, -567, -599, -616, -644, -649, -719, -722, -811, -814, -884, -891, -916, -942, -958, -960, -970, -1240, -1272, -1275, -1311, -1483, -1493, -1541, -1644, -1692, -1899, -1962

Nfil3 [*p*-value = 0.001]: -301, -884, -1692

Nfil3 [*p*-value = 0.0001]: none

Rora/Nr1d1/Nr1d2 [*p*-value = 0.01]: 91, 77, 37, 12, -78, -164, -192, -238, -425, -513, -535, -539, -660, -721, -736, -789, -901, -946, -961, -1008, -1176, -1195, -1216, -1233, -1244, -1298, -1400, -1417, -1497, -1529, -1663, -1669, -1683, -1779, -1814, -1888, -1900, -1938, -1952, -1967

Rora/Nr1d1/Nr1d2 [*p*-value = 0.001]: -1008, -1417, -1888, -1900, -1952

Rora/Nr1d1/Nr1d2 [*p*-value = 0.0001]: none

Promoter sequence of Ccl21a and Bmal1 canonical binding sites (as an example of methodology):

Red shows canonical (CAN NTG) Bmal1 binding site.

(-2000) gaaagaacat ccacacacat gaaataaaat cacttttita atttaaaga tcaagtcatt (-1941)

gaagtcaaaa gtgaaagtag ggacatcagt ataattgac ataaataaaa aaggtccaat (-1881)

aaaccgggtg tgggtgtgct tgcttttaat ccagactgg ggaggcaggg ggaggtggat (-1821)

ctctgagttc aaagccagcc tgctctacag agcaagttct aggatagcca gggctacaca (-1761)

gagaaacct gtctcaaac aaaaaacaaa caacaaagca aaaaacaaac aaacaaaaag (-1701)

agtggtctat gtatgactct gttccaacct agtgaaatg gataaattcc aaactcaca (-1641)

aatctacaaa aatcagctgg agaggaaacg cacctccgag tgcattcaca **ccacgtg**aga (-1581)

acacggaata aggagtaaca attgccaaat acccaacta agaaaatacc aggtccaatg (-1521)

gcttcagtgt gaattctct caacatcaca acagttttaa catccattgt tctcaaagtt (-1461)

tccaaaagtc tgaagagctg gcattcccta acacagtgtc tgaggtcagc gttacctgat (-1401)

cctgaggctg gaaaacgagc ctacaggaaa acagcagacc aacccccat cctcatacat (-1341)

gaaaacacaa aagtcctcca caaatatta aaaaaaaaaac aaactcagca gcacagtga (-1281)

gtattatata ctacgac **caa gtg**gggtctg ctctcaggtt aaaacaagac cacattaaca (-1221)

tgaaggggaa acccatactt ctccgatca ggaacataca agatgctcac ttcaacccaa (-1161)

cagtccaagc tatagtgag agagggaggg agggagagag agagagagag agagagagag (-1101)

agagagagag agagagagag agagagagaa ctattagcaa ttaataattc cagcactcag (-1041)

aggcagaggc aggtagatct ctgtgagttc aaggccaacc tggctatga atcccagaac (-981)

agccaaggct **catgtg**aca ttgtgtctca aaaaagtaac aacaataaca acaacaacaa (-921)

aattccaaaa ggaataaag aacacaatta tattataac agcaccaaac agaatactta (-861)

cagacaaatt taatccagta ggtataagac ttatactgtg aaaaatacaa aacattctaa (-801)

ttaaaggagg cctaataatgaa taaaagccta tcccttattc ttggattgaa ttctaatttt (-741)
 acaaagacag tgataacgac gtaagtggtc ctcagattca gtacaatattc tattagaatc (-610)
 cctagggagg gatggaaagg ggacagttgt gtaattatat tataatccca aaagctaaaa (-621)
 gaaataataa taaataaaac ataagggagg ggcagaaaga tggctcagca cttatggaag (-561)
 ggtgttgctc ttgagagga cctgagttca gttccctgca ccctcaccta ccaactccac (-501)
 ttacagccac acaaaaatac acattgtttt aaaaagcaga ggaaagtttc atgggcttgg (-441)
 atctgttaat gatcggttca gtgtgatgac gcggtagtaa catcacagct agtaggggaa (-381)
 gagggggagt tgggtttcac aaaacttaa aatttgtgc gctactatca ggaagtctat (-321)
 agactgagag gatgcagtta tatatcatatgtctaaaata aggcctattg tcagggatct (-261)
 ataaagaact cctagtattc agctagatta ttacttgccg aaaggagagg agatgtgtgg (-201)
 ggccctaagg gcagggagga agcaatcatg ctttggggac agtggctgga aggaccaggg (-141)
 agagatgagg agctgaacag ctaggagctg actgtatgct cacactaatg ccatctgac (-81)
 caactcacag gaaaaggagg gggagcaggg gaagcgaag tctcagactg cataaatagg (-21)
 cagcaagcca gtcgcagccc (0) ACACACACAG ACCCCAATT GCGGCTGTCC ATCTCACCTA (+40)
 CAGCTCTGGT CTCATCTCA ACTCAACCAC AATCATGGCT CAGATGATGA CTCTGAGCCTC (+100)

Ccl21b/c

Arntl [p-value = 0.01]: -1761, -1760, -1579, -1558, -1516, -1435, -1418, -1402, -1395, -1341, -1330, -967, -966, -449, -448, -418, -293, -292, -172, -105, -98, -86, -73, -72, 82, 83

Arntl [p-value = 0.001]: -1761, -1760, -966

Arntl [p-value = 0.0001]: -1760

Dbp [p-value = 0.01]: -1608, -1580, -1579, -1519, -1518, -1448, -1447, -1361, -1360, -957, -956, -740, -721, -720, -651, -650, -565, -414, -413, -400, -399, -363, -362, -300, -82, -81, -29, 49

Dbp [p-value = 0.001]: -651, -650

Dbp [p-value = 0.0001]: none

Nfil3 [p-value = 0.01]: -1866, -1715, -1667, -1657, -1520, -1449, -1446, -1414, -1362, -1281, -970, -960, -958, -942, -916, -891, -884, -814, -811, -722, -719, -649, -644, -616, -599, -567, -564, -472, -412, -401, -31

Nfil3 [p-value = 0.001]: -1866, -884

Nfil3 [p-value = 0.0001]: none

Rora/Nr1d1/Nr1d2 [p-value = 0.01]: -1988, -1953, -1857, -1843, -1837, -1703, -1671, -1591, -1574, -1472, -1418, -1407, -1390, -1336, -1271, -1243, -1222, -1213, -1194, -1008, -961, -946, -901, -789, -736, -721, -660, -539, -535, -513, -425, -238, -192, -164, -108, -78, 12, 37, 77, 91

Rora/Nr1d1/Nr1d2 [p-value = 0.001]: -1591, -1407, -1008

Rora/Nr1d1/Nr1d2 [p-value = 0.0001]: -1008

Lyve1

Arntl [p-value = 0.01]: 31, -54, -147, -148, -177, -239, -275, -276, -355, -372, -454, -455, -553, -554, -617, -618, -673, -696, -796, -836, -853, -916, -917, -1139, -1153, -1171, -1339, -1340, -1381, -1382, -1402, -1457, -1478, -1489, -1490, -1515, -1516, -1558, -1592, -1671, -1694, -1818, -1846, -1872

Arntl [p-value = 0.001]: -276, -455, -916, -917, -1339, -1516

Arntl [p-value = 0.0001]: -276

Dbp [p-value = 0.01]: -123, -172, -173, -330, -331, -374, -375, -448, -449, -536, -537, -644, -645, -742, -743, -800, -801, -819, -820, -848, -849, -887, -950, -951, -1024, -1025, -1212, -1213, -1314, -1351, -1352, -1471, -1472, -1597, -1711, -1712, -1740, -1741, -1763, -1764, -1888, -1889, -1956

Dbp [p-value = 0.001]: -819, -820, -848, -849, -1471, -1472, -1888, -1889

Dbp [p-value = 0.0001]: none

Nfil3 [p -value = 0.01]: -376, -414, -447, -505, -729, -741, -744, -799, -802, -821, -847, -949, -1140, -1211, -1317, -1350, -1353, -1470, -1473, -1509, -1679, -1710, -1713, -1739, -1842, -1887, -1890, -1919

Nfil3 [p -value = 0.001]: -741, -799, -1890

Nfil3 [p -value = 0.0001]: -1890

Rora/Nr1d1/Nr1d2 [p -value = 0.01]: 67, -68, -72, -123, -135, -149, -172, -365, -441, -456, -510, -543, -562, -644, -731, -848, -922, -1073, -1194, -1207, -1235, -1254, -1258, -1278, -1297, -1315, -1322, -1340, -1372, -1392, -1437, -1472, -1521, -1562, -1569, -1699, -1722, -1749, -1815, -1910, -1944, -1968

Rora/Nr1d1/Nr1d2 [p -value = 0.001]: -1073, -1562, -1749, -1910

Rora/Nr1d1/Nr1d2 [p -value = 0.0001]: none

Jam3

Arntl [p -value = 0.01]: 86, 51, 0, -35, -36, -96, -97, -180, -181, -226, -351, -352, -412, -413, -449, -471, -496, -518, -519, -550, -574, -895

Arntl [p -value = 0.001]: -519

Arntl [p -value = 0.0001]: none

Dbp [p -value = 0.01]: -255, -256, -294, -295, -461, -524, -562, -684, -685, -769, -770, -836, -837, -895, -896

Dbp [p -value = 0.001]: none

Dbp [p -value = 0.0001]: none

Nfil3 [p -value = 0.01]: -87, -186, -254, -257, -275, -282, -541, -562, -587, -621, -683, -705, -768, -835, -838, -894, -897, -973, -974, -987, -990

Nfil3 [p -value = 0.001]: none

Nfil3 [p -value = 0.0001]: none

Rora/Nr1d1/Nr1d2 [p -value = 0.01]: 88, 64, -7, -128, -135, -166, -201, -309, -367, -371, -401, -441, -454, -532, -579, -611, -704, -780, -793, -825, -858, -873, -935

Rora/Nr1d1/Nr1d2 [p -value = 0.001]: -128, -454, -611

Rora/Nr1d1/Nr1d2 [p -value = 0.0001]: none

F11r

Arntl [p -value = 0.01]: -1975, -1880, -1879, -1698, -1536, -1533, -1107, -1106, -1026, -841, -840, -371, -356, -337, -211, -137, -136, 9, 10

Arntl [p -value = 0.001]: none

Arntl [p -value = 0.0001]: none

Dbp [p -value = 0.01]: -1980, -1979, -1594, -1359, -1358, -810, -805, -773, -772

Dbp [p -value = 0.001]: none

Dbp [p -value = 0.0001]: none

Nfil3 [p -value = 0.01]: -1981, -1978, -1769, -1532, -1384, -1307, -1207, -1067, -1037, -1022, -804, -774, -771, -747, -670, -577, -547, -468

Nfil3 [p -value = 0.001]: -747

Nfil3 [p -value = 0.0001]: none

Rora/Nr1d1/Nr1d2 [p -value = 0.01]: -1940, -1910, -1893, -1874, -1828, -1801, -1795, -1760, -1724, -1716, -1707, -1693, -1664, -1644, -1602, -1557, -1541, -1497, -1437, -1418, -1364, -1350, -1329, -1324, -1277, -1218, -1192, -1175, -1163, -1066, -1031, -956, -846, -727, -696, -644, -620, -589, -573, -545, -345, -312, -207, -196, -186, -26, -4

Rora/Nr1d1/Nr1d2 [p -value = 0.001]: -1801, -1602, -1175, -644, -589, -345

Rora/Nr1d1/Nr1d2 [p -value = 0.0001]: none

CD99L2

Arntl [p -value = 0.01]: 42, 41, -13, -58, -59, -79, -96, -97, -135, -167, -220, -223, -324, -325, -379, -408, -486, -487, -545, -558, -575, -576, -748, -769, -770, -844, -849, -1030, -1187, -1188, -1234, -1331, -1463, -1464, -1690, -1691, -1715, -1716, -1880, -1881, -1917, -1960, -1961, -1979, -1980

Arntl [p -value = 0.001]: 41

Arntl [*p*-value = 0.0001]: none

Dbp [*p*-value = 0.01]: -162, -163, -227, -228, -390, -433, -434, -495, -496, -758, -1118, -1119, -1195, -1196, -1357, -1451, -1452, -1468, -1469, -1544, -1545, -1664, -1958, -1959, -1976

Dbp [*p*-value = 0.001]: -1118

Dbp [*p*-value = 0.0001]: none

Nfil3 [*p*-value = 0.01]: -139, -350, -392, -517, -980, -1107, -1117, -1120, -1194, -1228, -1283, -1358, -1453, -1457, -1522, -1536, -1543, -1960

Nfil3 [*p*-value = 0.001]: -1117, -1453

Nfil3 [*p*-value = 0.0001]: none

Rora/Nr1d1/Nr1d2 [*p*-value = 0.01]: 60, -35, -53, -64, -162, -215, -257, -261, -281, -306, -380, -428, -451, -507, -550, -711, -779, -783, -827, -946, -978, -1138, -1171, -1207, -1246, -1276, -1325, -1364, -1387, -1406, -1458, -1487, -1642, -1703, -1813, -1850, -1875, -1886, -1952, -1984

Rora/Nr1d1/Nr1d2 [*p*-value = 0.001]: -64, -257, -1952

Rora/Nr1d1/Nr1d2 [*p*-value = 0.0001]: -1952

Reln

Arntl [*p*-value = 0.01]: 93, 75, 74, 22, 21, -7, -39, -71, -72, -97, -117, -133, -134, -153, -154, -218, -247, -263, -264, -294, -363, -433, -445, -454, -475, -499, -500, -555, -556, -623, -742, -818, -821, -834, -835, -854, -855, -880, -888, -921, -1107, -1202, -1203, -1245, -1246, -1317, -1404, -1411, -1463, -1464, -1570, -1605, -1672, -1757, -1758, -1769, -1770, -1892, -1904, -1987, -1988

Arntl [*p*-value = 0.001]: 21, -71, -72, -854, -1203, -1570, -1757, -1758, -1987

Arntl [*p*-value = 0.0001]: -72

Dbp [*p*-value = 0.01]: -537, -996, -997, -1083, -1084, -1216, -1217, -1269, -1270, -1639, -1849, -1850, -1908, -1909

Dbp [*p*-value = 0.001]: none

Dbp [*p*-value = 0.0001]: none

Nfil3 [*p*-value = 0.01]: -712, -812, -861, -995, -1072, -1082, -1268, -1271, -1515, -1521, -1583, -1586, -1601, -1637, -1655, -1693, -1872, -1910

Nfil3 [*p*-value = 0.001]: -1601

Nfil3 [*p*-value = 0.0001]: none

Rora/Nr1d1/Nr1d2 [*p*-value = 0.01]: -26, -246, -266, -403, -426, -444, -501, -536, -698, -721, -734, -810, -942, -996, -1036, -1064, -1136, -1177, -1255, -1343, -1364, -1552, -1593, -1665, -1745, -1799, -1838, -1881, -1897, -1969

Rora/Nr1d1/Nr1d2 [*p*-value = 0.001]: -1838

Rora/Nr1d1/Nr1d2 [*p*-value = 0.0001]: none

Ackr4

Arntl [*p*-value = 0.01]: 78, -44, -71, -72, -96, -97, -172, -173, -229, -230, -402, -456, -472, -512, -766, -767, -1149, -1150, -1168, -1237, -1288, -1456, -1484, -1485, -1587, -1601, -1615, -1616, -1738, -1739, -1835, -1873

Arntl [*p*-value = 0.001]: -1149, -1150

Arntl [*p*-value = 0.0001]: none

Dbp [*p*-value = 0.01]: -60, -73, -74, -148, -288, -289, -304, -410, -953, -976, -1048, -1049, -1157, -1158, -1460, -1461, -1473, -1474, -1582, -1583, -1599, -1632, -1633, -1757, -1839, -1840

Dbp [*p*-value = 0.001]: -1757

Dbp [*p*-value = 0.0001]: none

Nfil3 [*p*-value = 0.01]: -201, -331, -646, -694, -954, -975, -1000, -1047, -1050, -1159, -1211, -1385, -1388, -1553, -1581, -1584, -1707, -1720, -1751, -1756, -1770, -1861, -1959, -1980

Nfil3 [*p*-value = 0.001]: -1707, -1751

Nfil3 [*p*-value = 0.0001]: none

Rora/Nr1d1/Nr1d2 [*p*-value = 0.01]: 3, -34, -62, -85, -122, -161, -183, -210, -228, -344, -517, -543, -597, -621, -632, -647, -696, -746, -777, -789, -805, -945, -998, -1035, -1061, -1130, -1146, -1197, -1273, -1325, -1338, -1444, -1512, -1557, -1600, -1744, -1792, -1820, -1868, -1885, -1924

Rora/Nr1d1/Nr1d2 [p-value = 0.001]: -85, -1061, -1557

Rora/Nr1d1/Nr1d2 [p-value = 0.0001]: none

Ccr7

Arntl [p-value = 0.01]: 51, 50, -54, -85, -93, -103, -116, -257, -258, -324, -373, -374, -484, -485, -740, -748, -769, -770, -887, -914, -915, -937, -965, -966, -990, -991, -1025, -1057, -1085, -1135, -1136, -1187, -1188, -1269, -1270, -1337, -1338, -1507, -1529, -1530, -1555, -1669, -1670, -1751, -1935, -1936, -1952, -1953, -1963

Arntl [p-value = 0.001]: -914, -915, -965, -966, -990, -1269

Arntl [p-value = 0.0001]: none

Dbp [p-value = 0.01]: -199, -200, -341, -428, -429, -568, -569, -771, -772, -955, -956, -1198, -1199, -1430, -1610, -1611, -1646, -1647, -1755

Dbp [p-value = 0.001]: -428, -429

Dbp [p-value = 0.0001]: none

Nfil3 [p-value = 0.01]: -97, -116, -198, -245, -430, -499, -667, -857, -873, -1024, -1126, -1418, -1429, -1551, -1612, -1630, -1648, -1704, -1818, -1821

Nfil3 [p-value = 0.001]: -198, -1612

Nfil3 [p-value = 0.0001]: none

Rora/Nr1d1/Nr1d2 [p-value = 0.01]: 88, 85, -80, -261, -303, -323, -326, -386, -490, -560, -665, -684, -704, -764, -787, -802, -856, -868, -973, -985, -1042, -1056, -1067, -1197, -1220, -1264, -1300, -1405, -1423, -1438, -1441, -1475, -1502, -1568, -1596, -1627, -1655, -1754, -1823, -1847, -1865, -1886, -1958, -1971

Rora/Nr1d1/Nr1d2 [p-value = 0.001]: -323, -490, -684, -787, -1264, -1958

Rora/Nr1d1/Nr1d2 [p-value = 0.0001]: none

Cd80

Arntl [p-value = 0.01]: -1904, -1883, -1858, -1769, -1745, -1644, -1643, -1525, -1524, -1464, -1426, -1414, -1413, -1334, -1309, -1289, -1288, -1132, -1131, -1069, -1068, -992, -796, -795, -586, -432, -431, -226, -192, -87, -19, 78

Arntl [p-value = 0.001]: -1769, -1643, -1525, -1413, -431

Arntl [p-value = 0.0001]: none

Dbp [p-value = 0.01]: -1623, -1622, -1545, -1544, -828, -771, -665, -540, -539, -503, -469, -468, -330, -315, -314, 15, 16, 83, 84

Dbp [p-value = 0.001]: none

Dbp [p-value = 0.0001]: none

Nfil3 [p-value = 0.01]: -1899, -1868, -1685, -1652, -1546, -1452, -1423, -1393, -1276, -1233, -959, -948, -897, -875, -780, -663, -502, -467, -435, -336, -313, -195, -154, 17, 43, 82

Nfil3 [p-value = 0.001]: -897, 17

Nfil3 [p-value = 0.0001]: none

Rora/Nr1d1/Nr1d2 [p-value = 0.01]: -1934, -1863, -1845, -1829, -1787, -1774, -1633, -1590, -1532, -1507, -1467, -1431, -1396, -1327, -1239, -1228, -1216, -1197, -1147, -1115, -1099, -1005, -987, -916, -882, -841, -794, -649, -620, -589, -567, -412, -378, -236, -113, -100, -86, -34, -22, -9

Rora/Nr1d1/Nr1d2 [p-value = 0.001]: -620, -412

Rora/Nr1d1/Nr1d2 [p-value = 0.0001]: none

Cd86

Arntl [p-value = 0.01]: 87, 58, -150, -161, -251, -380, -405, -423, -496, -564, -752, -818, -900, -961, -962, -1001, -1002, -1026, -1027, -1135, -1152, -1251, -1259, -1401, -1476, -1477, -1535, -1536, -1564, -1681, -1765, -1792, -1793, -1843, -1844, -1905, -1906

Arntl [p-value = 0.001]: none

Arntl [p-value = 0.0001]: none

Dbp [p-value = 0.01]: -141, -396, -397, -450, -459, -495, -496, -520, -521, -592, -680, -681, -801, -802, -1254, -1255, -1509, -1510, -1664, -1686, -1977, -1978

Dbp [p-value = 0.001]: -1664

Dbp [p-value = 0.0001]: none

Nfil3 [p-value = 0.01]: -31, -265, -347, -395, -451, -519, -615, -682, -756, -803, -894, -1052, -1088, -1215, -1362, -1394, -1662, -1665, -1685, -1979

Nfil3 [p-value = 0.001]: -451, -519, -682

Nfil3 [p-value = 0.0001]: none

Rora/Nr1d1/Nr1d2 [p-value = 0.01]: -4, -24, -77, -104, -152, -287, -357, -376, -410, -495, -520, -555, -569, -670, -1015, -1074, -1090, -1107, -1157, -1187, -1380, -1527, -1569, -1619, -1631, -1717, -1723, -1782, -1794, -1915, -1946

Rora/Nr1d1/Nr1d2 [p-value = 0.001]: -410, -1717

Rora/Nr1d1/Nr1d2 [p-value = 0.0001]: none

Cd40

Arntl [p-value = 0.01]: -1911, -1870, -1869, -1832, -1791, -1722, -1486, -1415, -1414, -1344, -1234, -1199, -1143, -1142, -1092, -1089, -1002, -1001, -812, -811, -610, -609, -599, -596, -476, -359, -304, -22, -10, -2, 89, 90

Arntl [p-value = 0.001]: -610, -609

Arntl [p-value = 0.0001]: none

Dbp [p-value = 0.01]: -1130, -1129, -1044, -1043, -1014, -1013, -377, -376, -226, -225

Dbp [p-value = 0.001]: -1013

Dbp [p-value = 0.0001]: none

Nfil3 [p-value = 0.01]: -1896, -1625, -1365, -1286, -1012, -690, -227, -224

Nfil3 [p-value = 0.001]: -1012, -690

Nfil3 [p-value = 0.0001]: none

Rora/Nr1d1/Nr1d2 [p-value = 0.01]: -1974, -1944, -1895, -1882, -1860, -1827, -1794, -1741, -1606, -1586, -1519, -1420, -1406, -1349, -1313, -1294, -1229, -1186, -1137, -1084, -1079, -841, -835, -824, -806, -693, -624, -571, -514, -454, -435, -362, -269, -265, -200, -155, -24

Rora/Nr1d1/Nr1d2 [p-value = 0.001]: -1586, -1313, -1137, -693

Rora/Nr1d1/Nr1d2 [p-value = 0.0001]: none

7.5 List of publications

Manuscript in preparation	Time-of-day dependent leukocyte trafficking across lymphatics: Holtkamp, <i>et al.</i>
09/2020	<i>Ex-Vivo</i> whole mount imaging of the bone marrow: Holtkamp, Scheiermann, Springer (<i>in press</i>)
01/2020	Molecular interactions between components of the circadian clock and the immune system: Hergenhan, Holtkamp <i>et</i> Scheiermann, <i>Journal of Molecular Biology</i>
10/2018	A Circadian Zip Code guides leukocyte homing: He, Holtkamp <i>et al.</i> , <i>Immunity</i>

7.6 Affidavit

Stephan Jonas Holtkamp
Biomedizinisches Zentrum LMU
Großhaderner Straße 9
82152 Planegg-Martinsried
Germany

I hereby declare, that the submitted thesis entitled

Time-of-day dependent trafficking of leukocytes across lymphatics

is my own work. I have only used the sources indicated and have not made unauthorized use of services of a third party. Where the work of others has been quoted or reproduced, the source is always given.

I further declare that the submitted thesis or parts thereof have not been presented as part of an examination degree to any other university.

Munich, 08/10/2020

Place, Date

Stephan Jonas Holtkamp

Signature doctoral candidate

7.7 Confirmation of congruency between printed and electronic version of the doctoral thesis

Stephan Jonas Holtkamp
Biomedizinisches Zentrum LMU
Großhaderner Straße 9
82152 Planegg-Martinsried
Germany

hereby declare that the electronic version of the submitted thesis, entitled

Time-of-day dependent trafficking of leukocytes across lymphatics

is congruent with the printed version both in content and format.

Munich, 08/10/2020

Place, Date

Stephan Jonas Holtkamp

Signature doctoral candidate